Interference Reduction Techniques for Somatosensory Evoked Potential Enhancement

by

Vijay Parsa

B.E. — Osmania University, India.

M.Sc.E — University of New Brunswick.

A Thesis Submitted in Partial Fulfillment of

the Requirements for the Degree of

Doctor of Philosophy

in the

Dept. of Electrical Engineering

THE UNIVERSITY OF NEW BRUNSWICK

November, 1996

Abstract

Somatosensory Evoked Potentials (SEPs) are clinically valuable signals whose importance is highlighted in such applications as the diagnosis of neuromuscular disorders and in peripheral nerve and spinal cord monitoring. The main problem associated with SEP measurement is poor Signal-to-Noise Ratio (SNR). The prominent interference sources which corrupt the SEP are Myoelectric Interference (MEI), ECG and Stimulus Artifact (SA). Digital signal processing techniques are developed in this thesis which significantly reduce each of the abovementioned interferences.

Different Crosstalk Resistant Adaptive Noise Cancellers (CRANCs) are applied to the task of MEI reduction and their performance is scrutinized under a wide variety of operating conditions. A novel Multichannel CRANC (MCRANC) architecture is developed and its performance is evaluated analytically and through processing simulated and experimental MEI data.

Nonlinear Adaptive Filters (NAFs) based on truncated Volterra series are applied for the first time to the SA reduction problem. Various parameters which influence the SA reduction ability of the NAFs are identified and recommendations are made to compensate for these parameters.

The performance of various ECG cancellation techniques such as clipping, gating, and adaptive filtering is studied in detail. Modifications are made to the basic adaptive filter structure for ECG reduction and a method called the "template subtraction" and its adaptive version, the "Adaptive Template Subtraction (ATS)" are developed which display superior ECG cancellation results.

Contents

List of Tables

List of Figures

List of Symbols

A, C_1, C_2, D	scaling constants
B	signal blocking matrix in the GSC filter
c_n	MEI spectral shaping parameter
c_s	SEP spectral shaping parameter
$G(z)$	SEP crosstalk transfer function
$H(z)$	MEI transfer function between the primary and reference channels
I	frequency independent power performance index
$I(z)$	frequency dependent power performance index
k	discrete time index
$n_p(k)$	primary MEI component
$n_{ri}(k)$	MEI component in the *ith* reference channel
	(for single reference channel ANCs, the index i is dropped.)
R	myoelectric residue index
$R(z)$	frequency dependent myoelectric residue index
$SA(k)$	stimulus artifact waveform
SNR_i	input SNR
SNR_o	output SNR
$S_{p_{max}}$	SEP peak amplitude
$s_p(k)$	primary SEP signal
$s_{ri}(k)$	SEP signal in the *ith* reference channel
T_s	sampling period in seconds

$u_p(k)$	primary uncorrelated noise
$u_{ri}(k)$	uncorrelated noise in the *ith* reference channel
$\phi_{N_pN_p}(z)$	primary MEI power spectral density
$\phi_{N_{ri}N_{ri}}(z)$	MEI power spectral density in *ith* reference channel
$\phi_{S_pS_p}(z)$	primary SEP power spectral density
$\phi_{S_{ri}S_{ri}}(z)$	SEP power spectral density in *ith* reference channel
$\phi_{U_pU_p}(z)$	primary uncorrelated noise power spectral density
$\phi_{U_{ri}U_{ri}}(z)$	uncorrelated noise power spectral density in *ith* reference channel
β	crosstalk level
δ	SEP propagation delay in samples
Δ	MEI propagation delay in samples
γ	SNRGAIN
κ	reciprocal of τ (see below)
σ_n^2	variance of the MEI
σ_u^2	variance of the uncorrelated noise
$\Gamma(z)$	ratio of uncorrelated noise and MEI power spectral densities
τ	ratio of uncorrelated noise and MEI variances
ω	frequency in radians per sec
ω_s	sampling frequency in radians per sec
ρ	distortion index
φ	difference in MEI and SEP propagation delays

Acronyms

AF	Adaptive Filter
ANC	Adaptive Noise Canceller
ATS	Adaptive Template Subtraction
B & K	Bruel and Kjaer
BAEP	Brainstem Auditory Evoked Potential
CEP	Cortical Evoked Potential
CMRR	Common Mode Rejection Ratio
CCRANC	Constrained Crosstalk Resistant Adaptive Noise Canceller
CRANC	Crosstalk Resistant Adaptive Noise Canceller
CTS	Carpal Tunnel Syndrome
DDAP	Delay and Difference Array Processor
DSB	Delay and Sum Beamformer
ECG	Electrocardiogram
ECRANC	Ensemble-averaged Crosstalk Resistant Adaptive Noise Canceller
EEG	Electroencephalogram
EMG	Electromyogram
EP	Evoked Potential
FIR	Finite Impulse Response
GSC	Generalized Sidelobe Canceller

IBME	Institute of Biomedical Engineering
IIR	Infinite Impulse Response
LMS	Least Mean Square algorithm
MEI	Myoelectric Interference
MCRANC	Multichannel Crosstalk Resistant Adaptive Noise Canceller
MRANC	Multireference Adaptive Noise Canceller
MSEP	Median nerve Somatosensory Evoked Potential
NAF	Nonlinear Adaptive Filter
RLS	Recursive Least Squares algorithm
SA	Stimulus Artifact
SD	Steepest Descent algorithm
SEP	Somatosensory Evoked Potential
SIR	Signal-to-Interference Ratio
SIU	Stimulus Isolation Unit
SNR	Signal-to-Noise-Ratio
SUNR	Signal-to-Uncorrelated Noise Ratio
SSEP	Spinal cord Somatosensory Evoked Potential
UNB	University of New Brunswick, Fredericton, Canada
VEP	Visual Evoked Potential

Acknowledgements

Words fail me in expressing my deep gratitude to Prof. Parker and Prof. Scott, who are instrumental to the success of this thesis. Their superb guidance and constant support throughout the course of this study is gratefully acknowledged. Many thanks to Dr. Maryhelen Stevenson for her help in solving various signal processing problems, Linda McLean for her expertise in physiology and help in experimental work, to Richard Grieve for many fruitful discussions on SEP signal processing problems mainly the stimulus artifact problem, to Jean Luc Berube for helping me understand the array processing fundamentals and for his SSEP data repository, and to Sreeraman Rajan for his help towards the end of this thesis. Special thanks to all the subjects who volunteered their valuable time for this thesis. The support shown by the Institute of Biomedical Engineering staff and students is also gratefully acknowledged. The financial support from Natural Sciences and Engineering Research Council (NSERC) and Medical Research Council (MRC) is acknowledged with a big "thank you".

Last but not the least, I would like to thank my special friend Rayvathy Kanayson for her constant encouragement, support and friendship.

Chapter 1

Introduction

Summary

Somatosensory Evoked Potentials (SEPs) are signals emanating from the central or peripheral nervous system in response to external stimuli. These SEPs contain clinically valuable information useful in the diagnosis of various neuromuscular disorders and in peripheral nerve monitoring. The main problem associated with the SEPs is their abysmal Signal-to-Noise Ratio (SNR). In this chapter a brief description of the genesis of the SEP along with its characteristics is presented. The various sources of interference that typically influence SEP recordings are discussed briefly. The concrete objectives of this research are stated towards the end of the chapter.

1.1 Introduction

Biomedical signal processing is a general area in the biomedical engineering field which deals with the electrical signals emanating from physiological systems. Examples of

some important biomedical signals include the Electrocardiogram (ECG) which represents the electrical activity associated with the heart[1], the Electroencephalogram (EEG) which represents the integrated electrical activity of the brain and the Electromyogram (EMG) which is the electrical manifestation of the contracting muscles. Various time domain and spectral parameters extracted from these signals form a very important diagnostic tool-set as they are valuable in assessing the condition of the underlying physiological systems and also in monitoring the physiological system state. For example, parameters extracted from the ECG can be used to detect cardiac arrhythmias [62] and the EMG parameters can be used to control an artificial limb [45].

The responses of the central or peripheral nervous system to external stimuli form an important class of these biomedical signals. These signals, called Evoked Potentials (EPs), are very important in understanding the functioning of the nervous system, in testing the integrity of the nervous system and in the diagnosis of various neuromuscular disorders [53, 14]. EPs recorded in the past have been from three modalities: a) Visual Evoked Potentials (VEPs), b) Brainstem Auditory Evoked Potentials (BAEPs), and c) Somatosensory Evoked Potentials (SEPs) [53]. VEPs are generally recorded, using surface electrodes placed on the scalp, in response to such visual stimuli as a flashing light, checkerboard or other pattern based visual stimulus [53, 14]. BAEPs are also acquired, by placing electrodes on the scalp, in response to auditory stimuli such as a click, tone burst or white noise [53]. Both VEPs and BAEPs are also called Cortical Evoked Potentials (CEPs) as they are recorded on the scalp. The SEPs, on the other hand, can be recorded either cortically, on the peripheral nervous system or on the spinal cord [53]. This thesis concentrates on issues related to the acquisition and processing of two subclasses of the SEP *viz.* the Median nerve SEP (MSEP) and the Spinal cord SEP (SSEP). A brief description of

[1]For an overview of the field of biomedical signal processing and a description of some of the important biomedical signals, refer to [62] and [14].

the genesis of each of these SEPs is given in the following section.

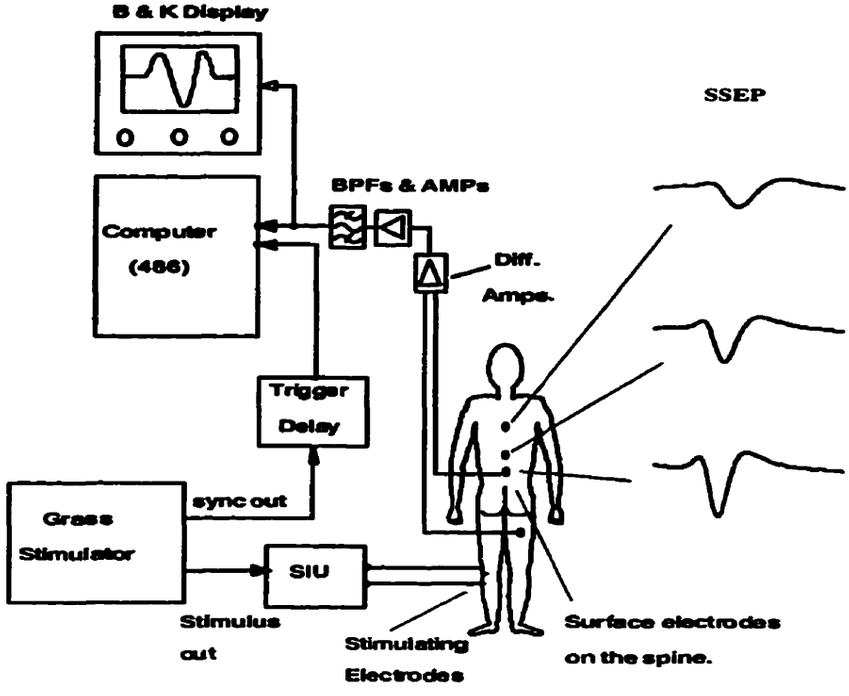

Figure 1.1: *Typical experimental setup to acquire SSEPs. The same experimental setup can be used to measure MSEPs by appropriate placement of the stimulating and recording electrodes.*

1.2 Somatosensory Evoked Potentials

Before discussing the genesis of the SEPs, it is worthwhile to describe the experimental protocol that is usually followed to acquire these signals. Figure 1.1 depicts the instrumentation used at the Institute of Biomedical Engineering, UNB which is typical

of the experimental setup used for the acquisition of the SEPs. The system is shown here for acquiring SSEPs, but the same instrumentation system can be utilized to obtain MSEPs by appropriately placing the stimulating and recording electrodes (this point will be further discussed later in this section).

The instrumentation system can broadly be classified into three subsystems: a) the stimulating system, b) the amplification system, and c) the data processing system. The stimulation system consists of a stimulator (in our case Grass Model S11B) which outputs an electrical stimulus pulse of variable duration, frequency and amplitude and a transformer coupled stimulus isolation unit (SIU) to reduce stimulus artifact and enhance subject safety. The output of the stimulus isolation unit is given to the stimulating electrodes which are carefully placed on the nerve site. In Figure 1.1, the stimulating electrodes are shown placed over the tibial nerve, which is accessible behind the knee. The amplification system comprises a fixed gain preamplifier stage with high Common Mode Rejection Ratio (CMRR), a bandpass filter typically with a passband of 15-1000 Hz [53] for SSEP studies and a variable gain amplifier. The SSEPs are recorded using standard Ag-AgCl electrodes placed along the spinal cord. The filtered and amplified signal is digitized and stored in a computer for further processing. The signal analyzer (B & K 4 channel module type 3023) performs real-time averaging of the SSEP and facilitates visual inspection of the SSEP while the experiment is being performed. For the acquisition of the median nerve SEPs, the stimulating electrodes are usually wrapped around the index finger, with the cathode proximal to the base of the finger. The resulting MSEP can be measured by placing recording electrodes at the wrist region.

The genesis of an SEP can be best understood from the basic anatomical unit of a nerve, the nerve fiber [14]. At rest, these nerve fibers are said to be "polarized" as there exists a potential difference (of approximately 70 mV) between the interior of the fiber and the external medium. When an electrical stimulus of adequate intensity is applied, the nerve fibers underneath the stimulating electrodes depolarize. An ionic

current from the surrounding polarized region flows into this depolarized region. This current is adequate to depolarize the surrounding regions and wavefronts of depolarization - repolarization associated with different nerve fibers travel away from the stimulus electrodes. These traveling wavefronts can then be captured by placing the recording electrodes in the direction of their propagation. The resulting monopolar SEP is therefore a summation of all the action potentials arising from the active nerve fibers and is generally a triphasic waveform whose shape and amplitude are affected by such factors as the low pass filtering action of the tissue between the active nerve fibers and the recording electrodes and the differences in conduction velocities of the active nerve fibers. In Figure 1.1, a simulated SSEP is shown to be captured as it propagates along the spinal cord. Note that the reference electrode for recording the SSEP is placed at the back of the thigh to obtain monopolar recording [39]. Two characteristic traits, both mainly due to the differences in conduction velocities of the active nerve fibers, can be observed from the propagating SSEP waveforms: a) decrease in amplitude as the SSEP propagates to higher levels of the spinal cord, and b) dispersion or "smearing" of the waveform.

An important application of the SSEPs is spinal cord integrity monitoring during surgery. Scoliosis is a lateral curvature of the spine, which can eventually lead to such complications as disfiguration, respiratory problems, and heart disease [43]. The most common procedure to compensate for the scoliosis is the Harrington rod procedure [43]. As some possible surgical complications affecting the spinal cord are reversible if detected immediately, monitoring of spinal cord integrity is desirable. SSEPs offer an attractive solution to monitor the spinal cord. The SSEPs propagating along the spinal cord can be captured as shown in Figure 1.1, effectively "mapping" the sensory nerve conduction along the spinal cord. Any significant deviation from the normal SSEP (which is obtained prior to the surgery) in terms of amplitude and latency parameters can indicate damage to the spinal cord.

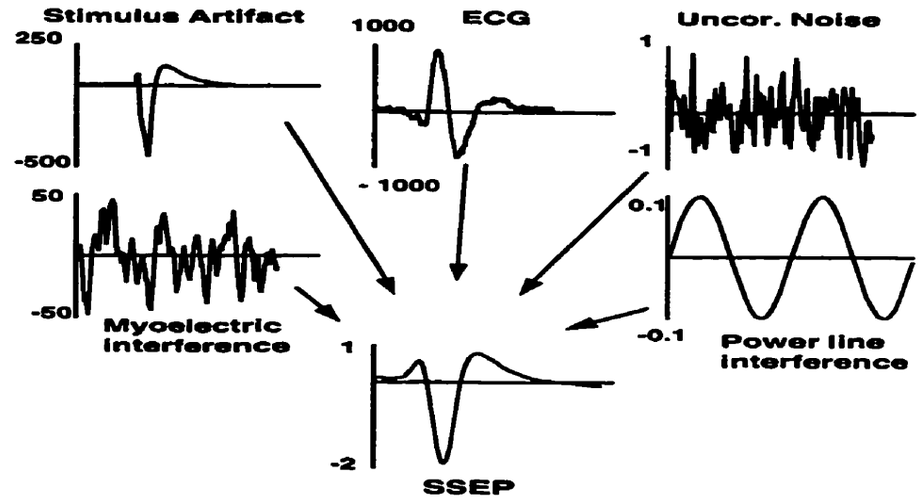

Figure 1.2: *Different interference sources that influence the SSEP measurements. The same interference sources, with the exception of the ECG, also influence MSEP recordings.*

1.3 SEP Measurement Environment

The SEP measured using surface electrodes poses a challenging problem as it is obscured by different interference sources. The Signal-to-Noise Ratio (SNR) that is usually encountered in SEP studies is usually less than 0 dB. The time series acquired using the recording electrodes consists of four components: 1) the stimulus evoked SEP whose genesis is detailed before, 2) a larger stimulus evoked artifact, 3) other ongoing, stimulus independent biological activity (ECG and myoelectric interference in Figure 1.2), and 4) nonbiological noise which is also stimulus independent but originating outside the human body (uncorrelated noise in Figure 1.2). Figure

1.2 illustrates each of the noise sources along with their typical voltage levels when recorded at the lower lumbar region of the spine. The same interference sources, with the exception of the ECG and with slightly different amplitude levels, also influence the MSEP recordings. A brief description of each of these interference sources is given below.

The **Stimulus Artifact (SA)** waveform is generally a spike followed by a decaying response whose amplitude and time constant depend upon such diverse factors as the geometry and type of the stimulating and recording electrodes, the stimulator characteristics, and the filtering characteristics of the preamplification stage. The SA waveform is most irksome when the tail of the artifact interferes with the SEP waveform resulting in erroneous SEP estimates. The **ECG** is the electrical signal associated with the cardiac activity. The MSEPs are usually not affected by the ECG interference, due to the placement of the recording electrodes on the wrist region. The SSEP recordings, on the other hand, are predominantly influenced by the ECG and the problem becomes worse as we move towards the thoracic levels of the spinal cord due to the proximity of the recording electrodes to the chest cavity. The **EMG** or the **Myoelectric Interference (MEI)** is the electrical manifestation of the surrounding active muscle fibers. The influence of the MEI also increases at the thoracic levels of the spinal cord where the MEI originates mainly from the muscles associated with breathing. With MSEP recordings, MEI forms the chief contributor to the poor SNR. The **Uncorrelated noise** is mainly composed of the instrumentation noise and the electrical noise generated by the electrode-skin interface at the recording electrodes. This interference can be modelled as a white Gaussian random noise whose power levels are often on par with the SEP. The **60-Hz** or power line interference is mainly due to the capacitive coupling between the 60-Hz power distribution system and the measurement system. The 60-Hz interference is generally a "milder" interference in most of the SSEP recordings as good skin preparation and high CMRR front-end amplification stage will significantly reduce the amount of power-line interference. Thus

the **SA, MEI and ECG** form the **significant interference set.**

Explicitly stated, the main problem associated with the SEP recording is its dismal SNR. Thus dedicated signal processing techniques are required to reduce the influence of each of the significant interferences thereby enhancing the SEP.

1.4 Goals of the Research

Traditionally, ensemble averaging is the procedure used to increase the poor SNR associated with the SEP. In the presence of aforementioned interferences, however, a large number of SEP records need to be averaged to obtain a good quality SEP. This will result in long recording times and consequently discomfort to the subject if not anaesthesized. In addition, stimulus artifact interference is not affected by ensemble averaging as it occurs in synchrony with the SEP. Thus the main objective of this research work is to develop effective signal processing techniques to reduce each of the interferences thereby enhancing the SEP. The goal of this research work is:

- **to investigate and devise efficient signal processing techniques to reduce each of the abovementioned significant interference sources while maintaining all the essential features of the underlying SEP. The objective is to enhance the quality of the SEP while reducing the recording time.**

1.5 Thesis Organization

The organization of the thesis is as follows: In Chapter 2, a detailed literature survey is conducted to review the previous work done to reduce each of the interference sources. In Chapter 3, fundamentals of adaptive noise cancellation technique are detailed which form the basis for the rest of this thesis. In this chapter, various parameters influencing an adaptive noise cancelling filter are described. Chapter 4

concerns itself with temporal and spatio-temporal filtering of the myoelectric interference. Novel crosstalk resistant adaptive noise cancelling structures are introduced in this chapter and their performance is evaluated analytically and through processing simulated and experimental data. Chapter 5 presents results pertaining to SA reduction. Nonlinear filtering techniques, which have never been applied to SA reduction before, are discussed in this chapter and their performance is rigorously scrutinized. In Chapter 6, various signal processing techniques are investigated for ECG reduction and a method, called Adaptive Template Subtraction (ATS) method is developed. The thesis is concluded with Chapter 7 where a summary of the research work is presented along with the major contributions of this thesis and suggestions for future work.

Chapter 2

Literature Review

Summary

An in-depth literature survey is undertaken in this chapter to review the previous SEP research. Various clinical applications which highlight the significance of SEPs are described. Each of the main interference sources that are responsible for the poor SEP SNR is considered separately with a description of its characteristics and methods of reduction. The relative merits and demerits of the different interference reduction methods are discussed and a preview of the proposed reduction methods which circumvent some of the difficulties is given.

2.1 Clinical Applications of the SEPs

Since Dawson's first reported findings of the SEPs in 1947 [12], there has been growing interest in the clinical application of the SEPs mainly in the domain of neurological damage assessment of the peripheral and central nervous system. Both cortical and noncortical SEPs are clinically used to detect any abnormalities. SEPs recorded from

the scalp generally are composed of early components corresponding to peripheral nerve action potentials, early components generated in the brainstem, short- and medium-latency cortical action potentials and finally an afterdischarge [53]. The resulting SEP is often composed of several peaks and troughs each of which has significance in assessing the integrity of the nervous system under scrutiny [53]. However cortical and subcortical SEPs are sensitive to such variables as subject wakefulness [56], level of anesthetic agents [11, 57], temperature changes, changes in arterial blood pressure or respiratory gases and changes in hormonal activity [21]. This sensitive nature undermines the effectiveness of cortical SEPs in accurately assessing the functioning of the nervous system. Thus Spinal cord SEPs (SSEPs) and Median nerve SEPs (MSEPs) are more attractive as they are less influenced by anesthetic agents [20, 3], and are more physiologically controlled [39].

Operating room procedures which benefit from SSEP recordings include the assessment of conduction through possibly damaged segments prior to decompression or nerve graft, and monitoring of sensory pathways during potentially dangerous surgical maneuvers including scoliosis correction, [53]. There has been considerable interest in the use of SSEPs to test conduction in the sensory spinal column pathways after spinal cord injuries. It is deemed that continued absence of SSEPs is a poor prognostic sign, whereas the persistence or reappearance of SSEPs, even in a clinically complete lesion, is an encouraging sign.

SSEP conduction has been exploited for spinal cord monitoring during operative procedures such as Scoliosis treatment. Scoliosis is a lateral curvature of the spine which is most frequently a problem in adolescent girls [43]. Surgical correction techniques employ mechanical fixation devices such as Harrington Rod instrument to apply distractive and compressive forces to correct the abnormal curvature of the spine [31]. However, neurological complications may arise due to this procedure and it has been reported that the prognosis for recovery is vastly improved if the Harrington rod is removed within 3 hours of the diagnosis of a complication [31]. A commonly

used intra-operative test for assessing spinal cord integrity, called the Stagnara "Wake up" test [65], relies on bringing the patient out of anaesthesia to determine his/her voluntary control of the extremities such as the toes and fingers. If the patient has difficulty in responding to this test, the tension associated with the Harrington rod is reduced. There are several difficulties inherent to this procedure, most of which are associated with bringing the patient out of anesthesia with all the anesthetic intubation devices in place. SSEPs overcome these difficulties and offer a very attractive solution to spinal cord monitoring without any voluntary effort from the patient. SSEPs have also been applied to spinal cord monitoring during operations for thoracic aortic aneurysms [26], treatment of spinal cord tumors and spinal cord ischemia [53].

The conduction properties of the MSEPs were exploited for the diagnosis of median nerve injuries [58]. Injury to the median nerve results in impairment of two of the most important movements of the body – grip and pronation. One of the most common median nerve injuries is the compression of the median nerve at the wrist, called the Carpal Tunnel Syndrome (CTS) [58]. In the wrist, the median nerve passes through a narrow aperture called the carpal tunnel. At this point the nerve is vulnerable to any changes in the surrounding medium whether due to edema, trauma, inflammation or any other conditions. This condition commonly occurs in subjects who are engaged in vigorous manual work, especially if they are unused to such work. This syndrome can be effectively diagnosed using the MSEP conduction characteristics [58].

In any of the above SEP diagnostic applications, two main SEP parameters *viz.* the latency and the amplitude are used to detect any abnormalities [53, 39]. The SEP latency refers to the time delay between the stimulus onset and the initial peak of the SEP. Since the distance between the stimulating and recording electrodes can be measured, nerve conduction velocity can be readily calculated from the latency value. In many clinical studies, it is the increase in the latency value (or equivalently

decrease in conduction velocity) that is taken as a positive indication of the pathology. For example, latency increases of 3 ms have been used as the warning levels for SSEP monitoring during spinal surgery [32]. For patients suffering from CTS, the sensory distal latency of the MSEP was around 2 ms above the normal value and this distal latency parameter is shown to be the most effective indicator of CTS [40]. Amplitude measurements have been used in the diagnosis of pathology as well. One significant issue with amplitude measurements is that the SEP waveform is highly dependent on different variables such as the depth of the nerve, the tissue between the nerve fibers and the recording electrode, the distribution of fiber types and their conduction velocities and the position of the stimulating electrodes. Thus it is difficult to establish norms for the amplitude levels of an SEP. An alternative approach for utilizing amplitude measurements is to obtain premorbid amplitude values and compare them to the postmorbid amplitude values. For example in spinal cord surgery applications, the amplitude values of the SSEP obtained prior to the surgery can be used as guidelines for detecting any neurological complications. In spinal cord monitoring applications, an amplitude drop by 50% has been suggested as a warning threshold [32]. Table 2.1, adopted from Regan [53], assigns a diagnostic value to different SEP parameters.

In essence, the SEPs contain information which is very helpful in clinical diagnosis. An important factor which determines the usefulness of any SEP instrument in a clinical setting is its ability to detect early any deviation from the normal SEP parameters and immediately warn the physician. Current SEP measurement systems mostly rely on ensemble averaging to estimate the SEP waveform and then perform the diagnostics. Due to the initial poor SNR associated with the SEP, as many as several thousand records need to be averaged to obtain a good quality SEP, which results in long recording times. Thus interference reduction techniques need to be incorporated which facilitate an early detection of SEP abnormalities.

Abnormality	Value
1) Total absence of SEP	5.0
2) Absence of a component	1.5
3) Prolonged latency (> 3 SDs above normal mean)	4.0
4) Amplitude reduction (> 50 %)	4.0
5) Increased dispersion (dispersion factor > 3)	1.5

Table 2.1: ***Diagnostic value associated with different SEP parameters (after [52].)***

2.2 Interference Reduction

As mentioned before, a major problem associated with SEP recordings is the presence of more powerful interferences which mask the SEP. To quote McGillem *et al.* [37], "The most important problem in evoked potential research is the signal extraction itself". There is a cornucopia of research work in this field attempting to improve the poor SNR of the SEP. For the sake of clarity, the literature addressing the reduction of each of the individual interference sources is grouped together.

2.2.1 Myoelectric Interference Reduction

As mentioned earlier, the SNR associated with the SEPs is typically less than 0 dB and less than -20 dB in the presence of larger Myoelectric Interference[1] (MEI) [53, 54]. One of the most widely utilized tools to increase the poor SNR of the SEP is

[1] It is worthwhile mentioning here that the MEI will not be a concern in intra-operative monitoring where muscle relaxants are utilized. Therefore in such situations, no MEI reduction filters are required.

ensemble averaging [37]. If a deterministic and repetitive signal is added to random noise and the time of occurrence is accurately known, averaging becomes a very effective tool. Ensemble averaging decreases the noise power in a manner inversely proportional to the number of SEPs in the ensemble. Due to the initial poor SNR, a large number of these SEP records are needed for an acceptable estimate of the SEP. This results in long recording times, discomfort to the subject if awake, and unacceptable interruption of the surgical procedure in intra-operative monitoring. Since the SEP and the MEI occupy similar bandwidths, any fixed filtering procedures result in SEP distortion. Matched filtering techniques have been applied to SEP enhancement [68, 33, 43]. A matched filter is an optimum detector for a known signal in additive white noise. However, the application of matched filtering to SEP enhancement has two main drawbacks *viz.* the need for a good quality initial signal estimate which requires averaging a large number of SEP records, and the presence of the myoelectric interference which has a non-white spectrum. Also significant is the inability of the matched filter to yield an estimate of the SEP waveform. Some authors attempted to use the Wiener filter to reduce the MEI [44, 13, 66]. Unfortunately, the design of a Wiener filter requires an ***a priori*** knowledge of the spectral content of the SEP and the MEI, and the condition that both SEP and MEI be stationary.

Adaptive filters bypass the above ***a priori*** condition while still being able to converge to the optimal solution. They also offer an additional advantage of tracking any nonstationarities present in the input data. Adaptive Noise Cancellers (ANCs) are a subclass of adaptive filters which have been successfully employed in reducing the MEI [54, 52]. In its basic form, an ANC consists of a primary recording channel containing the SEP and the MEI and a reference recording channel containing only a correlated component of the MEI. The ANC performs as a correlation canceller thereby leaving MEI free SEP at its output. The performance of a basic ANC is however affected by several factors. One such factor is the presence of uncorrelated noise sources in the reference input. The presence of these noise sources drives the

adaptive filter away from the desired solution, resulting in unsatisfactory results. The author [52, 46, 49], in an earlier study, has shown that the damaging effect of uncorrelated noise sources can be compensated by using a Multi-Reference Adaptive Noise Canceller (MRANC). It has been shown by the author in [49] that the effect of uncorrelated noise diminishes with the increase in the number of channels. However both ANC and MRANC suffer from another phenomenon, signal crosstalk. In practical MEI cancellation experiments, the primary and reference sensors need to be close together to acquire highly correlated MEI inputs. This will inevitably lead to the presence of SEP components in the reference channel(s). This SEP "crosstalk" results in undesirable signal distortion at the output of the ANC [69, 70, 34, 42] which is even worse in the case of the MRANC [49]. The signal distortion due to this SEP leakage into the reference channel is inversely proportional to the SNR in the reference channel. Thus Crosstalk Resistant Adaptive Noise Canceller (CRANC) structures are required which achieve maximum MEI reduction while being robust to the presence of signal crosstalk.

Recently a few CRANC structures have been reported [2, 34, 42]. The CRANC structure presented by Madhavan *et al.* [34] (CRAF #1) consists of a cascade of three ANCs with the first ANC reducing the interference while the second and third ANCs compensate for the signal distortion due to crosstalk. The author [52], in his master's thesis showed that the third ANC in this CRANC structure is unnecessary and a two ANC CRANC structure was developed. A constrained CRANC was developed by the author in a later publication[2] [48] which further reduces the computational complexity of the CRANC filter. The CRANC architecture presented by Al-Kindi *et al.* [2] (CRAF #2) is composed of two ANCs connected in a feedback structure and attempts to separate the signal and interference components using a decorrelation approach. Mirchandani *et al.* [42] proposed a similar CRANC structure but their

[2]This constrained CRANC algorithm is derived in Appendix I and the simulation results demonstrating the efficacy of the constrained algorithm are given in Chapter 4

algorithm was derived on the basis of the joint energy minimization problem. These feedback CRANC structures, however, suffer from instability and they need to be initialized properly [42].

The problem of crosstalk resistant adaptive noise cancellation is a subset of a more general problem *viz.* the separation of sources. The source separation problem can be stated as follows: Given P independent sources and M sensors ($M > P$) each of which receives a combination of the P sources, estimate the P independent sources. This topic is hotly pursued under the heading "blind separation of sources" and finds its roots mainly from communications and array processing fields [25, 29]. When the signals received at the individual sensors are linear combinations of the sources, a neural network based signal separator can be designed [25]. Van Gerven *et al.* [63] derived a Symmetric Adaptive Decorrelator (SAD) for the source separation problem for the two channel case. A frequency domain source separation algorithm was presented by Wienstien *et al.* [67]. Finally, a source separation algorithm based on higher order statistics was proposed by Lacoume *et al.* [29] which overcomes some of the problems arising from using the second order statistics.

A significant factor that is neglected in most of the above publications is the presence of uncorrelated noise sources. In our case, the uncorrelated noise emanates primarily from the instrumentation and from the electrode-tissue interfaces at the recording electrodes. As mentioned before, the uncorrelated noise is as powerful as the SEP and hence it needs to be taken into consideration. The author [52, 47, 51], in his masters thesis, has shown that the performance of CRAF #1 is sensitive to the presence of uncorrelated noise sources. It is shown through simulations and experimental results [52, 47], that the performance of CRAF #1 is similar to the performance of an ANC in the presence of uncorrelated noise sources. The effect of uncorrelated noise on CRAF #2 will be even more detrimental due to the innate feedback structure of CRAF #2. It is not clear how the source separation algorithms behave with the addition of uncorrelated noise sources. Thus in this thesis new

approaches for crosstalk resistant MEI cancellation are undertaken which exhibit improved tolerance to the presence of uncorrelated noise sources.

Discrimination based on the propagation properties of the SEP and MEI can be used as a different approach to MEI reduction. As explained before, when a nerve is stimulated, the resulting SEP travels away from the point of excitation. The same is true for the MEI where the MEI travels along the active muscle fibers. The difference in the conduction velocities can be used as a basis for designing a spatiotemporal filter to achieve the distinction between the SEP and the MEI [7]. Bérubé compared the performance of different spatiotemporal filters for the task of reducing MEI from SSEP records [6]. A fundamental spatiotemporal filter is the Delay and Sum Beamformer (DSB) wherein an array of sensors with added delays coherently sums the incident signal [38, 6, 8]. The delays are designed in such a way that the SEP is summed coherently while the MEI is incoherently summed. Thus the DSB requires an ***a priori*** knowledge of the SEP and MEI propagation characteristics to determine the delay values [38, 6]. Another factor that affects the performance of the DSB is the high correlation of the MEI interference across the sensors, which reduces the amount of MEI cancellation. Another spatiotemporal filter is the Generalized Sidelobe Canceller (GSC) which is similar to the MRANC and it, under certain condition, circumvents the crosstalk problem that is generally present with MRANC. The GSC exploits the propagation characteristics of the SEP and creates a "signal blocking matrix" which reduces the SEP leakage into the reference channels. Thus the GSC enjoys the improved uncorrelated noise tolerance associated with the MRANC while overcoming the problem of signal distortion due to crosstalk. However, for an effective design of the signal blocking matrix, ***a priori*** knowledge of the SEP propagation delay at each sensor is required and moreover, the SEP needs to be a plane wave [6].

An alternative approach is to create an "interference blocking matrix" and then implement a multichannel SEP enhancer. Due to the larger amplitude of the MEI interference, the MEI propagation delays needed for the blocking matrix can be easily

estimated using the crosscorrelation technique. The performance of this alternate spatiotemporal filter and its variations will be scrutinized in Chapter 4.

An important point that is not discussed above is the presence of other correlated interference sources across the primary and reference sensors. Three potential interference sources which fit this scenario are the stimulus artifact, ECG and the power line interference. Thus these interferences should be removed from both the primary and reference channels of the MEI reduction system to achieve maximum MEI reduction. The following sections review the literature concerned with the reduction of these interferences.

2.2.2 SA Reduction Methods

As mentioned before, the SA waveform is typically a spike followed by an exponential decay response whose amplitude and time constant are dependent upon the stimulator system characteristics, geometry and type of the stimulation and recording electrodes, preamplifier characteristics and interelectrode impedance [17]. The SA waveform can be modeled as a linear combination of three different components which are coupled into the recording system by three independent mechanisms [55, 39]. The first and the most obvious component results from the voltage gradient across the recording electrodes resulting from the conduction of stimulus current through the limb [55, 17]. The second coupling mechanism arises from imperfect stimulus isolation. Since the main stimulator is grounded, imperfect isolation results in a stray capacitance between the stimulating electrodes and the grounded stimulator. This capacitance together with the stray capacitance between the subject and ground results in a second current which once again creates a voltage gradient at the recording electrodes. The third component is due to electromagnetic coupling between the stimulating and recording leads. The contribution of this component is highly dependent on the impedance of the recording electrodes, quality of shielding on leads and the position of the leads in space [55]. Based on this conceptual model of the SA, Mclean [39] made

recommendations for the reduction of each of the abovementioned components[3].

Traditionally, reduction of the stimulus artifact has been achieved using special hardware. Options include sample and hold circuits which sample the input signal the instant the stimulus is applied and hold that voltage level during the stimulus artifact period [19, 16], trigger delay circuits which control the data acquisition process such that no stimulus artifact is recorded [41], and circuits which utilize slew rate limiting and time windowing [27]. Some other reported techniques of stimulus artifact reduction include biphasic stimulator circuits [59], stimulus isolation techniques [27] and positioning of the recording electrodes on stimulus artifact isopotential lines [28].

It is important to note here that with any stimulus artifact blanking circuit there is a high probability of losing some signal information. In SEP conduction studies where the precise time location of the onset of the SEP waveform is required, these circuits may give rise to erroneous estimates of the onset of the SEP waveform. This is especially true if the stimulus and recording sites are close together where the tail of the SA waveform may interfere with the SEP thereby distorting the SEP. A different approach to stimulus artifact reduction is to somehow obtain an estimate of the stimulus artifact and subtract it from the contaminated signal. McGill *et al.* [17] followed this approach and obtained estimates of the stimulus artifact by using a) subthreshold stimulation, b) an auxiliary recording channel off the nerve axis, and c) stimulation during the refractory period. While each of these techniques showed promising results, none of them completely removed the stimulus artifact and all are nonadaptive to possible changes in the SA during the course of the experiment.

The presence of residual SA following application of all of the above methods is probably due to two factors *viz* nonlinearity in SA generation and a possible time varying nature of the underlying system. The nonlinearity in the SA generation

[3]These are discussed in detail in Chapter 5.

system originates from the square-law behavior of V/I characteristics of the electrode-tissue interface at the stimulating electrodes. At high current densities, the electrode-tissue interface can be modeled as a nonlinear resistor in parallel with a fixed capacitor [60, 17]. Stevens [60] and Barker [4] have analytically derived an expression for the current/voltage characteristics, $I = aV + bV^2$, and empirically validated it. In addition, the SA waveform may possess a time-varying nature due to the changes in the stimulating and recording electrode impedances due to sweating, drying of the electrode paste, movement of the limbs etc.

Thus any signal processing system attempting to eliminate the SA must be able to compensate for the nonlinear and time-varying nature of the SA. In this thesis nonlinear adaptive filters are applied to the problem of SA reduction.

2.2.3 ECG Reduction Techniques

While designing an ANC for the elimination of the MEI in SSEP records, Harrison [22] observed that the presence of the ECG in the primary and reference channels of the ANC is a detrimental factor. This is due to the fact that the ECG also appears as a correlated component across the primary and reference sensors and affects the MEI cancelling ability of the ANC. He concluded that the ECG is the main interference that needs to be reduced and designed a separate ANC for ECG reduction. In a complimentary work, Harrison and Lovely [64] conducted an experimental study to determine the relative power levels of different interference sources at different levels of the spinal cord and concluded that ECG forms a significant component at all levels of the spinal cord. In a later study, Black [9, 10] compared the performance of three different ECG reduction techniques in the absence of an SSEP *viz.* clipping, gating, and ANC procedures. In the ***clipping*** procedure, the input amplitude is clipped at a certain threshold level. The performance of this technique is obviously dependent on the magnitude of the threshold value. While this technique can be argued as an ECG reduction technique, it is more useful in increasing the dynamic range of the SSEP.

Without any clipping action in place, the amplification factor of the amplification stage in the data acquisition system is dictated by the ECG amplitude values such that no saturation takes place. This will result in poor A/D resolution of the very small amplitude SSEP signal. This effect will be more pronounced at the higher levels of the spinal cord where the ECG magnitude is larger and the SSEP amplitude is smaller compared to the lower levels. With the clipping circuits in place and by judiciously selecting the threshold level, the amplification factor can be increased thereby increasing the A/D resolution of the SSEP. In the ***gating*** method of ECG reduction, all amplitude values above a certain threshold level are set to zero. Thus this technique will result in very good ECG cancellation. A drawback with this technique, however, is the SSEP loss if the SSEP occurs during the gated ECG segment. Since the probability of ECG occurring in a SSEP record is relatively small[4], this technique might still be useful when large number of SSEP records are averaged. Black reported that, of all the three techniques, the ANC method offered the best ECG reduction performance. With the ANC, once again, we have the problem of uncorrelated noise sources and the possibility of SSEP crosstalk. The presence of uncorrelated noise sources in ECG reduction is a relatively minor issue as the ECG is several times more powerful than the uncorrelated noise. The SSEP crosstalk, however, is a crucial factor. The placement of the reference electrode pair such that no SSEP components are recorded while still obtaining a correlated ECG component is not a trivial issue. Harrison [22] placed the reference electrode pair on the chest while Black [9] placed an electrode on either side of the spinal column equidistant from the spine. Assuming uniform tissue properties and SSEP conduction along the spinal cord in a straight line, a differential signal obtained using the abovementioned electrode pair will result in negligible SSEP component. However, in practical situations, there are always

[4]A rough calculation of the probability of ECG occurence during an SEP record is given in Appendix VI.

tissue inhomogenities which will result in non-zero differential SSEP signal. Thus additional strategies are required for the ANC such that a SSEP crosstalk-free reference input is obtained. A possible way of obtaining a crosstalk-free reference channel is to record the ECG input prior to the stimulation procedure. This reference ECG input can later be used to cancel the ECG in the primary input acquired using the same electrodes but during the stimulation stage. This method called the "template subtraction" and its adaptive version "Adaptive Template Subtraction (ATS)" are scrutinized in Chapter 6.

2.2.4 60-Hz Interference

Of all the interferences affecting the SEP waveform, the 60-Hz interference is probably the easiest to reduce. The 60-Hz interference can be reduced significantly by careful skin preparation, using generous amounts of electrode paste for good electrode contact and employing an amplification stage with high CMRR. While one can envisage an ANC structure for 60-Hz interference reduction, it is not considered in this thesis and appropriate precautions are taken while measuring *in vivo* signals to make sure that the experimental data is not significantly contaminated by the 60-Hz interference.

2.3 A Look Ahead

In summary, this chapter reviewed the literature addressing the clinical significance of SEPs and the reduction of different interferences. The relative merits and demerits of these techniques are discussed. The following items explicitly state the work done in this thesis based on this background:

- **Crosstalk Resistant Architectures for MEI Reduction**. Robust CRANC architectures are developed for the MEI reduction. Spatiotemporal filters which further exploit the propagation characteristics are scrutinized. The performance

of these techniques is analyzed analytically and through processing simulated and experimental data.

- **Nonlinear Adaptive Filtering for SA Reduction**. Nonlinear Adaptive Filters (NAFs) based on the truncated Volterra series are applied for the first time to the problem of SA reduction. The SA reduction performance along with the convergence behavior of the NAFs with different adaption algorithms and under different operating conditions is rigorously evaluated. Recommendations are made as to the best method of SA reduction for a wide variety of operating conditions.

- **Adaptive Filter Structures for ECG reduction**. The performances of different adaptive filter structures for ECG reduction are evaluated and the best ECG reduction scheme is identified.

Chapter 3

Adaptive Noise Cancellation

Summary

The fundamentals of adaptive noise cancellation are detailed in this chapter. The objective of this chapter is to identify different variables that affect the interference cancelling ability of an Adaptive Noise Canceller (ANC) and offer recommendations to compensate for them. A theoretical framework for the analysis of a general ANC is developed and this is extended to a multichannel (MRANC) case. For the particular case of MEI reduction, theoretical expressions for the performance of the ANC and the MRANC in the presence of uncorrelated noise and signal crosstalk are derived. These analytical results are further validated by processing simulated SEP, MEI and uncorrelated noise data to gain further insight into the functioning of an ANC.

3.1 Basic Adaptive Noise Canceller (ANC)

In its basic form, an ANC consists of a primary recording channel consisting of the desired signal plus the noise and a reference recording channel containing only a correlated component of the noise.

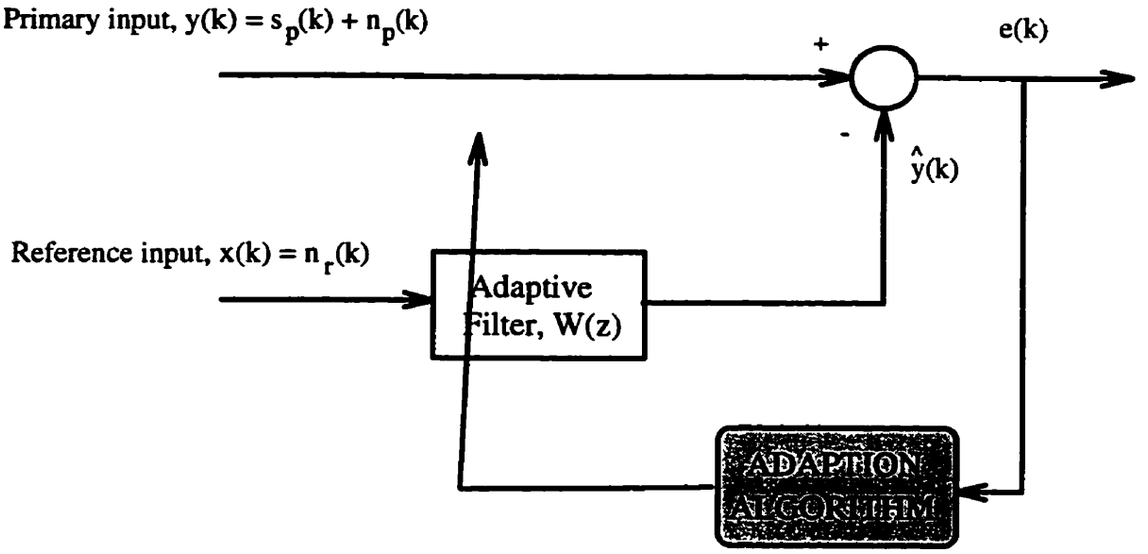

Figure 3.1: *Block diagram representation of a typical adaptive noise cancellation scenario.*

Referring to Figure 3.1, we have,

$$y(k) = s_p(k) + n_p(k),$$

$$\text{and assuming linearity} \qquad x(k) = n_r(k) = h(k) * n_p(k) \tag{3.1}$$

where $s_p(k)$ is the desired signal in the primary input, $n_p(k)$ is the primary noise component, $n_r(k)$ is the reference noise component, $h(k)$ represents the transfer function between the primary and reference noise components and * is the convolution operator. Also in Figure 3.1, $\hat{y}(k)$ denotes the filtered reference input, $e(k)$ represents the error residue and $W(z)$ stands for the transfer function of the adaptive filter in the discrete Z domain. The optimal solution for the adaptive filter can be derived

easily in the discrete Z domain,

$$W_{opt}(z) = \frac{\phi_{yx}(z)}{\phi_{xx}(z)} = \frac{\phi_{N_pN_p}(z)H(z^{-1})}{\phi_{N_pN_p(z)}|H(z)|^2} = \frac{1}{H(z)} \quad (3.2)$$

where $\phi_{yx}(z)$ is the cross-spectral density, $\phi_{xx}(z)$ is the auto-spectral density of the reference input, and $\phi_{N_pN_p}(z)$ is the spectral density of the primary noise. Several factors need to be considered before an ANC is applied to any noise reduction problem. The following sections discuss the four main factors that directly influence the performance of an ANC.

3.2 Choice of the Filter Structure

There are two main choices for the implementation of the adaptive filter: a) a Finite Impulse Response (FIR) filter and b) an Infinite Impulse Response (IIR) filter [23, 70]. FIR filters are computationally simpler to implement, inherently stable and easier to analyze. The main drawback with the FIR filters is the need for large filter orders in certain situations, which increases the computational burden on the adaptive system. IIR filters, on the other hand, require very few coefficients to reach the optimal solution but they suffer from instability (due to the inherent feedback structure) and local minima problems. All the adaptive filters in this thesis therefore are implemented in the FIR form. The computational penalty due to large filter lengths of the FIR adaptive filter is endured to avert the potential instability of the IIR filter.

The FIR filter has been implemented in three different structures *viz* the transversal structure, the lattice structure and more recently, the systolic array structure [23]. In the transversal structure or tapped delay line, the reference input is passed through a set of unit delays (whose number is equivalent to the filter length), multiplied by the corresponding weights and then summed. The transversal filter is appealing from

the implementation point of view due to its simplicity and its robustness with the iterative algorithms. Lattice filters are modular in structure in that they consist of a number of individual stages, each of which has a lattice form [23]. While the lattice structure is found to have superior convergence capabilities and low round-off noise in fixed word length implementations, it is computationally more intense than the transversal filter. A systolic array architecture is a parallel computing system which possesses many desirable qualities such as modularity, local interconnections, and a pipelined and synchronized architecture. The systolic array concept was invented mainly to implement complex filter algorithms in a VLSI chip [23]. In this thesis, the transversal structure based FIR filters will be used to implement all the adaptive filtering operations.

3.3 Choice of the Adaption Algorithm

There are several adaption algorithms reported in the literature and the choice is still a hotly pursued research area. The most pervasive of these algorithms attempt to minimize some form of cost function based on the squared error. The adaption algorithms can be broadly categorized into two classes: a) stochastic and b) exact [23, 70]. In choosing an algorithm from these two classes, several factors such as the rate of convergence (defined as the number of iterations to reach the optimal solution), misadjustment (defined as the ratio of the excess mean-squared error and the minimum mean-squared error), tracking in nonstationary environments, robustness to ill-conditioned data, and computational complexity (calculated in terms of the number of arithmetic operations) play an important role. Three main algorithms were employed in this thesis to realize the adaptive filtering operation: the steepest descent (SD) algorithm, the Least Mean Square (LMS) algorithm and the Recursive Least Squares (RLS) algorithm[1]. Both the SD and the LMS algorithms fall into the

[1]Refer to Appendix V for a detailed description of these algorithms. Although the algorithms are developed in a nonlinear adaptive filtering context in Appendix V, the same comments apply to

category of the stochastic gradient algorithms wherein the mean squared error is iteratively minimized. The RLS algorithm is an example of an exact adaption algorithm wherein the exact squared error is minimized. There is a trade-off between the LMS and RLS algorithms in terms of computational complexity and convergence rate. The LMS algorithm is computationally simpler but often exhibits slower convergence. The RLS algorithm, on the other hand, exhibits faster convergence but is computationally complex especially for larger adaptive filter lengths. In this thesis, unless otherwise stated, only the simulation and experimental results obtained using the RLS algorithm are included. Since all of the data processing in this thesis was done offline, the computational complexity of the RLS algorithm was not a significant issue.

3.4 Presence of Uncorrelated Noise Sources

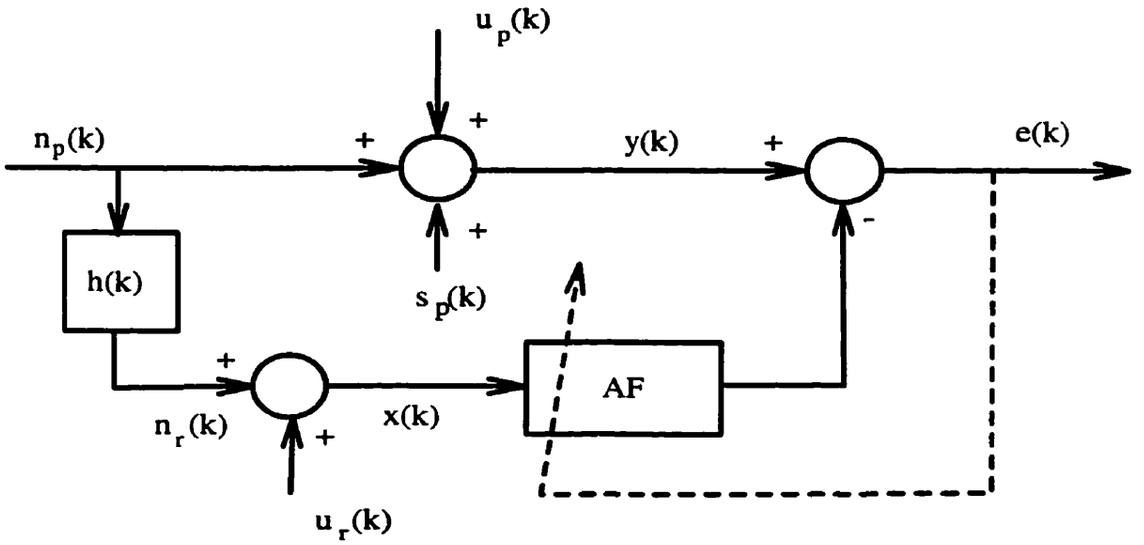

Figure 3.2: *ANC with uncorrelated noise components.*

The block diagram of an ANC in the presence of uncorrelated noise components

linear FIR adaptive filtering as well.

is shown in Figure 3.2, where AF represents the adaptive filter, and $u_p(k)$ and $u_r(k)$ represent the primary and reference uncorrelated noise sources respectively. The unconstrained Wiener solution for the ANC now takes the form of

$$\begin{aligned} W_{opt}(z) &= \frac{\phi_{N_pN_p}(z)H(z^{-1})}{\phi_{N_pN_p}(z)\,|H(z)|^2 + \phi_{U_rU_r}(z)} \\ &= \frac{1}{H(z)\{1+\Gamma_r(z)\}} \end{aligned} \tag{3.3}$$

where $\phi_{U_rU_r}(z)$ is the uncorrelated noise power spectral density in the reference input and $\Gamma_r(z)$ is the ratio of uncorrelated and correlated noise power spectral densities in the reference input. The power spectral densities of the residual noise components at the output of the ANC can be expressed as

$$\phi_{N_oN_o}(z) = \phi_{N_pN_p}(z)\,|1 - H(z)W_{opt}(z)|^2 \tag{3.4}$$

$$\phi_{U_oU_o}(z) = \phi_{U_pU_p}(z) + \phi_{U_rU_r}(z)\,|W_{opt}(z)|^2\,. \tag{3.5}$$

Based on the above equations, two performance indices which quantify the interference cancelling ability of the ANC can be defined as,

$$I(z) = \frac{\phi_{N_pN_p}(z) + \phi_{U_pU_p}(z)}{\phi_{N_oN_o}(z) + \phi_{U_oU_o}(z)} \tag{3.6}$$

$$R(z) = \frac{\phi_{N_pN_p}(z)}{\phi_{N_oN_o}(z)} \tag{3.7}$$

where $I(z)$ represents the overall power reduction achieved by the ANC and $R(z)$ quantifies the amount of correlated interference reduction accomplished by the ANC. Since the desired signal passes through the ANC unchanged, $I(z)$ can also be interpreted as the SNRGAIN achieved by the ANC. Note that both $I(z)$ and $R(z)$ are frequency dependent performance measures and frequency independent performance measures can be calculated by integrating the spectral densities in Eqs. 3.6 and 3.7 to obtain individual powers. Substituting $z = exp(j2\pi\omega/\omega_s)$, with ω_s the sampling frequency, and integrating, the frequency independent performance measures can be

written as,

$$I = \frac{\int_0^{\omega_s/2} [\phi_{N_p N_p}(\omega) + \phi_{U_p U_p}(\omega)] d\omega}{\int_0^{\omega_s/2} [\phi_{N_o N_o}(\omega) + \phi_{U_o U_o}(\omega)] d\omega} \tag{3.8}$$

$$R = \frac{\int_0^{\omega_s/2} \phi_{N_p N_p}(\omega) d\omega}{\int_0^{\omega_s/2} \phi_{N_o N_o}(\omega) d\omega}. \tag{3.9}$$

Thus if the power spectral densities of the correlated and uncorrelated noise sources in the primary and reference channels are available, the performance of the ANC can be easily quantified using the above equations.

To relate the above expressions to the myoelectric interference (MEI) reduction problem, simulated MEI and uncorrelated noise data was processed by an ANC. The simulated MEI was generated by passing white Gaussian noise of unit variance through a shaping filter whose impulse response, $p(k)$, is given by [6],

$$p(k) = C_1 k T_s (2 - c_n k T_s) e^{-c_n k T_s} \qquad \text{k=0...P-1} \tag{3.10}$$

where C_1 is a scale factor, T_s is the sample period, P is the length of the shaping filter and c_n is the MEI spectral shaping parameter and from experimental measurements has a typical value of 500. The resulting MEI power spectral density can be easily shown to be equal to

$$\phi_{N_p N_p}(\omega) = \frac{D\omega^2}{(\omega^2 + c_n^2)^3} \tag{3.11}$$

where D is a constant. The MEI transfer function between the primary and reference channels was modeled as a fifth order lowpass filter given by

$$H(z) = \frac{1}{1 + 0.2z^{-1} - 0.075z^{-2} - 0.076z^{-3} + 0.112z^{-4}}. \tag{3.12}$$

The primary and reference uncorrelated noise were white Gaussian noise sources whose variance was varied to achieve the desired level of uncorrelated noise[2], τ, which

[2]It is assumed throughout the thesis that the power levels of uncorrelated noise sources in both the primary and reference inputs are approximately the same.

was defined as,

$$\tau = \frac{\sigma^2_{U_\tau}}{\sigma^2_{N_\tau}} \tag{3.13}$$

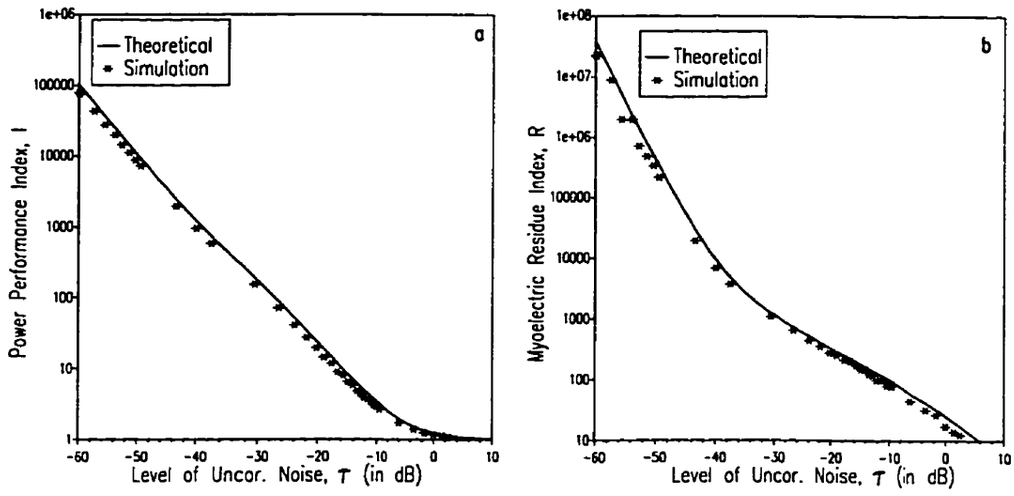

Figure 3.3: *ANC performance vs level of uncorrelated noise.*

where $\sigma^2_{N_\tau}$ is the reference MEI variance, and $\sigma^2_{U_\tau}$ is the reference uncorrelated noise variance. 10,000 data points were used to run a 40th order adaptive filter which was driven by the RLS algorithm. Note that the Wiener solution used in the analytical development of the ANC is in the frequency domain and hence could be non-causal. To compensate for this possible noncausality with simulated data, a delay of half the filter length was utilized in the primary input of the ANC. The steady-state weights of the adaptive filter were then retrieved and used to filter the MEI and uncorrelated noise sources separately. This facilitated the calculation of the power performance and myoelectric residue measures given by Eqs. 3.8 and 3.9 respectively. Figure 3.3 depicts the results obtained for various levels of uncorrelated noise, along with the theoretical predictions[3]. The decrease in both power performance and myoelectric residue indices due to increasing uncorrelated noise levels is obvious in these plots. Also good agreement between the theoretical and simulation results is seen in these

[3]The theoretical predictions are computed by numerically evaluating the integrals for I and R, given by Eqs. 3.8 and 3.9, as closed form solutions could not be found.

figures. Any discrepancies between these two values are attributed to the convergence properties of the adaptive filter and also to the fact that theoretical expressions utilize exact spectral expressions for MEI and uncorrelated noise while in simulations these are only being approximated.

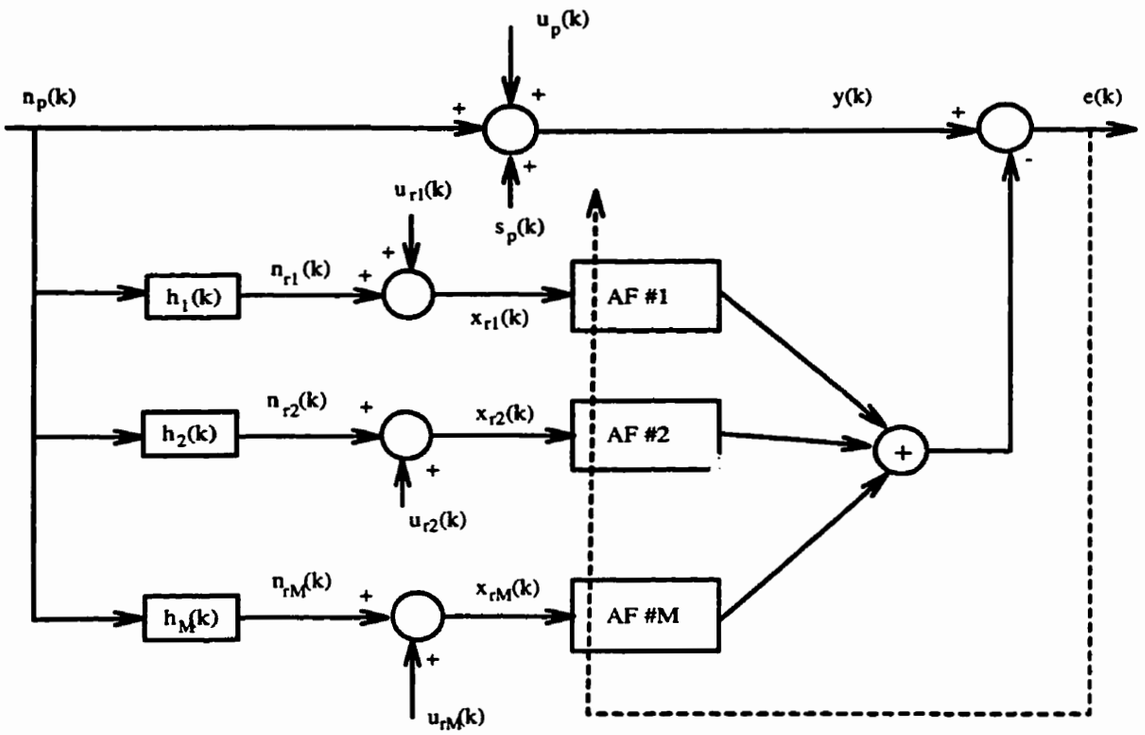

Figure 3.4: *Block diagram of the MRANC.*

The detrimental effect of the uncorrelated noise sources can be alleviated by devising a Multi-Reference Adaptive Noise Canceller (MRANC). The block diagram of an MRANC is shown in Figure 3.4, where M is the number of reference channels and $u_i(k)$ represents the spatially uncorrelated noise source in the *ith* channel. The author in his master's thesis [52] and subsequent publications [49, 50] carried out an exhaustive analysis of the MRANC structure in MEI reduction application. Theoretical expressions for power performance and myoelectric residue indices were derived [49]

and the frequency dependent performance measures in the z domain were expressed as

$$I(z) = \frac{\phi_{N_pN_p}(z) + \phi_{U_pU_p}(z)}{\frac{\phi_{N_pN_p}(z)}{1+\kappa(z)} + \phi_{U_pU_p}(z)} \tag{3.14}$$

$$R(z) = (1+\kappa(z))^2 \tag{3.15}$$

where $\kappa(z) = \sum_{i=1}^{M} \kappa_i(z)$ with $\kappa_i(z)$ being the ratio of MEI to uncorrelated noise spectral densities in the *ith* reference channel. The frequency independent measures were then derived as [49],

$$I = \frac{\kappa_p + 1}{1 + \frac{2}{\sigma^2_{U_p}\omega_s}\int_0^{\omega_s/2} \frac{\phi_{N_pN_p}(\omega)}{1+\kappa(\omega)} d\omega} \tag{3.16}$$

$$R = \frac{\int_0^{\omega/2} \phi_{N_pN_p}(\omega) d\omega}{\int_0^{\omega/2} \frac{\phi_{N_pN_p}(\omega)}{(1+\kappa(\omega))^2} d\omega} \tag{3.17}$$

where κ_p is the ratio of MEI and uncorrelated noise variances in the primary input. Two important conclusions can be drawn based on these performance measures:

- For a given level of uncorrelated noise, the power performance measure, I, has an upper bound given by $1 + \kappa_p$. This is due to the primary uncorrelated noise, $u_p(k)$, which is unaffected by the filtering operation and hence saturates the performance.

- The myoelectric residue index, R, increases monotonically with an increase in the number of reference inputs. As the number of reference channels tends to infinity, R also tends to infinity implying that total myoelectric cancellation can be achieved even in the presence of uncorrelated noise.

The following simulations further illustrate the advantages of an MRANC in exhibiting improved uncorrelated noise tolerance. The primary MEI data and the uncorrelated noise data were generated as described earlier. The MEI transfer functions between the primary and reference inputs were modeled as first order low pass filters given by

$$H_{ri}(z) = \frac{A_i}{1 - \alpha_i z^{-1}} \tag{3.18}$$

where A_i is a scaling constant and α_i was varied to generate a different myoelectric signal for each of the reference channels and was chosen in such a way that the correlation coefficient between the primary and reference channels decreased with i, reflecting experimental conditions. The theoretical expressions for the MRANC output power spectral density and residual MEI power spectral density can be easily derived and are graphically portrayed in Figures 3.5 and 3.6. These results illustrate quite effectively the previous statements that the MRANC output spectral density saturates to a value dependent upon the primary uncorrelated noise and the MEI residue will gradually diminish to zero even in the presence of uncorrelated noise sources.

The theoretical results were further authenticated by processing simulated MEI and uncorrelated noise data. The RLS algorithm was used to implement the MRANC filter and ten thousand samples of MEI and uncorrelated noise data were used to ensure MRANC filter convergence. The MEI and uncorrelated noise were then passed through the MRANC separately and both the power performance measure and MEI reduction index were computed. These results are plotted in Figures 3.7 a and b for an uncorrelated noise level (τ) of 0.006. The increase in power performance and MEI residue indices with an increase in the number of reference channels is apparent in these graphs. The simulation results are once again close to their theoretical counterparts and the differences are mainly attributed to the convergence properties of the M adaptive filters and the approximation of MEI and uncorrelated spectra in simulations. Note that this approximation will result in greater differences for the

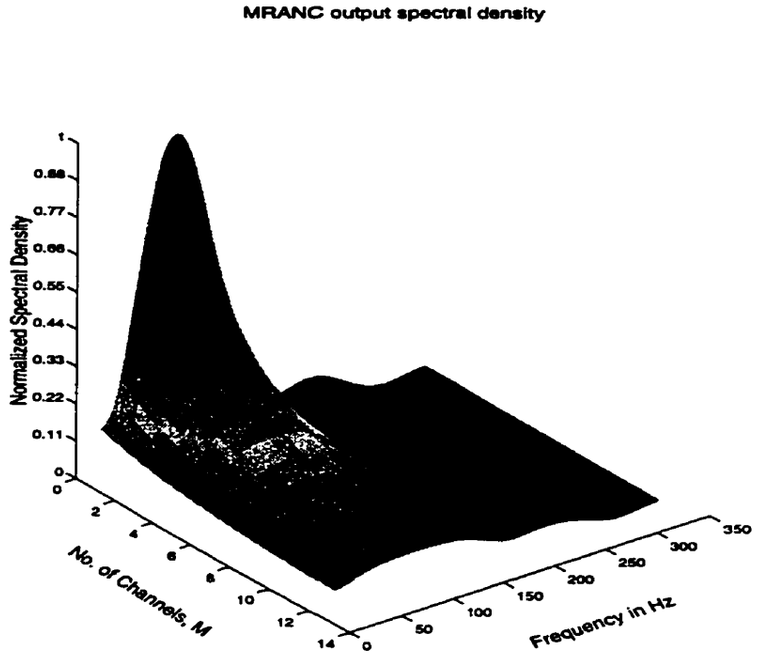

Figure 3.5: *Theoretical MRANC output power spectral density, $\tau = 0.006$.*

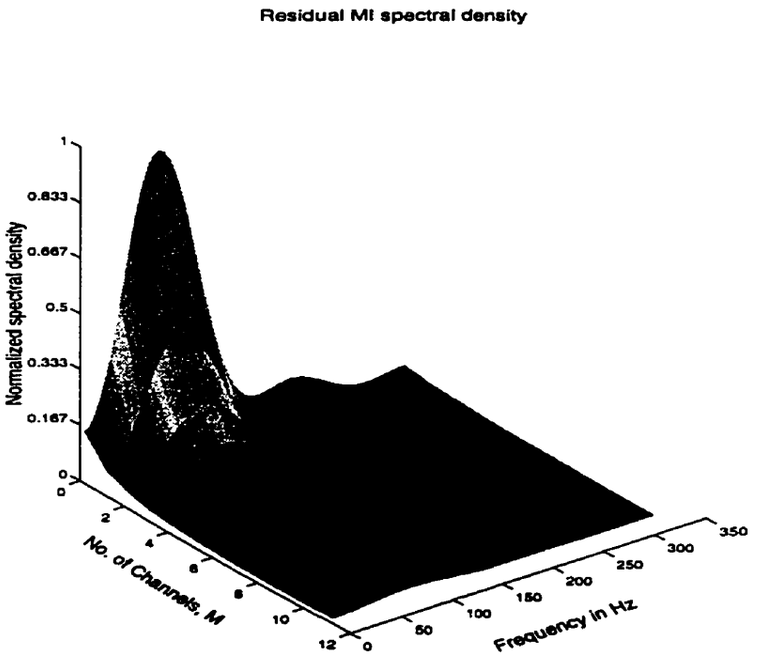

Figure 3.6: *Theoretical MEI residual power spectral density at the MRANC output, $\tau = 0.006$.*

MEI residue index, R, where the theoretical expression given by Eq. 3.17 includes second order terms. Further simulation results and related issues are discussed in a recent publication by the author [49].

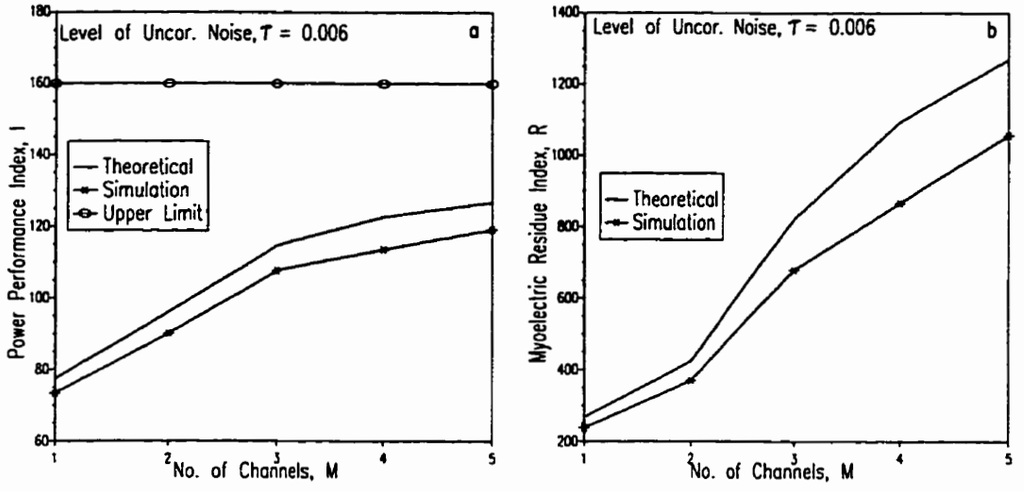

Figure 3.7: *MRANC performance Vs No. of Channels.*

3.5 Crosstalk Phenomenon

A physical constraint in many of the adaptive noise cancellation applications is the presence of desired signal components in the reference input of the ANC. This signal "crosstalk" affects the noise cancelling ability of the ANC and also results in output signal distortion. The block diagram of the ANC infected by signal crosstalk is shown in Figure 3.8, where $g(k)$ represents the crosstalk transfer function. The Wiener solution to the ANC is now given by,

$$W_{opt}(z) = \frac{\phi_{N_pN_p}(z)H(z^{-1}) + \phi_{S_pS_p}(z)G(z^{-1})}{\phi_{N_pN_p}(z)\,|H(z)|^2 + \phi_{S_pS_p}(z)\,|G(z)|^2 + \phi_{U_rU_r}(z)} \tag{3.19}$$

where $\phi_{S_pS_p}(z)$ is the signal power spectral density and $G(z)$ is the z domain crosstalk transfer function. It can be observed from the above equation that the optimal

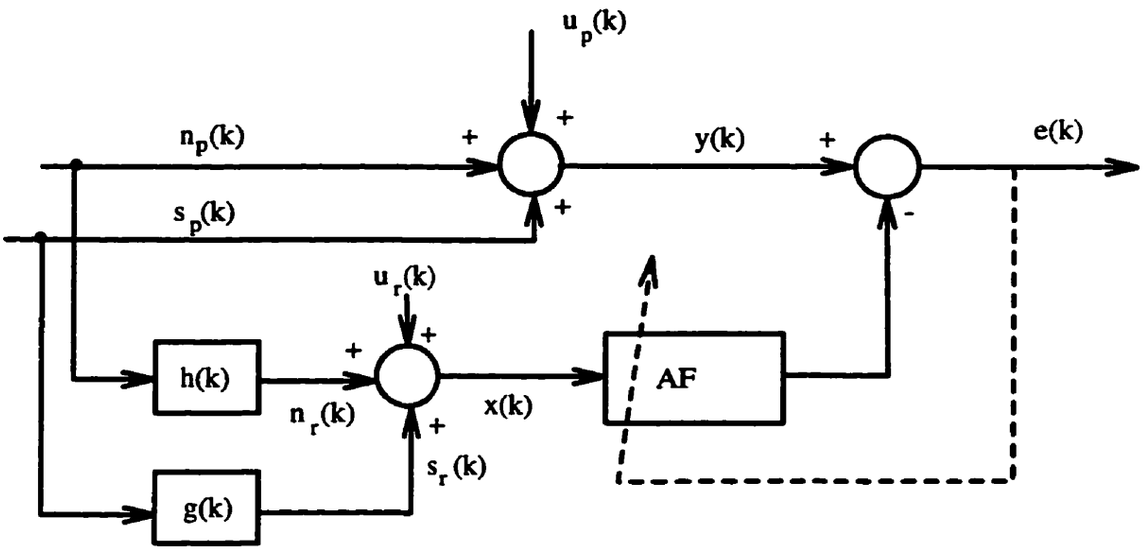

Figure 3.8: ***ANC with uncorrelated noise and signal crosstalk components.***

solution is now also dependent on the crosstalk transfer function. This dependency manifests itself in reduced correlated-noise reduction at the ANC output. Since signal components also pass through the ANC, the signal estimate at the output of the ANC is distorted. In situations where the signal is intermittent and the correlated-noise is persistent, a milder remedy to this problem is to let the ANC function only in the absence of the desired signal. In this way, the effect of signal crosstalk on the adaptation of the ANC disappears and the Wiener solution given above simplifies to the one given in Eq. 3.3. While this guarantees better correlated-noise reduction, the signal distortion, however, still persists.

To demonstrate the effect of the signal crosstalk, simulations were performed once again. The SEP, which is the desired signal in our case, was generated using the following equation [54, 52],

$$s_p(k) = C_2 k T_s (2 - c_s k T_s) e^{-c_s k T_s} \quad \text{k=0...L-1} \tag{3.20}$$

where C_2 is a scaling parameters, c_s is the SEP spectral shaping parameter with a typical value around 2500 and L is the length (in samples) of the SEP. This SEP waveform was repeated the desired number of times to generate an SEP train. To this SEP train, the MEI and uncorrelated noise, whose generation was described earlier, were added. For simplicity, the crosstalk transfer function was made equal to a scaling constant, $\beta < 1$. The signal distortion incurred due to the ANC filter is quantified using a distortion index measure given by

$$\rho = \frac{\sum_{k=0}^{L-1}(s_p(k) - \widehat{s}_p(k))^2}{\sum_{k=0}^{L-1} s_p^2(k)} \tag{3.21}$$

where $\widehat{s}_p(k)$ is the signal estimate at the ANC output. Using Parseval's relation, the distortion index can be expressed in the frequency domain as,

$$\rho = \frac{\int_0^{\omega_s/2} \phi_{S_pS_p}(\omega)d\omega + \int_0^{\omega_s/2} \phi_{\widehat{S}_p\widehat{S}_p}(\omega)d\omega - 2\int_0^{\omega_s/2} \Re\{\phi_{S_p\widehat{S}_p}(\omega)\}d\omega}{\int_0^{\omega_s/2} \phi_{S_pS_p}(\omega)d\omega} \tag{3.22}$$

where $\Re\{\phi_{S_p\widehat{S}_p}(\omega)\}$ is the real part of the cross-spectral density between the original SEP and its estimate. The input SNR was defined as

$$SNR_i = \frac{S_{pmax}^2}{\sigma_{N_p}^2 + \sigma_{U_p}^2} \tag{3.23}$$

and the output SNR as,

$$SNR_o = \frac{\widehat{S}_{pmax}^2}{\sigma_{N_o}^2 + \sigma_{U_o}^2} \tag{3.24}$$

where S_{pmax} and $\widehat{S}_{pmax}$ are respectively the SEP peak amplitude levels at the input and the output of the ANC, $\sigma_{N_o}^2$ is the variance of the residual MEI component at the output of the ANC and $\sigma_{U_o}^2$ is the uncorrelated noise component at the output of the ANC. The SNRGAIN achieved by the ANC can be expressed as,

$$\gamma = \frac{SNR_o}{SNR_i} = \frac{\widehat{S}_{pmax}^2}{S_{pmax}^2}\frac{\sigma_{N_p}^2 + \sigma_{U_p}^2}{\sigma_{N_o}^2 + \sigma_{U_o}^2}. \tag{3.25}$$

Notice that in the absence of any signal crosstalk, the above SNRGAIN expression simplifies to the power performance index, I given by Eq. 3.8. Thus the power performance index I can be used as an upper limit for the SNRGAIN accomplished by the ANC.

Figures 3.9 a and b depict the performance of the ANC with increasing crosstalk levels. For these results, a twenty tap FIR filter driven by the RLS algorithm was used to implement the adaptive filter. Once the convergence of the ANC is established, the steady-state weights of the ANC are retrieved and are used to filter the SEP, MEI and uncorrelated noise sources separately and both the distortion index and the SNRGAIN were calculated according to Eqs. 3.21 and 3.25 respectively. From the results, we can observe that the distortion index increases steadily with the level of crosstalk while the SNRGAIN drops considerably.

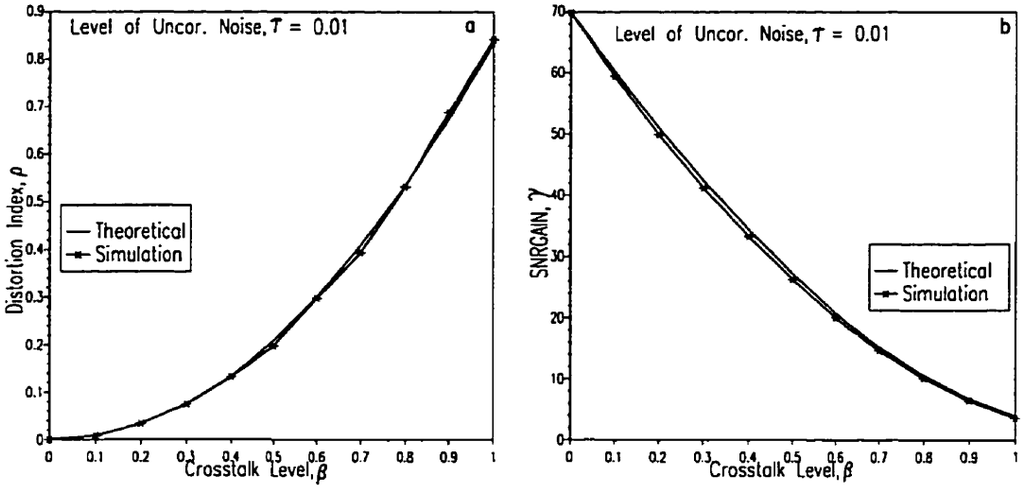

Figure 3.9: *ANC performance in the presence of crosstalk.*

Earlier we have demonstrated that an MRANC provides better performance compared to the ANC in the presence of uncorrelated noise sources. In the presence of signal crosstalk between the primary and reference channels, however, the signal estimate produced by the MRANC is more distorted than the ANC. In this situation, the spatiotemporal properties of the SEP can be used to diminish the

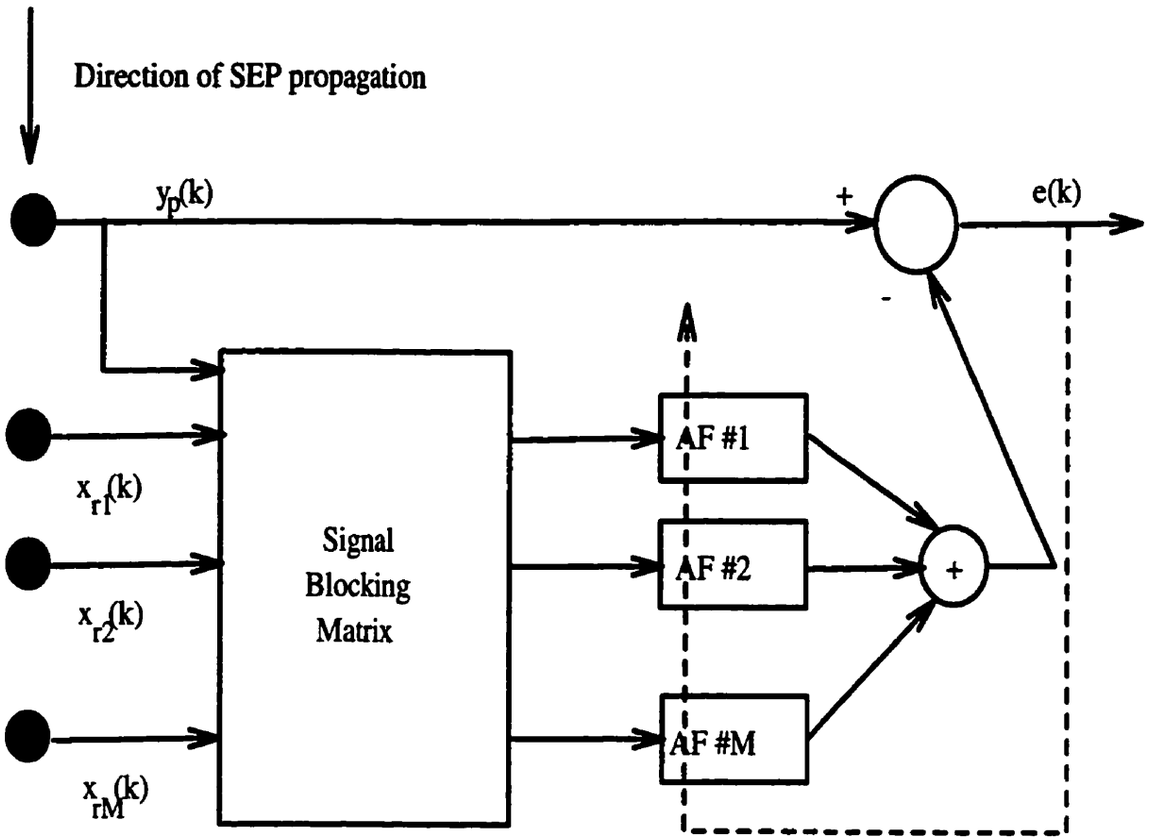

Figure 3.10: ***Block diagram of the Generalized Sidelobe Canceller (GSC).***

damaging effects of SEP crosstalk while still retaining the attractive features of the MRANC. Figure 3.10 portrays the block diagram of a special version of the MRANC, *viz.* the Generalized Sidelobe Canceller (GSC) [70, 6]. Here the primary input is $y_p(k) = s_p(k) + n_p(k) + u_p(k)$ where $s_p(k)$, $n_p(k)$ and $u_p(k)$ are respectively the SEP, MEI and uncorrelated noise sources in the primary input, and the *ith* reference input is $x_{ri}(k) = s_{ri}(k) + n_{ri}(k) + u_{ri}(k)$ where $s_{ri}(k)$, $n_{ri}(k)$ and $u_{ri}(k)$ are the SEP, MEI and uncorrelated noise components in the *ith* reference input respectively. The main difference between the MRANC and the GSC is the "signal blocking matrix" block. This matrix, B, is derived from an ***a priori*** knowledge of the propagation parameters of the desired signal. A simple signal blocking matrix for a four-channel GSC can be

constructed as,

$$\mathbf{B} = \begin{pmatrix} z^{-\delta} & 0 & 0 & 0 \\ -1 & z^{-\delta} & 0 & 0 \\ 0 & -1 & z^{-\delta} & 0 \\ 0 & 0 & -1 & z^{-\delta} \\ 0 & 0 & 0 & -1 \end{pmatrix} \tag{3.26}$$

where δ is the propagation delay of the SEP signal between adjacent sensors. Assuming ideal propagation of the SEP, the above matrix essentially nulls the SEP components in the reference channels thereby avoiding the possibility of signal distortion due to crosstalk. Needless to say, the exact value of the δ parameter in the above matrix is crucial for the successful operation of the GSC. In practical SEP experiments, the value of the δ parameter is usually not known *a priori*. In addition, uniform SEP propagation across the sensors is required to ensure that the signal components are nullified in the reference channels. In practice, this condition is reasonably satisfied for smaller array sizes.

Simulations were performed to compare the SEP distortion incurred in MRANC and GSC structures. The SEP signal was generated according to Eq. 3.20 and was simulated to propagate with a conduction velocity of 100 m/s. The generation of the MEI and uncorrelated noise sources was described earlier. Both MRANC and GSC structures were allowed to operate until the ANCs reached convergence. The converged ANC weights were then used to filter the SEP signal separately and the NMSE distortion measure given by Eq. 3.21 was computed between the original SEP signal and the SEP signal at the output of the MRANC and GSC structures. In Figure 3.11 the distortion indices obtained from the MRANC and the GSC are plotted. The increase in SEP distortion with an increase in the number of reference channels in the case of the MRANC is apparent in this plot. With ideal SEP propagation across the sensors, the GSC outputs a distortion-free SEP resulting in a zero distortion index.

However, deviations from the ideal result in non-zero distortion indices by the GSC. In the case of non-uniform SEP propagation, where the SEP signal was simulated to attenuate as it travels down the sensors, the GSC structure introduces some distortion into the SEP, which is still significantly lower than the SEP distortion at the output of the MRANC. In the event of using a wrong signal blocking matrix, where the δ parameter in the matrix was one time sample off the true value, the GSC can be seen to produce substantial SEP distortion.

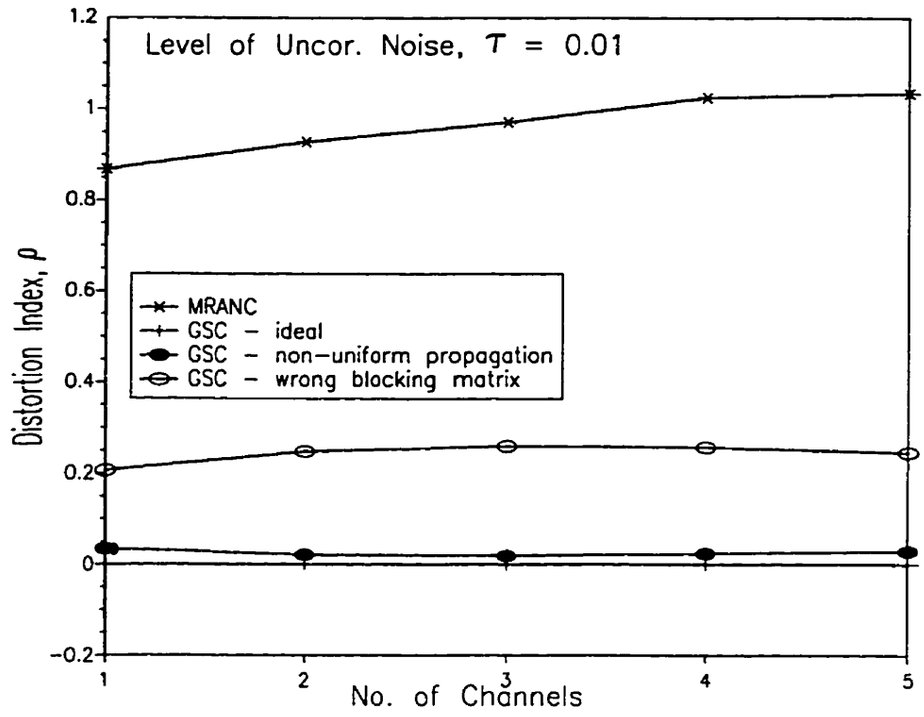

Figure 3.11: ***Performance of the Generalize Sidelobe Canceller under a variety of SEP propagation conditions.***

The above simulation results show that the successful operation of the GSC depends on the accuracy of the signal blocking matrix. To ensure this accuracy, an ***a priori*** knowledge of the propagation parameters of the SEP is required. Since this is not usually available in practical SEP studies, the application of GSC may also result

in SEP distortion. In addition, the performance of the GSC will be affected by the SEP dispersion as it travels along the array. Thus crosstalk resistant noise cancelling structures are required which do not require any ***a priori*** knowledge of the SEP and MEI properties.

3.6 Conclusions

The main objective of this chapter was to introduce the reader to the fundamentals of adaptive noise cancellation. A thorough theoretical development of the ANC is given and the analytical results are further authenticated by processing simulated data. The following points reflect the gist of this chapter:

- Adaptive Noise Cancellers (ANCs) are very useful in many interference reduction applications as they do not require any ***a priori*** knowledge of the signal and interference properties. In addition, they offer signal and interference tracking abilities in nonstationary environments.

- The interference cancelling ability of the ANC is dependent mainly upon four factors: filter structure, adaption algorithm, presence of uncorrelated noise sources and crosstalk of the desired signal. The first two are associated with the implementation of the adaptive filter (either in hardware or software) while the last two are tied to the physical nature of the interference reduction problem.

- The performance of an ANC is a function of the level of uncorrelated noise in its reference input. It has been shown analytically and through simulations that the interference reduction capability of the ANC decreases with increasing levels of uncorrelated noise.

- The effect of uncorrelated noise can be mitigated through using multiple reference channels. The MRANC acts as a spatial averager for the uncorrelated

noise while still maintaining the temporal relationships between the correlated interferences. Theoretical expressions and simulation results are included which demonstrate the performance of the MRANC.

- The performance of an ANC is further deteriorated by the signal "leakage" into the reference input. This signal crosstalk results in undesirable output signal distortion which is worse in the case of the MRANC.

- The spatiotemporal properties of the signal can be exploited to create an MRANC with no distortion. The GSC structure includes a signal blocking matrix which nulls the signal components in the reference channels. However, to create an effective signal blocking matrix, ***a priori*** knowledge of the signal propagation characteristics are required which are not usually available. Thus crosstalk resistant adaptive noise cancelling structures which do not need any ***a priori*** knowledge about the signal parameters are necessary.

Chapter 4

MEI Reduction

Summary

The focus of this chapter is on a Crosstalk Resistant Adaptive Noise Canceller (CRANC) filter which is a cascade of two ANCs. In the absence of uncorrelated noise sources, this CRANC structure is shown to compensate for the signal distortion incurred in a single ANC. Two novel variations of this CRANC structure are developed which reduce the computational complexity by exploiting the SEP and MEI properties. In the presence of uncorrelated noise sources, however, the performance of these CRANC structures is shown to be comparable to the single ANC. A multichannel CRANC (MCRANC) structure is innovated which offers improved tolerance to uncorrelated noise sources. Rigorous analytical treatment of the MCRANC is provided along with simulation results which demonstrate some of the interesting properties of the MCRANC. In addition, an Ensemble-averaged CRANC (ECRANC) filter structure is developed which is particularly useful in low SNR situations. The performance of these CRANC structures with real SEP and MEI data is also scrutinized.

4.1 CRANC Filter in the Absence of Uncorrelated Noise

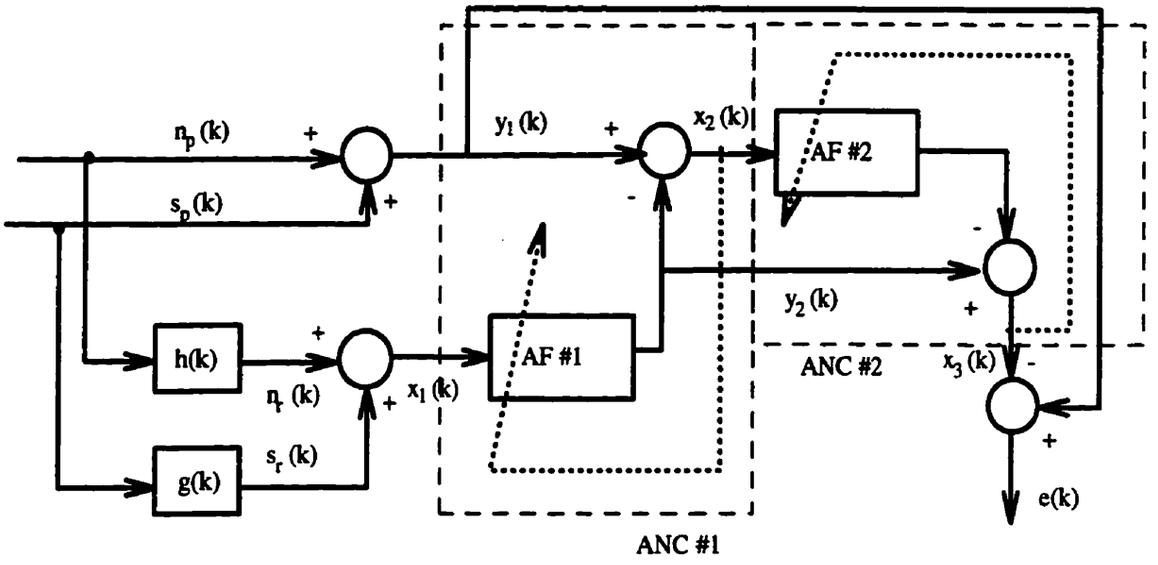

Figure 4.1: *Block diagram of the CRANC filter in the absence of uncorrelated noise sources. Here $s(k)$s denote the SEP components, and $n(k)$s denote the MEI components with p associated with the primary input and r associated with the reference input. In addition, $h(k)$ is the MEI transfer function, $g(k)$ is the crosstalk transfer function and AF represents an adaptive filter.*

The block diagram of the Crosstalk Resistant Adaptive Noise Canceller (CRANC) filter structure in the absence of uncorrelated noise sources is shown in Figure 4.1, where $s_p(k)$ is the desired SEP signal, and $n_p(k)$ and $n_r(k)$ are primary and reference MEI inputs respectively. Essential for the successful operation of this CRANC structure is allowing AF #1 to converge to its optimal solution before the advent of the signal *i.e.* in our application before the nerve is stimulated. This facilitates the estimation of the inverse of the interference transfer function $h(k)$ by AF #1. With this condition, the Wiener solution for the first ANC is given by,

$$W_1(z) = \frac{\phi_{y_1 x_1}(z)}{\phi_{x_1 x_1}(z)} = \frac{\phi_{N_p N_p}(z) H(z^{-1})}{\phi_{N_p N_p}(z) |H(z)|^2}$$

$$= \frac{1}{H(z)}. \tag{4.1}$$

Once AF #1 has converged, further adaptation of it is stopped and the SEP signal is applied. The primary and reference inputs to AF #2 are therefore given by,

$$\begin{aligned} Y_2(z) &= (S_p(z)G(z) + N_p(z)H(z))W_1(z) \\ &= S_p(z)G(z)W_1(z) + N_p(z) \end{aligned} \tag{4.2}$$

and

$$\begin{aligned} X_2(z) &= S_p(z) + N_p(z) - (S_p(z)G(z) + N_p(z)H(z))W_1(z) \\ &= S_p(z) - S_p(z)G(z)W_1(z). \end{aligned} \tag{4.3}$$

Expressing the auto and cross-spectral densities for the second ANC as

$$\begin{aligned} \phi_{y_2x_2}(z) &= \phi_{s_ps_p}(z)\{G(z)W_1(z) - |G(z)W_1(z)|^2\} \\ \phi_{x_2x_2}(z) &= \phi_{s_ps_p}(z)\,|1 - G(z)W_1(z)|^2 \end{aligned} \tag{4.4}$$

we can compute the Wiener solution for AF #2 as

$$W_2(z) = \frac{G(z)W_1(z)}{1 - G(z)W_1(z)} \tag{4.5}$$

Hence the output of the second ANC is given by

$$\begin{aligned} X_3(z) &= N_p(z) + S_p(z)G(z)W_1(z) - \{S_p(z) - S_p(z)G(z)W_1(z)\}\{\frac{G(z)W_1(z)}{1 - G(z)W_1(z)}\} \\ &= N_p(z). \end{aligned} \tag{4.6}$$

Hence at the output of the second ANC we have just the myoelectric interference, $N_p(z)$. This when subtracted from the primary input $Y_1(z)$ results in the SEP alone. Thus in the absence of the uncorrelated noise the CRANC filter successfully eliminates both the crosstalk and the interference but only if the following conditions are satisfied:

- **The myoelectric interference transfer function, $h(k)$, should be time invariant.** Since the first AF is fixed during the SEP duration, violation of the above condition results in substantial residual MEI component at the output of the first stage.

- **The zeros of the transfer function $1 - G(z)W_1(z)$ should be inside the unit circle.** In other words, the $1 - G(z)W_1(z)$ should be a minimum phase transfer function which ensures that the optimal transfer function of AF #2 is stable. If this condition is not satisfied, the CRANC structure fails in compensating for the distortion caused by the signal crosstalk.

During the rest of this chapter, it is assumed that both the above conditions are satisfied. The discussion on the point about the time-varying nature of the MEI transfer function is deferred until the "Experimental Results" section where suggestions are made to work around this problem. It is worthwhile to note here once more that a single ANC (just ANC #1) outputs an interference-free but distorted SEP. The distortion incurred through AF #1 is dependent on the crosstalk transfer function, $G(z)$, as is evident from the Eq. 4.3.

The first set of simulations compared the ability of CRANC and ANC in extracting the SEP from the myoelectric interference in the absence of uncorrelated noise sources. The simulated MEI and SEP data were generated as described in Section 3.5. The primary Signal-to-Interference Ratio (SIR) is defined as $\frac{S_{Pmax}^2}{\sigma_{N_p}^2}$ where once again S_{pmax} is the primary SEP peak amplitude value and $\sigma_{N_p}^2$ is the variance of the primary MEI. As mentioned before, it is critical for the successful operation of CRANC that the first AF be in steady-state before the signal is present. Hence the primary and reference inputs to the CRANC were of 4000 samples of which the first 2000 samples were MEI data. The next 2000 samples were a composite of the SEP signal and the MEI. A ten-tap transversal filter driven by the RLS algorithms was employed as AF #1 and it was allowed to converge in the first 2000 samples. After convergence, the

adaptation was stopped and the remaining 2000 samples of the reference input, $x_1(k)$ in Figure 4.1, were filtered using the steady-state weights. This filtered reference input ($y_2(k)$) was then subtracted from the primary input of AF #1 to give the error output. The filtered reference input and the error output of AF #1 formed the primary and the reference inputs respectively to AF #2 (refer to Fig. 4.1). AF #2 was implemented using a twenty-tap transversal filter driven by the RLS algorithm. Twenty five independent trials were conducted and the final weights of AF #1 and AF #2 were averaged over these twenty five trials. These averaged filter weights were then used to filter the input SEP and MEI indenpendently to generate the output SEP and MEI estimates.

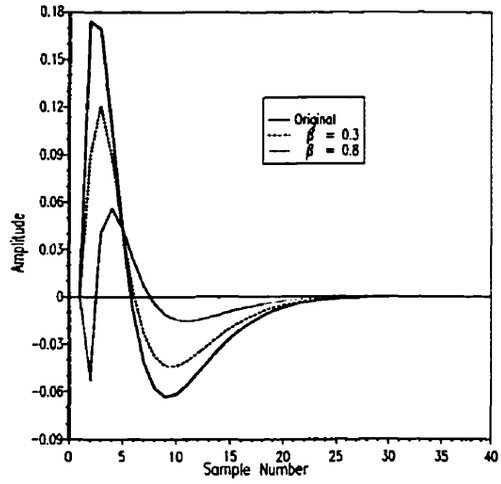

Figure 4.2a: SEP estimate by ANC

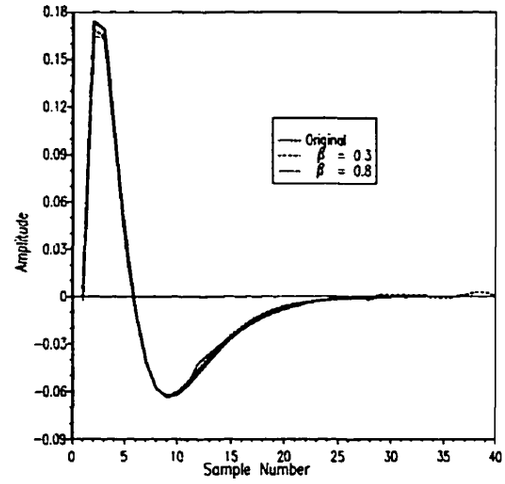

Figure 4.2b: SEP estimate by the CRANC

Figure 4.2: *CRANC vs ANC in the absence of uncorrelated noise sources, SIR = 0.04.*

Figures 4.2a and 4.2b show the outputs of ANC #1 and the CRANC in the absence of uncorrelated noise for two different crosstalk levels. With no uncorrelated noise present, it can be seen that the CRANC produces a distortion- and noise-free estimate of the SEP irrespective of the crosstalk level, while a single ANC is unable to provide such an estimate. Even though the SIR at the output of ANC #1 is infinity, the increase in signal distortion at the output of ANC #1 with increasing crosstalk level

is clearly evident in Fig. 4.2a. The main reasons for the slight differences between the waveforms recovered by the CRANC and the original signal are the finite data and filter lengths. Theoretically, the presence of MEI in the primary of ANC #2 should not affect its convergence. However, in practice, due to finite data length, this does have an impact and even after 25 averages the filter weights are slightly off the Wiener solution.

This basic CRANC structure can be further modified by exploiting certain properties thereby enhancing its performance. The following section focuses on these variations of the basic CRANC structure.

4.2 Variations of the CRANC Structure

4.2.1 Variation #1: Constrained CRANC filter

From Eq. 4.5, we observe that the Wiener solution for the second AF is an IIR transfer function. Thus a large number of filter taps may be required to approximate this transfer function using an FIR filter for the second ANC. This is especially true if either of the filters $G(z)$ or $H(z)$ or both happen to be of long duration. An example can be easily concocted to realize this situation: Let G(z) be a fourth order FIR filter given by,

$$G(z) = -0.2 + 0.25z^{-1} + 0.6z^{-2} + 0.1z^{-3} \tag{4.7}$$

and the interference transfer function be

$$H(z) = 1 + 0.95z^{-1} + 0.91z^{-2} + 0.88z^{-3} + 0.85z^{-4}. \tag{4.8}$$

The resulting impulse response for the optimal solution of AF #2 is shown in Figure 4.3. It can be observed from this graph that the second ANC needs to be at least one hundred taps long (if implemented as an FIR filter), to adequately compensate for the distortion due to signal crosstalk. The computational complexity associated

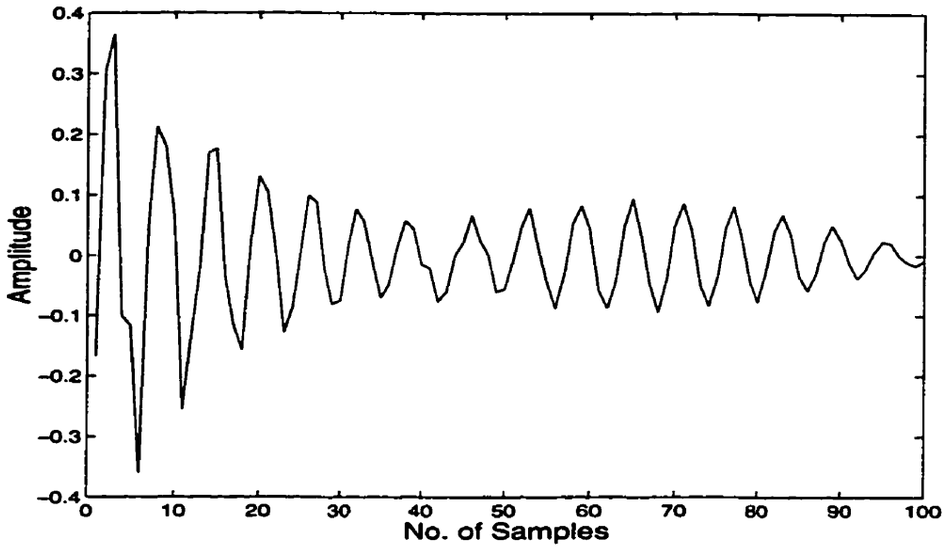

Figure 4.3: *Optimal impulse response of AF #2 for* $G(z) = -0.2+0.25z^{-1}+0.6z^{-2}+0.1z^{-3}$, *and* $H(z) = 1 + 0.95z^{-1} + 0.91z^{-2} + 0.88z^{-3} + 0.85z^{-4}$.

with a hundred tap FIR filter is quite substantial, even with a simpler algorithm such as the LMS algorithm. An appealing way to alleviate this complexity is to constrain the adaption of AF #2 such that only a small part of the coefficients is adapted. The constrained algorithm stems from the fact that $W_2(z)$ contains $W_1(z)$ which was already computed by AF #1. This information can be used to restrict the adaption of AF #2 such that only $G(z)$ parameters are updated at each reduction. This not only results in substantial computational savings but also facilitates a direct estimation of the crosstalk transfer function $G(z)$. A stochastic gradient constrained algorithm for the adaption of $G(z)$ is derived in Appendix I.

The performance of the constrained algorithm is evaluated through processing simulated data. The SEP and MEI data were generated as described earlier. The simulations were performed for three different SIRs to demonstrate the efficacy of the algorithm. Figures 4.4a-f show the convergence of the $G(z)$ weights and the resulting impulse responses of AF #2. For all these results, $G(z)$ was modeled as

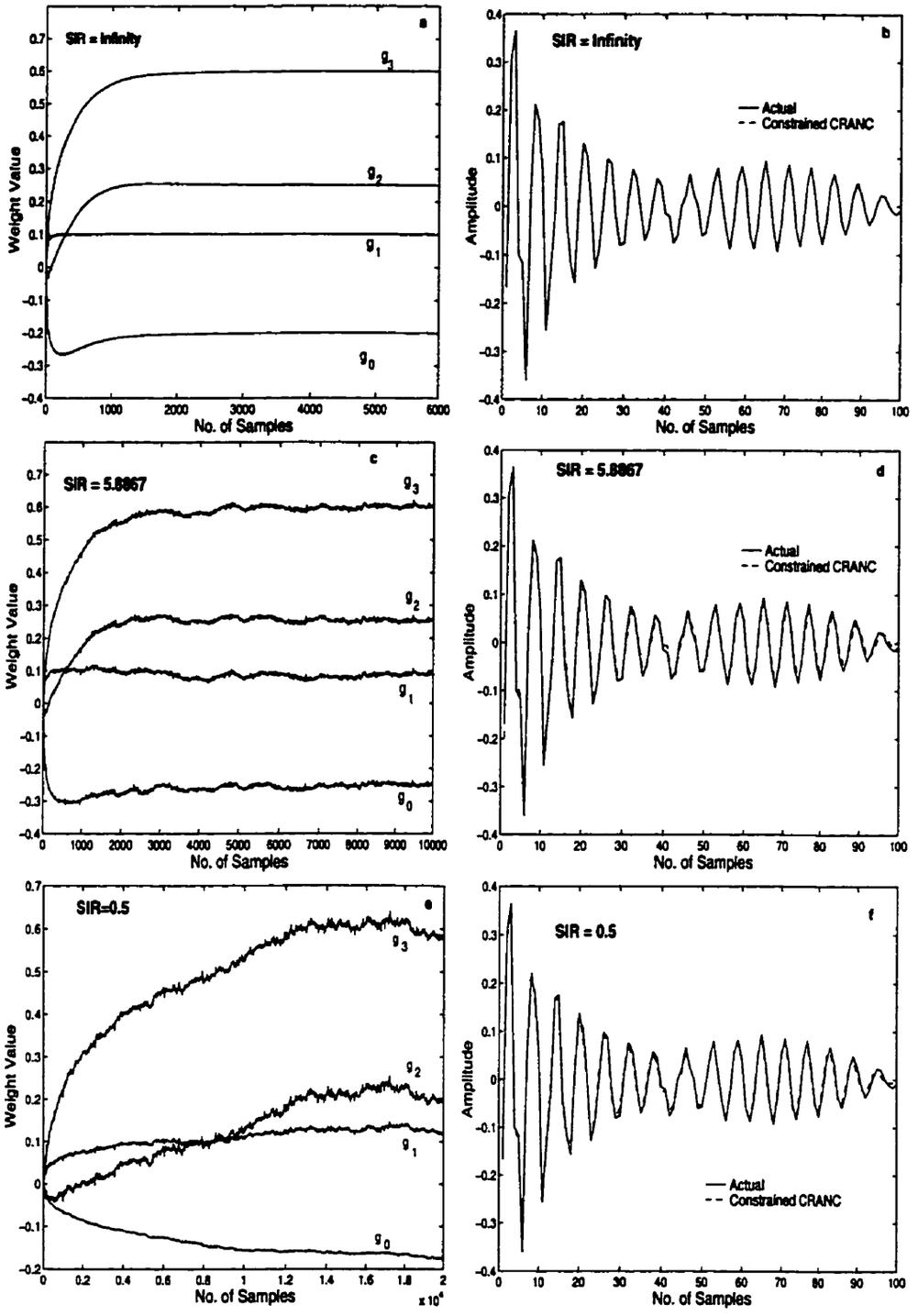

Figure 4.4: *Convergence of the CCRANC algorithm for three different SIRs. Figs. a, c, and e show the weight trajectories while b,d, and f display the corresponding impulse responses of AF #2. The convergence constant μ for the first case was 0.05, and 0.01 for the second. For the third case, μ was a vector = $[0.001, 0.0025, 0.006\ 0.006]^T$. (Refer to text for details.)*

$g_0+g_1z^{-1}+g_2z^{-2}+g_3z^{-3}$ and the "g" values were updated according to the constrained CRANC algorithm. A characteristic trait in the second column of these results is that the constrained CRANC algorithm models the optimal impulse response of the second AF for a variety of SIRs **with only four coefficients**. From the first column in Figure 4.4, the effect of the SIR value on weight convergence can be noticed. Without any MEI present, the algorithm converges to its optimal value almost perfectly and in fewer iterations. However, in the presence of MEI, the weight convergence becomes noisy and for lower values of the SIR the adaption has to be carried out with a lower convergence constant which will result in a slower convergence. This fact can be seen from Figure 4.4e where different convergence constants had to be used for adaption of different weights to ensure that the MEI in the primary input of ANC #2 does not have a detrimental effect.

4.2.2 Variation #2: Delay and Difference Array Processor

As mentioned before, both SEP and MEI are propagating waveforms. Thus the spatiotemporal properties of SEP and MEI can be exploited to further simplify the computational complexity associated with the basic CRANC. The Delay and Difference Array Processor (DDAP), shown in Figure 4.5, is an example of one such filter where the propagating SEP and MEI are tapped using two sensors placed along their direction of propagation[1]. Here $s(k)$ is the SEP signal, $n(k)$ is the MEI with δ and Δ being their respective time delays across the two sensors and AF stands for adaptive filter. Both $s(k)$ and $n(k)$ are assumed to possess uniform propagation characteristics along the array. The first stage of the DDAP estimates the time delay associated with the MEI which can be easily calculated from the cross-correlation information between the two sensors, prior to the application of the stimulus. Thus at the second

[1]It is assumed here that both SEP and MEI propagate in the same direction. While this may not be true in all cases, one can always **project** the SEP and MEI waveforms with arbitrary directions of arrival onto to the line of the array by making appropriate changes to their velocity.(refer to [70] for an introduction to array processing).

stage of the DDAP, we have,

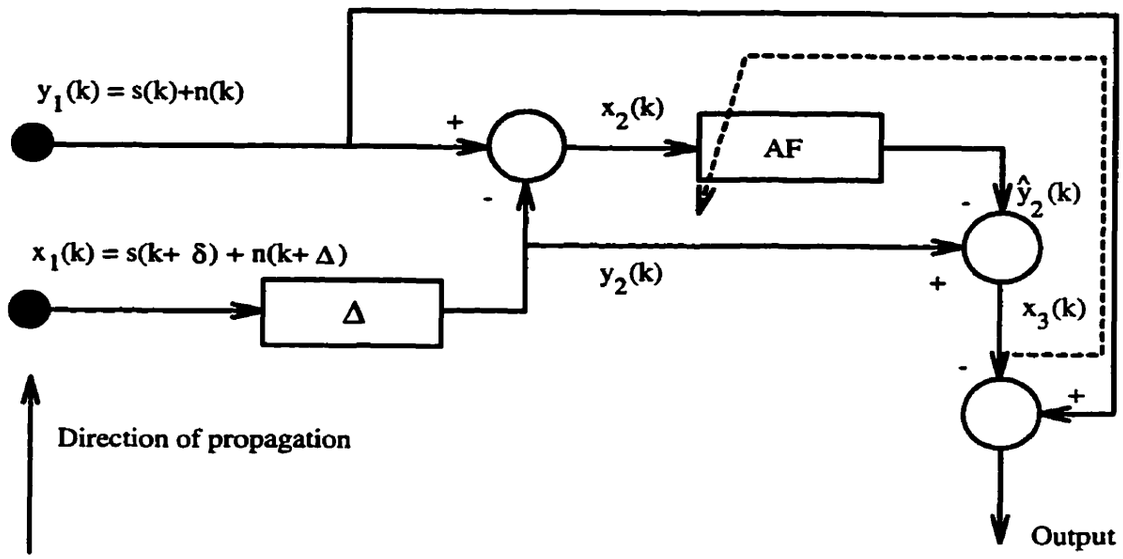

Figure 4.5: *Block diagram of the basic Delay and Difference Array Processor (DDAP) where $s(k)$ is the SEP signal, $n(k)$ is the MEI with δ and Δ being their respective time delays across the primary and reference sensors.*

$$y_2(k) = s(k+\delta-\Delta)+n(k) \tag{4.9}$$

$$x_2(k) = s(k)-s(k+\delta-\Delta). \tag{4.10}$$

The Wiener solution to the adaptive filter is

$$W(z) = \frac{z^{-\varphi}}{1-z^{-\varphi}} \tag{4.11}$$

where $\varphi = \Delta - \delta$ is the difference in MEI and SEP propagating time delays. When the AF attains this optimal solution, the output of the second stage is just $n(k)$. This, when subtracted from the primary input $y_1(k)$, results in an interference free signal estimate. Several observations are in order with respect to this basic DDAP structure:

- By exploiting the propagation characteristics of the MEI, the DDAP reduces the computational complexity associated with the first stage in the basic CRANC structure. The transfer function estimation problem collapses to a simpler time delay estimation problem. This of course is based on the assumption that the MEI propagates uniformly across the array.

- The second stage of the DDAP also involves estimating a time delay parameter, *viz.* the φ parameter. Note that the optimal solution for the second stage, given by Eq. 4.11, is once again an IIR transfer function. But this time, the IIR transfer function is only marginally stable as there are multiple poles (their number determined by the φ parameter) placed on the unit circle. This results in two drawbacks: a) any presence of residual MEI or any other noise will result in an amplified output, and b) truncation using an FIR filter requires a significantly large number of filter taps. Also, explicit adaptation for the φ parameter becomes impossible. This point is addressed in Appendix II.

The drawbacks associated with the basic DDAP can be overcome by designing a three sensor DDAP as shown in Figure 4.6. Assuming both SEP and MEI are plane waves, the composites at the three sensors are respectively $s(k+2\delta)+n(k+2\Delta)$, $s(k+\delta)+n(k+\Delta)$ and $s(k)+n(k)$. As mentioned before, it is fairly straightforward to estimate the Δ parameter. Once this MEI delay parameter is estimated, the outputs at node #1 and #2 are given by

$$y(k) = s(k) - s(k+2\delta-2\Delta) = s(k) - s(k-2\varphi) \tag{4.12}$$

$$x(k) = s(k) - s(k+\delta-\Delta) = s(k) - s(k-\varphi) \tag{4.13}$$

where φ is once again the difference in the time delay values of the MEI and the SEP. The problem now is to estimate the φ parameter. If we employ an adaptive filter with $y(k)$ as the primary input and $x(k)$ as the reference input, the Wiener solution

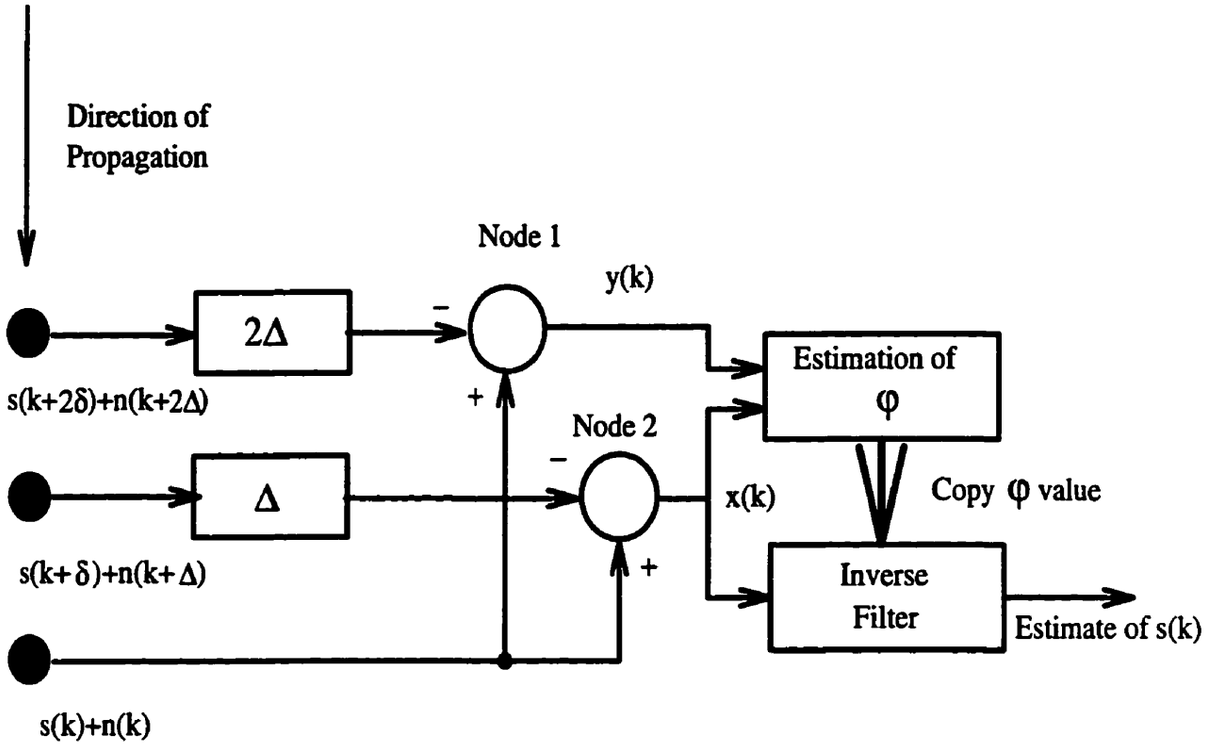

Figure 4.6: *Modified DDAP.*

to that adaptive filter is,

$$W(z) = \frac{1 - z^{-2\varphi}}{1 - z^{-\varphi}} = 1 + z^{-\varphi}. \tag{4.14}$$

Thus, if an FIR filter is used to realize this adaptive filter, both the first weight and the weight corresponding to a delay value equal to φ will go to unity as the adaptive filter reaches its optimal solution. A very important issue here is the length of the FIR filter which should have an adequate memory to estimate the φ value. However, this will give rise to computational complexity and convergence problems if the φ parameter is large. An alternative approach is to adapt only the time delay parameter. This explicit time delay adaptation will require adaptation of only one weight and hence is computationally very appealing. A stochastic gradient algorithm for an explicit adaptation of the φ parameter is derived in Appendix II.

At this point, the desired signal still needs to be recovered. To do this, the output at node #2 is given to an inverse filter whose transfer function is given by

$$IF(z) = \frac{1}{1 - z^{-\varphi}} \tag{4.15}$$

The output of this inverse filter is an interference- and distortion-free SEP estimate. Note that the inverse filter has multiple poles on the unit circle and hence is only marginally stable. Thus in the presence of any residual noise, ensemble averaging must be performed at the input of the inverse filter to correctly recover the SEP waveform.

The following simulations scrutinize the performance of the modified DDAP. The generation of the SEP and MEI waveforms are as described earlier. Both SEP and MEI were modeled as plane propagating waves with δ and Δ parameters set to 2 and 20 samples respectively. Figure 4.7 displays the results produced by the modified DDAP. Figure 4.7a depicts the SEP+MEI composite collected at the third sensor. The Δ parameter was first estimated from the peaks of the cross-correlation estimates between the sensors. Using this parameter, the outputs at nodes 1 and 2 are computed. Figure 4.7b displays the output at node #2 which is clearly distorted. Using the output at node #1 as the primary input and the output at node #2 as the reference input, the time-delay estimation algorithm (detailed in Appendix II) was invoked to estimate the φ value. The convergence of the φ estimate is graphed in Figure 4.7c where correct convergence of the algorithm can be observed. The converged value is then used to construct the inverse filter given by Eq. 4.15. The output of the inverse filter is shown in Figure 4.7c which can be seen to be devoid of any distortion.

So far, in developing the constrained CRANC filter and the modified DDAP, we have dealt only with desired-signal and interference waveforms with ideal propagation characteristics and in the absence of any other noise sources. While this may be true in some signal processing applications (where the above techniques will be most useful), deviations from ideality are a norm with practical SEP signal processing scenarios.

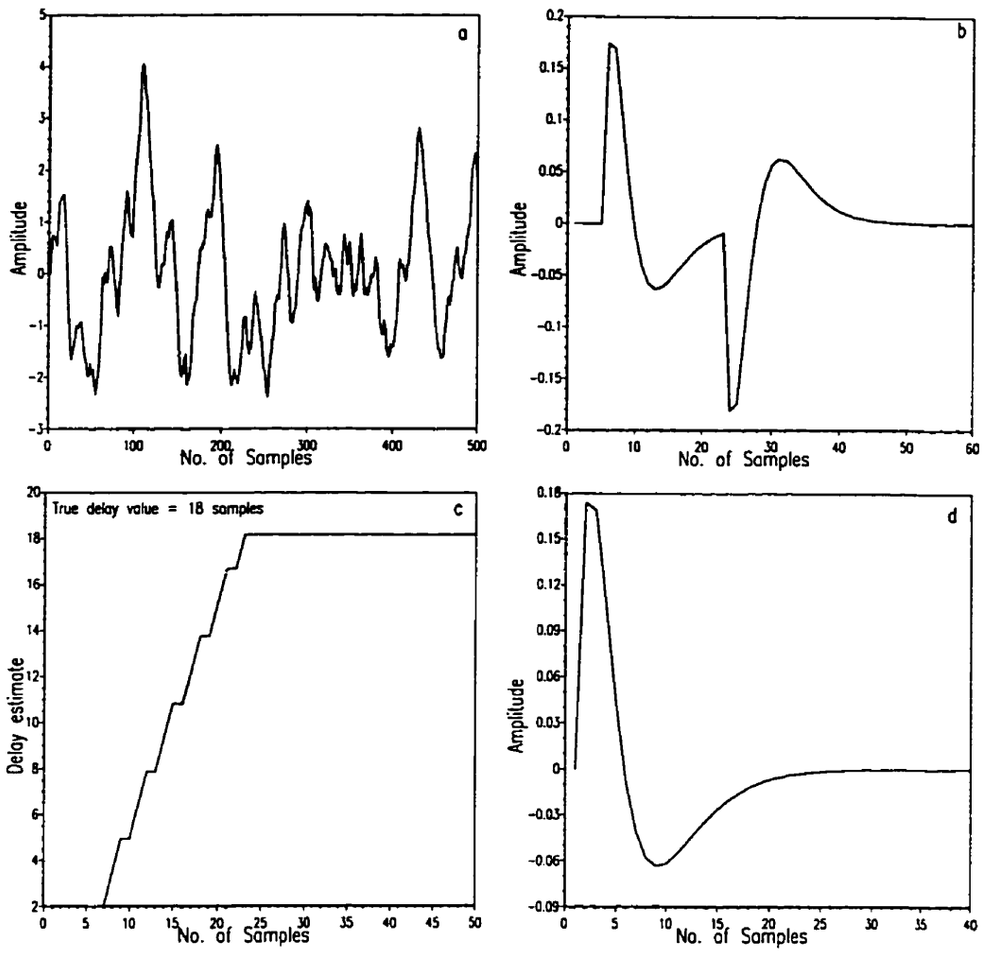

Figure 4.7: *Performance of the modified DDAP. a) SEP+MEI composite at the third sensor at an SIR of 0.01, b) distorted SEP at node #2, c) convergence of the φ estimate, and d) the output of the inverse filter.*

Thus the effect of these deviations on the abovementioned techniques has to be studied.

4.3 Deviations from the Ideal

4.3.1 Effect of Uncorrelated Noise on the Basic CRANC

Let us first investigate the effect of uncorrelated noise sources on the basic CRANC. The block diagram of the CRANC filter with uncorrelated noise sources is shown in Figure 4.8 where $u_p(k)$ and $u_r(k)$ are the primary and reference uncorrelated noise sources respectively. With the addition of uncorrelated noise, the Wiener solution to AF #1 becomes (noting that once again AF #1 is adapted before the advent of the signal),

$$\begin{aligned} W_1(z) &= \frac{\phi_{N_pN_p}(z)H(z^{-1})}{\phi_{N_pN_p}(z)\,|H(z)|^2 + \phi_{U_rU_r}(z)} \\ &= \frac{1}{H(z)\{1+\Gamma_r(z)\}} \end{aligned} \tag{4.16}$$

where

$$\Gamma_r(z) = \frac{\phi_{U_rU_r}(z)}{\phi_{N_pN_p}(z)\,|H(z)|^2} \tag{4.17}$$

is the ratio of uncorrelated to myoelectric interference spectral densities in the reference input. The primary and reference inputs to AF #2 can be expressed respectively as,

$$Y_2(z) = S_p(z)G(z)W_1(z) + N_p(z)H(z)W_1(z) + U_r(z)W_1(z) \tag{4.18}$$

and

$$\begin{aligned} X_2(z) &= \{S_p(z) + N_p(z) + U_p(z)\} - \{S_p(z)G(z) + N_p(z)H(z) + U_r(z)\}W_1(z) \\ &= S_p(z)\{1 - G(z)W_1(z)\} + N_p(z)\{1 - H(z)W_1(z)\} + U_p(z) - U_r(z)W_1(z) \\ &= S_p(z)\{1 - G(z)W_1(z)\} + N_p(z)\{1 - \tfrac{1}{1+\Gamma_r(z)}\} + U_p(z) - U_r(z)W_1(z) \end{aligned} \tag{4.19}$$

The cross-spectral density of the primary and reference inputs for the second ANC can therefore be expressed as

$$\begin{aligned} \phi_{Y_2X_2}(z) &= \phi_{S_pS_p}(z)G(z)W_1(z)\{1 - G(z^{-1})W_1(z^{-1})\} + \\ &\phi_{N_pN_p}(z)H(z)W_1(z)\{1 - H(z^{-1})W_1(z^{-1})\} - \phi_{U_rU_r}(z)\,|W_1(z)|^2 \end{aligned} \tag{4.20}$$

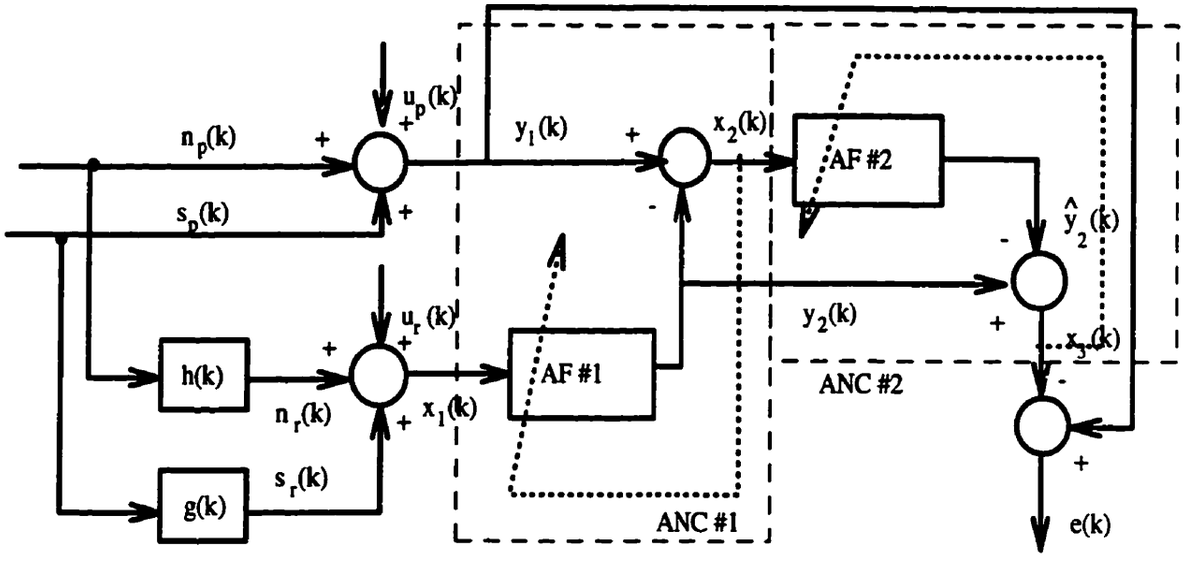

Figure 4.8: ***Block diagram of the CRANC filter in the presence of uncorrelated noise sources. In addition to the terms defined in Figure 4.1, $u_p(k)$ and $u_r(k)$ are the uncorrelated noise components in the primary and reference respectively.***

which can be simplified upon substitution of Eqs. 4.16 and 4.17 to

$$\phi_{Y_2X_2}(z) = \phi_{S_pS_p}(z)G(z)W_1(z)\{1 - G(z^{-1})W_1(z^{-1})\} \tag{4.21}$$

Interestingly, the cross-spectral density is unaffected by the presence of the uncorrelated noise sources and is the same as in Eq. 4.4. The autospectral density of the reference input is given by

$$\phi_{X_2X_2}(z) = \phi_{S_pS_p}(z)\,|1 - G(z)W_1(z)|^2 + \phi_{N_pN_p}(z)\,|1 - H(z)W_1(z)|^2 + \phi_{U_pU_p}(z) + \phi_{U_rU_r}(z)\,|W_1(z)|^2\,. \tag{4.22}$$

The Wiener solution for the second AF is the ratio of the spectral densities given in Eqs 4.21 and 4.22. Thus from Equations 4.16, 4.21 and 4.22, we can see that the presence of uncorrelated noise sources drives $W_1(z)$ and $W_2(z)$ away from the desired

solutions given by Equations 4.1 and 4.5 respectively. The power spectral densities of SEP, MEI and uncorrelated noise sources can be expressed respectively as

$$\phi_{S_oS_o}(z) = \phi_{S_pS_p}(z)\,|(1 - G(z)W_1(z))(1 + W_2(z))|^2 \tag{4.23}$$

$$\phi_{N_oN_o}(z) = \phi_{N_pN_p}(z)\,|(1 - H(z)W_1(z))(1 + W_2(z))|^2 \tag{4.24}$$

$$\phi_{U_oU_o}(z) = \{\phi_{U_pU_p}(z) + \phi_{U_rU_r}(z)\,|W_1(z)|^2\}(1 + |W_2(z)|^2). \tag{4.25}$$

The above equations represent the general form of the spectral content at the output of the CRANC. In order to quantify the performance of both the CRANC and the ANC, spectral information is therefore required. Given this spectral information, theoretical performance indices can be computed. These can then be compared against the performance obtained through simulations giving us an insight into the operation of the CRANC and the ANC in the presence of both the uncorrelated noise and the signal crosstalk. The theoretical predictions are once again calculated numerically due to the unwieldy integrals for distortion index, ρ and SNRGAIN, γ especially with the complex equations for adaptive filter transfer functions given by Eqs. 4.16, 4.21 and 4.22. The power spectral density of the SEP can be found numerically using Equation 3.20. The primary steps involved in estimating the spectrum are computing the Fast Fourier Transform (FFT) of $s_p(k)$, squaring the magnitude of the result and scaling it by the data length of $s_p(k)$. Since the MEI is modelled as white Gaussian noise of unit variance passing through the shaping filter, $p(k)$ given by Equation 3.10, its power spectrum can be computed by calculating the FFT of $p(k)$ and squaring the magnitude of the result. The uncorrelated noise sources can be assumed to have flat spectra in the bandwidth of interest. With this spectral information it is straight forward to compute the filter transfer functions, $W_1(z)$ and $W_2(z)$. Once we compute these transfer functions, the output spectral density functions can be calculated using Equations 4.23, 4.24 and 4.25. With this information, the theoretical performance measures of the CRANC and ANC can be calculated.

Figures 4.9 and 4.10 show the SNRGAIN performance surfaces of both the ANC

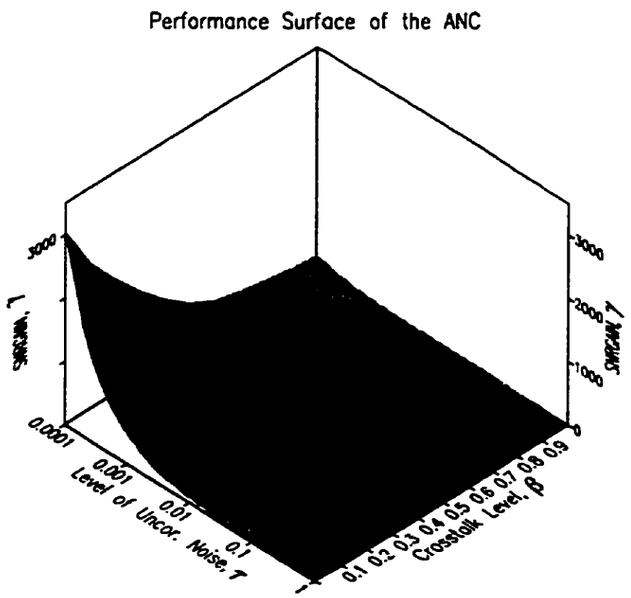

Figure 4.9: *Theoretical performance surface of the ANC, SIR = 0.04.*

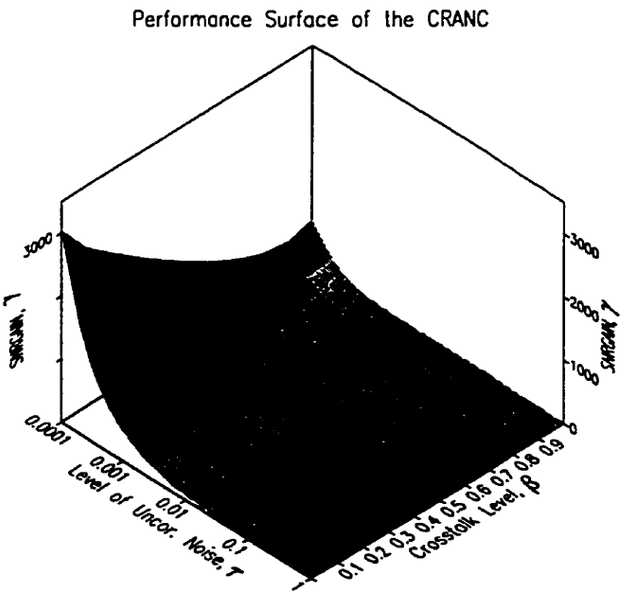

Figure 4.10: *Theoretical performance surface of the CRANC, SIR = 0.04.*

and the CRANC for varying levels of uncorrelated noise and crosstalk. The effect of uncorrelated noise on the ANC and the CRANC is apparent in these plots. At low levels of uncorrelated noise, the CRANC structure exhibits some resistance to crosstalk compared to the ANC. At higher levels of uncorrelated noise, however, its performance deteriorates. Another interesting factor is that the effect of uncorrelated noise on the CRANC is more severe at higher crosstalk levels. Figure 4.11 compares the SNRGAIN obtained from the CRANC and the ANC at different levels of uncorrelated noise. It is obvious from this picture that for $\tau > 0.01$ the performances of the CRANC and the ANC are almost the same. Thus for levels of uncorrelated noise greater than 0.01, the additional computational needs of the CRANC are not justified on the basis of the SNRGAIN.

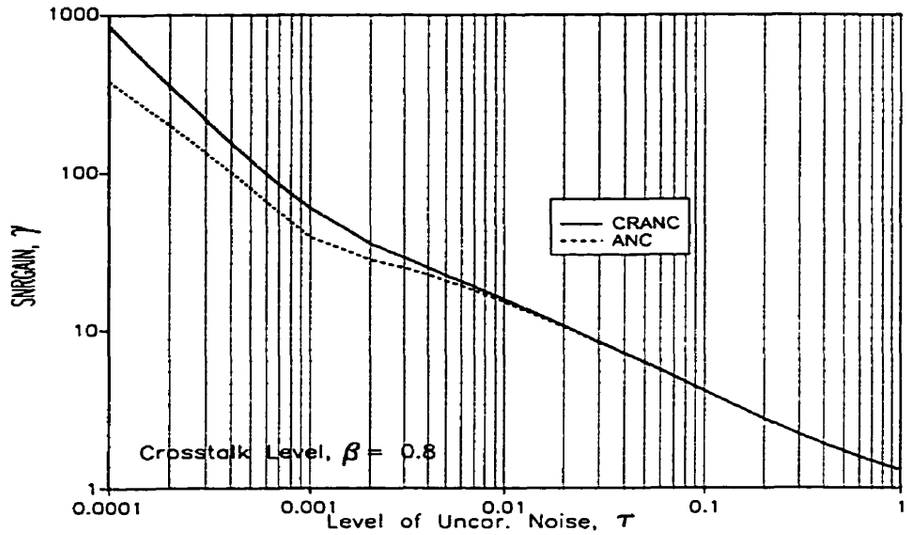

Figure 4.11: ***Performance comparison of the CRANC and the ANC, SIR = 0.02 and β = 0.8.***

Simulations were performed to compare the performances of the CRANC and the ANC in the presence of the uncorrelated noise to further probe the above conjecture. The SEP and the MEI were generated as described previously. The uncorrelated

noise sources were white Gaussian noise sources whose variance was varied to achieve the desired level of uncorrelated noise, τ. The first and second stages of the CRANC were realized by twenty-tap transversal filters driven by the RLS algorithm. The simulations were performed for two different levels of uncorrelated noise. For each of these two levels twenty five independent simulations were performed and the steady-state adaptive filter weights at the end of each run were averaged. These averaged weights were then used to filter the SEP, MEI and uncorrelated noise sources. Thus estimates of the SEP, MEI and uncorrelated noise at the output of the CRANC and the ANC could be obtained. Using this information, the distortion index and the SNRGAIN were calculated employing Equations 3.21 and 3.25. Figures 4.12a-d show the performance comparison of the CRANC and the ANC for these two levels of uncorrelated noise. In Figure 4.12a the distortion index, ρ, obtained from the CRANC and the ANC is compared. The increase in crosstalk level can be seen to increase the distortion index calculated from the CRANC and the ANC with the CRANC slightly outperforming the ANC. The simulation results can be seen to be in close agreement with the theory. The differences between the simulation and theory are mainly attributed to the convergence properties of the adaptive filters due to the finite data and filter lengths. These effects tend to be more pronounced in the case of the CRANC filter since it employs two adaptive filters. Also in the theoretical development exact spectral information of each of the signal and noise components was used while in simulation these are only approximated. Figure 4.12b portrays the SNRGAINs achieved by the CRANC and the ANC at different levels of crosstalk for $\tau = 0.0025$. Again we see that an increase in crosstalk results in a degraded performance for both the CRANC and the ANC with CRANC exhibiting a marginally better performance compared to the ANC. Again the simulations are in close agreement with the theory. Figures 4.12c and 4.12d compare the distortion index and SNRGAIN obtained by the CRANC and the ANC at $\tau = 0.01$ respectively. Here we observe that the performance indices obtained from the CRANC and the ANC

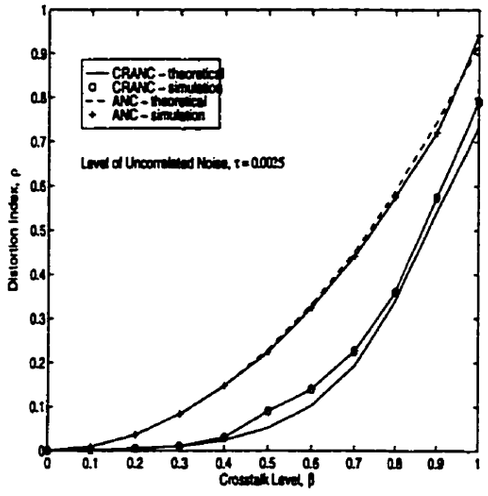

Figure 4.12a: Distortion Index Vs Crosstalk

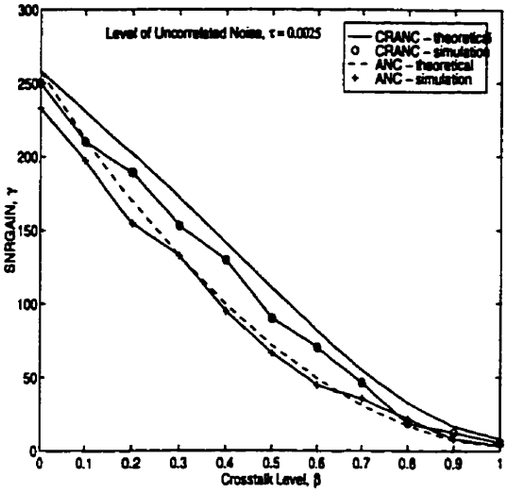

Figure 4.12b: SNRGAIN Vs Crosstalk

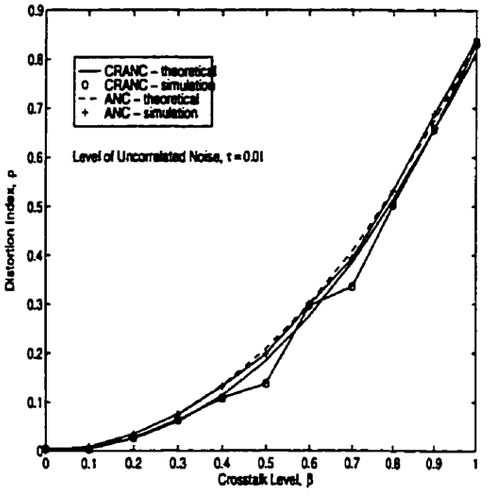

Figure 4.12c: Distortion Index Vs Crosstalk

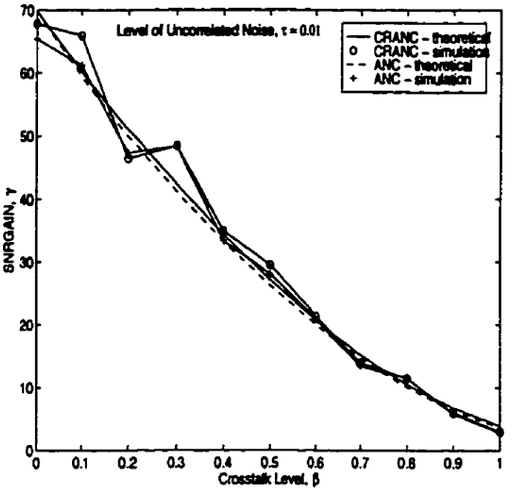

Figure 4.12d: SNRGAIN Vs Crosstalk

Figure 4.12: *CRANC vs ANC in the presence of uncorrelated noise sources.*

are almost identical at each and every level of the crosstalk. Thus higher levels of uncorrelated noise render the second ANC in the CRANC filter structure practically useless.

4.3.2 Effect of Uncorrelated Noise on CRANC Variations

Let us first look at the effect of uncorrelated noise sources on the constrained CRANC algorithm. With the addition of uncorrelated noise sources, the equivalent structure of the second stage of the CRANC filter can be depicted as shown in Figure 4.13, where $W_2(z)$ is the optimal transfer function for AF #2 of the CRANC filter from Eqs. 4.21 and 4.22. In the absence of any uncorrelated noise sources, $W_2(z)$ has a form similar to $\widehat{G}(z)W_1(z)/(1-\widehat{G}(z)W_1(z))$ and hence constrained CRANC algorithm will converge to the correct $G(z)$ transfer function. In the presence of uncorrelated noise sources, $W_2(z)$ is a complex ratio of the spectral densities given by Eqs. 4.21 and 4.22, and hence the constrained algorithm will return biased $G(z)$ values. The amount of bias depends on two factors:

- The ratio of the uncorrelated to myoelectric power spectral densities in the reference input of AF #1, $\tau_r(z)$. If $\tau_r(z)$ is very small at all frequencies, then AF #1 will converge to the inverse of the myoelectric transfer function and there will be negligible myoelectric residue at the reference input of AF #2. If this condition is not true, the myoelectric residue in the reference input of AF #2 will introduce bias in the convergence of the constrained CRANC algorithm.

- The spectral ratio of the SEP and uncorrelated noise should be $>> 1$. If this is not the case, the convergence of the constrained algorithm is significantly influenced by the uncorrelated noise sources and hence the resulting $G(z)$ estimates will be biased.

Figures 4.14 a and b show the convergence of the constrained CRANC algorithm in the presence of uncorrelated noise sources. Two different sets of simulations were

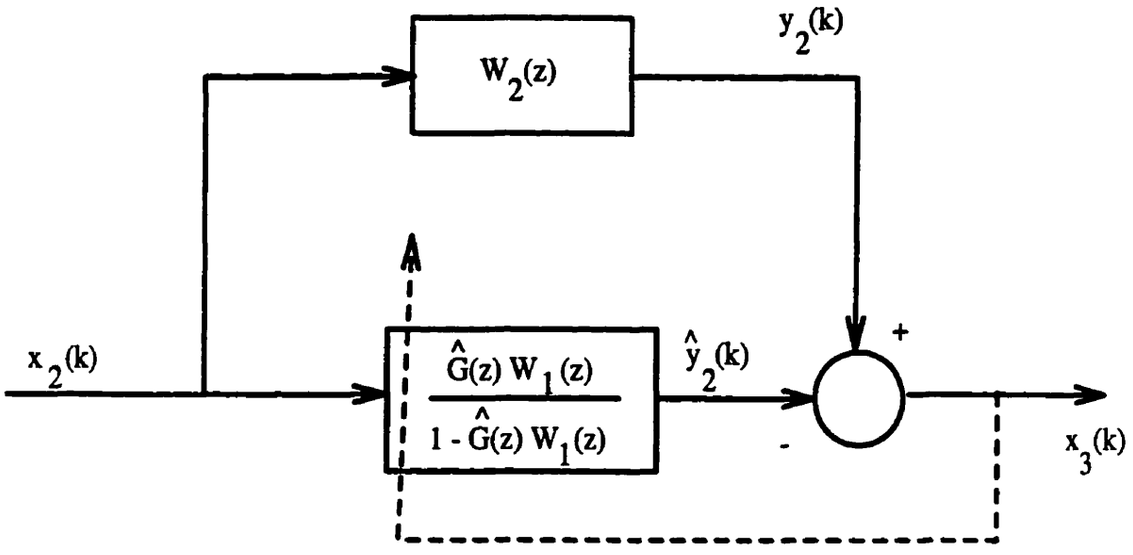

Figure 4.13: ***Equivalent block diagram for the second stage of the constrained CRANC filter.***

performed for two different values of the level of uncorrelated noise, τ. Comparing these graphs with the convergence plots in Figure 4.3, we can observe that uncorrelated noise sources introduce bias into the convergence of the constrained CRANC algorithm. This bias can be seen to worsen as the level of uncorrelated noise increases. The converged weight values in Figure 4.14b are nowhere near the true $G(z)$ values given in Equation 4.7.

The effect of uncorrelated noise on the modified DDAP is scrutinized next. White Gaussian noise sources were added to the propagating SEP and MEI waveforms. Once again simulations were performed for two different τ values *viz.* for $\tau = 0.01$ and 0.001. The Δ parameter was estimated from the peak of the cross-correlation function between the sensors. Note that the uncorrelated noise does not effect the Δ parameter estimation significantly as the MEI is at least one hundred times more powerful than the uncorrelated noise sources. Figures 4.15 a and b show the convergence of the time delay estimate, $\hat{\varphi}$, for both the simulation cases. A characteristic feature in both these

plots is the convergence of the time delay estimate to the true value **in the mean.** This can be shown theoretically using the update equation for the time-delay estimate given by, (from Appendix II)

$$\widehat{\varphi}(k+1) = \widehat{\varphi}(k) + \mu e(k)\{x(k-\widehat{\varphi}-1) - x(k-\widehat{\varphi}+1)\}. \tag{4.26}$$

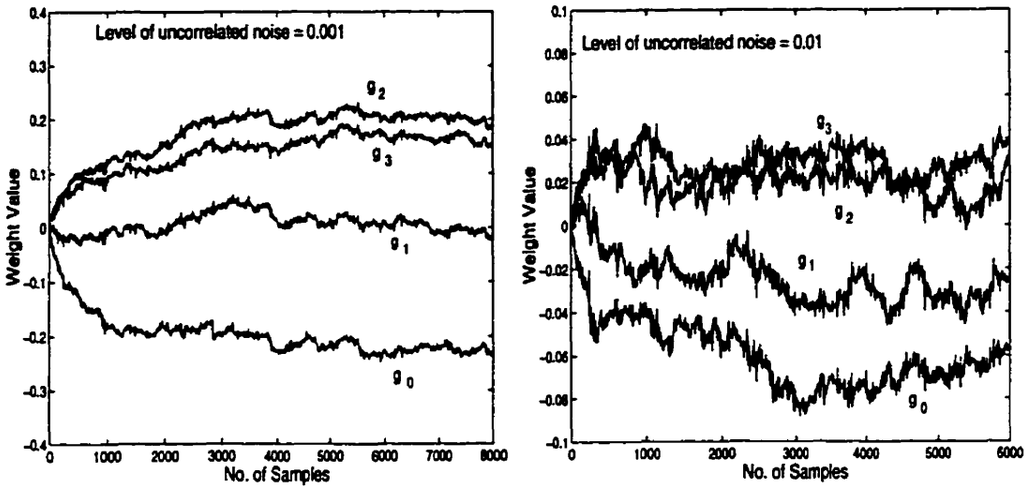

Figure 4.14: *Convergence characteristics of the constrained CRANC algorithm in the presence of uncorrelated noise sources where g_0, g_1, g_2 and g_3 are the filter weights.*

If we take expectations on both sides and assuming, for the time being, that there are no uncorrelated noise components, we have

$$E'(\widehat{\varphi}(k+1)) = E'(\widehat{\varphi}(k)) + \mu E'(e(k)\{x(k-\widehat{\varphi}-1) - x(k-\widehat{\varphi}+1)\}). \tag{4.27}$$

Noting that $e(k) = y(k) - \widehat{y}(k)$, $y(k) = x(k) + x(k-\varphi)$ and $\widehat{y}(k) = x(k) + x(k-\widehat{\varphi})$ (refer to Figure II.3 in Appendix II), the above equation simplifies to,

$$E'(\widehat{\varphi}(k+1)) = E'(\widehat{\varphi}(k)) + \mu E'\{x(k-\varphi)x(k-\widehat{\varphi}-1) -$$
$$x(k-\widehat{\varphi})x(k-\widehat{\varphi}-1) - x(k-\varphi)x(k-\widehat{\varphi}+1) + x(k-\widehat{\varphi})x(k-\widehat{\varphi}+1)\} \tag{4.28}$$

which simplifies to

$$E'(\widehat{\varphi}(k+1)) = E'(\widehat{\varphi}(k)) + \mu\{R_{XX}(\varphi-\widehat{\varphi}-1) - R_{XX}(\varphi-\widehat{\varphi}+1)\} \tag{4.29}$$

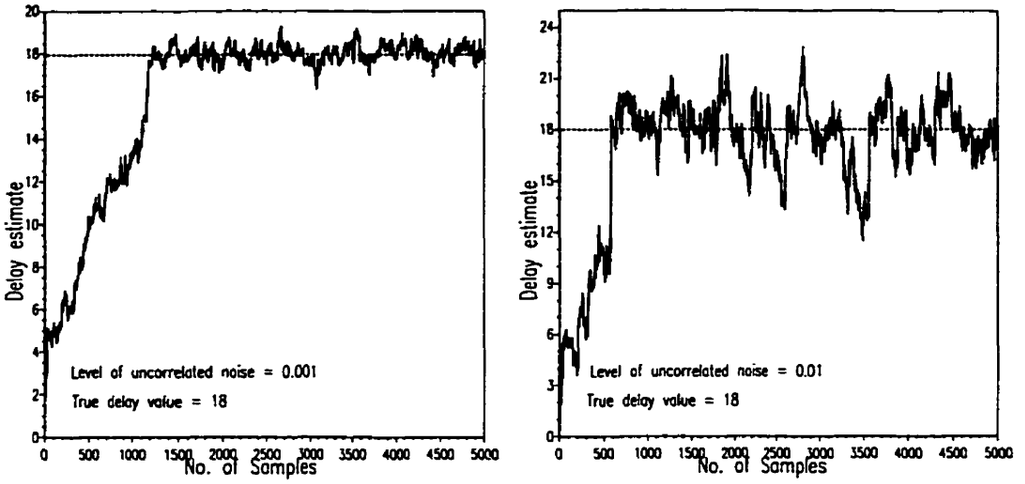

Figure 4.15: ***Convergence characteristics of delay estimate algorithm for the modified DDAP.***

where R_{XX} is the time-averaged autocorrelation function of x(k). It is now shown that the addition of uncorrelated noise sources do not affect the mean trajectory of the convergence of the delay estimate. Let $u_1(k)$ and $u_2(k)$ be the uncorrelated noise components in the primary and reference of the adaptive filter respectively and let $y_u(k) = y(k) + u_1(k)$ and $x_u(k) = x(k) + u_2(k)$. The update equation for the delay estimate is now given by

$$\hat{\varphi}(k+1) = \hat{\varphi}(k) + \mu e(k)\{x_u(k - \hat{\varphi} - 1) - x_u(k - \hat{\varphi} + 1)\}. \tag{4.30}$$

where $e(k) = y_u(k) - \hat{y}_u(k)$, $y_u(k) = x(k) + x(k - \varphi) + u_1(k)$ and $\hat{y}_u(k) = x(x(k) + x(k - \hat{\varphi}) + u_2(k - \hat{\varphi})$. Once again taking expectations on both sides and simplifying,

$$E'(\hat{\varphi}(k+1)) = E'(\hat{\varphi}(k)) + \mu E'\{[x(k - \varphi) + u_1(k) - x(k - \hat{\varphi}) - u_2(k - \hat{\varphi})]\}$$
$$\{[x(k - \hat{\varphi} - 1) - x(k - \hat{\varphi} + 1) + u_2(k - \hat{\varphi} - 1) - u_2(k - \hat{\varphi} + 1)]\} \tag{4.31}$$

Since $u_1(k)$ and $u_2(k)$ are uncorrelated white noise sources, the above expression simplifies to,

$$E'(\hat{\varphi}(k+1)) = E'(\hat{\varphi}(k)) + \mu\{R_{XX}(\varphi - \hat{\varphi} - 1) - R_{XX}(\varphi - \hat{\varphi} + 1)\} \tag{4.32}$$

Thus the delay estimate converges in the mean to its true value even in the presence of uncorrelated noise sources. The variance of the delay estimate, however, is dependent on the power of the uncorrelated noise sources. This can be seen from Figures 4.15 a and b where higher values of τ result in delay estimates of larger variance.

The presence of uncorrelated noise sources poses another problem for the modified DDAP: signal recovery. As mentioned before, an inverse filter needs to be constructed to successfully recover the SEP signal. This inverse filter, given by Eq. 4.15, has poles on the unit circle and is therefore only marginally stable. Thus in the presence of extraneous noise sources, the estimate at the output of the inverse filter is severely affected. Figure 4.16 illustrates this phenomenon. In Figure 4.16 a and b the output signals at node #2 are depicted for two different values of τ. Compared to Figure 4.7b, we see that the SEP component is significantly masked by the uncorrelated noise sources. The SEP estimate obtained using the inverse filter in each of these cases is shown in Figures 4.16 c and d along with the true SEP. As noted earlier, the uncorrelated noise power is magnified and the SEP estimate is submerged under the amplified uncorrelated noise. The only way to combat this problem is to enhance the SEP-to-Uncorrelated Noise Ratio (SUNR) at the input of the inverse filter. In Figures 4.16 e and f, the SEP estimates obtained by the inverse filter when its inputs are averaged over one hundred SEP records, is shown. Now it can be seen that the estimates are closer to the true SEP signal.

4.3.3 Effects of Non-planar Propagation

Until now, it has been assumed that both the SEP and MEI are ideal plane waves. In such a case, the modified DDAP will recover the SEP perfectly without any *a priori* knowledge of its propagation characteristics. Even in the presence of uncorrelated noise, we can recover the SEP if both MEI and SEP possess ideal propagation characteristics. However, in practice, MEI and SEP are known to exhibit non-planar

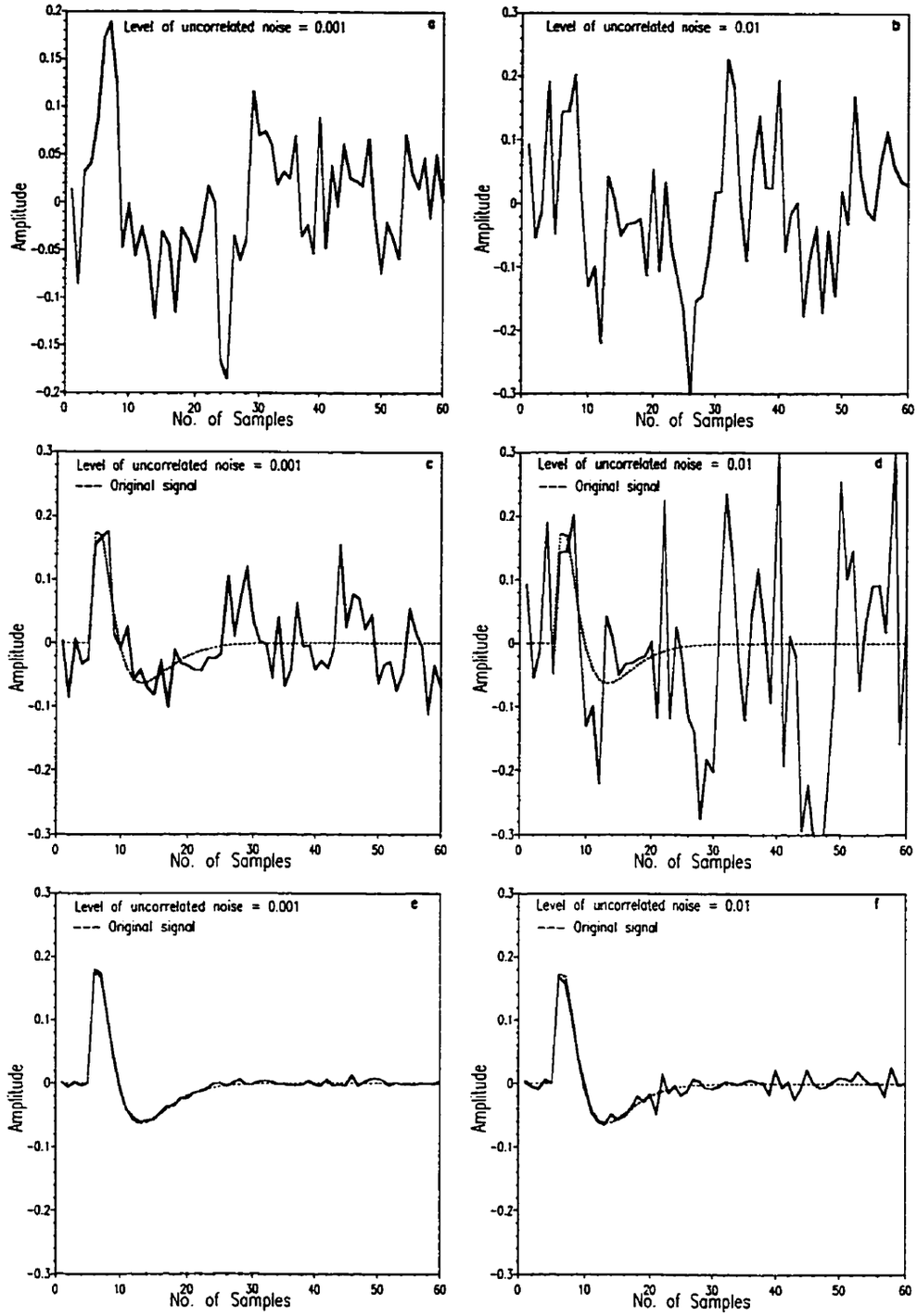

Figure 4.16: ***Effect of uncorrelated noise on inverse filtering. a & b) Outputs at node #2 for*** $\tau = 0.001\&0.01$ ***respectively, c & d) corresponding inverse filter estimates, and e & f) inverse filter estimates with averaged node #2 outputs.***

propagation characteristics. The effect of these deviations from the ideal will have a pronounced effect on the performance of the DDAP as discussed below:

- **Ideal MEI propagation and non-ideal SEP propagation.** In this case, the first stage of the modified DDAP will eliminate the MEI. However, since the SEP signals at nodes #1 and #2 now differ by more than just a time delay parameter, delay estimation and inverse filtering will not be enough to recover the SEP signal. A FIR filter has to be employed to estimate the transfer function between the SEP components at nodes #1 and #2.

- **Ideal SEP propagation and non-ideal MEI propagation.** In this case, simple cross-correlation based estimation of Δ parameter will not suffice. Due to the non-planar propagation, the simple delay and difference operation will leave a substantial amount of MEI residue at both nodes #1 and #2 which will invariably affect the delay estimation routine in the second stage. Thus a FIR filter has to be placed in the first stage to compensate for the non-ideal propagation. The second stage will still be a delay estimation stage as the SEP components at nodes #1 and #2 differ only by a time delay parameter. However, the algorithm derived in Appendix II needs to be modified to account for the effect of the non-planar MEI propagation.

- **Non-ideal SEP and MEI propagation.** The delay and difference array processor will be least effective in such a case and an adaptive filter structure such as the basic CRANC should be used to compensate for the non-planar propagation of both the SEP and MEI.

4.4 Multichannel CRANC - A Remedy

From the analysis so far, the main deterrent to the application of the CRANC filter for SEP enhancement is the presence of uncorrelated noise sources. The presence of

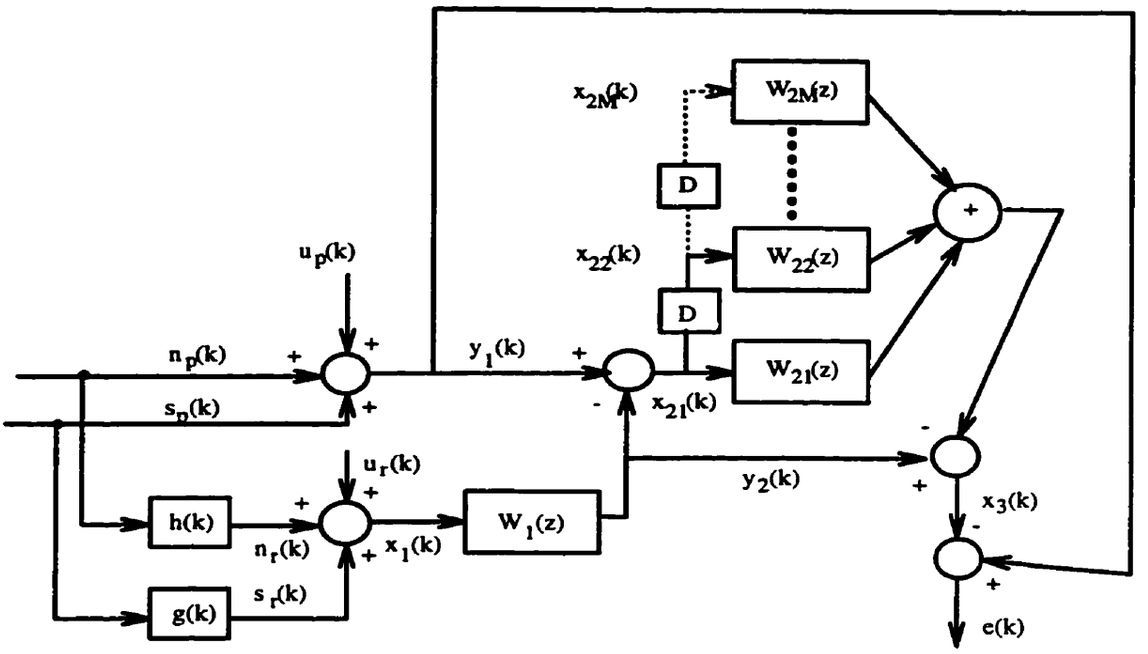

Figure 4.17: *Block diagram of the MCRANC.*

these sources results in the following undesirable effects:

1. **Increased MEI residue.** In the presence of uncorrelated noise sources, AF #1 in the CRANC structure fails to implement the inverse of the MEI transfer function and hence results in substantial MEI residue. The amount of MEI residue depends upon the relative power of the uncorrelated noise sources. With SEP measurements, the MEI is usually several times stronger than the uncorrelated noise sources and hence the effect of uncorrelated noise on the performance of AF #1 may be tolerable.

2. **Decreased resistance to SEP crosstalk.** The second stage in the CRANC structure compensates for the distortion induced by SEP crosstalk. In the presence of uncorrelated noise sources, however, the ability of AF #2 to do so weakens and signal distortion results.

Of the two points mentioned above, the second one is the most important one as the

uncorrelated noise sources are at best as powerful as the SEP. The effect of uncorrelated noise on the performance of AF #2 can be alleviated by ensemble averaging at the primary and reference inputs of AF #2. The ensemble averaging process reduces the power of the uncorrelated noise sources in the reference input of AF #2 and hence AF #2 performs better. However, if the SEP exhibits time varying latency and waveform characteristics, then ensemble averaging introduces a "smearing" effect into the SEP. This results in further degradation of the underlying SEP signal which will not be rectified by the second ANC. Thus an adaptive structure which can track the possible stimulus-to-stimulus variations of the SEP while still mitigating the effect of uncorrelated noise is beneficial in these situations.

As discussed in Chapter 3, the effect of uncorrelated noise on an ANC can be alleviated by developing a multichannel ANC. It is shown in Chapter 3 that a multichannel ANC gives a performance improvement over a single ANC in a manner directly proportional to the number of reference channels. Thus a CRANC structure involving a multichannel ANC may provide improved uncorrelated noise tolerance. It is worthwhile to note here again that AF #2 in the CRANC filter (Fig. 4.1) attempts to cancel the SEP signal in its primary. The presence of uncorrelated noise prevents it from doing so and signal distortion results. The employment of a multichannel ANC in the second stage of the CRANC would result in better signal cancellation and therefore less signal distortion. There is an improved signal cancellation as the number of channels increases and therefore the signal distortion steadily decreases as the number of channels increases eventually reaching zero as the number of channels goes to infinity.

As detailed in Chapter 1, in SEP studies the nerve is stimulated periodically to generate an SEP train. Thus it is possible to develop a Multichannel CRANC (MCRANC) by deriving multiple reference channels from the reference channel of AF #2 in the CRANC filter structure. The block diagram of the MCRANC filter is shown in Figure 4.17, where $W_{21}(z), W_{22}(z), \ldots, W_{2M}(z)$ represent the M adaptive

filters in the second stage of the CRANC and D is the stimulus period. For example, if the stimulus rate is 5 Hz, the D parameter is equivalent to 200 ms. A complete analytical treatment of the MCRANC structure is undertaken in Appendix III. The output SEP, MEI and uncorrelated noise spectral densities are derived as,

$$\phi_{S_oS_o}(z) = \phi_{S_pS_p}(z)\,|(1 - G(z)W_1(z))(1 + MW_{21}(z))|^2 \tag{4.33}$$

$$\phi_{N_oN_o}(z) = \phi_{N_pN_p}(z)\left|(1 - H(z)W_1(z))(1 + (1 + z^{-D} + \ldots + z^{-(M-1)D})\right|^2 |(1 + W_{21}(z))|^2 \tag{4.34}$$

$$\phi_{U_oU_o} = \phi_{U_pU_p}(z)\left|1 + (1 + z^{-D} + \ldots + z^{-(M-1)D})W_{21}(z)\right|^2 + \phi_{U_rU_r}(z)\left|W_1(z) + (1 + z^{-D} + \ldots + z^{-(M-1)D})W_1(z)W_{21}(z)\right|^2 \tag{4.35}$$

With this spectral information, it is straightforward to calculate the theoretical distortion index and SNRGAIN. Figures 4.18 and 4.19 show the theoretical performance indices of the MCRANC. The SNRGAIN can be seen to increase with the number of reference channels in the MCRANC until it reaches a saturation value regardless of the crosstalk level. This saturation value is decided by the power spectral densities of the primary and reference uncorrelated noise sources and the myoelectric residual power spectral density at the output of ANC #1. An exact expression for the maximum SNRGAIN achieved by the MCRANC is derived in Appendix III. The distortion index, on the other hand, monotonically decreases to zero with the increase in the number of reference channels irrespective of the signal crosstalk level. Thus the MCRANC offers improved immunity to the perils caused by SEP crosstalk.

It has to be noted here that if the SEP is stationary then an M-channel MCRANC filter is equivalent to ensemble averaging M records at the reference input of AF #2 and then using a single adaptive filter. This can be seen from the fact that the optimal transfer functions for the M adaptive filters in the second stage of the MCRANC are identical (refer to Appendix III for the exact expressions for optimal transfer functions). The real application of the MCRANC filter is in situations where the SEP possesses time-varying characteristics such as latency and waveform changes. In

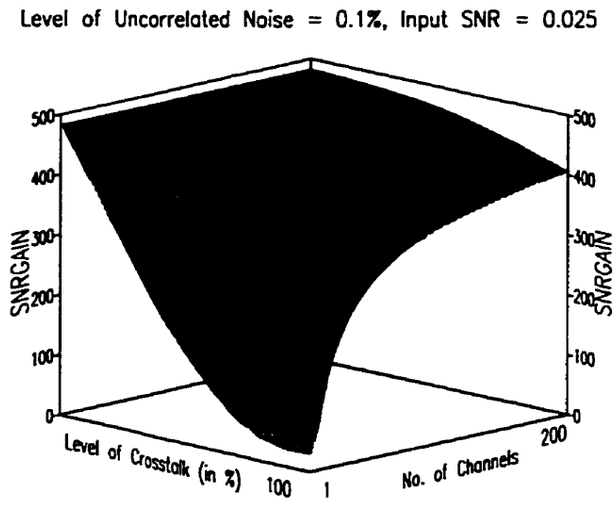

Figure 4.18: ***Theoretical MCRANC SNRGAIN***, $\tau = 0.001$, ***SNR = 0.025.***

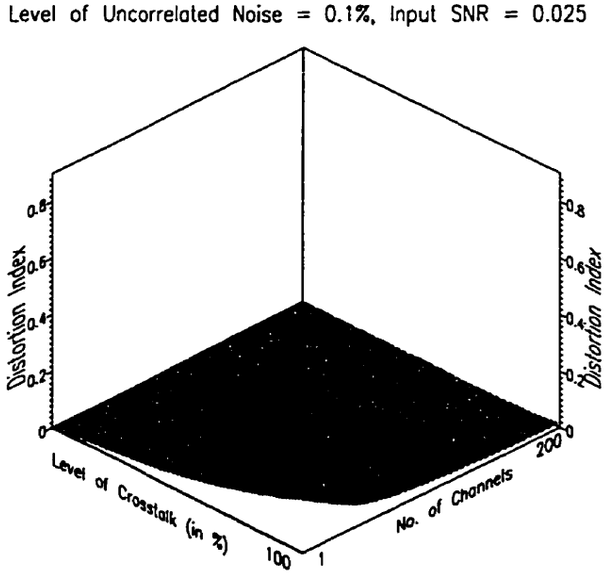

Figure 4.19: ***Theoretical MCRANC Distortion Index***, $\tau = 0.001$, ***SNR = 0.025.***

such situations, the MCRANC has an advantage over the ensemble averaged CRANC (E-CRANC) as the M adaptive filters allow the tracking of stimulus-to-stimulus variations while enhancing the SEP from uncorrelated noise.

The effectiveness of this MCRANC structure in comparison to an E-CRANC for different SEP latency characteristics was evaluated through simulations. Three different SEP latency characteristics were simulated: 1) the normal SEP latency where the SEP repeats unchanged, 2) sudden change in latency, where a sudden time delay is introduced after 50 SEP records and 3) slowly varying latency, where the latency is changed every 40 SEP records. The MEI and the uncorrelated noise sources were generated as described earlier. Each of the M adaptive filters in the second stage of the MCRANC were realized using thirty-tap transversal filters. The RLS algorithm was used to achieve the minimum mean square solution. Once again, all the adaptive filter weights were averaged over 50 independent simulation runs. These averaged weights were then used to filter the input SEP, MEI and uncorrelated noise and the distortion index and the SNRGAIN were calculated. This procedure was carried out for different values of M from 1 to 5. For the E-CRANC the same procedure was followed except that the reference input of the second ANC was ensemble averaged over M SEP records (M ranging from 1 to 5) before the adaptation of the second ANC.

The performances achieved by the MCRANC and the E-CRANC for a particular level of uncorrelated noise and crosstalk are shown in Figures 4.20 and 4.21. In Figure 4.20 the distortion index, ρ can be seen to decrease with an increase in the number of channels irrespective of the nature of the SEP latency. On the other hand, the E-CRANC exhibits similar performance as the MCRANC only if the SEP is stationary. In the case of latency changes, ensemble averaging introduces an additional SEP degradation resulting in higher distortion indices. These results are complemented by the results shown in Figure 4.21 where the SNRGAIN, γ, can be seen to increase with the number of reference channels for the MCRANC. The SNRGAIN can also be

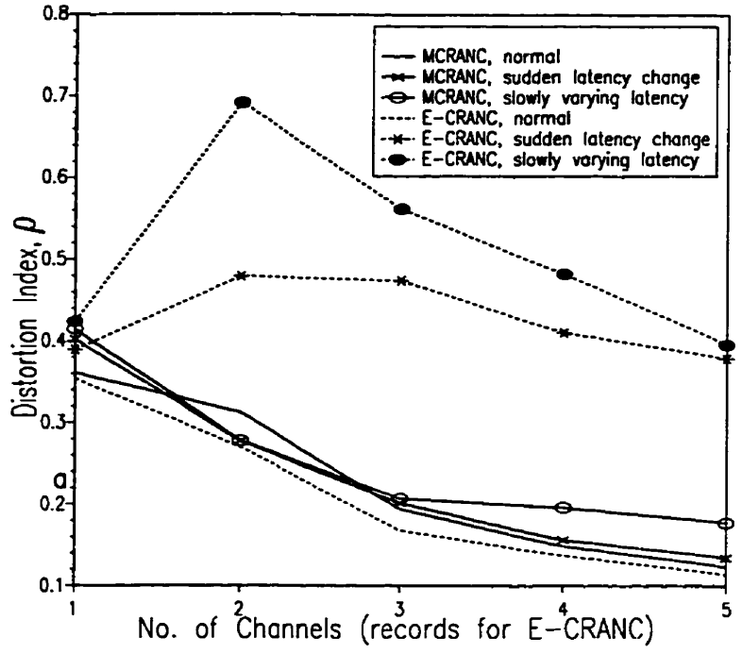

Figure 4.20: ***Distortion index for MCRANC and E-CRANC.***

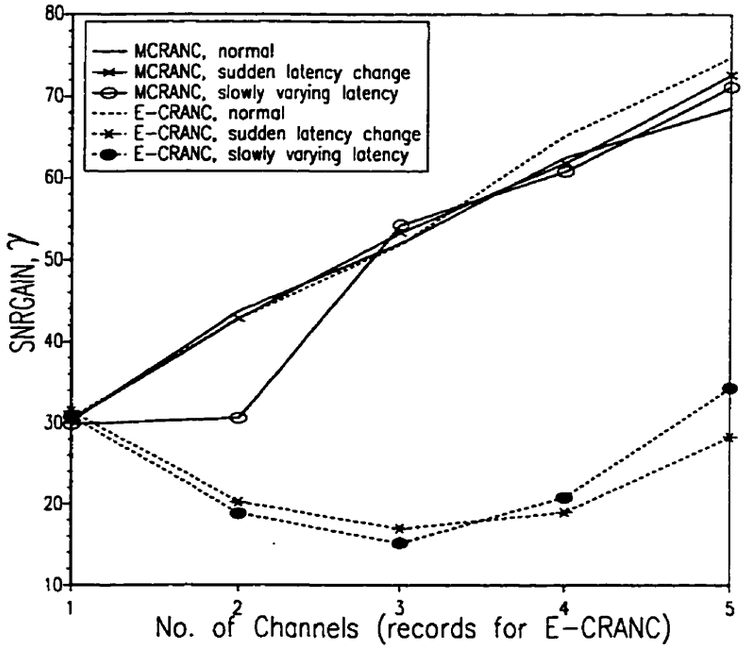

Figure 4.21: ***SNRGAIN for MCRANC and E-CRANC.***

seen to drop for the E-CRANC filter in the case of time-varying latency. To compare the performances of the ANC, CRANC, E-CRANC and MCRANC qualitatively, the SEP estimates at the output of each of these filters are presented in Figures 4.22a-c. In all these figures, the underlying original SEP signal is shown in solid lines. In Figure 4.22a, the input to each of these filters which is a composite of the SEP, MEI and uncorrelated noise and which is averaged over 50 SEP records is shown. It is apparent that the original SEP, which is shown by the solid line, is swamped by the larger myoelectric interference. Figure 4.22a also depicts the output of the ANC and CRANC which again are averaged over 50 SEP records. Here we see that the larger low frequency MEI has been reduced in both the cases. However, due to the presence of crosstalk and uncorrelated noise, the signals are severely distorted and the SEP estimates do not resemble the original signal. Figure 4.22b compares the SEP estimates obtained by the MCRANC and E-CRANC with M=5 for the same simulation data. From this figure, we can observe that the MCRANC and E-CRANC output similar SEP estimates which are comparatively better than the estimates provided by the ANC and the CRANC. Figure 4.22c compares the SEP estimates obtained by the MCRANC and E-CRANC for the nonstationary SEP case. The quality of the SEP estimate obtained by the MCRANC can be seen to be better compared to the SEP estimate from the E-CRANC.

While the MCRANC presents an impressive solution to mitigate the effects of uncorrelated noise on crosstalk resistant MEI reduction, it may not be practical in experimental conditions where the SEP SNR is very low. In such conditions, a large number of reference channels is required in the second stage of MCRANC to output a distortion free SEP, which increases the computational burden on the system. This factor, coupled with the requirement of large amounts of data by the MCRANC to achieve convergence in low SNR situations, defeats the purpose of having an SEP signal processing system - to reduce the SEP recording time. Figure 4.23 displays the theoretical curve between the input SNR and the number of channels required

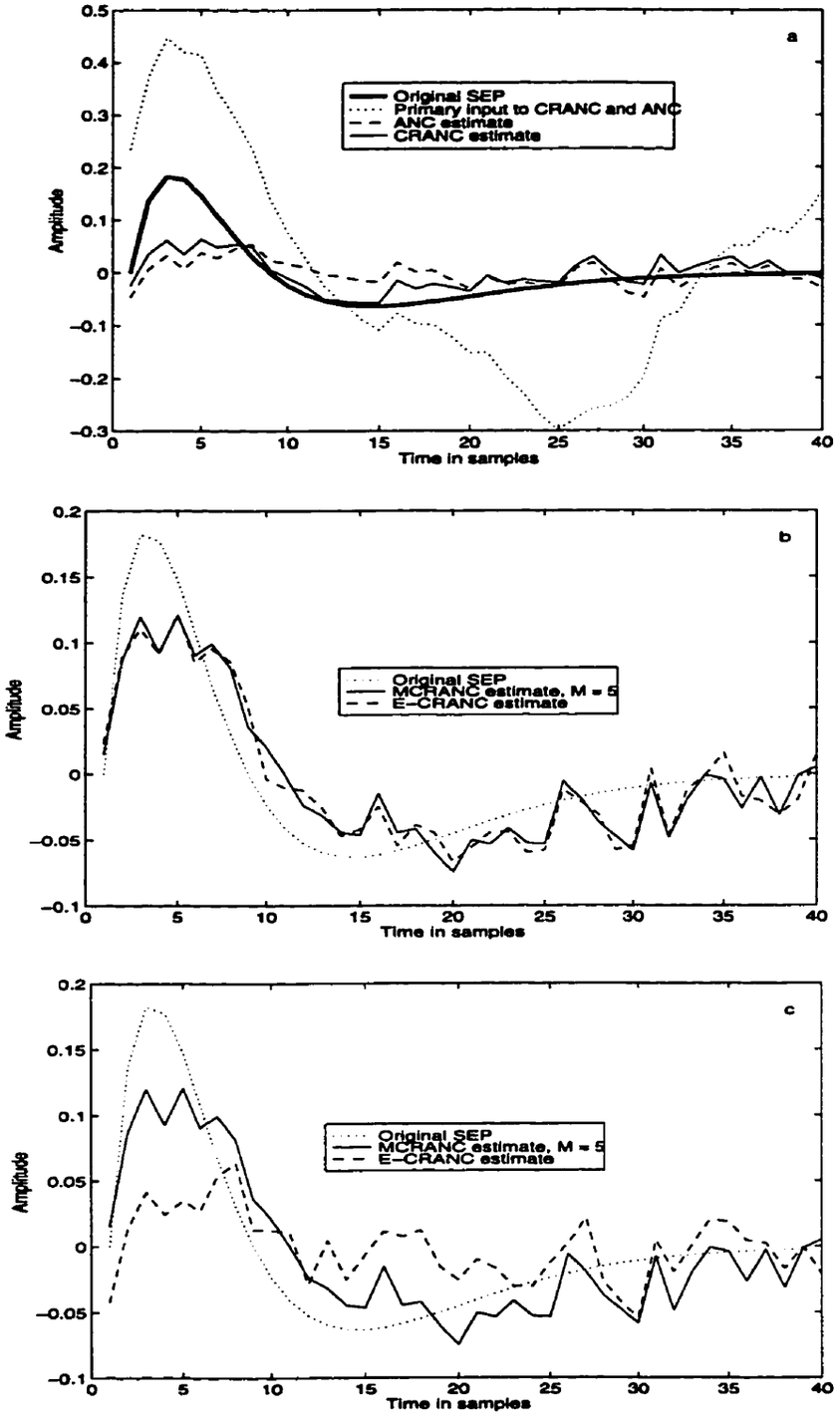

Figure 4.22: *Qualitative comparison of ANC, CRANC, MCRANC and E-CRANC.*

by the MCRANC to provide a distortion index of 0.25. From this curve, it can be observed that for input SNR values less than 0.01 more than ten reference channels are required to achieve a distortion index of 0.25.

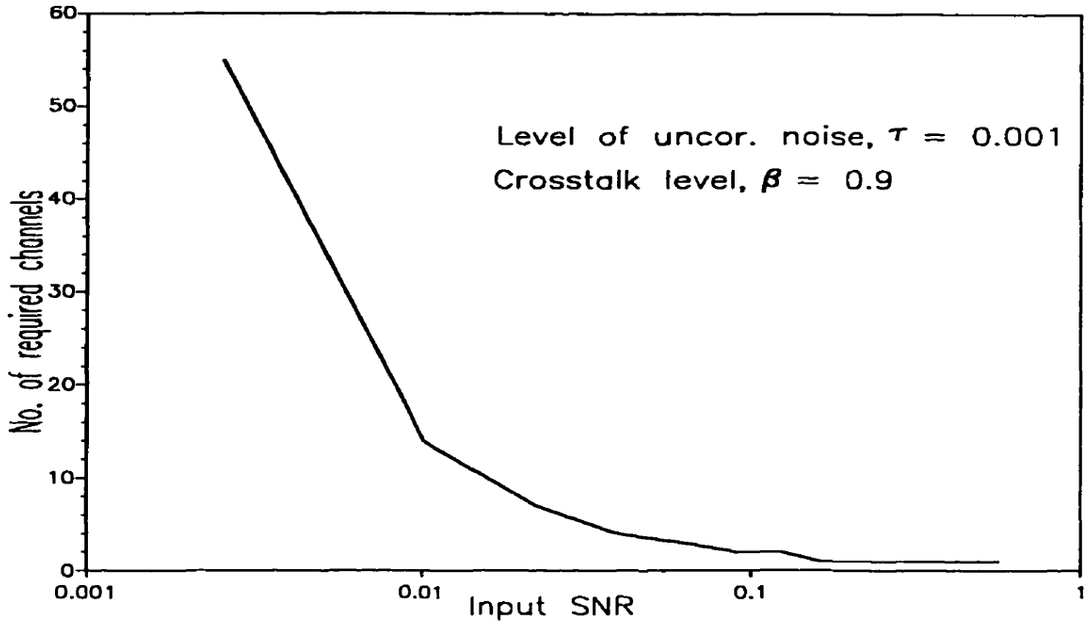

Figure 4.23: ***Required number of channels in the second stage of the MCRANC structure as a function of input SNR to achieve a distortion index of 0.25.***

Therefore, from a computational point of view, it is better to employ an E-CRANC in place of MCRANC in practical situations where the SEP SNR is very low (for example, SSEP experiments where the SNR is usually around 0.01). An interesting ECRANC model can be derived from the CRANC structure which provides a practical solution to SEP retrieval at low SNRs. Figure 4.24 depicts the block diagram of the modified ECRANC filter structure where the blocks denoted "AVG" perform ensemble averaging. The auto-spectral density of the reference input to the second ANC is now,

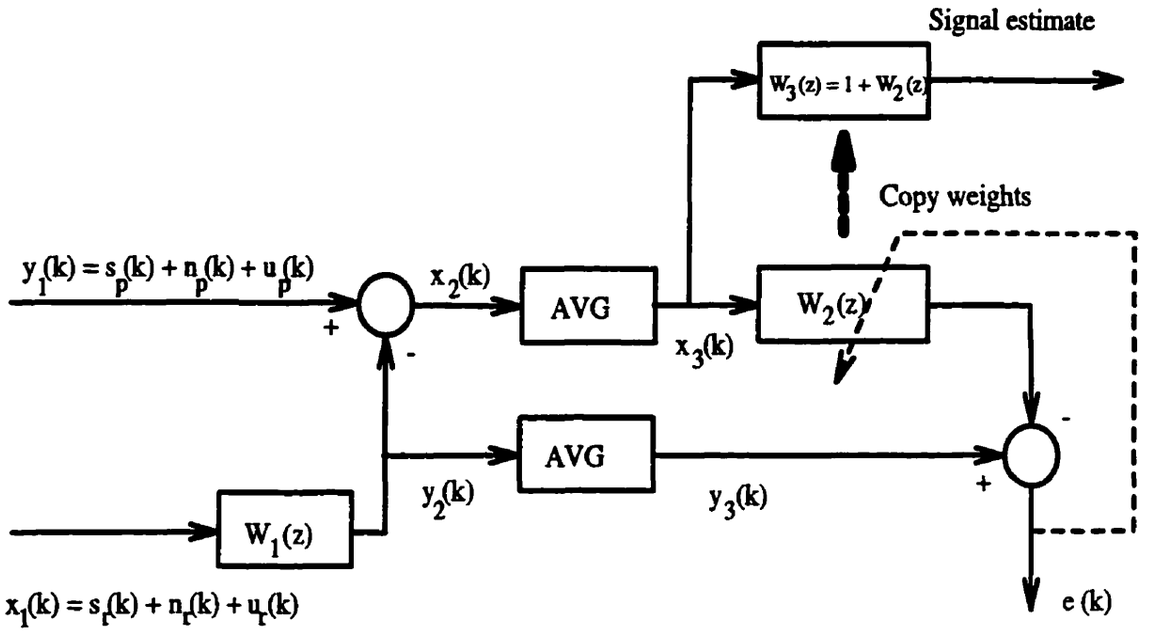

Figure 4.24: ***Block diagram of the modified ECRANC.***

$$\phi_{X_3X_3}(z) = \phi_{S_pS_p}(z)\,|1 - G(z)W_1(z)|^2 + \frac{1}{M}\phi_{N_pN_p}(z)\,|1 - H(z)W_1(z)|^2 + \frac{1}{M}\phi_{U_pU_p}(z) + \frac{1}{M}\phi_{U_rU_r}(z)\,|W_1(z)|^2 . \quad (4.36)$$

where M is the number of averaged SEP records. The cross-spectral density between the primary and reference inputs of the second ANC is the same as given by Eq. 4.21. As M increases, the influence of MEI and uncorrelated noise sources on $W_2(z)$ decreases. In the limit of M approaching infinity, the optimal transfer function for the second AF becomes,

$$\lim_{M\to\infty} W_2(z) = \frac{G(z)W_1(z)}{1 - G(z)W_1(z)}. \quad (4.37)$$

Now the SEP signal at the output of the averager is given by

$$S_3(z) = S_p(z)\{1 - G(z)W_1(z)\}. \quad (4.38)$$

If we construct a new filter based on $W_2(z)$ as

$$W_3(z) = 1 + W_2(z) \tag{4.39}$$

then

$$\lim_{M\to\infty} W_3(z) = 1 + \frac{G(z)W_1(z)}{1 - G(z)W_1(z)} = \frac{1}{1 - G(z)W_1(z)}. \tag{4.40}$$

Thus by using $W_3(z)$ to filter the SEP signal at the output of the averager, we can obtain an estimate of the SEP waveform. The salient points regarding the operation of this structure are itemized below:

- The ECRANC structure is computationally simpler than the MCRANC structure. It is much faster to compute an ensemble average of M records than to implement an M channel CRANC structure.

- The success of the ECRANC structure obviously depends on the number of SEP records averaged before the second stage. However, since the first ANC removes most of the larger MEI, it is expected that a relatively low number of averages is required to obtain a signal estimate of good quality.

- The main drawback associated with this structure, as mentioned previously, is the SEP "smearing" effect if the SEP exhibits time-varying characteristics. Since this ECRANC structure is aimed mainly at low SEP SNR situations, — where averaging is a must to retrieve the SEP — this "smearing" effect is traded-off for shorter acquisition times.

The following simulation demonstrates the effectiveness of the ECRANC structure in low SNR situations. The SEP, MEI and uncorrelated noise sources were simulated as described previously. Once again, the first stage of the ECRANC structure was

allowed to converge during the MEI phase of the input data and the steady-state weights were used to filter the data containing the SEP. Ensemble averaging was then performed on the outputs of the first stage, and these averaged SEP data were used to drive the second AF in the ECRANC structure. Once convergence of the second AF was established, the weights were copied into a third filter ($W_3(z)$ in Figure 4.24) and the averaged SEP data were passed through. From the resulting SEP estimate, the distortion index and SNRGAIN values were calculated.

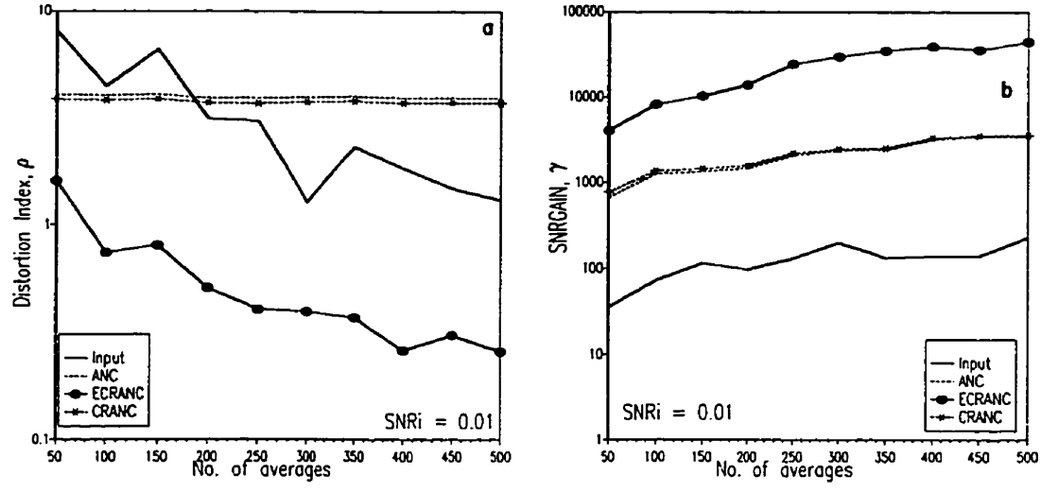

Figure 4.25: ***Distortion index, ρ and SNRGAIN, γ as a function of the number of averages.***

Figure 4.25 depicts the results obtained from this simulation study. Figure 4.25a portrays the distortion index as a function of the number of SEP records averaged for four different data: a) the raw input with no processing, b) the output of the first stage of the ECRANC, c) the output of the CRANC structure shown in Fig. 4.8 and d) the ECRANC structure shown in Fig. 4.24. The superior performance of the ECRANC structure is obvious in this plot. These results are complemented by the SNRGAIN function for the same data. Once again, the performance improvement of the ECRANC over other techniques is lucid in this graph.

4.5 Experimental Results

The discussion up until this point has been based on theoretical models and simulation results. While every attempt has been made to generate simulated data which are close to the real world data, simulated data are still ***simulated.*** To quote Bérubé [6] : "Theoretical models and simulation results may offer interesting insights, but the true test for any signal processing method is the real world signals". Thus this section is devoted to results obtained through processing ***in vivo*** SEP and MEI data by the aforementioned signal processing methods. A detailed explanation of the experimental setup for MSEP and SSEP data acquisition along with a discussion of the relevant issues is given in the following sections. The same experimental setup was also used for the data acquired in Chapters 5 and 6.

4.5.1 MSEP Acquisition Setup

The experimental setup for acquiring MSEPs is displayed in Figure 4.26. As briefly discussed in Chapter 1, the instrumentation system can be briefly divided into a) the stimulator system, b) the recording and amplification system and c) the data acquisition system.

A Grass Instruments S11 dual-channel stimulator was utilized to provide the stimulus pulse. The stimulus pulse width was set to 0.2 ***msec*** and the stimulus period was set to 391.7[2] ***msec*** for all the ***in vivo*** experiments involving the SEP data. The output of the stimulator was input to a Grass SIU 8TB isolation unit which has an additional provision for varying the stimulus amplitude. The output of the isolation unit was input to the stimulating electrodes. For all the experiments involving MSEP data, the median nerve was stimulated at the index finger with the cathode electrode

[2]This stimulus period was set to this value to minimize the possibility of any powerline harmonics being in synchrony with the stimulus [39].

proximal to the base of the index finger and the anode approximately 2 *cm* away towards the tip. For most of the experiments the stimulating electrodes were standard Ag-AgCl electrodes, which were wrapped around the index finger and firmly taped. Prior to the placement of these electrodes, the surface of the index finger was prepared by first rubbing with an alcohol swab, applying electrode paste (EKGSol by Medi-Trace) and removing the excess paste with a tissue saturated with alcohol.

The MSEP signal was acquired using a pair of stainless steel electrode arrays, shown in Figure 4.23 (The same electrode array was used in [38] and [6].). The active electrode array was placed on the ventral side of the forearm with the array elements perpendicular to the direction of the MSEP propagation. The indifferent electrode array was placed on the dorsal side of the forearm and differential signals between these two arrays were given to the amplification system. Once again, extensive skin preparation was undertaken prior to the placement of each of these arrays by first rubbing with an alcohol swab, applying electrode paste and removing the excess paste with a tissue. In addition, a thick electrode paste, ASI A-E-12 Ten 20 electrode paste, was applied to each of the individual sensors to ensure good conduction with extra care taken to ensure that adjacent sensors were not shorted. The arrays were securely held to the forearm by a pair of elastic rubber bands and some tape.

Four channels of MSEP data were collected from the array electrodes. Each one of these channels was first input to a pre-amplification stage. These pre-amplifiers provide a variable gain factor in the range of 100 to 1000 and are custom built in the Institute of Biomedical Engineering (IBME) for low noise SEP and MEI data acquisition. The second amplification stage consisted of commercial differential amplifiers (Tektronix model AM 592) which also provided adjustable gain, in the range of 100 to 100000 with the option of a divide by 100 setting. These amplifiers also possess adjustable band pass filters to limit the bandwidth of the input signals. A 4 channel Gould digital oscilloscope (model 1604) was utilized to visually monitor the array signals. While measuring MSEP data, the signals from the first two differential pairs

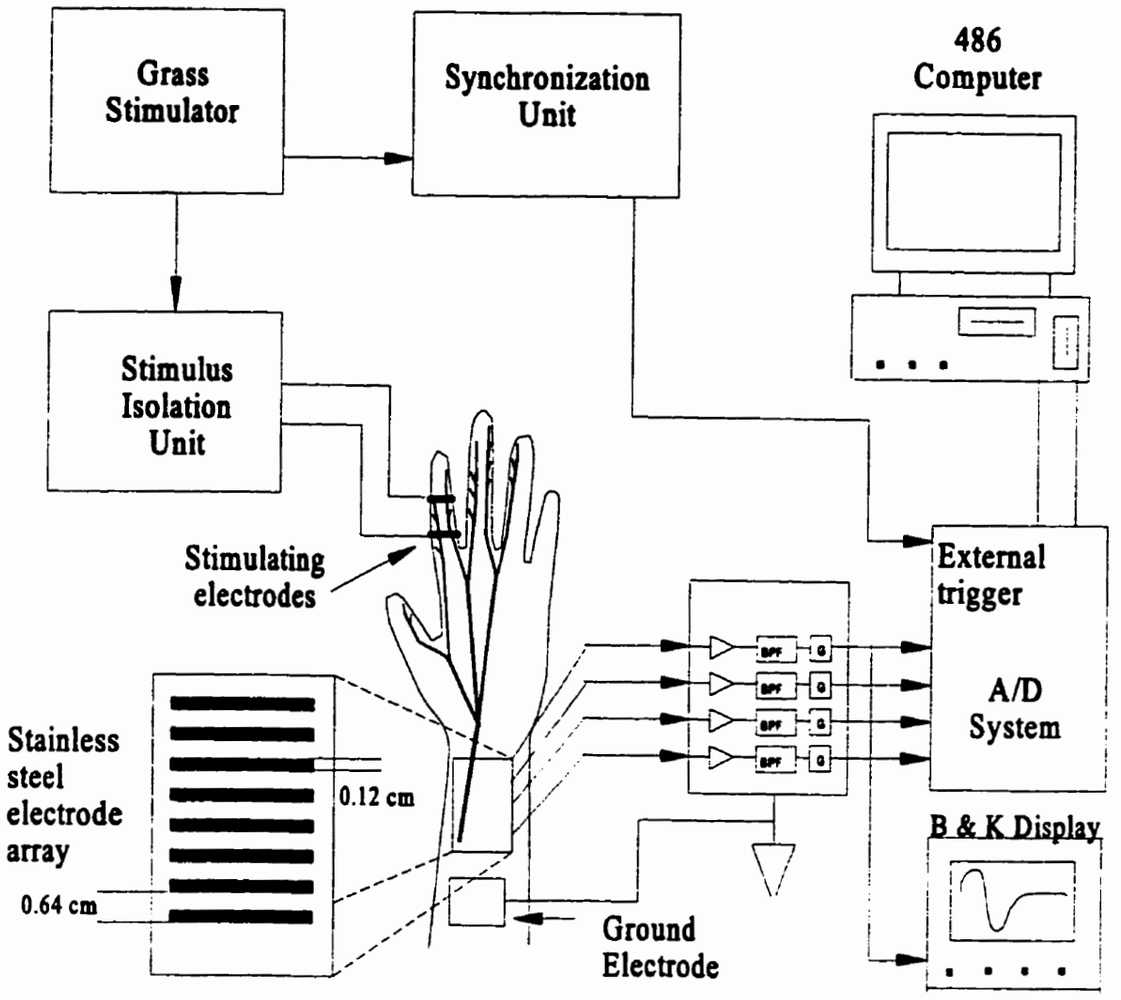

Figure 4.26: *Experimental setup for MSEP data acquisition. The neuromuscular data was acquired using the stainless steel electrode array shown in this figure. See text for a detailed description on the stimulation, amplification and digitization systems.*

in the electrode array configuration were input to a dual channel Brüel and Kjær (B&K 4 channel module type 3023) real time signal analyzer. The B&K performed real-time ensemble averaging of the input data thereby providing visual information on such factors as the nature of the MSEP, the extent of the stimulus artifact and auto/crosscorrelation functions for propagation time measurements.

The amplified signals were then fed to a CIO-DAS16/330i data acquisition board residing in a 486 PC clone and driven by custom made, graphical, user friendly data acquisition software. The data acquisition software acquired the signals at a prescribed sampling rate, digitized them and stored them on a hard-disk for processing at a later time.

When a large number of SEP records need to be acquired, there is a considerable strain on the data storage requirements. This is due to the fact that the stimulus rate is approximately three per second and the MSEP usually occurs within a 20 *msec* window following the application of the stimulus. Thus a huge amount of unwanted data will be collected if the data acquisition process is allowed to run continuously. This is where the "synchronization unit" is very useful. The programmable synchronization unit provides an external clock input to the data acquisition system following a stimulus pulse. The duration and frequency of this clock is programmable. This clock input enables the A/D system to acquire only a window of data following a stimulus. Thus the SEP can be efficiently stored using this data "chopping" procedure.

4.5.2 SSEP Acquisition Setup

For acquiring the SSEPs, an experimental setup similar to the one shown in Figure 1.1, Chapter 1 was utilized with a change in the position of the stimulating electrodes. In order to minimize the effects of the stimulus artifact interference, the stimulating electrodes were placed at the ankle for stimulating the posterior tibial nerve. The stimulating electrodes were once again Ag-AgCl electrodes, with the negative electrode placed at the distal end of, and posterior to, the left medial malleolus, directly

over the posterior tibial nerve. The positive electrode was placed slightly lateral to the sustentaculum tali at the anterior margin of the lateral malleolus. Minor adjustments were made to these placements such that the stimulus was comfortable for the subject. Prior to the placement of stimulating electrodes, careful skin preparation was performed as in Section 4.5.1.

The recording electrode array was placed on the spine between the L2 and L4 vertebrae with the first array element placed approximately over the L4 vertebra. The reference array was placed on the right side of the subject's back, parallel to and at the same height as the primary array. The distance between the primary and reference arrays varied from subject to subject, as the reference array was placed as far as possible from the primary array. Differential inputs from the corresponding array elements were given to the pre-amplification stage. The rest of the experimental procedure was similar to the protocol described above for MSEP measurements.

4.5.3 MEI reduction

To investigate the relative performance of different MEI reduction techniques, myoelectric data were collected from different subjects prior to the stimulation procedure. Once the recording arrays were in place, the subjects were asked to relax and the resulting data were collected from the recording electrodes. These data primarily represent the uncorrelated noise sources and were later used to determine the uncorrelated noise power levels and subsequently, the τ parameter. The subjects were then asked to produce an isometric contraction of the muscles surrounding the recording area and the resulting myoelectric data were collected. MEI Data were collected at two different contraction levels resulting in MEI data sets with two different τ values per subject.

Each of these MEI data sets were then put through different signal processing techniques. First, the MEI propagation velocity for each of the data sets was computed using the cross-correlation technique. The cross-correlation function between the MEI data obtained from the first and fourth sensors was computed and the MEI propagation delay was calculated using the peak value of the cross-correlation function. From the propagation delay and the distance between the sensors in the array, the MEI conduction velocity was calculated. The MEI conduction velocities for different subjects and for different recording electrode placements are given in Tables 4.1 and 4.2 respectively. Once the propagation delay was calculated, the MEI residues at nodes #1 and #2 of the DDAP structure ($y(k)$ and $x(k)$ respectively in Fig. 4.6 with added uncorrelated noise sources) and the power performance parameter, I, were calculated. The theoretical values for the DDAP performance measures were calculated assuming ideal MEI propagation.

The MEI data from the first two sensors were then used to drive a thirty tap ANC filter driven by the RLS algorithm. Once convergence of the ANC was established, the residual MEI at the output of the ANC was retrieved and the power performance index, I was computed. The theoretical estimates of the performance index were computed from the actual spectra of the primary and reference inputs of the ANC. These results along with the performance indices predicted by the MEI model used in the simulation study (detailed in Chapter 3) for the same τ values and the associated MEI residue indices are tabulated in Tables 4.1 and 4.2 for the MEI data obtained from the wrist and lower back regions respectively.

The propagation velocities for the MEI data obtained from the wrist region are somewhat higher than normal muscle conduction velocity values. This is probably due to the position of the recording array at the wrist region which is more likely to be above the muscle tendon area. Infinite conduction velocities were observed for the MEI data collected from the lower back region. This apparent behavior is probably due to the MEI impinging on the array perpendicular to the array axis or the array

Table 4.1: *MEI reduction performance of various signal processing schemes considered in this thesis. The MEI data were collected from the wrist region.*

Subject		Apparent Prop. Velocity (cm/s)	Performance Index, I				
			DDAP (node #1)	DDAP (node #2)	DDAP (theory)	ANC (exp.)	ANC (theory)
# 1	τ= 0.0491	1200	1.78	6.59	10.68	9.21	9.20
	τ= 0.0034	1200	4.22	7.09	147.55	26.91	26.97
# 2	τ= 0.0382	1600	0.55	3.51	13.59	7.37	7.52
	τ= 0.0012	1600	0.67	4.22	417.17	9.31	9.37
# 3	τ= 0.0231	∞	3.95	19.96	22.15	38.83	38.76
	τ= 0.0062	2400	3.99	21.93	81.15	45.40	46.39

Subject		Apparent Prop. Velocity (cm/s)	Performance Index, I				
			DDAP (node #1)	DDAP (node #2)	DDAP (theory)	ANC (exp.)	ANC (theory)
# 1	τ= 0.0055	∞	4.20	18.92	91.41	21.38	21.45
	τ= 0.0019	∞	5.25	17.80	263.66	20.23	20.39
# 2	τ= 0.0060	-2133	1.70	2.88	83.13	3.76	3.77
	τ= 0.0012	-3200	2.00	4.70	417.17	5.74	5.77
# 3	τ= 0.0019	∞	4.78	17.30	263.66	20.22	20.23
	τ= 0.0044	∞	3.79	13.04	114.14	15.12	15.13

Table 4.2: *MEI reduction performance of various signal processing schemes considered in this thesis. The MEI data were collected from the lower lumbar region of the spinal cord.*

covering the motor points.

For the MEI data obtained from the wrist region, the performance achieved by the DDAP at node #2 is closer to its theoretical estimate at higher τ values. However, the performance index calculated at node #1 is substantially smaller than the theoretical values, strongly indicating non-ideal propagation of the MEI. For lower τ values, the performance indices at nodes #1 and #2 are both much lower than the theoretical values. At low τ values (*i.e* higher contraction levels), several muscle groups are activated and the propagation delay calculated using the peak cross-correlation function reflects only an ***average*** conduction velocity. Thus substantial MEI residue remains at the DDAP output even at node #1 when this average propagation delay is used. The same observation can be made with respect to the results obtained from the lower back. Due to this relatively poor performance of the DDAP structure with experimental MEI data, it was not considered in SEP enhancement results detailed in the following section[3].

The ANC outperforms the DDAP for all the MEI data sets. Close agreement between the theoretical performance indices and those computed from the experimental data can be observed. For the MEI data collected from the wrist with higher τ values, the performance indices correspond to those calculated using the MEI model in the simulations. At lower τ values and for data collected from the lower back, the model breaks down and the performance indices are significantly lower than expected. Once again, at lower τ values, the MEI is a manifestation of several active motor units, and the "crosstalk" between these limits the overall performance of the ANC.

In Chapter 3, it is shown through simulations that the performance of an ANC can be improved using a multichannel structure. Figure 4.27 depicts the performance of the MRANC for some of the data sets tabulated in Tables 4.1 and 4.2. Thirty tap FIR filters driven by the LMS algorithm were used to cancel the MEI. Once the MRANC

[3]It was found that the DDAP usually results in distortion indices greater than 2 when employed on SEP datasets.

has converged, the residual MEI component was retrieved and the power performance index was calculated. Figures 4.27a, 4.27c and 4.27e show that the performance of the MRANC increases as the number of reference channels increase. Figures 4.27b, 4.27d and 4.27f depict the spectral content of MEI residue as the number of reference channels increase. As observed in Chapter 3 with simulated data, an increase in the number of reference channels results in whitening of the residual myoelectric spectrum and brings it down to the level of the uncorrelated noise sources.

4.5.4 SEP Enhancement

In Chapter 3, it was shown that the performance of an ANC is drastically affected by the presence of crosstalk. At the beginning of this chapter, a crosstalk resistant ANC structure and its variations were studied. It was shown analytically and through simulations that the presence of uncorrelated noise sources renders the CRANC filter less resistant to crosstalk. Two structures, MCRANC and ECRANC, were then developed which were shown to be more robust in the presence of uncorrelated noise sources. This section evaluates all these techniques with experimental data collected from the median nerve and the spinal cord.

The experimental setups for acquiring the MSEPs and SSEPs were discussed earlier. The stimulus level was adjusted to a comfortable level for the subject and raw SEP data was acquired under three conditions - at rest, light muscle contraction and medium muscle contraction. To gain visual appreciation of the SEP, realtime ensemble averaging was performed on the B&K spectrum analyzer. Five hundred records were averaged for the MSEP experiments and a thousand records for the SSEP experiments which formed the "gold standard" for evaluating the performance of differnt SEP enhancement algorithms. At the same time, raw SEP data was digitized and stored on a 486 computer for post-processing.

It was mentioned before that for successful MEI reduction using the MCRANC filter, the MEI transfer function must be time-invariant. With experimental data

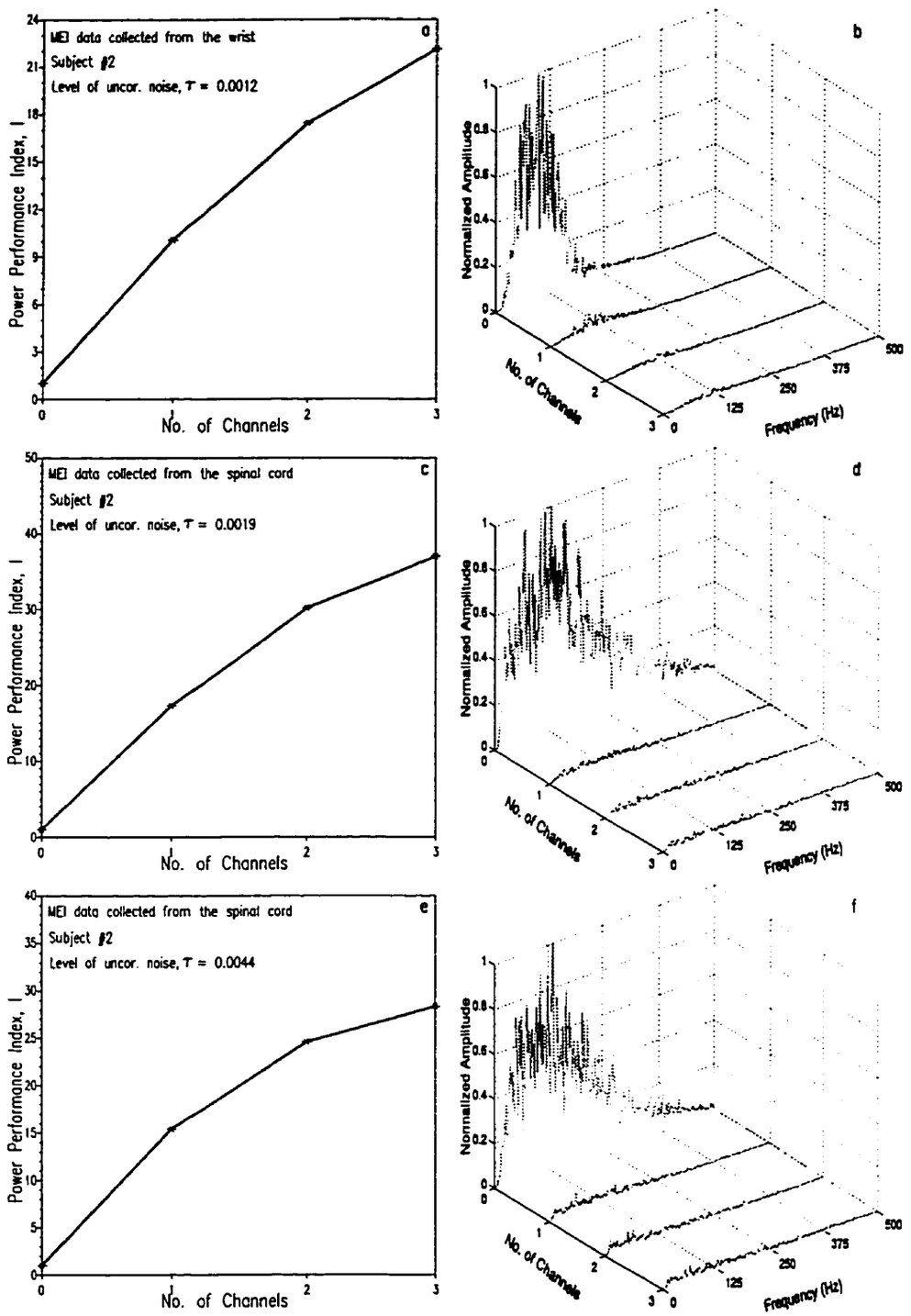

Figure 4.27: ***MEI reduction performance achieved by the MRANC. The second column shows the power spectral density of the MRANC output with an increasing number of reference channels. Note that the primary input is represented by "0" reference channels in these graphs.***

however, this condition may not be satisfied. Hence a small change was made to the experimental data collection protocol. The Grass stimulator unit was programmed in such a way that the stimulus was delivered a certain time after the data acquisition process was triggered. Thus a chunk of the MEI data was captured before the advent of each SEP. This MEI data was used to update the weights of the first ANC in the CRANC structure. At the onset of the SEP record, the adaptation of the first ANC is stopped and the SEP data is filtered using the updated AF #1 weights. The filtered SEP data is then used to drive the second stage of the MCRANC structure.

Figure 4.28 shows the results obtained using raw MSEP data. Fig. 4.28a depicts a raw MSEP record along with a MSEP waveform which was averaged over 250 records. The larger, low frequency component in the raw MSEP record is the MEI. Notice that the level of the uncorrelated noise sources here is quite low. Fig 4.28b displays the SEP estimate obtained using a single ANC. While the low frequency component has been reduced, distortion is introduced into the original MSEP waveform. Figure 4.28c portrays the MSEP estimate provided by a five channel MCRANC. By observing this estimate, we can notice that in addition to the reduction of the low frequency MEI, the effect of crosstalk has also been compensated.

Tables 4.3 and 4.4 offer a more comprehensive look at the performance of MCRANC with experimental SEP data. In Table 4.3, the performance of the MCRANC in terms of the distortion index and SNRGAIN for the MSEP data collected from different subjects is tabulated. One can observe that the performance of the MCRANC gets consistently better with the increase in the number of reference channels in its second stage. As observed with the simulated data, the performances obtained using an ANC and a CRANC (M=1) are approximately the same. Notice that the input SNR values for the MSEP data are relatively higher and hence the good performance exhibited by the MCRANC. Table 4.4 shows similar results for the SSEP data. Here we see that the performance of the MCRANC is not significantly different from an ANC. With the SSEP data, the input SNR values are usually quite low. Thus the

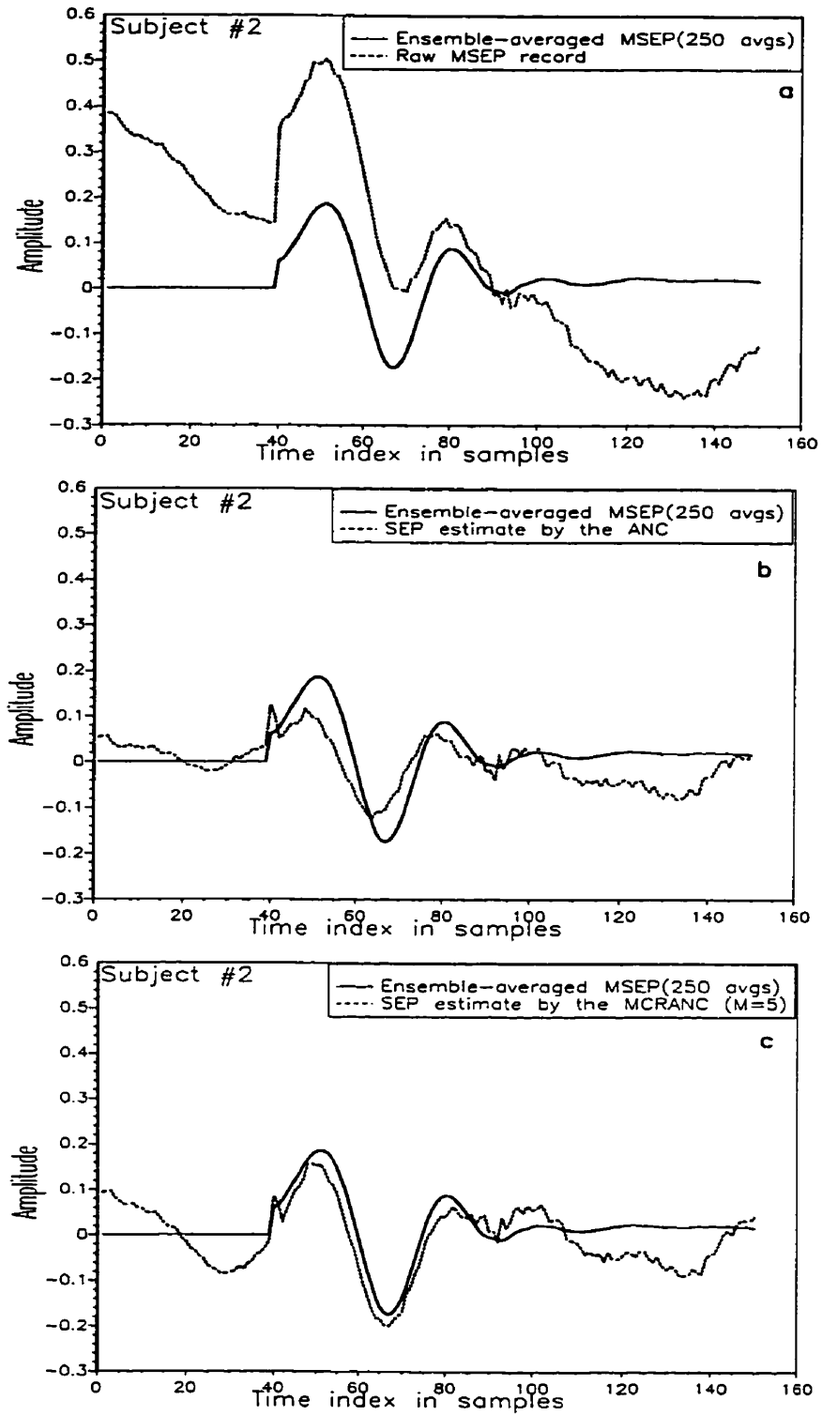

Figure 4.28: ***Qualitative comparison of ANC and MCRANC with experimental MSEP data. Level of crosstalk, $\beta = 1.01$.***

Subject	Distortion Index, ρ						SNRGAIN, γ					
	ANC	MCRANC, M =					ANC	MCRANC, M =				
		1	2	3	4	5		1	2	3	4	5
Subject #1 SNRin =0.14 $\beta = 0.73$	0.20	0.18	0.13	0.11	0.08	0.07	3.69	3.64	3.64	5.55	5.79	8.26
Subject #2 SNRin =0.07 $\beta = 0.96$	1.68	1.20	0.32	0.29	0.26	0.24	3.00	1.20	2.73	2.77	3.08	4.30
Subject #3 SNRin =0.15 $\beta = 0.90$	0.36	0.42	0.36	0.28	0.27	0.21	2.32	2.25	3.41	3.88	3.89	4.53

Table 4.3: *MSEP enhancement results using the MCRANC.*

MCRANC filter requires a large number of reference channels in its second stage to accomplish the task of crosstalk compensation. The presence of a large MEI component also results in longer convergence times for the second stage of the MCRANC filter, usually thrice the number of SEP records used while processing MSEP data.

In these situations, it is better to employ an ECRANC filter instead of a MCRANC filter. By employing an averager in the second stage of the CRANC structure, ECRANC reduces the effects of the residual MEI and uncorrelated noise sources on the convergence of the second stage. This results in a better estimate of the crosstalk transfer function which leads to a better SEP estimate. The performance of the

Subject	Distortion Index, ρ						SNRGAIN, γ					
	ANC	MCRANC, M =					ANC	MCRANC, M =				
		1	2	3	4	5		1	2	3	4	5
Subject #1 SNRi =0.0013 $\beta = 0.97$	19.18	19.12	15.18	16.05	19.07	13.29	1.54	1.56	1.20	1.15	1.45	0.85
Subject #2 SNRi =0.02 $\beta = 1.06$	1.51	1.71	1.70	1.66	1.54	1.59	1.56	1.57	1.62	1.55	1.61	1.56
Subject #3 SNRi =0.02 $\beta = 0.90$	4.01	3.47	3.79	3.91	3.77	3.72	1.22	1.09	1.22	1.23	1.20	1.18

Table 4.4: *SSEP enhancement results using the MCRANC.*

ECRANC filter for the three data sets shown in Table 4.4 was quantified using the distortion index parameter and is shown in Figures 4.29a-c. These graphs demonstrate that the ECRANC provides a better quality signal estimate compared to the other two techniques. In addition, these graphs show that the ECRANC provides better distortion indices compared to plain ensemble averaging of the input (solid line in Figures 4.29a-c). Since the ensemble averaging process is computationally cheap, the computational overhead associated with the ECRANC structure compared to the other two is minimal.

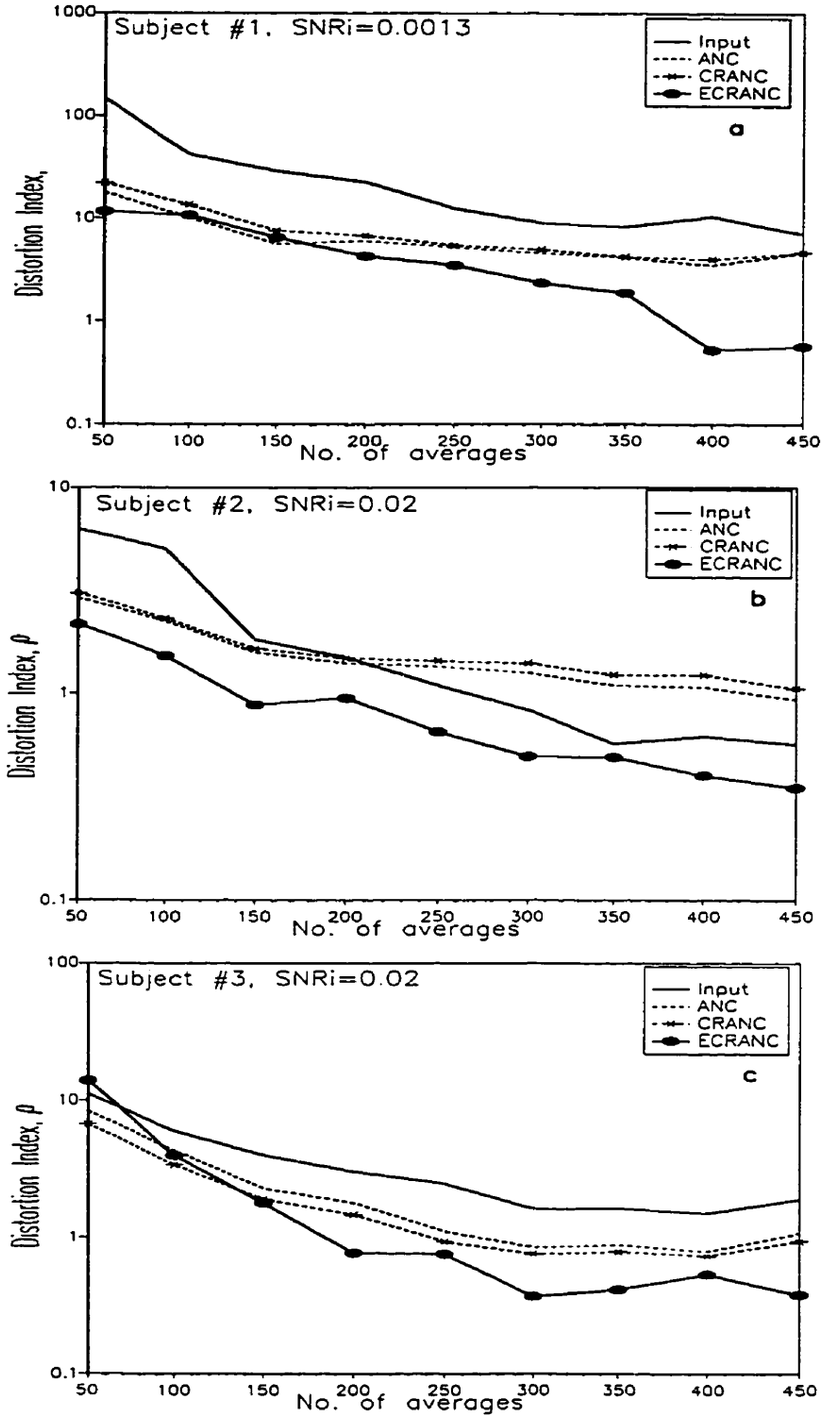

Figure 4.29: ***Distortion indices associated with the ECRANC SSEP estimates for different subjects.***

4.6 Conclusions

Electrical activity emanating from the surrounding active muscles forms a significant source of interference in surface measurements of SEP waveforms. Since the spectral content of this myoelectric activity overlaps with that of the SEP, bandpass filtering without distorting the SEP characteristics is impossible. Ensemble averaging is an effective way of reducing the Myoelectric Interference (MEI) as it is asynchronous with the SEP but a large number of SEP records may need to be averaged to obtain a good quality SEP.

Adaptive noise cancelling techniques offer a promising solution to the MEI reduction problem. However, the quality of SEP estimated by an ANC deteriorates in the presence of SEP crosstalk between the primary and reference sensors. The distortion resulting from this crosstalk can be compensated by cascading a second ANC. This two-stage CRANC structure achieves the dual objectives of crosstalk compensation and interference reduction.

The performance of the CRANC filter, however, suffers from another physical process, *viz.* the presence of other extraneous noise sources which are uncorrelated to both the MEI and the SEP. The mere presence of these uncorrelated noise sources affects the crosstalk resistivity of the CRANC structure. For uncorrelated noise levels comparable to the SEP level, the CRANC structure is as good as a single ANC – nothing extra is gained by using a second ANC.

Multiple reference ANC structures are always better in noisy situations. The parallel reference channels act to "average" out the uncorrelated noise sources while still maintaining the temporal relationships between the correlated components. Thus a multireference ANC can be used in both first and second stages of the CRANC structure. The performance of the MCRANC structure is directly proportional to the number of channels – the more the number of channels, the more it is robust to the influence of uncorrelated noise sources and the better is its performance. Simulations

and experimental results from MSEP data validate this point.

The MCRANC structure poses another problem in poor SNR situations encountered with SSEP measurements. A large number of reference channels is required in the second stage of the MCRANC filter, to "average" out the powerful background noise while still compensating for the crosstalk. This places a strain on the computational requirements of the processing system.

In these situations, it is better to employ a CRANC system which replaces the multireference structure with a straight averager thereby reducing its computational complexity. The SSEP results show that an ECRANC is a much wiser choice when dealing with SEPs of very low SNR.

The SSEP results also justify the application of ECRANC to the problem of SSEP enhancement instead of simple ensemble averaging. The ECRANC filter structure requires approximately half the number of SEP records to achieve the same distortion index as the ensemble averaging. With the advent of faster digital signal processors, it is expected that the ECRANC filter structure can be realized in realtime for spinal cord monitoring applications.

Chapter 5

Stimulus Artifact Reduction

Summary

Various issues concerning the Stimulus Artifact (SA) reduction problem are explored in this chapter. The chapter begins with a generation model of the SA followed by some experimental studies investigating the nonlinearity in SA. Nonlinear Adaptive Filters (NAFs) based on a truncated Volterra series are introduced and their efficacy in reducing the SA interference is demonstrated through processing both simulation and experimental data. Several parameters which degrade the performance of the NAF are identified and recommendations are made to negate these influences.

5.1 Stimulus Artifact (SA) Generation

Typically, the SA waveform is a spike followed by a decay response whose amplitude and time constant depend upon the type of stimulator used, the stimulating and recording electrode characteristics, and the filtering characteristics of the preamplifier stage of the recording system. This SA waveform has been modeled as a linear combination of three different components which are coupled into the recording

system by three independent mechanisms [55].

The first and the most obvious mechanism is due to the conduction of stimulus current through the limb [55, 17]. This stimulus current creates at the recording electrodes a differential signal which experiences the full amplification of the recording system. It has been shown that this stimulus current is a nonlinear function of the stimulus voltage [15, 60]. At high current densities, the electrode-skin interface at the stimulating electrodes can be modeled as a nonlinear resistor in parallel with a fixed capacitor [60, 17]. Stevens [60] and Barker [4] have analytically derived an expression for the current/voltage characteristics, $I = aV + bV^2$, and experimentally validated it. This SA component attenuates rapidly as the recording electrodes are moved away from the stimulation site. Thus the effect of this SA component can be reduced by increasing the distance between the stimulating and recording electrodes [39]. McLean [39], in her Masters study, observed that this component reduced by around twenty three times as the distance between the stimulating and recording sites doubled. Another possible way to reduce this component is to place the recording electrode on the stimulus isopotential lines. However, it is shown in the literature [28] that the isopotential lines shift during the stimulus pulse duration and also that the direction and alignment of the isopotential lines differ for the three different SA components.

The second coupling mechanism arises from imperfect stimulus isolation. Most of the commercial stimulators come with an isolator unit which isolates the subject from the grounded stimulator. In many of the stimulator systems, this isolation is transformer based and there always exists a stray capacitance between the stimulating electrodes and ground due to imperfect isolation. As well, there is significant capacitance between the subject and ground. The resulting current, called the displacement current [39], also creates a differential signal at the recording electrodes. This SA component, unlike the first component, does not attenuate appreciably as the distance between the recording and stimulating electrodes increases and often

becomes the predominant component when they are far apart. This component can be significantly reduced by placing a ground electrode between the stimulating and the recording sites [39]. This ground electrode offers a low resistance path for the displacement current component and hence the magnitude of the SA component due to displacement current reduces.

The third component is due to the electromagnetic coupling between the stimulating and recording leads. The contribution of this SA component depends on the impedance of the recording electrodes, the location of the leads and the quality of shielding on the leads [55]. It becomes a significant component when the skin surface is underprepared or when the recording electrodes exhibit high impedance. Minimization of this component warrants usage of minimal length stimulating and recording leads, employment of low impedance electrodes, thorough skin preparation and adequate physical separation between the recording and stimulating leads.

Note that if the above precautions are taken, the influence of SA interference on the SEP waveform can be reduced to a great extent. However, in some situations there may still be some residual SA affecting the SEP characteristics. The objective of this chapter is to investigate the applicability of signal processing techniques to SA reduction in such situations. In particular, adaptive filters based on a truncated Volterra series expansion are employed to mitigate the SA interference. Before the theory of Volterra series expansion is reviewed, it is worthwhile to investigate the nonlinearities involved in SA generation.

5.2 Nonlinearity in SA Generation

Figure 5.1 depicts the SA generation mechanisms from a transfer function point of view. Here $H_1(z)$ represents the transfer function between the stimulating and the recording electrodes due to the stimulus conductive current, $H_2(z)$ is the transfer

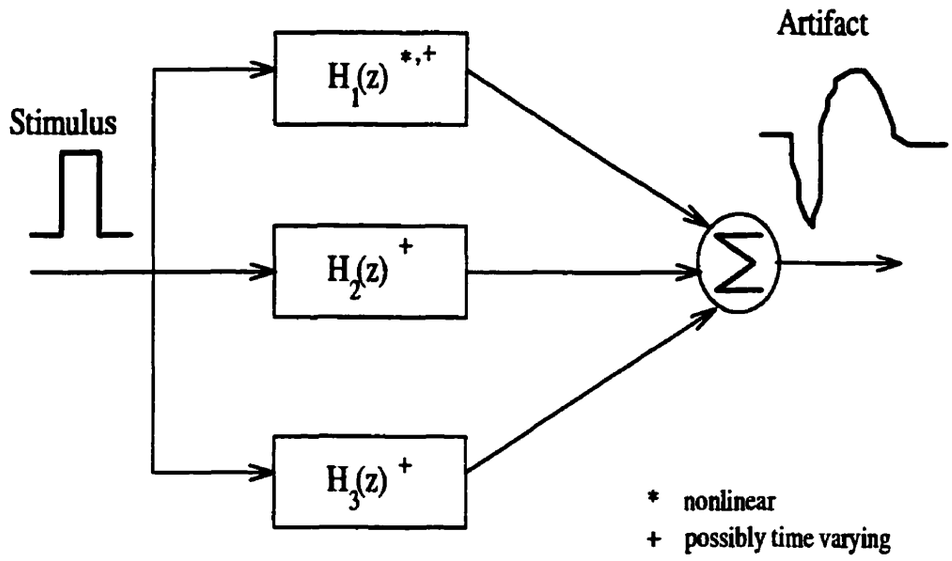

Figure 5.1: *SA generation model in the discrete Z domain.*

function of the stimulus displacement current component, and $H_3(z)$ is the electromagnetic coupling transfer function. Note that the transfer function due to the first component is nonlinear as explained before and all three transfer functions are possibly time varying as the impedances of the stimulating and recording electrodes change due to sweating, drying of the electrode paste, movement of the limb etc.

Two examples are given to provide experimental evidence of nonlinearity in the SA generation. Figure 5.2 depicts the results from the first experiment investigating the nonlinear V/I characteristics. Here the median nerve is stimulated at the index finger using conductive rubber electrodes. The resulting MSEP is acquired at the wrist using Ag-AgCl electrodes. The stimulus output is taken directly from the main stimulator bypassing the stimulation isolation unit to ensure that the displacement current component is nullified. The current through the stimulating electrodes was measured using the Tektronix type 134 current probe amplifier. The steady-state current values were noted down for various values of the stimulus input voltage. Figure 5.2 graphs the V/I characteristics resulting from this experiment. In this

figure, the measured current values are plotted against the stimulus input voltage along with the current values that would have resulted had the system been linear. The deviation from linearity is obvious when these values are compared. A second order polynomial fit to the measured current values is also shown in Figure 5.2 which appears to be a good fit.

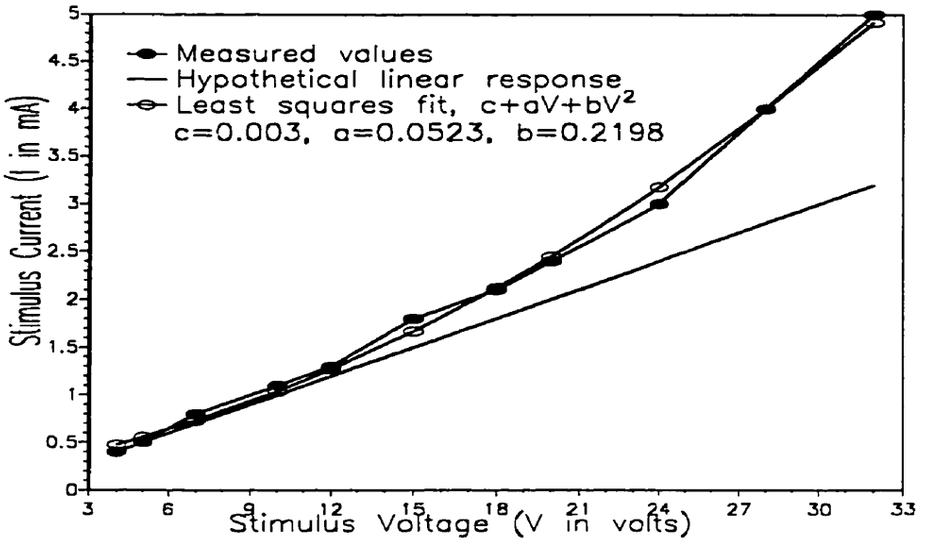

Figure 5.2: ***Nonlinear V/I characteristics at the stimulating electrodes.***

The results from another experiment which demonstrate the nonlinear nature of the SA are shown in Figure 5.3. In this experiment, called the refractory period experiment, two stimulus pulses of the same amplitude are given in such a way that the second stimulus pulse occurs during the refractory period of the nerve[1]. In this way, the first stimulus pulse evokes both SA and SEP waveforms while the stimulus pulse during the refractory period results only in the SA waveform. These two waveforms can then be subtracted to yield an estimate of the SA. Mathematically, if $SA(k)$ is

[1] All nerve fibers have a certain time duration immediately after a stimulus during which a second stimulus fails to evoke a response. This period is called the refractory period of the nerve.

the SA waveform and $s(k)$ is the SEP, then

$$\begin{aligned} x_1(k) &= SA(k) + s(k) \\ x_2(k) &= SA(k) + SA(k+\eta) + s(k) \qquad \textit{and} \\ x_3(k) &= x_2(k) - x_1(k) = SA(k+\eta) \end{aligned} \tag{5.1}$$

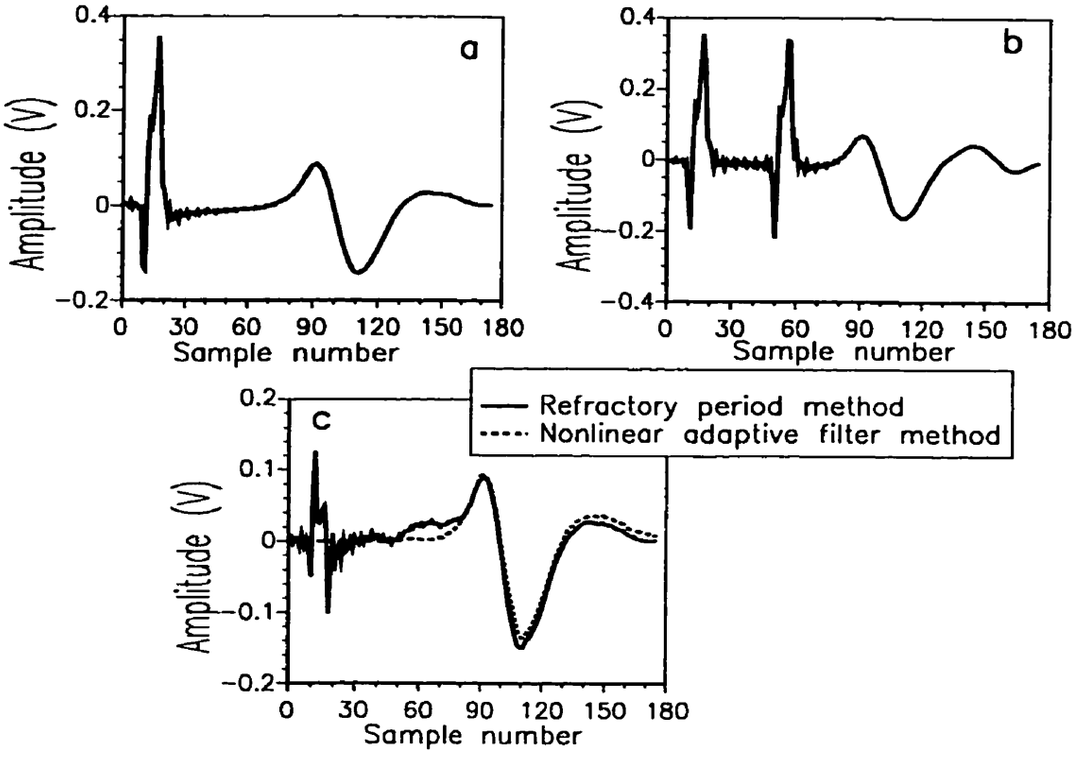

Figure 5.3: *SEP enhancement using refractory period method. a) SEP + SA composite, $x_1(k)$ during normal stimulus, b) SEP+SA composite, $x_2(k)$ during double stimulus and c) Enhanced SEP using refractory period method and NAF method.*

where k is the time index in samples, $x_1(k)$ is the composite SA and SEP waveform as a result of normal stimulus and $x_2(k)$ is the composite signal during the double stimulus phase with η being the time delay between the two stimulus pulses. Assuming that there are no time varying components, $x_3(k)$ results in a time delayed estimate

of the SA waveform which can be aligned with the SA in $x_1(k)$ and subtracted. This would result in an artifact free estimate of the SEP assuming that the two artifacts during the double stimulus phase superimpose linearly. Figure 5.3a shows the trace of $x_1(k)$ and Figure 5.3b portrays the trace of $x_2(k)$, each of which is an ensemble average of 200 such records. The SEP estimate obtained by this refractory period method is shown in Figure 5.3c. It can be observed that this estimate still contains a fair amount of the SA with the tail end of the artifact interfering with the initial SEP phase. This is due to the nonlinear superposition of the artifacts during the double stimulus input. Figure 5.3c also contains a preview of what a nonlinear adaptive filter can do with the same experimental data. The significant cancellation of the SA waveform in the SEP estimate is apparent in this nonlinear filter output.

Thus from the above discussion and experimental examples of SA, it is clear that a nonlinear adaptive system will model and hence cancel the SA better than any linear adaptive system. Unlike linear systems, which are completely characterized by their impulse response, there is no general model for arbitrary nonlinear system characterization. In the following section, we review a particular type of nonlinear system representation *viz.* the Volterra series representation.

5.3 Volterra Series for Nonlinear Systems

Any discrete time, causal nonlinear system response can be represented by the infinite Volterra series given by the following equation [35, 36]:

$$y(k) = h_0 + \sum_{a_1=0}^{\infty} h_1(a_1)x(k-a_1) + \cdots + \sum_{a_1=0}^{\infty}\sum_{a_2=0}^{\infty}\cdots\sum_{a_p=0}^{\infty} h_p(a_1,a_2,\ldots,a_p)x(k-a_1)x(k-a_2)\ldots x(k-a_p) + \cdots \quad (5.2)$$

where $x(k)$ is the input to the nonlinear system, $y(k)$ is the output and $h_p(a_1,\ldots,a_p)$ is the p-th order Volterra kernel of the nonlinear system. Without loss of generality,

the Volterra kernels can be assumed to be symmetric *i.e.,* the kernels are unchanged for any possible permutations of their indices [36]. The Volterra series representation has been successfully applied in such diverse applications as nonlinear communication channel equalizers [5], nonlinear echo cancellers [1], semiconductor device characterization [24], nonlinear ocean signal processing [36], and modelling of biological phenomena [35].

One of the disadvantages of the above Volterra expansion is that the nth order kernel is influenced by all kernels of order greater than n. This makes estimation of different kernels in the Volterra expansion quite burdensome [35]. Wiener showed that this problem can be circumvented by a simple variation of the Volterra expansion series and by using a Gaussian white noise signal as the input [71]. The Wiener expansion results in Wiener kernels which are mutually orthogonal, making their estimation relatively simple. Lee and Schetzen [30], in their landmark paper, proposed an efficient method of measuring nth order kernels based on the nth order cross-correlation function between the white noise input and the resulting system output. However, in our application problem of SA cancellation, the input to the nonlinear system is a periodic pulse train. While one can envisage applying a white noise stimulus and measuring the resulting SA, clinical stimulators do not have the capability of providing a white noise stimulus. Thus alternative methods of kernel estimation are required for the problem of SA cancellation.

While the infinite Volterra series expansion might precisely characterize a nonlinear system, due to constraints on the amount of data and computational resources one has to work with a truncated Volterra series expansion [36]. The second order truncated Volterra series response can be expressed as:

$$y(k) = h_0 + \sum_{i=0}^{N-1} h_1(i)x(k-i) + \sum_{i=0}^{N-1}\sum_{j=i}^{N-1} h_2(i,j)x(k-i)x(k-j) \qquad (5.3)$$

where N is the system memory, and h_0, h_1 and h_2 are the zero, first (the linear part), and second order (the nonlinear part) Volterra kernels respectively. Since it is

suggested in the literature that the SA generation probably involves a second order nonlinear system [60, 17], this truncated Volterra series expansion is expected to be adequate for SA cancellation.

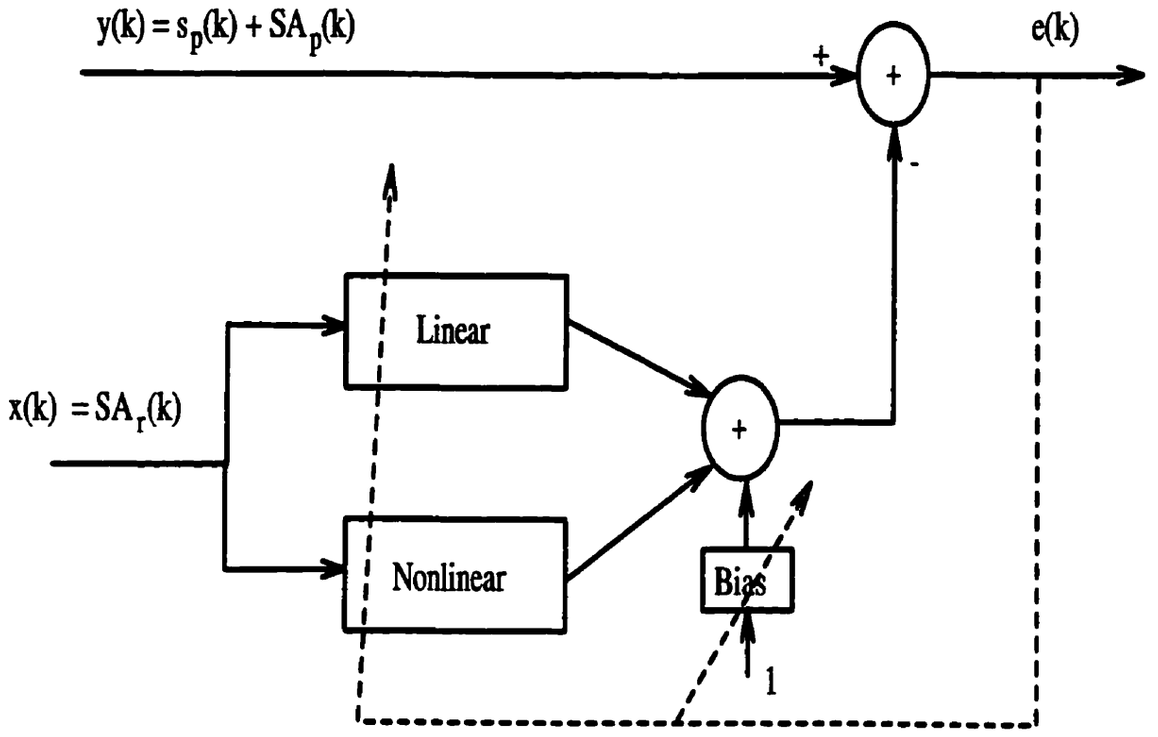

Figure 5.4: *Block diagram of the NAF structure as applied to SA cancellation.*

The zero, first and second order Volterra kernels in Eq. 5.3 can be estimated using adaptive signal processing techniques. Adaptive filter structures, like the one shown in Figure 5.4, with $x(k)$ as the reference input, $y(k)$ as the primary, and a structure based on Eq. 5.3 can estimate these kernels iteratively without invoking any assumptions on the input statistics. Moreover, the derivation of the adaption algorithms for the Nonlinear Adaptive Filters (NAFs) closely follows the derivation of adaption algorithms for linear FIR filters [36]. The derivation stems from the following problem statement:- let y(k) be the primary input to an NAF and x(k) be

its reference input, then update the kernels such that the error signal between y(k) and its NAF estimate, $\hat{y}(k)$, is minimized in the mean square sense. Mathematically,

$$\hat{y}(k) = H^T(k)X(k) \tag{5.4}$$

$$\text{and} \qquad e(k) = y(k) - \hat{y}(k) \tag{5.5}$$

where $H^T(k) = [h_0(k), h_1(0;k), \ldots, h_1(N-1;k), h_2(0,0;k), h_2(0,1;k), \ldots, h_2(N-1, N-1;k)]$ is the kernel vector and $X^T(k) = [1, x(k), \ldots, x(k-N+1), x^2(k), x(k)x(k-1), \ldots, x(k)x(k-N+1), \ldots, x^2(k-N+1)]$ is the input data vector. The Least Mean Square (LMS) algorithm which minimizes the cost function $E(e^2(k))$ by updating the kernel vector H using a steepest descent mechanism is now given by

$$H(k+1) = H(k) + \mu X(k)e(k) \tag{5.6}$$

where μ controls the speed of convergence of the LMS algorithm. The derivations for the misadjustment due to μ, convergence time and other convergence characteristics are straightforward extensions from the linear LMS algorithm. The Recursive Least Squares (RLS) algorithm, on the other hand, is an exact minimization of the squared error. The cost function, $J(k)$ that is minimized in this case is given by [23],

$$J(H) = \sum_{l=0}^{k} \lambda^{k-l}(y(l) - H^T X(l))^2 \tag{5.7}$$

where λ is the forgetting factor which controls the memory span of the NAF. The resulting adaptation procedure involves calculation of the input autocorrelation matrix and the input-output crosscorrelation vector. An advantage of the RLS algorithm, which is an important advantage when dealing with nonlinear data, is its relative insensitiveness to the eigenvalue spread in the input autocorrelation matrix compared to the LMS algorithm. Data from a nonlinear system usually exhibit large eigenvalue spread which prompts the usage of RLS based NAFs over the LMS based NAFs.

A simple simulation is performed to illustrate the convergence characteristics of the RLS and LMS based NAFs. An arbitrary five filter length second order Volterra

system is simulated using the kernel vector H_1 given by

$$H_1(k) = \begin{cases} 0, & \text{for k=0} \\ e^{\frac{-(k-1)}{10}}, & \text{for k = 1,2,...,20} \end{cases} \tag{5.8}$$

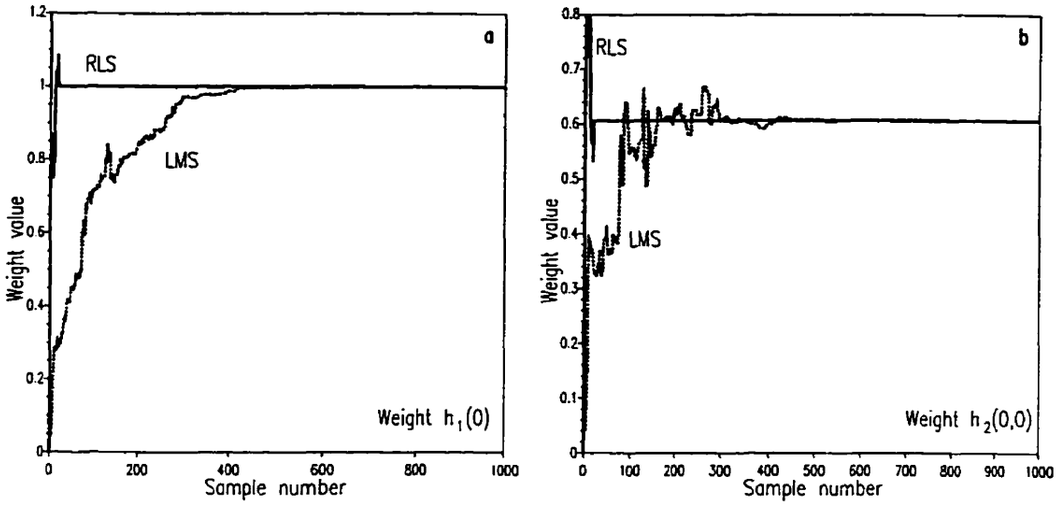

Figure 5.5: ***Convergence characteristics of RLS and LMS algorithms.***

The input to this nonlinear system, $x(k)$, is a zero mean Gaussian white noise of unit variance and the output is $y(k)$. A length five NAF driven separately by RLS and LMS algorithms is then employed with $y(k)$ as its primary input and $x(k)$ as the reference input. The convergence plots from both these algorithms are compared in Figure 5.5. From these graphs, it is evident that the RLS algorithm achieves significantly faster convergence in terms of the number of samples required. This faster convergence, however, comes at an expense of increased computational complexity which is of the order $O(N^4)$ multiplications per iteration (the LMS algorithm on the other hand, exhibits a complexity of $O(N^2)$). This higher computational complexity renders the application of RLS based NAFs in real-time SA cancellation impractical. However, since all the data processing for this thesis is performed offline, the computational complexity once again was not a significant issue and only the results proffered by the RLS based NAFs are displayed throughout this chapter. A detailed comparison of the

performance of the RLS and LMS algorithms in SA reduction is given in Appendix V.

5.4 Simulation Study

5.4.1 Introduction

The objective of the following simulation experiments is to identify the key parameters that influence SA cancellation by NAFs. Since this is the first study to examine the applicability of the Volterra expansion based NAFs to SA cancellation, it is important to investigate through simulations the issues that affect the performance of the NAFs before these NAFs are actually applied to the *in vivo* data. The main issues that are addressed in this section are:

1. Generation of simulated SEP and SA signals.
2. Performance measures.
3. Based on these performance measures, how is the performance of the NAF affected
    - when a suboptimal filter length is used for the NAF?
    - when the SEP is present in the primary and/or reference input?
    - when there is a significant amount of background noise, as is the case with the *in vivo* data?

5.4.2 Simulation Data and Performance Measures

The reference SA waveform, $SA_r(k)$, that is employed throughout this simulation study is an experimentally acquired *in vivo* SA waveform with sufficient ensemble averaging to eliminate the background noise. The primary SA waveform, $SA_p(k)$, is

obtained by nonlinearly filtering the $SA_r(k)$ using the kernel vector H_1 of Eq. V.21 in the filter of Eq. V.2. The SEP used in this study is generated using the mathematical model given in Chapter 3.

Three different performance measures are used to quantify the efficacy of the NAF in cancelling the SA in the absence of the SEP. These performance measures, γ_1^{SA}, γ_2^{SA} and γ_3^{SA}, are defined as

$$\gamma_1^{SA} = \frac{|SA_p(k)|_{max}}{|SA_o(k)|_{max}} \tag{5.9}$$

$$\gamma_2^{SA} = \left(\frac{\sigma_{SA_p(k)}}{\sigma_{SA_o(k)}}\right)_{k\in P} \tag{5.10}$$

$$\gamma_3^{SA} = \left(\frac{\sigma_{SA_p(k)}}{\sigma_{SA_o(k)}}\right)_{k\in \overline{P}} \tag{5.11}$$

where $SA_o(k)$ is the SA residual at the output of the NAF, $|SA_p(k)|_{max}$ and $|SA_o(k)|_{max}$ are the peak absolute voltage values of the input and residual artifacts respectively, σ denotes the standard deviation, P is the time interval covering the spike phase of the SA and $\overline{P}$ is the remaining time interval of the SA record. While each of these performance measures is important in assessing the effectiveness of the NAF in cancelling the SA, the parameter γ_3^{SA} is especially significant from the SEP enhancement point of view. Since it is the tail end of the artifact that interferes with the SEP waveform, γ_3^{SA} gives a good indication of the effectiveness of the NAF in terms of SEP quality improvement.

For simulations containing both the SA and the SEP, an additional performance measure is defined to measure the residual artifact interference as

$$\rho_1^{SA} = \frac{\sum_{n=0}^{L-1}(s_p(k) - \hat{s}_p(k))^2}{\sum_{n=0}^{L-1} s_p^2(k)} \tag{5.12}$$

where $\hat{s}_p(k)$ is the SEP estimate at the output of the NAF. This measure is similar to the distortin index given by Eq. 3.21. With *in vivo* data, however, since the underlying SEP signal is never available, ρ_1^{SA} cannot be computed. In these cases, visual appreciation of the SEP estimate and the performance measures quantifying

the SA cancellation given by Eqs. 5.9 and 5.10 are used to gauge the effectiveness of the NAF.

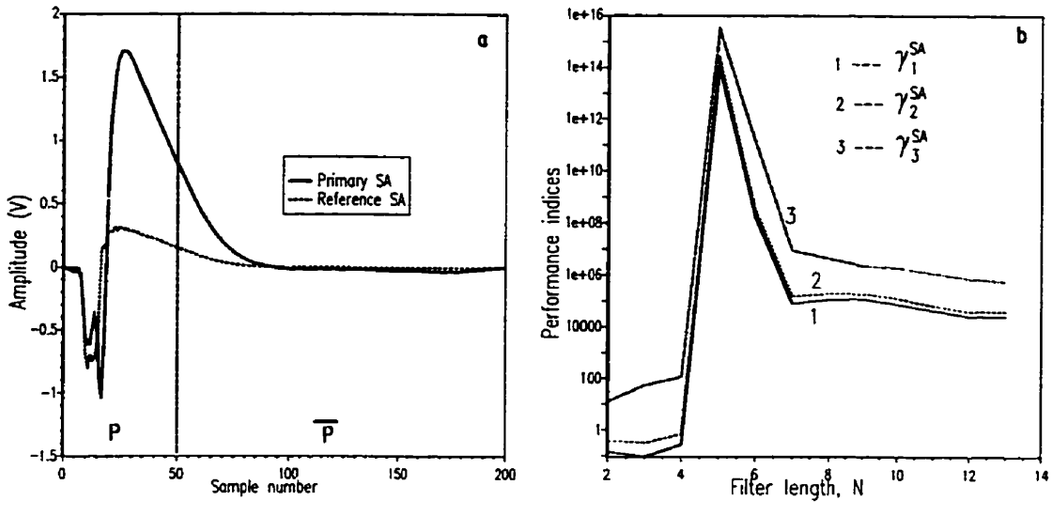

Figure 5.6: *Effects of suboptimal filter length of the NAF.*

5.4.3 Suboptimal Filter Length of the NAF

The purpose of this study is to investigate the effect on SA cancellation of choosing a suboptimal filter length. The primary and reference artifacts to the NAFs are generated as described in the previous section and are shown in Figure 5.6a. Also indicated in the Figure are the regions P and $\overline{P}$ used for the calculation of the performance indices. The NAF driven by the RLS algorithm is employed with varying filter lengths. The steady state output of the NAF is then obtained by recycling the primary and reference SA data through the RLS algorithm until the convergence of the kernel vector is achieved. This output is then used to calculate the performance indices given in Eqs. 5.9, 5.10, and 5.11. These performance indices are graphed in Figure 5.6b. Note that the optimal filter order for the NAF is five since the underlying nonlinear system, H_1, has a filter length of five. From the trend of the three performance indices, we can observe that orders less than optimal result in

highly degraded performance. This is to be expected because in nonlinear filtering, when the filter length is changed from $\mathbf{N}$ to $\mathbf{N+M}$, the actual number of elements in the kernel vector changes by $(\mathbf{M^2+3M+2MN})/\mathbf{2}$ (this can be easily calculated from Eq.V.2). For example, if the filter length of the NAF is decreased from 5 to 3, the reduction in the total number of coefficients in the NAF is 11! Thus the performance is greatly degraded even if we reduce the filter length from 5 to 3. Another interesting point to note is that for filter lengths greater than the optimal, the performance also degrades but then saturates. This is due to the effects of overfitting where any nonzero value of the extra filter weights contributes to a poorer performance. With *in vivo* data, where the filter length of the underlying nonlinear system is unknown, the approach will be to increase the filter length starting from a small value. The filter length at which the performance indices peak gives an indication of the optimal filter length. Note that the three performance indices all peak at the same filter length.

5.4.4 Effect of the SEP position

With *in vivo* SEP data, the SA is most irksome when the tail of the artifact masks the initial SEP portion. In cases where the SEP and SA are comfortably separated, a simple blanking scheme can be used to retrieve an artifact free SEP. Thus data containing interfering SEP and SA waveforms, which cannot be separated by simple means, form the most crucial test of the performance of the NAF. In this section, an investigation is undertaken to assess the performance of the NAF in such situations.

The primary and reference SA waveforms are generated as described earlier. The SEP waveform is delayed and summed with the primary SA to generate the composite SEP+SA waveform. Different records of such composites are shown in Figure 5.7a, where the SEP is "moved" gradually towards the peak of the artifact. A NAF of filter length 5 (optimal filter length for SA cancellation here) is then adapted with each of these composite waveforms as the primary and $SA_r(k)$ as the reference. Once the filter has reached steady state, the output SEP estimate is computed and is shown in

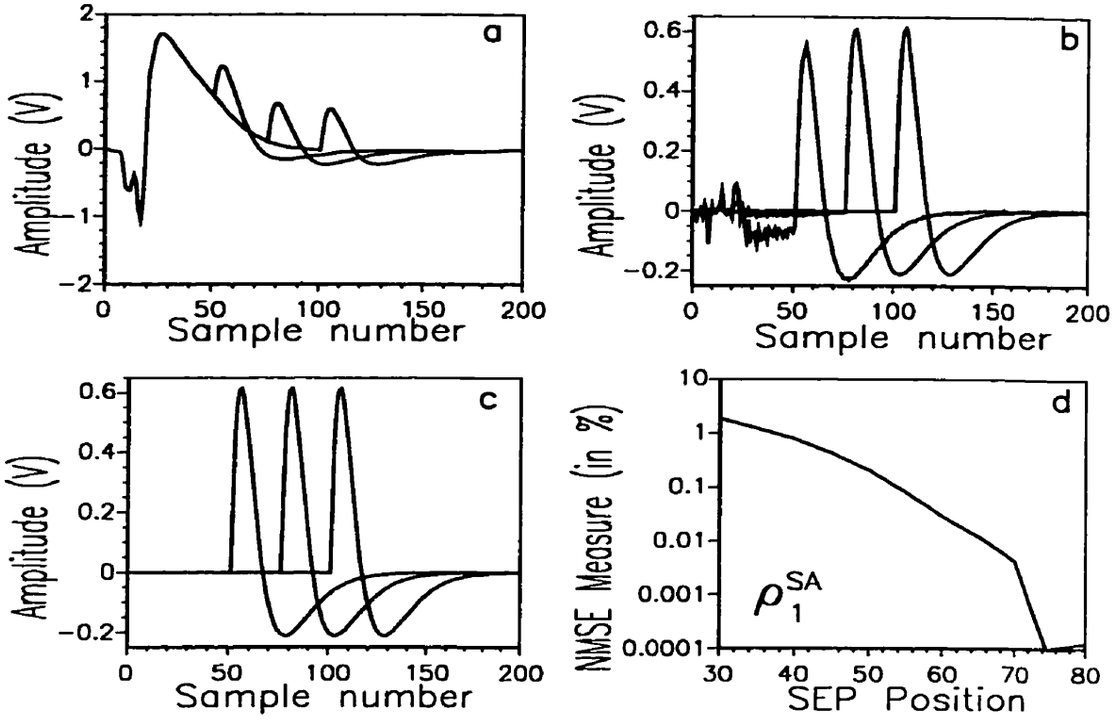

Figure 5.7: *The effect of the SEP position on the performance of the NAF, a) composite waveforms of SEP and SA in the primary input, b) corresponding SEP estimates at the output of the NAF, c) the true underlying SEP waveforms and d) the NMSE measure, ρ_1^{SA} with respect to the SEP position (measured in number of samples between the SA and SEP peaks).*

Figure 5.7b. For the sake of comparison, the underlying original SEP waveform is shown in Figure 5.7c. From these plots, we see that the position of the SEP does have an effect on the performance of the NAF. As the SEP is moved closer to the SA, there is more and more residual artifact at the output of the NAF and the SEP waveform is degraded in quality. This output SEP distortion is quantified in Figure 5.7d where the NMSE measure given by Eq. 5.12 is displayed. The SEP position in this plot is calculated as the distance, in number of samples, between the peak values of the SA and the SEP. While there is an increase in the NMSE measure as the SEP moves deep into the artifact tail, it has to be noted that interference is still less than

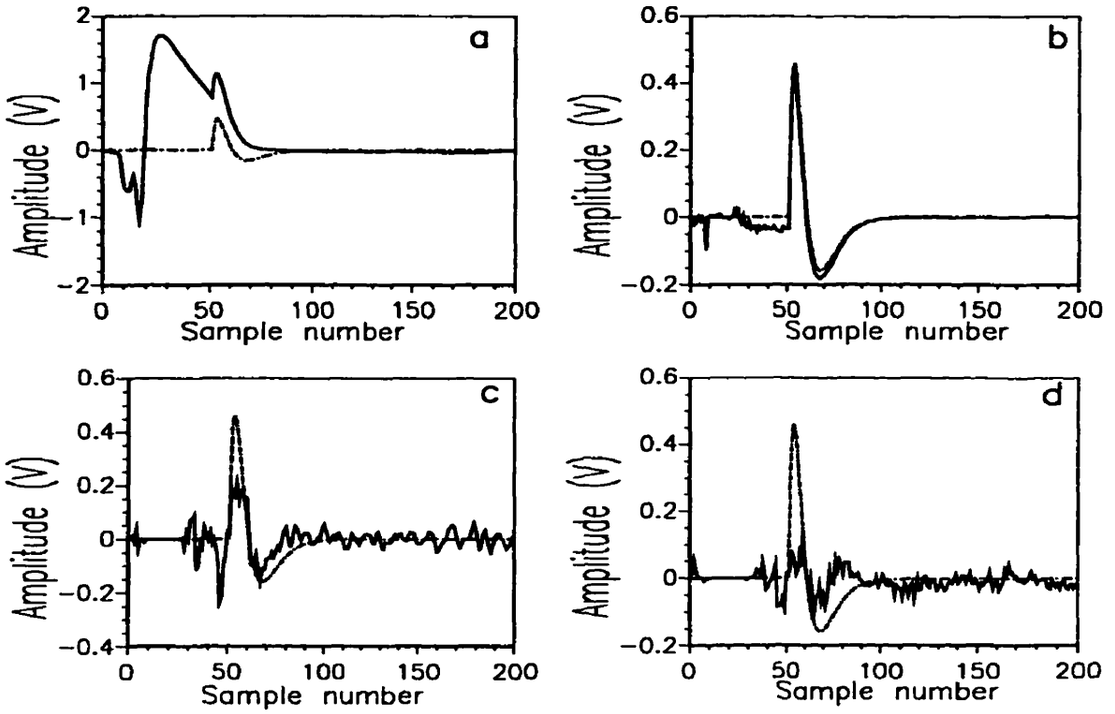

Figure 5.8: *The effect of increased filter length on SEP estimate. a) Primary SEP+SA composite and the true underlying SEP, b) SEP estimate produced by an NAF of filter length five, and c) SEP estimate provided by an NAF of filter length eight, and d) SEP estimate provided by an NAF of filter length ten. In all the plots, the dotted line represents the original SEP.*

5 %.

A closer look at the above simulation reveals a very interesting phenomenon. If the SA and SEP were uncorrelated, the presence of the SEP in the primary would not have had any effect on the performance of the NAF. The NAF primarily acts as a correlation canceller and the only correlated component would have been just the SA component. However, due to the deterministic nature of both SA and SEP waveforms, there is always a finite correlation between the SEP and the SA and this finite correlation influences the convergence of the NAF and consequently the SEP estimate at the output of the NAF is affected. In fact, if the filter length is

made arbitrarily large, the NAF will try to encompass the SEP-SA crosscorrelation and model the SEP+SA composite in the primary using the SA component in the reference! This fact is shown using the following simulation. Let us take the SEP+SA composite where the SEP starts around the 50th sample (shown in Figure 5.7a) as the primary input to the NAF. Two additional simulation runs were conducted with filter lengths of eight and ten respectively. Figure 5.8 shows the results from these simulation studies. In Figure 5.8a the SEP+SA composite in the primary input is shown along with the original underlying SEP (in dotted lines). Figure 5.8b displays the SEP estimate at the output of an NAF of filter length five. Figure 5.8c and 5.8d depict the corresponding SEP estimates for filter lengths of eight and ten respectively. The perilous effect of the adaptive filtering operation on the SEP, even though it is present in the primary, is obvious from these plots. Thus increasing filter lengths can severely degrade the SEP estimate at the output of the NAF. Further simulations and a more detailed description of this phenomenon are given in Appendix IV.

The above discussion is conflicting with the statement given in Section 5.4.5.: "With *in vivo* data, where the filter length of the underlying nonlinear system is unknown, the approach will be to increase the filter length starting from a small value". However, given the above simulation, it is obvious that increasing the filter length will lead to the NAF cancelling the SEP as well. A possible way of overcoming this problem is to let the NAF adapt only during the SA phase and let the data pass through without adaptation during the SEP phase. In this way the adaptation routine is "blind" to the SEP data and thus not only the possibility of the NAF affecting the SEP properties is averted but also the constraint on choosing the filter length is relaxed. Figure 5.9 shows the results from a simulation experiment probing the effectiveness of the abovementioned segmented adaptive filtering approach. Figure 5.9a shows the primary input to an NAF with a filter length of 5. The weights of the NAF are updated only during the "adapt" regions of the primary input. The weight values at the end of the "adapt" region are held constant and these are used

to filter the data in the "fixed" regions. The SEP estimates obtained by the segmented NAF and the normal NAF — which uses the entire data record for adaptation — are compared in Figure 5.9b. The performance improvement, in terms of the SA cancellation and the quality of the SEP estimate, achieved by the segmented NAF is apparent in this figure. Similar simulation results can be obtained with NAFs of filter lengths eight and ten.

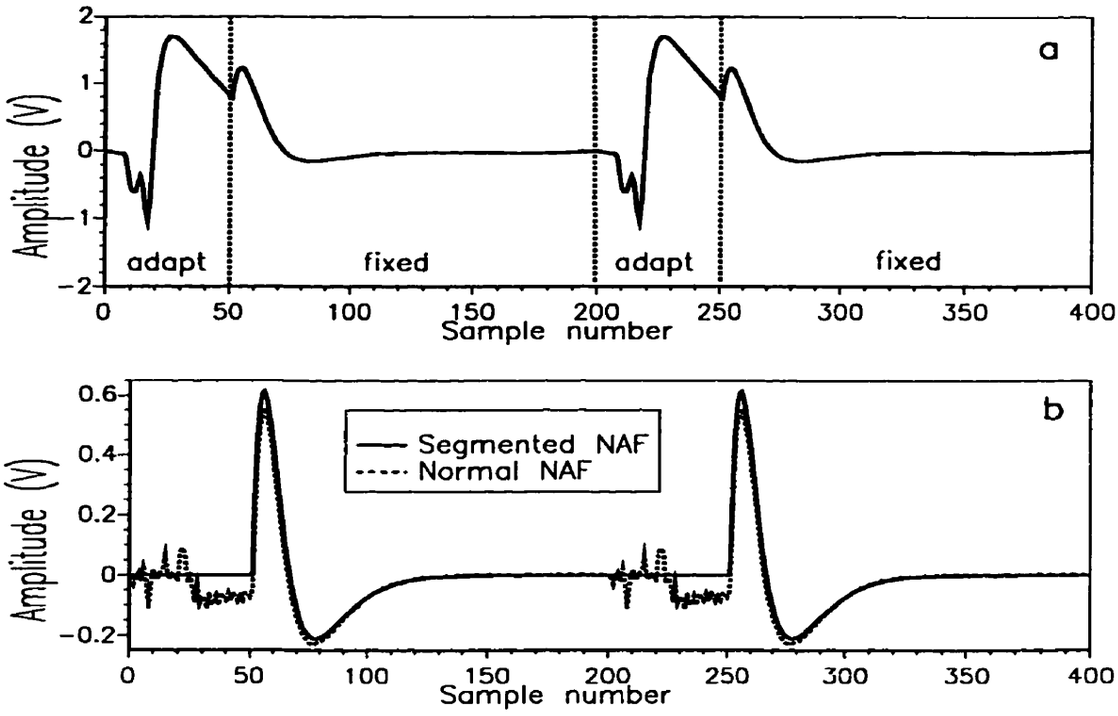

Figure 5.9: *Segmented adaptive filtering.*

Thus the segmented adaptation approach circumvents the pitfalls caused by the finite cross-correlation between the SEP and SA waveforms. Note that in practical SEP signal processing applications, there is always a noticeable time separation between the SEP and the SA. Thus it is not difficult to designate the "adapt" and "fixed" regions for the segmented adaptation procedure. Also the position of the

demarcation boundary can be biased towards the SA peak position if one is not sure where exactly the SEP starts.

5.4.5 Effect of Background Noise

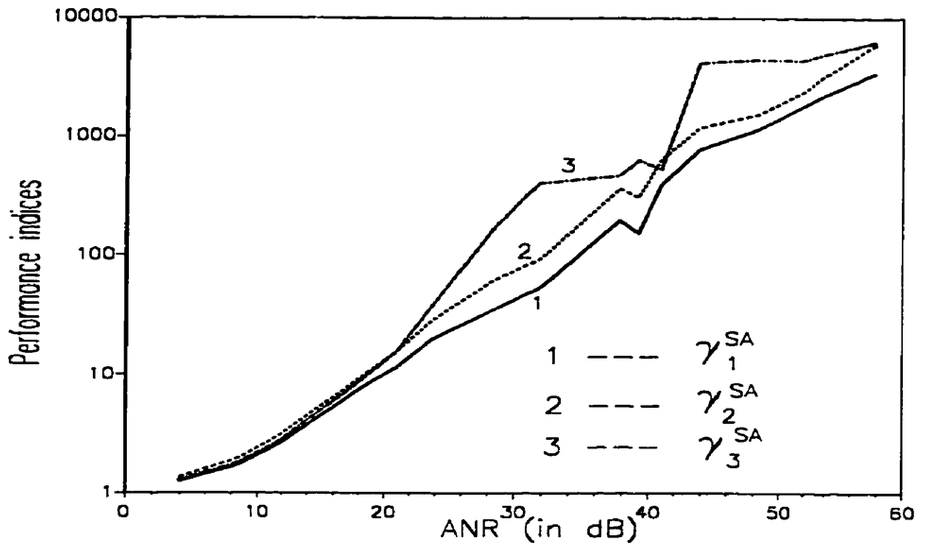

Figure 5.10: *The effect of background noise on the performance of the NAF.*

The simulations thus far have been carried out in a noise free environment. Unfortunately, *in vivo* SEP data are contaminated by the omnipresent background noise. In this section, a study is undertaken to examine the effects of the background noise on the performance of the NAF in the absence of the SEP. The primary and reference SA are the same as in Section 4.2. White Gaussian noise of varying power levels σ_U^2 is then added to the SA waveforms. The Artifact-to-Noise Ratio (ANR) is defined as

$$ANR_{dB} = 20 \log \left(\frac{|SA(k)|_{max}}{\sigma_N} \right). \tag{5.13}$$

An NAF of filter length five is then adapted with the noisy primary and reference SA until steady state is reached. Ten independent trials are performed for each

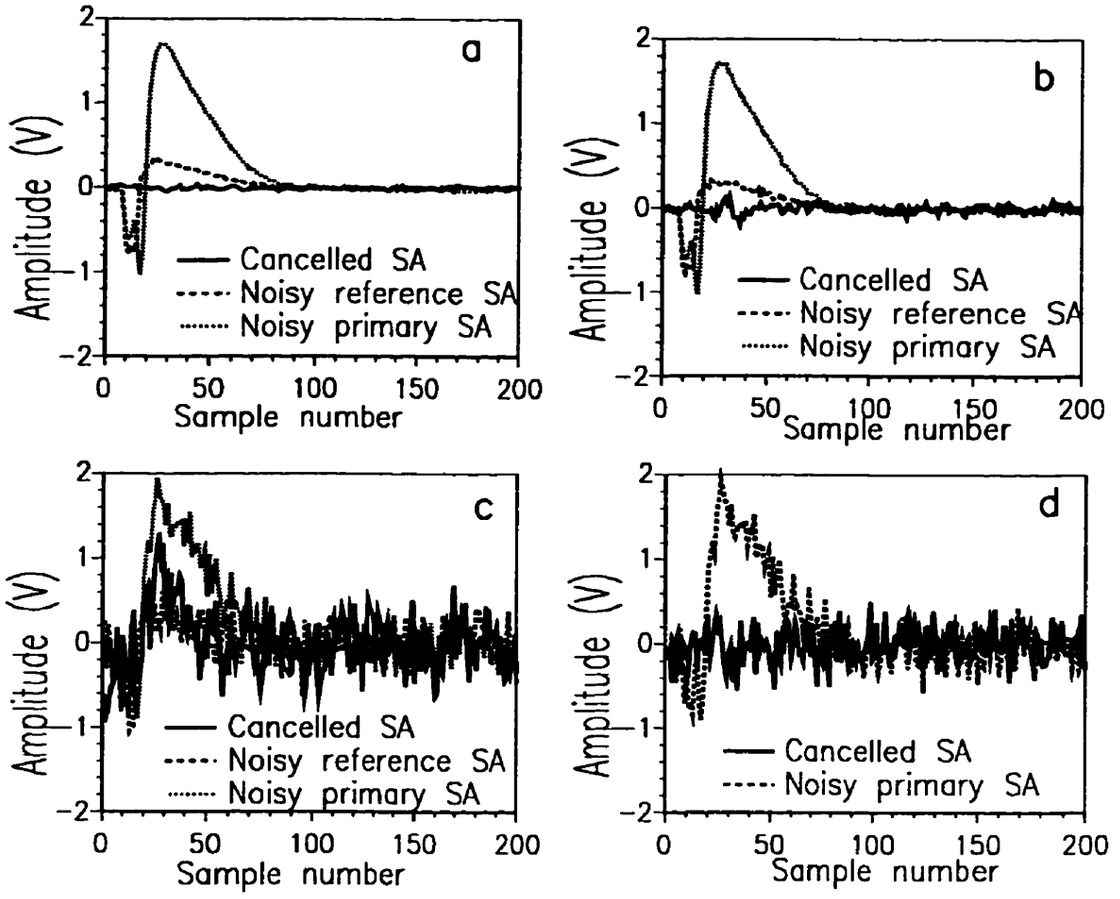

Figure 5.11: ***Performance of the NAF in the presence of the background noise. Figures 5.11a, 5.11b, and 5.11c display the noisy primary SA, noisy reference SA, and the cancelled SA for reference ANR levels of 40, 30, and 10 dB respectively. 5.11d depicts the cancelled SA when the primary SA from 5.11c and reference SA from 5.11b are used.***

noise power level and the final steady state filter weights are averaged over these ten realizations. These averaged filter weights are then used to nonlinearly filter the noise free reference SA which is then subtracted from the noise free primary SA. The resulting waveform is the SA residual and this is used in calculation of the performance measures. Figure 5.10 graphs the performance curves of the NAF for varying power levels of the noise. As one would expect, the performance monotonically deteriorates

as the power level of noise increases. Typical ANR levels encountered with *in vivo* data are 20-30 dB and thus a performance index of 100 can be expected.

Figure 5.11 gives a picture of the noisy NAF output for three different noise power levels. The noisy primary SA, noisy reference SA along with the output of the NAF after convergence are shown. It can be seen that at lower ANR levels, there is a substantial amount of SA still present in the output of the NAF. It is important to note here that the effect of noise will be more pronounced in the case of nonlinear filters as nonlinear filtering incorporates second order terms. The only way to mitigate this problem is to perform ensemble averaging on the reference input to the NAF so that we are higher up on the performance curves shown in Figure 5.10. Since the adaptation of the NAF depends mainly on the reference input, it is sufficient that only the reference SA input be averaged. This effect is shown in Figure 5.11d where a cleaner reference SA is used to cancel the same primary SA as in Figure 5.11c and the SA cancellation can be seen to be significantly better. The averaging procedure also reduces the possibility of the presence of other correlated noise components across the primary and reference inputs of the NAF, such as the MEI and the ECG.

5.5 Experimental SA Data Analysis

5.5.1 SA cancellation in the absence of the SEP

The first set of experiments concentrated on scrutinizing the effectiveness of the NAF in cancelling an experimentally acquired SA waveform. The experimental setup for obtaining median nerve and spinal cord SEP data is the same as in the previous chapter. The primary input to the NAF is obtained by stimulating the nerve in its subthreshold regime[2], collecting the resulting SA waveform, and ensemble averaging to reduce the background noise. The reference input is obtained in two different ways:

[2]A subthreshold stimulus is one which fails to evoked nervous response.

a) by collecting SA data simultaneously from a second recording channel again with ensemble averaging, and b) by performing a separate experiment in which the reference SA is acquired from the same electrodes as the primary, but at a lower stimulus voltage level. One thousand records are averaged for both the primary and reference SA waveforms acquired from the lumbar region and two hundred records are averaged for the SA data collected at the wrist region. A NAF of filter length ten driven by the RLS algorithm is then applied to cancel the primary SA waveform. Figure 5.12 shows the SA cancellation results from different subjects employing different recording procedures. In each of these plots the primary SA, the reference SA and the residual SA at the output of the NAF after its convergence are displayed. In Figure 5.12a, the primary SA is obtained from the lumbar region while the reference SA is acquired using the second recording channel. The primary and reference SAs shown in Figure 5.12b are measured in the lumbar region using only one set of recording electrodes with the reference SA obtained using a lower stimulus input voltage. The SA artifact data acquired from the wrist region using the stainless steel electrode array are shown in Figure 5.12c. Here the primary SA is acquired from the first element in the array and the reference SA using the second recording channel. Due to the proximity of the second recording channel to the stimulus site, the reference SA is several times larger than the primary SA. Finally the primary and reference SAs in Figure 5.12d are obtained at the wrist region using the Ag-AgCl electrodes with the reference SA obtained from a lower stimulus voltage level. A common feature in all these plots is the significant SA cancellation achieved by the NAF. These results indicate that the SA cancelling ability of the NAF is robust to a variety of experimental conditions and recording procedures.

5.5.2 Performance Comparison of the NAF and the LAF

In Section 5.2, two examples of nonlinearity in the SA generation were provided. It was surmised that a NAF would therefore be the appropriate candidate in reducing

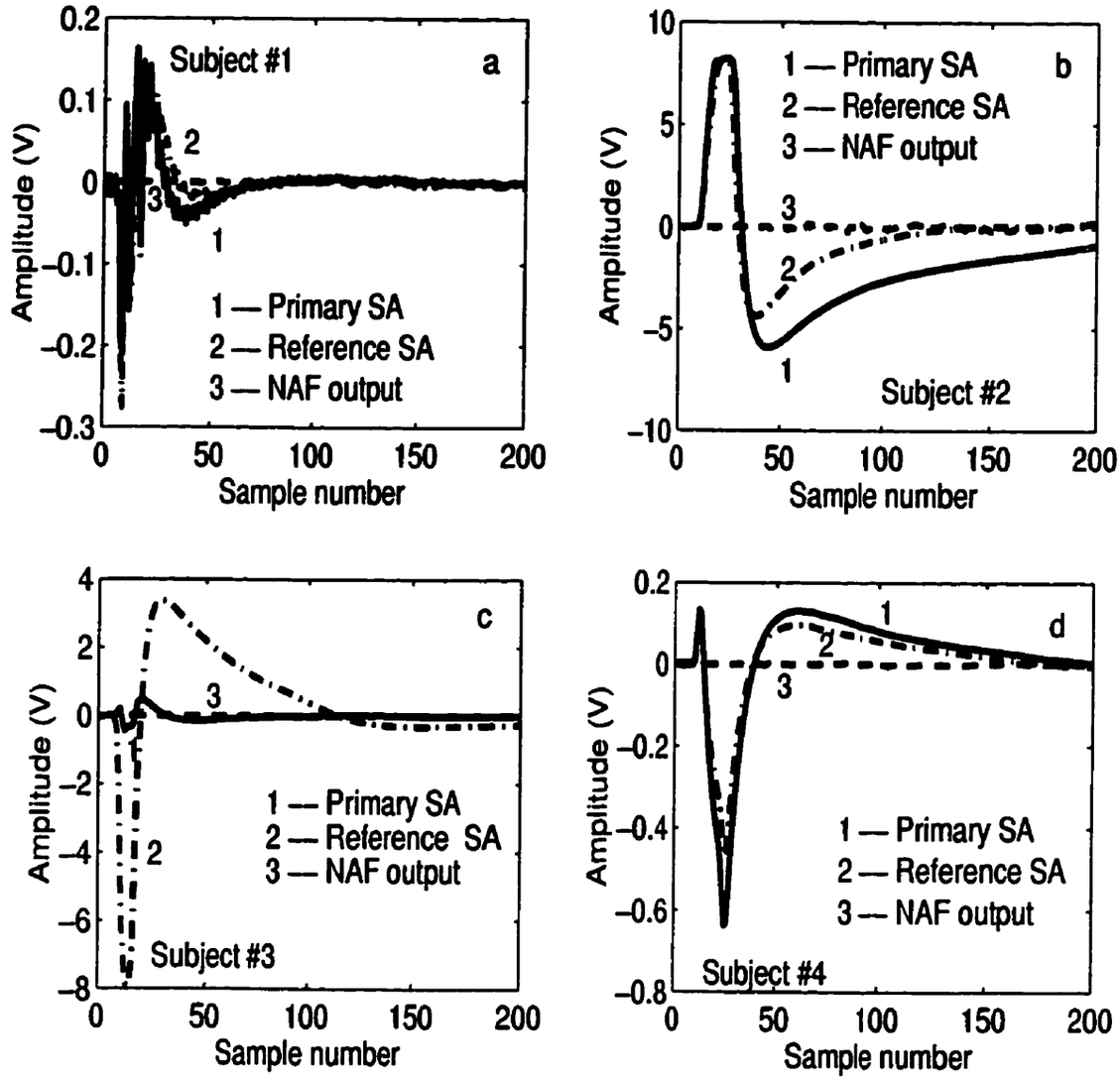

Figure 5.12: *Performance of the NAF in cancelling* in vivo *SA data collected from different subjects with different procedures (see text).*

the SA. Indeed, the previous section revealed that the NAF performs exceptionally well in cancelling the SA. This section takes this investigation one more step by comparing the performances of the NAF and the widely used FIR Linear Adaptive Filter (LAF). Also, the effect of the filter length on the performance of the NAF and the LAF is explored.

The indices defined by Eq.s 5.9, 5.10, and 5.11 are used to quantify the performance of both the NAF and the LAF. The primary and reference SAs displayed in Figure 5.12 were used as the inputs to the NAF and the LAF, and the RLS algorithm was used to adapt the coefficients of both the NAF and the LAF. In addition, a delay of half the filter length was introduced in the primary input of the LAF to compensate for any noncausality. The filter length was varied from 3 to 13 in the NAF case (the corresponding total number of coefficients were 10 and 105 respectively) , and from 3 to 100 for the LAF. For each filter length, the NAF and LAF were adapted separately and once the filter weights reached steady state, the residual SA at the output was retrieved and the performance indices were computed. Figure 5.13 graphs these performance indices against the filter length for different SA data sets. Figures 5.13a, 5.13b and 5.13c plot the three performance indices γ_1^{SA}, γ_2^{SA} and γ_3^{SA} obtained through filtering the data shown in Figure 5.12a by employing the NAF and the LAF. Figures 5.13d, 5.13e and 5.13f display the performance indices computed for data sets in Figure 5.12c, and Figures 5.13g and 5.13h are performance indices corresponding to the SA traces in Figure 5.12d. In each of these plots, the NAF can be seen to outperform the LAF quite convincingly. In most of the cases, the performance of the LAF appears to saturate for a filter length of around 100 while the performance indices of the NAF continue to increase even after a filter length of 13. This suggests that even at a filter length of 13, the NAF is still operating in its suboptimal regime. However a compelling factor for not employing larger NAF filter lengths, even though a better SA cancellation performance can be had with larger filter lengths, is the possibility of SEP distortion with larger NAF filter lengths as explored in the simulations section

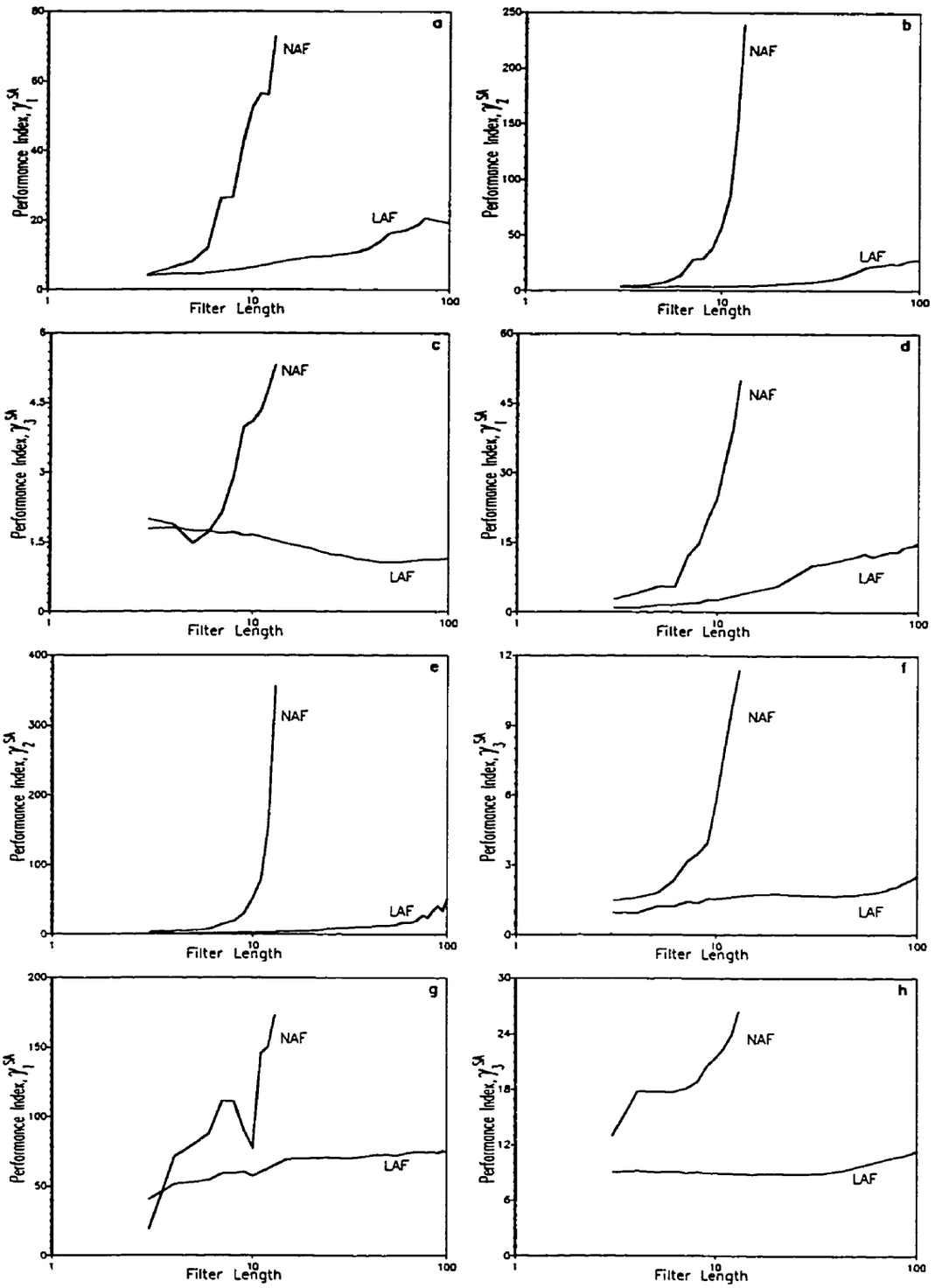

Figure 5.13: ***Performance comparison of the NAF and LAF in SA cancellation. (refer to Section 5.5.2 for details.)***

(refer to Figure 5.8). Thus in all ensuing SEP studies an NAF of filter length ten is utilized.

5.5.3 Effect of Background Noise

The experimental results obtained in the previous sections employed ensemble averaged primary and reference SA waveforms. In this section, an experimental example is provided to illustrate the effect of the background noise on the performance of the NAF. The SA data were collected at the wrist region using the stainless steel electrode array with the stimulus voltage below the threshold level of the median nerve. The SA waveform measured by the first element in the array is shown in Figure 5.14a and this formed the primary input to the NAF. The reference input to the NAF was recorded using the fourth element of the array. The reference ANR was calculated using Eq. 5.15 where the power level of the background noise was determined prior to stimulation and was found to be 20 dB. A ten filter length NAF was then employed to cancel the SA and its output is displayed in Figure 5.14b. From this Figure, it can be seen that the primary SA waveform has been reduced to the background noise level by the NAF. The primary input was then averaged over fifty SA records and this ensemble average is shown in Figure 5.14c. Also shown in 5.14c are the ensemble average (also of fifty records) of the NAF output in Figure 5.14b, and the ensemble average of the NAF output when a cleaner reference input was used. The cleaner reference input is obtained by averaging the reference input over 300 records. As observed in the simulation studies, there is an improvement in the SA cancelling ability of the NAF when a cleaner reference input is employed. To further investigate this issue, the performance indices, γ_1^{SA} and γ_2^{SA}, of the NAF are computed as the noise in the reference input is reduced by ensemble averaging and these indices are graphed in Figure 5.14d. An interesting point to note from this plot is that the performance indices increase in the beginning as the number of averages increases but then saturate. This, as expected, is because of the noise in the primary

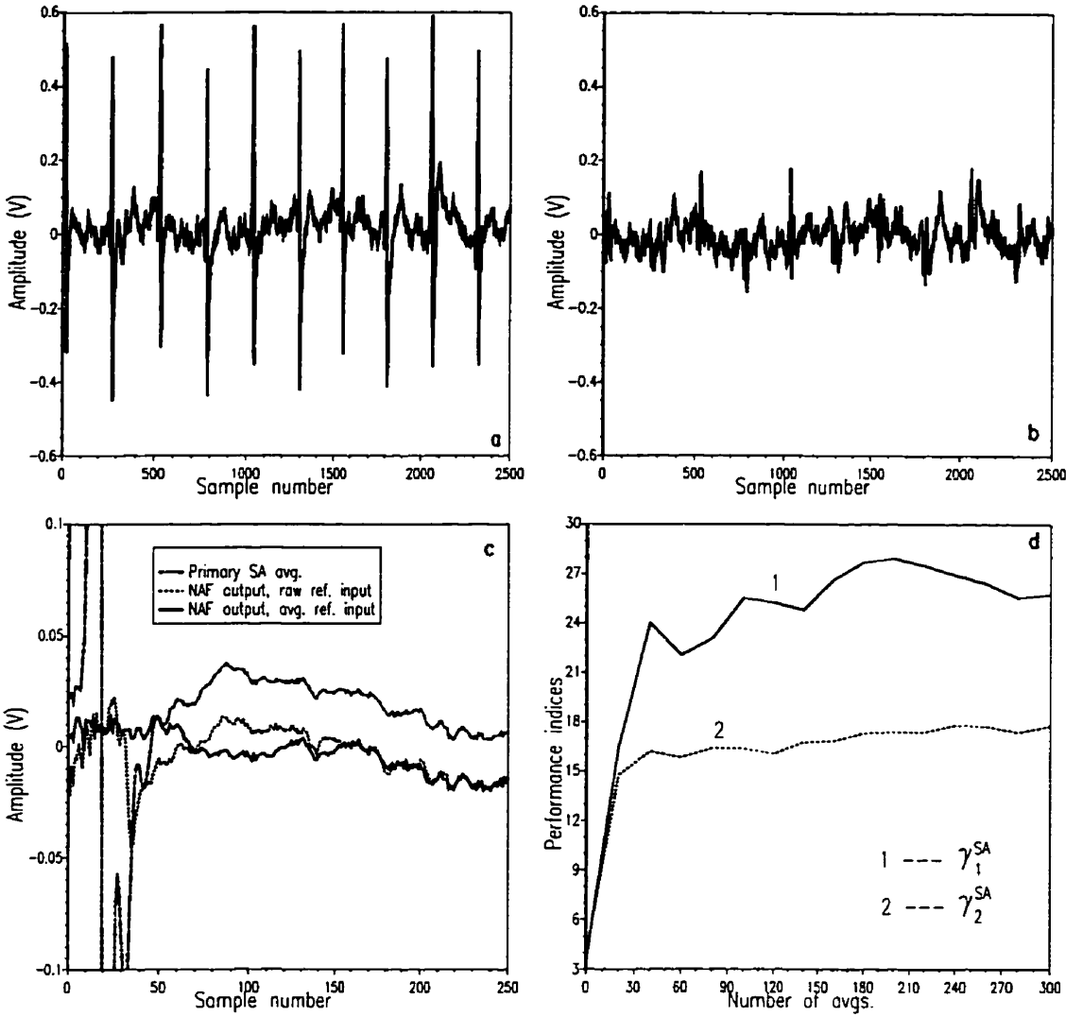

Figure 5.14: ***Performance of the NAF in cancelling*** in vivo ***SA in the presence of the background noise. a) noisy primary SA data, b) NAF output after convergence, c) primary and residual artifacts with noisy and "clean" reference inputs, d) performance indices Vs no.of SA records averaged in the reference input.***

input which passes through the NAF unfiltered and hence the performance indices, which compute the peak and standard deviation reduction between the primary input and the residual output, saturate eventhough the SA cancellation gets better as the number of averages increases.

5.5.4 SA Plus SEP Data

To investigate the efficacy of the NAF in enhancing the SEP in the presence of interfering SA, *in vivo* MSEP and SSEP data were collected. Figure 5.15 depicts the results obtained by processing SA contaminated SEP data acquired from different subjects. The first column in this picture shows the ensemble averaged SEP+SA composite waveform which is utilized as the primary input to the NAF, and an SA component obtained through either subthreshold stimulation or using a separate channel which is used as the reference input. In the second column, two different outputs are depicted: a) the SEP estimate obtained by the normal NAF which uses the entire SEP+SA record for its adaptation and, b) the SEP estimate obtained by the segmented NAF which uses only a part of the SEP+SA record for its adaptation.

The MSEP data measured using Ag-AgCl electrodes from one of the subjects is shown in Figure 5.15a. The reference SA waveform is acquired using a separate reference channel off the nerve axis. Each of these waveforms are a result of ensemble averaging 200 such records. The SEP estimates obtained by the normal and the segmented NAFs are displayed in Figure 5.15b. For the segmented NAF, the coefficients are adapted only during the first 100 samples of the SEP+SA composite waveform and the coefficients at the end of this "adapt" region are fixed through the remainder of the waveform. By comparing the two estimates, we can observe that the segmented NAF produces a "cleaner" SEP estimate compared to the normal NAF. Figures 5.15c and d show an example of one of the few cases where the NAF did not perform well. In Figure 5.15c the MSEP data acquired from the same subject using the stainless steel electrode array is portrayed. The interference due to the SA is obvious in this

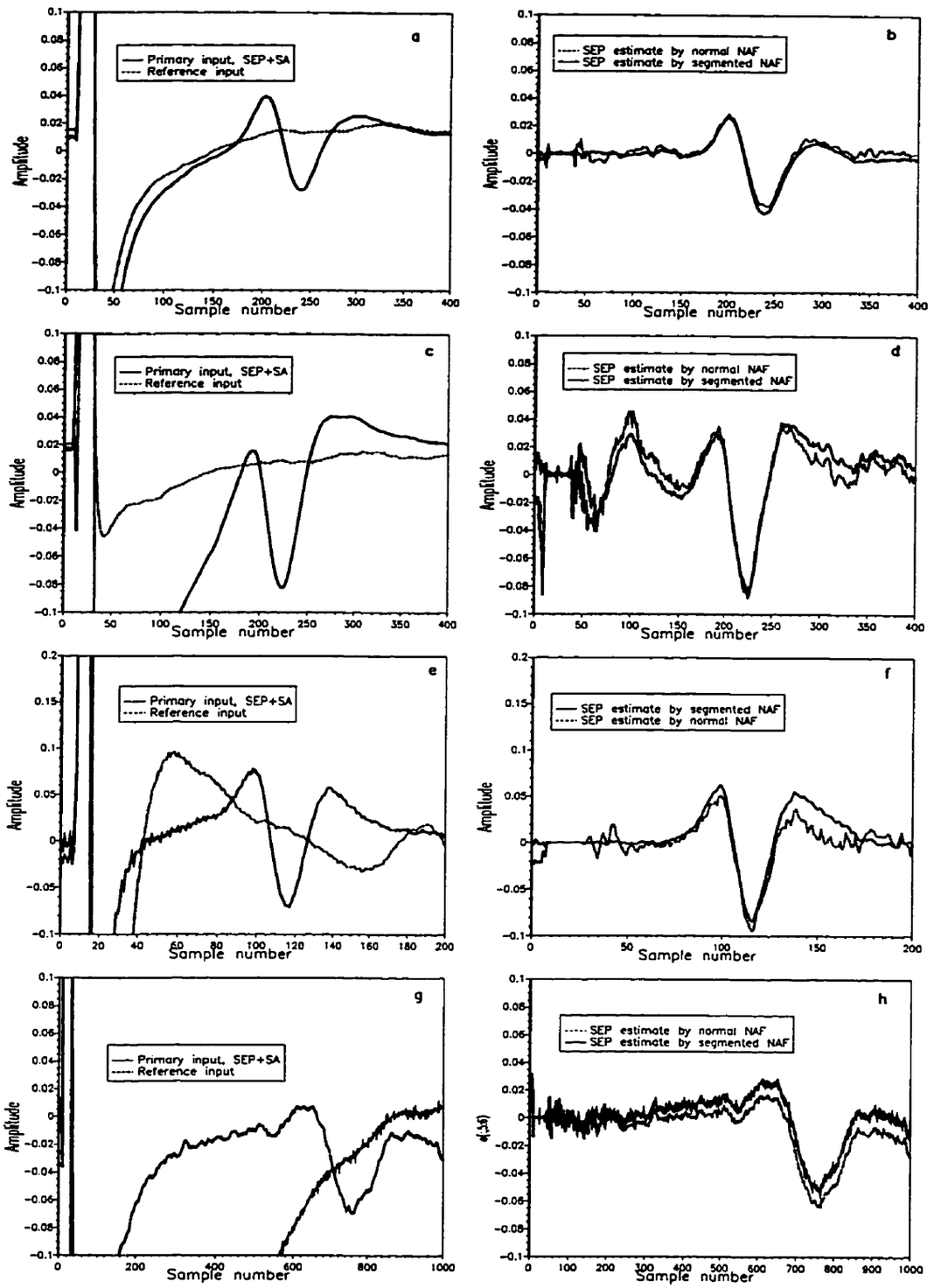

Figure 5.15: ***SEP enhancement by the NAF.***

plot. The reference SA in this case is obtained through subthreshold stimulation. Figure 15d shows the SEP estimates obtained by the normal and segmented NAFs. While both have made substantial improvements, the estimates still contain substantial amounts of SA. This is probably due to the "undermodelling" of the SA system by the NAF either due to a suboptimal filter length or the presence of higher order nonlinear terms. Figure 5.15e depicts the MSEP data acquired from a different subject using Ag-AgCl electrodes. In this Figure, it can be noticed that the tail end of the SA interferes with the MSEP waveform. The reference SA here is once again obtained through subthreshold stimulation. The SEP estimates at the output of the NAFs are shown in Figure 5.15f. The SEP estimate produced by the segmented NAF can be seen to be devoid of most of the interfering SA, while normal NAF can be seen to introduce some distortion in the SEP estimate. This is, as explained before, due to the non-zero correlation between the SEP and the reference SA waveforms. The SA+SSEP composite waveform measured from the lower lumbar region of the spinal cord, which is an ensemble average of 1500 such records, is shown in Figure 5.15g. Once again, it can be seen that the SA tail corrupts the SSEP waveform and that the SSEP waveform has a negative bias. The reference SA in this case is acquired from the second recording channel. The SEP estimate obtained by the segmented NAF, shown in 5.15h, not only seems to reduce most of the SA but also to remove the bias in the SSEP.

In all the results above, it can be observed that the segmented NAF produces a better quality SEP estimate compared to the normal NAF. To emphasize the effect of the NAF filter length (as observed while processing the simulated SEP+SA data), the *in vivo* SEP data shown in Figure 5.15e is analyzed for two different NAF filter lengths. Figures 5.16a and b depict the results of this analysis. In Figure 5.16a, the SEP estimates provided by the normal and segmented NAFs each with a filter length of ten is shown. In Figure 5.16b, the SEP estimates obtained through processing the same primary and reference data by the normal and segmented NAFs of filter length

fifteen. The degradation in the SEP quality at the output of a normal NAF with an increase in its filter length is clear from these plots. The segmented NAF, on the other hand, provides a similar SEP estimate for both the filter lengths. Thus, the segmented adaptation approach is recommended for enhancing the SEP from the SA interference.

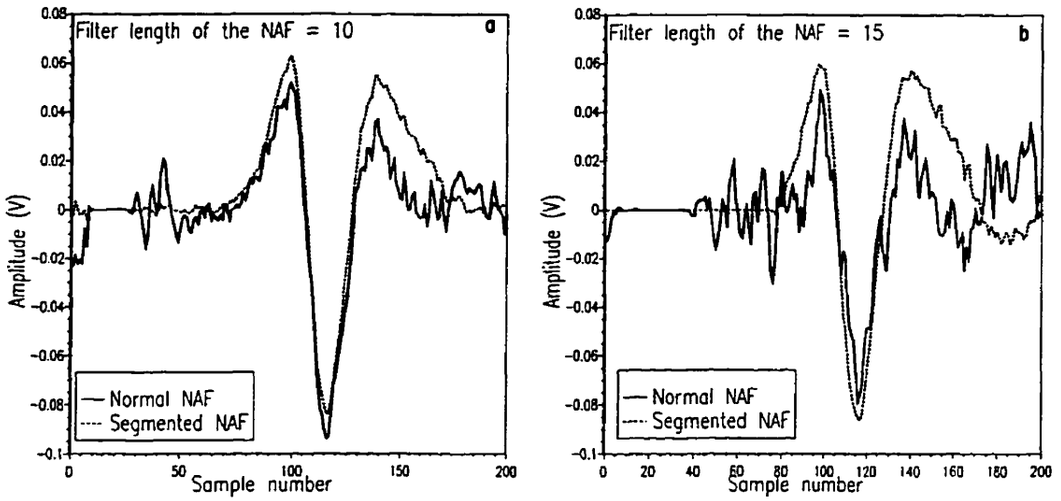

Figure 5.16: ***Effects of the NAF filter length on the enhancement of in vivo SEP data. a) SEP estimates produced by the normal and segmented NAFS with filter lengths of ten and b) SEP estimates provided by the normal and segmented NAFs with filter lengths of fifteen.***

5.5.5 SEP Enhancement in the Presence of Noise

The previous section illustrated the efficacy of the NAF in enhancing the SEP in the presence of the interfering SA using ensemble averaged SEP+SA composite waveforms. In most SEP processing applications ensemble averaging will be required, and thus it is only appropriate to use the NAF to reduce the SA after the averaging procedure. In some case, it may be desirable to reduce the SA from record to record and in such tests, the ANR will be lower and thus results in poorer SA reduction by the NAF. To investigate the performance of the NAF in such situations, raw SEP data is processed using the NAF and the results are displayed in Figure 5.17. Figure

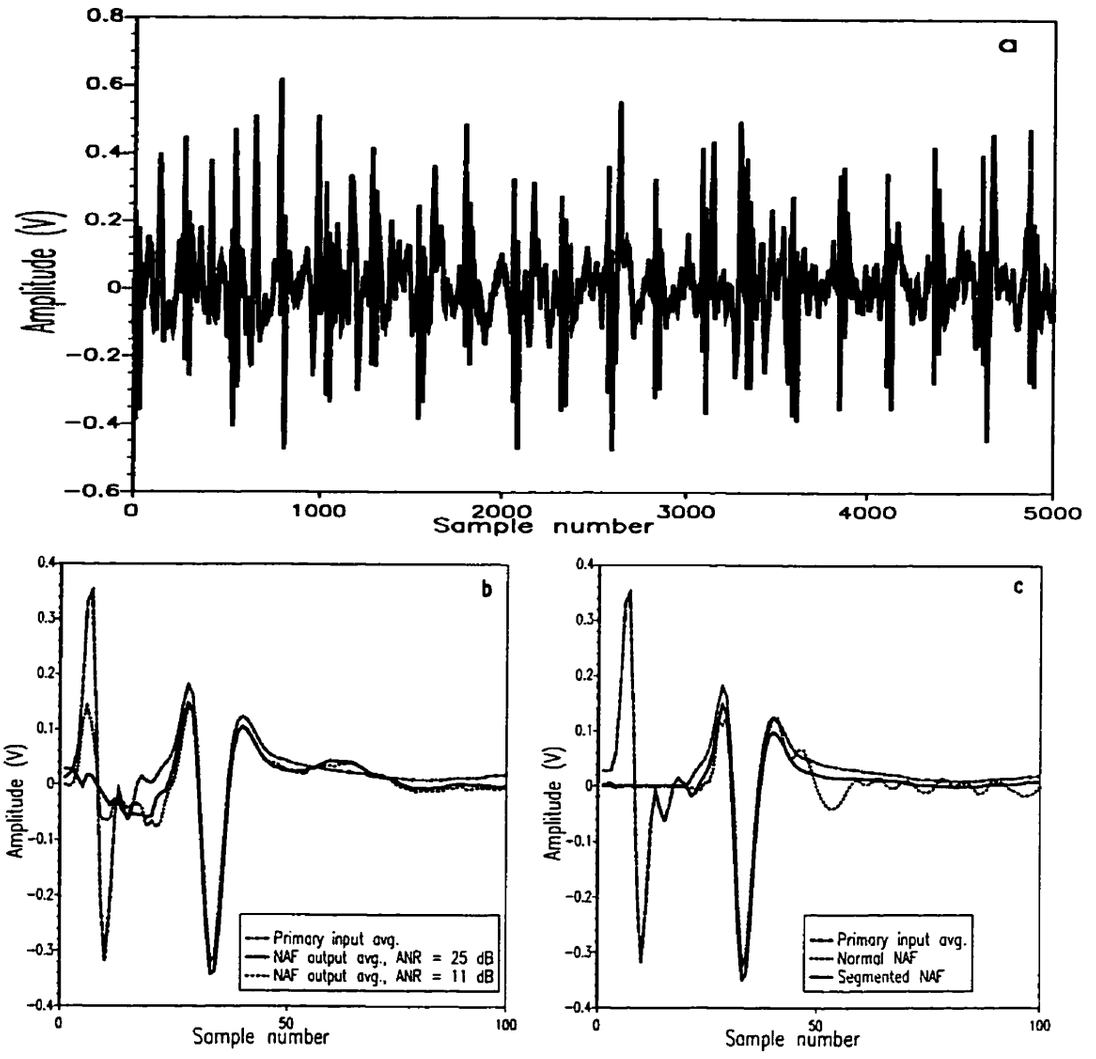

Figure 5.17: ***Performance of the NAF in enhancing the SEP from the corrupting SA in the presence of background noise.***

5.17a shows the raw MSEP data of ANR 11dB acquired from one of the subjects using Ag-AgCl electrodes which served as the primary input to a five filter length NAF. A smaller filter length is chosen as the time separation between the SEP and SA was small. The reference input is obtained through subthreshold stimulation of the median nerve. The enhanced SEP which is an ensemble average of 50 records at the output of the NAF is shown in Figure 5.17b. For the sake of comparison, the averaged SEP of 50 records in the primary input and the averaged SEP of 50 records at the output of an NAF employing a cleaner reference input, are also shown in this picture. Once again, it can be noticed that a cleaner reference input results in better SA cancellation. Figure 5.17c compares the outputs of the normal NAF and the segmented NAF, which used ensemble averaged SEP+SA composites for their adaptation. The segmented NAF can be seen to abolish the SA thereby enhancing the SEP and the SEP distortion due to normal NAF operation can also be observed.

5.6 Conclusions

In most SEP measurements, the stimulus evoked artifact waveform is a very bothersome interference. Since this artifact occurs in synchrony with the SEP, ensemble averaging cannot reduce the artifact. Conventional techniques for SA reduction rely on some form of blanking circuits which blank the input during the SA phase. However, these blanking circuits are ineffective when the SA waveform extends into the SEP waveform leaving the SEP waveform distorted. Hence effective signal processing methods are desired which can reduce the stimulus artifact while preserving the properties of the SEP. This chapter investigated the applicability of nonlinear adaptive filters, based on second order truncated Volterra series expansion, for SA reduction. On the basis of simulation and experimental results presented in this chapter, the following conclusions can be drawn.

- **The SA generation system is nonlinear.** The nonlinearity in the SA generation system arises from the nonlinear voltage/current characteristics at the stimulating electrodes at high current densities. The voltage/current curves given in Figure 5.1 clearly depict this nonlinearity. Due to this nonlinear nature of the SA, nonlinear SA cancellation schemes are more effective than the linear schemes. The validity of this point is also strengthened by the results shown in Figures 5.13 a-h where nonlinear filters handsomely outperformed their linear counterparts.

- **Nonlinear Volterra adaptive filters are well suited for SA cancellation.** Conventional nonlinear system identification techniques require the response of the nonlinear system to a white noise input. With the stimulus artifact, however, the input is the stimulus voltage pulse train. Adaptive Volterra filters model the underlying nonlinear system without imposing any restrictions on the nature of the input data and hence are more suitable for the SA cancellation.

- **RLS based NAFs significantly outperform the LMS based NAFs.** LMS based NAFs are very slow in their convergence due to the large eigenvalue spread associated with the data from a nonlinear system. Also, the performance achieved by the LMS based NAFs is much lower than the RLS based NAFs (Appendix V offers a detailed analysis and relevant results). RLS based NAFs, however, are more computationally involved than the LMS based NAFs thus rendering them close to impractical in real time SA cancellation.

- **The performance of the NAF is a function of the ANR.** Due to the second order terms involved in the structure of the NAF, the noise components that are present in the reference input of the NAF affect the performance of the NAF. Ensemble averaging increases the effective ANR giving an improved artifact rejection. Note that the ensemble averaging procedure need be performed only on the reference input. This point is very important from a multi-stage

SEP enhancement point of view. As discussed in the previous chapter, for efficient MEI reduction, there should be no other correlated components. Thus the SA components should be reduced from both the primary and reference inputs to the CRANC filter while still preserving the MEI characteristics. This can be achieved by first collecting the SA waveform using subthreshold stimulation and ensemble averaging it to reduce the background noise components. This averaged SA can then be used to diminish the SA components in the primary and reference MEI inputs to the CRANC filter.

- **The presence of the SEP in the primary input of the NAF also affects its performance.** This is a very crucial point and its importance cannot be overstressed. Due to finite correlation between the SEP and SA waveforms, the weight adaptation of the NAF is invariably affected by the SEP components in its primary input and consequently SEP distortion results. An attractive way of overcoming this problem is to let the NAF adapt only during the SA phase. In this way the adaptation routine is unaffected by the SEP components and is shown to achieve good results.

Chapter 6

ECG Reduction

Summary

Various signal processing techniques for ECG reduction are investigated in this chapter. Each of these techniques is analyzed for its performance, computational complexity, and robustness to the presence of SEP and extraneous noise sources. Of all the techniques scrutinized, the Adaptive Template Subtraction (ATS) method is shown to offer the best package in terms of all the abovementioned criteria. Detailed experimental analysis of the ATS technique is conducted along with other techniques and the analysis clearly demonstrates the superiority of the ATS technique.

6.1 Techniques for ECG Reduction

As mentioned in Chapter 2, there are several ECG reduction techniques and these are discussed in detail below.

In the **Clipping** method, the ECG waveform is clipped at a certain voltage level. This technique is more important in increasing the dynamic range of the digitized

SSEP waveform than ECG reduction per se. With unclipped ECG, the input amplification factor is chosen in such a way that the ECG does not overload the amplifier. During the A/D conversion procedure, this will result in lower SSEP resolution as the smaller amplitude values of the SSEP fall into the lower significant bits. The amplification factor can be increased with clipped ECG and therefore a better SSEP resolution is obtained. With respect to ECG cancellation, the clipping procedure does not completely remove the ECG, and the residual component may still affect the SNR of the SSEP.

In the **Gating** method, all the voltage levels above a certain threshold are set to zero. In this way,the problem of ECG remnants can be overcome as the predominant ECG components are now "gated" to zero. A potential problem with this technique is the SSEP loss if the SSEP occurs in the same time frame as the ECG. However, since the probability of an ECG occurence in an SSEP record is quite low, this problem is not significant when a large number of SSEP records are averaged. A relevant point here is that the analog implementations of the gating procedure may result in switching transients which further deteriorate the SSEP SNR.

All the methods described before work on continuous raw data. In SSEP recordings, where a large number of SSEP records are collected, the continuous data collection procedure leads to huge amounts of data. A plausible way to overcome this problem is to program the A/D conversion scheme in such a way that only a prescribed number of samples are converted with each stimulus pulse. This procedure will result in unwanted data between the stimuli being discarded and thus lead to efficient SSEP data representation. In case of an ECG occurence (which can be determined using a threshold voltage level), that particular record is discarded. This **"Chop and discard routine"** thus results in efficient elimination of the ill-effects of the ECG. Once again, since the probability of ECG occurence in an SSEP record is small, only a few SSEP records need to be discarded. A disadvantage with this method is the special programming of the A/D converter required to collect the SSEP

data.

Adaptive filters offer an attractive solution to ECG cancellation as they do not require any ***a priori*** information about the ECG. The adaptive filters, however, do require an additional reference ECG input and they often come with extra computational baggage and implementing these filters in realtime often requires high speed DSP boards. Perhaps the most crucial factor in determining the ECG cancellation performance of an ANC is the placement of the reference electrode pair. The placement is constrained by the following two factors:

1. The reference electrode pair must be placed away from the SSEP source. As mentioned at several points during this thesis, to avoid risk of any potential SSEP distortion the reference input to the ANC should be devoid of any trace of SSEP components. Thus the reference electrode pair must be placed in such a way that no SSEP component is recorded while still obtaining a correlated ECG component. One way to obtain this reference signal is to place an electrode on either side of the spine equidistant from the spinal column [9]. Assuming uniform tissue properties and SSEP conduction along the spinal cord, this will result in zero SSEP component when a differential signal is obtained using the above electrode pair. In reality, it is difficult to determine the exact location on either side of the spinal cord such that the differential SSEP component is zero.

2. The reference electrode pair must be placed in such a way that it does not tap other correlated interferences. These interferences include MEI and the SA (assuming that the 60-Hz interference does not pose a problem). Any presence of these interferences in **both** primary and reference channels will result in poor ECG reduction results.

A very attractive alternative for obtaining a reference ECG input is to collect the ECG signal prior to the stimulation . This eliminates the possibility of the SSEP and SA "crosstalk" into the reference input. In offline ECG cancellation scenarios,

this ECG reference input can be ensemble averaged to diminish the background noise level and can be stored in a separate data file as a template. This ECG template can be employed later to cancel the ECG in the SSEP data that is obtained using the same electrode pair in two ways: a) plain **template subtraction**, which assumes that the underlying ECG waveform is time-invariant or b) **Adaptive Template Subtraction (ATS)**, where an adaptive filter is utilized to iteratively reduce the ECG components in the SSEP data. This adaptive nature is desirable as the ECG, in addition to being quasi-periodic, is significantly non-stationary. In realtime ECG cancellation scenarios, these approaches can still be employed by storing an averaged ECG template in a buffer and utilizing this template to cancel the ECG in the SSEP data as it occurs. Of course this requires additional software programs to synchronize the reference ECG template with the primary ECG and then implement the adaptive cancellation routine.

Given these methods and issues, an attempt is made in this chapter to assess the performance of each of these techniques and to determine which technique is most suitable for high performance and computationally efficient ECG cancellation under different operating conditions.

6.2 Experimental Results

6.2.1 ECG Reduction in the Absence of an SSEP

The first set of experimental results concentrate on continuous ECG data cancellation. For these data, no stimulus was given to the subjects and hence these results demonstrate the ECG cancellation capabilities of the clipping, gating, ANC and template subtraction procedures in the absence of an SSEP. One minute of ECG data was collected for each of these subjects at a sampling rate of 10 KHz, digitized and stored on a 486 computer and processed offline. The threshold level for the clipping

and gating procedures was the maximum background noise voltage level estimated between the ECG occurences. The reference input for the ANC was acquired from the chest with the following rationale: a) at the chest region, the magnitude of the ECG is many times larger than either the SSEP or the SA and hence their influence on ECG cancellation is insignificant and b) since the reference channel is now far away from the primary channel (which is placed at the lower lumbar level of the spinal cord), the possibility of the presence of correlated MEI components in both the primary and the reference is greatly reduced. Note that, due to the above placement, there is always an ECG propagation delay between the primary and reference ECG waveforms. In all the ensuing ECG reduction results involving the ANC, this delay effect is compensated first by estimating the propagation delay through the cross-correlation function between the primary and reference ECG waveforms and then appropriately shifting the reference ECG. The ECG template required for the template subtraction and ATS methods was obtained by ensemble averaging the ECG input. The amount of ECG cancellation achieved by each of these techniques was quantified using the following measure, γ_{ECG},

$$\gamma_{ECG} = \frac{\sigma^2_{prim}}{\sigma^2_{res}} \tag{6.1}$$

where σ^2_{prim} and σ^2_{res} are respectively the primary and residual ECG variances computed during a single ECG interval. The results obtained from different subjects are displayed graphically in Figures 6.1 and 6.2. In Figure 6.1, the performances of the template subtraction, ATS and ANC are compared. The LMS algorithm was used to update the filter weights for the ANC and a delay of half the filter length was incorporated in the primary input of the ANC to compensate for any noncausality. The convergence parameter required for the LMS algorithm was chosen one-tenth of its upper bound [70]. For the template subtraction procedure, the averaged ECG template which was collected earlier was aligned via crosscorrelation with each of the ECG waveforms in the primary input and then subtracted. For the ATS, the same ECG template was given to a ten tap adaptive FIR filter as a reference input. Figure

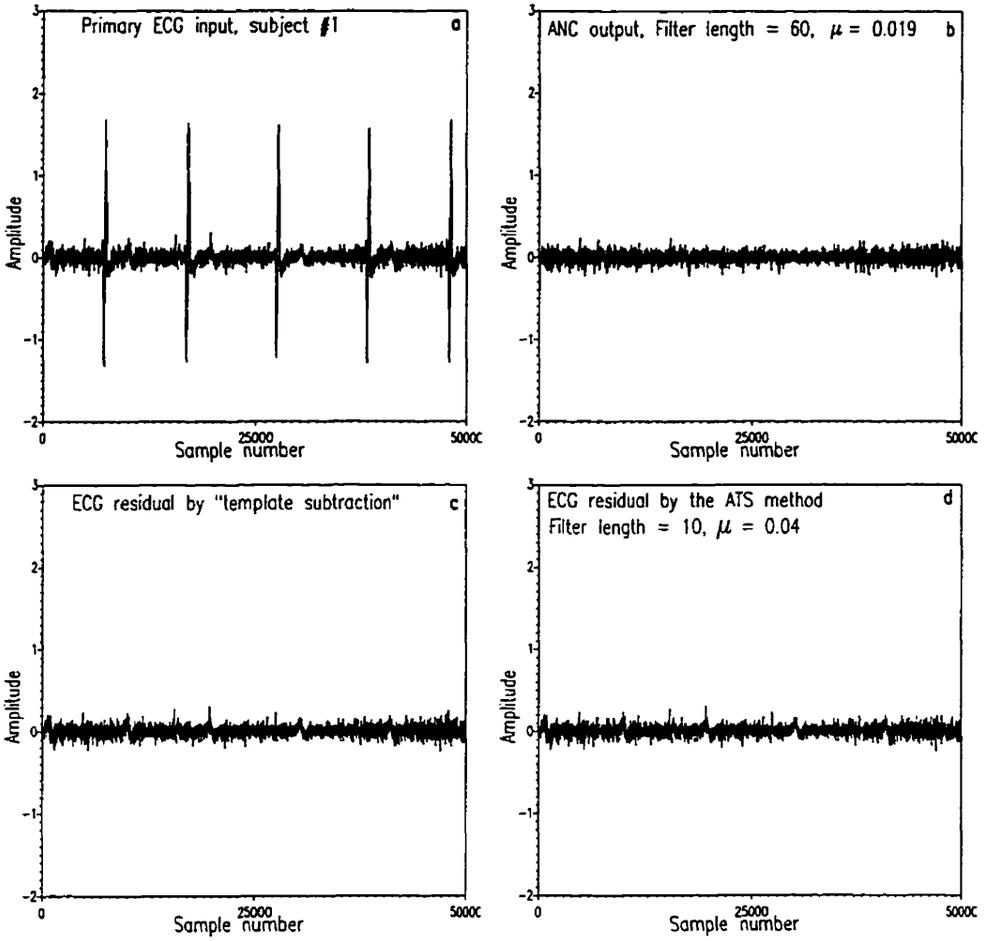

Figure 6.1: ***ECG cancellation by ANC, template subtraction and ATS. a) Primary ECG input, b) residual ECG using ANC method, c) residual ECG using template subtraction, and d) residual ECG using ATS technique.***

6.1a shows the raw ECG data collected from one of the subjects. The output of a sixty tap linear FIR ANC filter with the chest ECG as the reference input and driven by the LMS algorithm is depicted in Figure 6.1b. It can be seen from this picture, that the ANC has been quite successful in reducing the ECG down to the background noise level. Figure 6.1c displays the residual ECG for the same primary input using the template subtraction method and ECG cancellation similar to Fig 6.1b can be observed. The output of the ATS method, where a ten tap adaptive filter

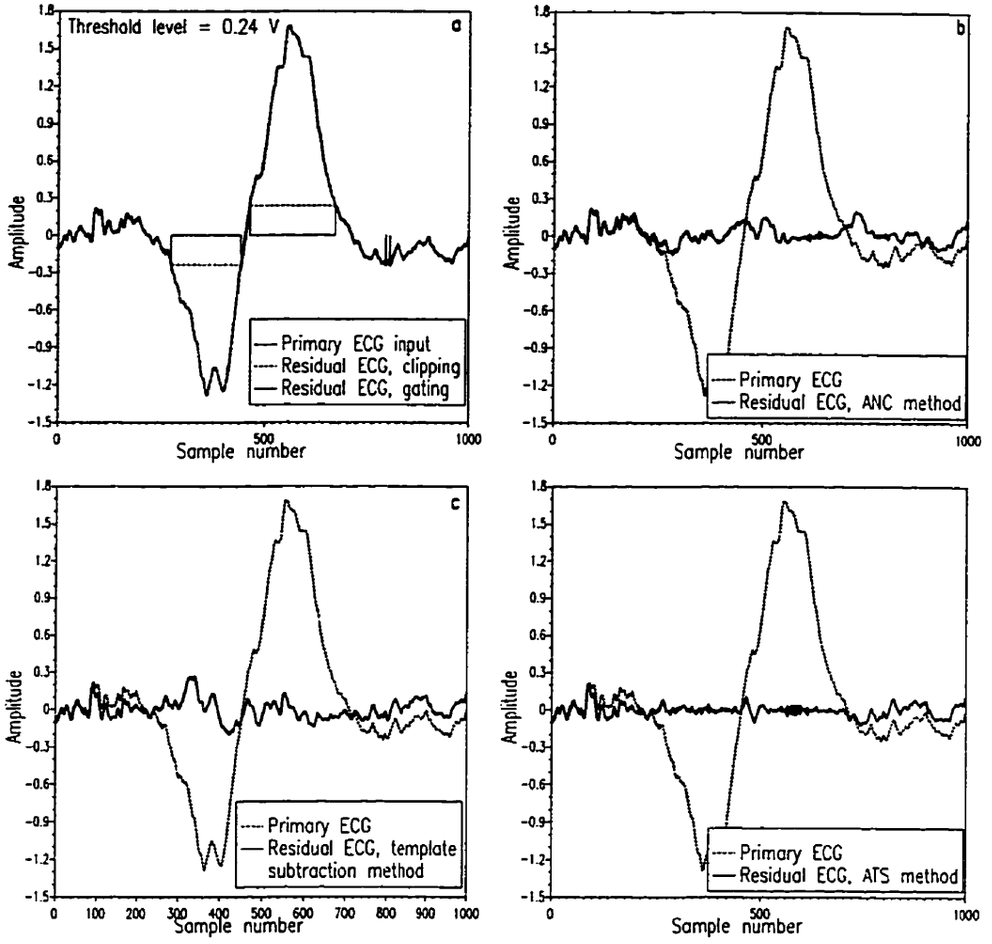

Figure 6.2: ***Qualitative comparison of clipping, gating, ANC, ATS and template subtraction methods. a) Primary ECG segment along with residual ECG waveforms produced by gating and clipping methods, b), c) and d) Primary ECG and ECG remnants by ANC, template subtraction and ATS respectively.***

was utilized to cancel the primary ECG using the same aligned ECG template, is displayed in Figure 6.1d. Once again, good ECG cancellation can be observed in this figure.

To obtain a clearer picture of the performance of these techniques, the residual ECG outputs produced by clipping, gating, template subtraction, ANC and ATS procedures during a single ECG interval are shown in Figures 6.2a-d. Comparing these plots, it can be observed that gating, template subtraction, ATS and ANC

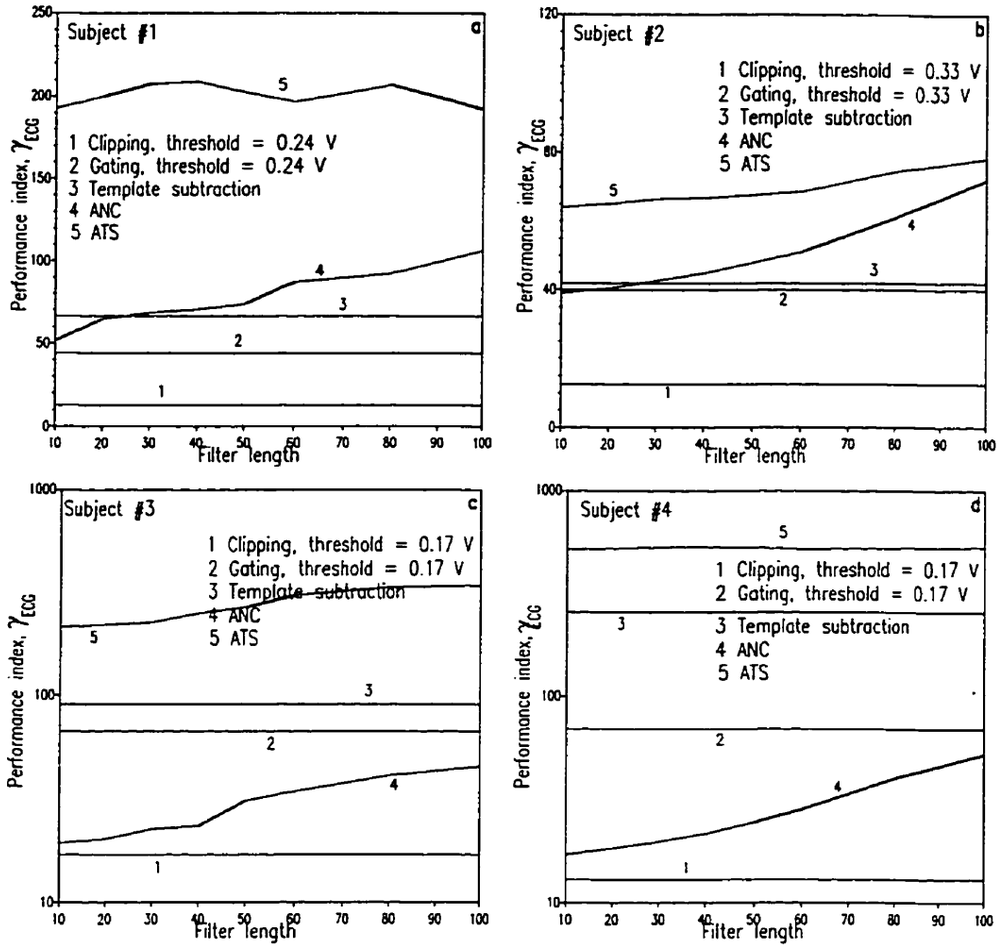

Figure 6.3: ***Absolute performance of different ECG reduction techniques.***

procedures give superior ECG cancellation results compared to the clipping method and that the ATS method appears to provide the best ECG cancellation.

In order to compare the absolute performance of each of these methods, the performance index given by Eq. 6.1 was computed for ECG data collected from several subjects and the results are depicted in Figure 6.3. The primary and residual ECG variances required for measuring the performance index, γ_{ECG} were calculated using the last ECG record in the raw data. For the ANC method, the performance index was calculated for different filter lengths, with a delay of half the filter length introduced in the primary input to compensate for noncausality. Several points can be

drawn from this figure:

- As expected, the clipping method displays the worst performance index for all the subjects.

- The performance of the ANC monotonically increases with the filter order and does not appear to saturate even for 100 filter taps for all the subjects. This indicates that large filter orders are often required for the ANC implementation for good ECG cancellation results.

- The template subtraction method outperforms the gating procedure for all the subjects and is better than the ANC for subjects #3 and #4. The inferior performance of the ANC in these cases is due to a small filter order which is relatively ineffective in modelling the transfer function function between the primary ECG input and the reference ECG input, hence resulting in poorer performance.

- The adaptive template subtraction method offers the best ECG cancellation performance among all the techniques for all the subjects. The significant improvement in employing an adaptive subtraction approach rather than the fixed template subtraction method is obvious for each of these subjects. These results back the assertion that the ECG possesses certain time varying features and hence the need for adaptive filters. Interestingly, for most of the subjects the performance of this method is relatively constant for increasing filter orders. Thus lower filter orders can be used which makes this method computationally appealing.

- The performance index values show variability across the subjects. This is to be expected because a) the transfer function between the primary and reference inputs is different for different subjects and hence the ANC displays different performance values, b) the performance index given by Eq. 6.1 is sensitive to the

ECG interval over which the variances are computed, and c) the performance indices of the clipping and gating procedures are sensitive to the threshold value also. The last two points are addressed next.

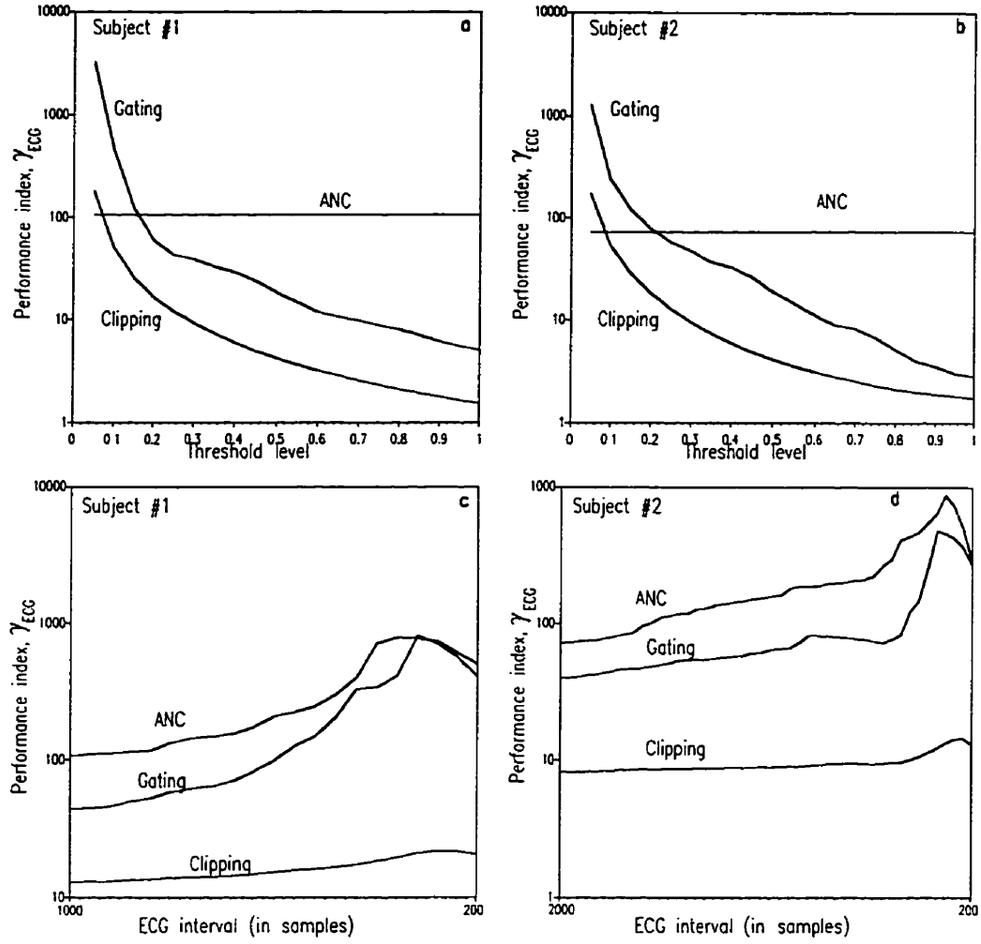

Figure 6.4: ***Effect of threshold and interval length on the computation of performance indices.***

Figure 6.4 depicts the effect of the selection of the threshold value and ECG interval on the computation of the performance index, γ_{ECG}. Figure 6.4 a and b show the performance index for decreasing threshold levels. As expected, the performance monotonically drops as the threshold value increases. The performance of the ANC (also template subtraction and ATS) is constant as it is independent of the threshold

value. It can be observed that by lowering the threshold value, it is possible for the clipping procedure to provide better performance than the ANC. Figures 6.4 c and d graph the performance index with respect to the ECG measurement interval. To calculate the performance for different ECG interval lengths, the initial ECG waveform (for example, Fig 6.2a) window is gradually shrunk symmetrically from either end in steps of 50 samples and the performance index is computed. From Figures 6.4 c and d we can see that all the performance indices are sensitive to the computation interval, more so in the case of ANC and gating. The same is true for performance indices resulting from template subtraction and ATS methods. Thus the ECG interval is a crucial parameter in calculating the performance index. Note that if the computation interval is confined to the time period where the ECG is gated to zero, the performance index of the gating procedure returns a value of infinity. Hence the ECG interval should be judiciously chosen such that a fair comparison between different methods can be undertaken. In general a window adequately covering the ECG complex is deemed sufficient.

6.2.2 ECG Reduction in SSEP data

All of the results discussed so far were obtained through processing continuous ECG data in the absence of an SSEP. As mentioned before, continuous data collection for SSEP measurements can be quite taxing on the computer storage requirements and hence the data needs to be "chopped". This is especially true if the stimulus rate is lower and a large number of SSEP records need to be collected. In this section, the "chopped" SSEP records which are contaminated by the ECG interference are analyzed. 1024 data samples, sampled at a rate of 20 KHz, were collected from the primary and reference channels with each stimulus pulse (the stimulus period was 391.7 ms). These data samples constituted one SSEP record, and 1000 such records were collected and stored on the computer. A computer program was written to identify the primary and reference records which contain traces of the ECG. These

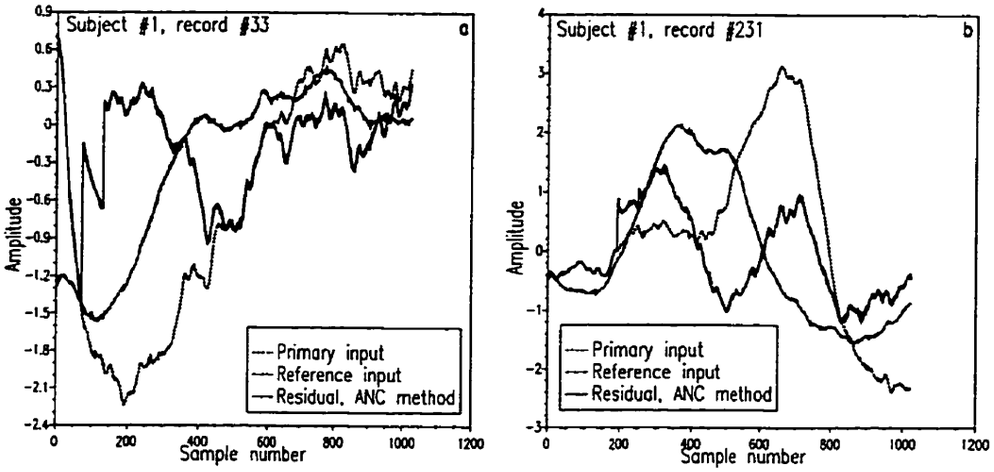

Figure 6.5: ***Performance of ANC with "chopped" SSEP data. Two SSEP records contaminated by the ECG along with the residual ECG produced by a forty tap ANC filter are shown here.***

records were then input to the ANC filter for cancellation. The filter length of the ANC was fixed at forty. Even though it was shown in the previous section that the ANC requires large filter lengths for good ECG cancellation results, filter lengths more than forty were not implemented for the fear of introducing SSEP distortion, as discussed in Chapter 5, Section 5.4.4. Figures 6.5 a and b display two primary SSEP records contaminated by the ECG interference along with the corresponding reference ECG inputs obtained from the chest. The ECG residuals produced by the ANC operation are also shown in this figure. While the ANC has removed part of the ECG interference in both the records, there is still a substantial ECG remnant. This is in contrast to the performance of the ANC in reducing continuous ECG (shown in Figure 6.1b). This is due to a combination of two factors: a) lower filter length - it was discussed in the previous section that large filter lengths are required by the ANC for significant ECG reduction, and b) limited ECG information, as the chopping procedure results in only a part of the ECG segment being acquired. Thus the performance of an ANC will be inferior with "chopped" data compared to continuous ECG cancellation.

The application of template subtraction and ATS methods of ECG reduction to chopped data poses a new challenge. Since our objective now is to reduce that segment of the ECG waveform which contaminates the SSEP record (rather than the whole ECG waveform as in continuous ECG cancellation), these two techniques have to be modified. Essentially, given an ECG template and an SSEP record contaminated with an ECG segment, the template subtraction and ATS techniques have to first extract the contaminating ECG segment from the ECG template and then perform the cancellation operation. This can be done by carrying out the following procedure:

1. take a contiguous ECG segment (ECG window) of 1024 samples from the start of the ECG template.

2. calculate the mean-squared error between this ECG segment and the SSEP record and store the mean-squared error value along with the window starting point.

3. move the ECG window by one sample and repeat the above step. Perform this procedure until the whole ECG template is exhausted.

4. Find the minimum of the stored mean-squared error values which points to the "matching" ECG template.

Figures 6.6 a-e demonstrate the ECG reduction results obtained through the template subtraction and ATS methods for the "chopped" SSEP data. The ECG template, which was obtained prior to the stimulation and ensemble averaged over ten ECG records, is shown in Figure 6.6a. From this ECG template, the ECG segment which best matches the interfering ECG segment in a SSEP record is extracted following the abovementioned procedure. This is shown in Figures 6.6 b-e which depict the contaminated SSEP records along with the ECG segment extracted from the ECG template. It can be observed that the extracted ECG segment matches the interfering ECG waveform quite nicely in both the SSEP records. Figures 6.6b and 6.6d display

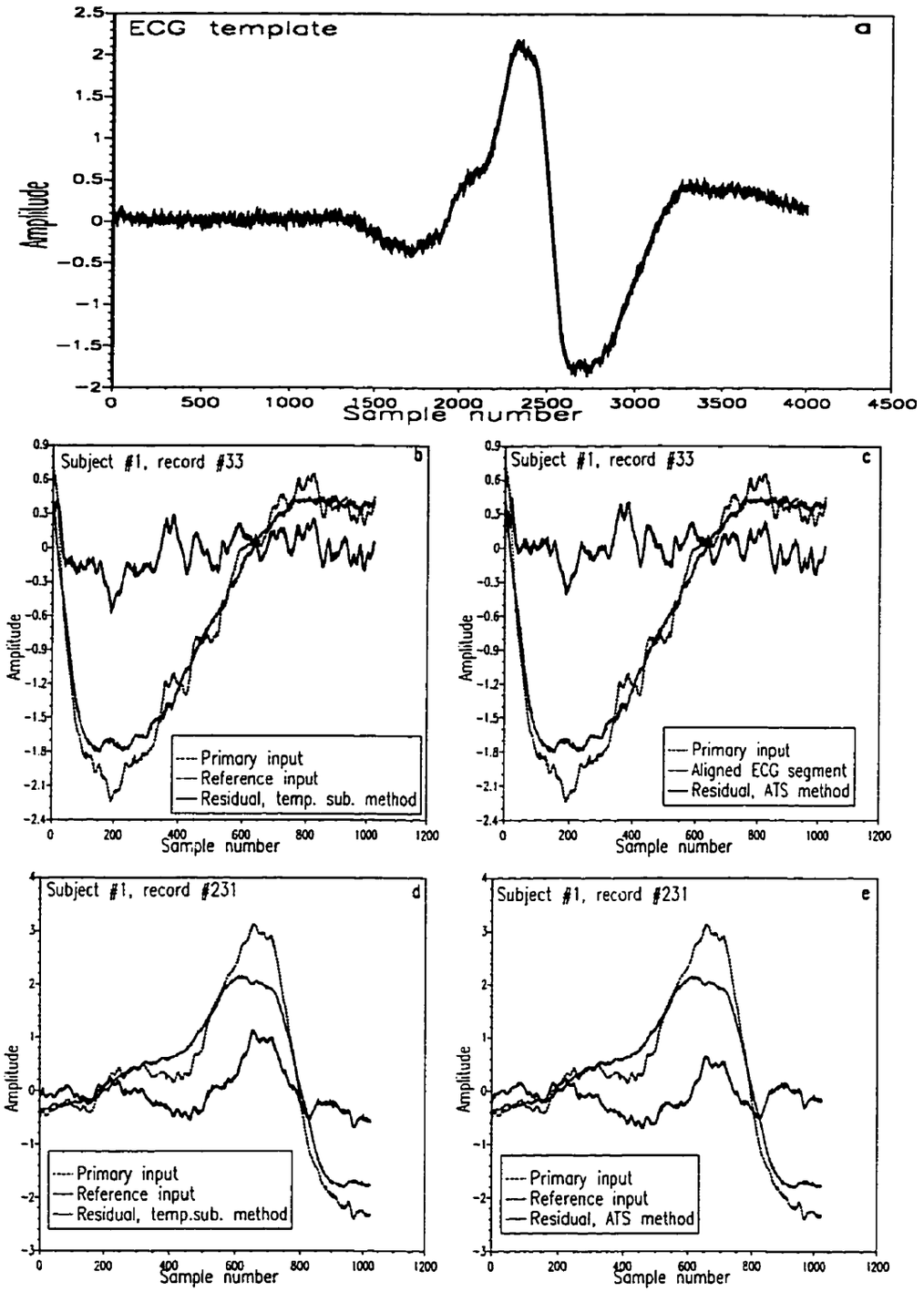

Figure 6.6: ***Template subtraction and ATS methods with "chopped" SSEP records. a) ECG template, b) & d) SSEP records along with the extracted ECG segment and the ECG residual produced by the template subtraction method, and c) & e) ECG residuals by the ATS method for the same SSEP records.***

the performance of the template subtraction method qualitatively. Substantial ECG reduction is evident in these figures especially when compared to the ANC cancellation performance shown in Figures 6.5 a and b. Figures 6.6c and 6.6e show the ECG reduction results using the ATS method. Here the matching ECG segment extracted from the ECG template is given to a twenty tap adaptive filter driven by the LMS algorithm. Once again, good ECG cancellation results are apparent and are better than both template subtraction and ANC procedures.

To further demonstrate the performance of these techniques, the improvement in the quality of the SSEP at the output of each of the ANC, template subtraction and ATS procedures is compared and these results are shown in Figure 6.7. Figure 6.7a displays the SSEP record which was ensemble averaged over 1000 records (assumed as the true underlying SSEP waveform) along with the ensemble average of 100 SSEP records contaminated by the ECG. It is obvious from this figure that the ECG interference completely obscures the SSEP information. The ensemble averaged SSEP estimate at the output of the ANC is shown in Figure 6.7b. While the ANC is successful in partly removing the interfering ECG, there is still a substantial ECG "left-over" and consequently the SSEP estimate is of poor quality. The results using the template subtraction method is shown in Figure 6.7c. Here we can see that much of the ECG interference has been reduced and the SSEP estimate resembles the underlying SSEP waveform. Finally, the SSEP estimate produced by the ATS method is shown in Figure 6.7d where an SSEP estimate "closest" to the underlying SSEP waveform can be observed.

The "closeness" of each of these SSEP estimates to the true SSEP waveform is quantified using the following normalized mean squared error measure,

$$\rho_{ECG} = \frac{\sum_{k=0}^{L}(s(k) - \hat{s}(k))^2}{\sum_{k=0}^{L} s^2(k)} \tag{6.2}$$

where $s(k)$ is the SSEP waveform and $\hat{s}(k)$ is the SSEP estimate produced by any of

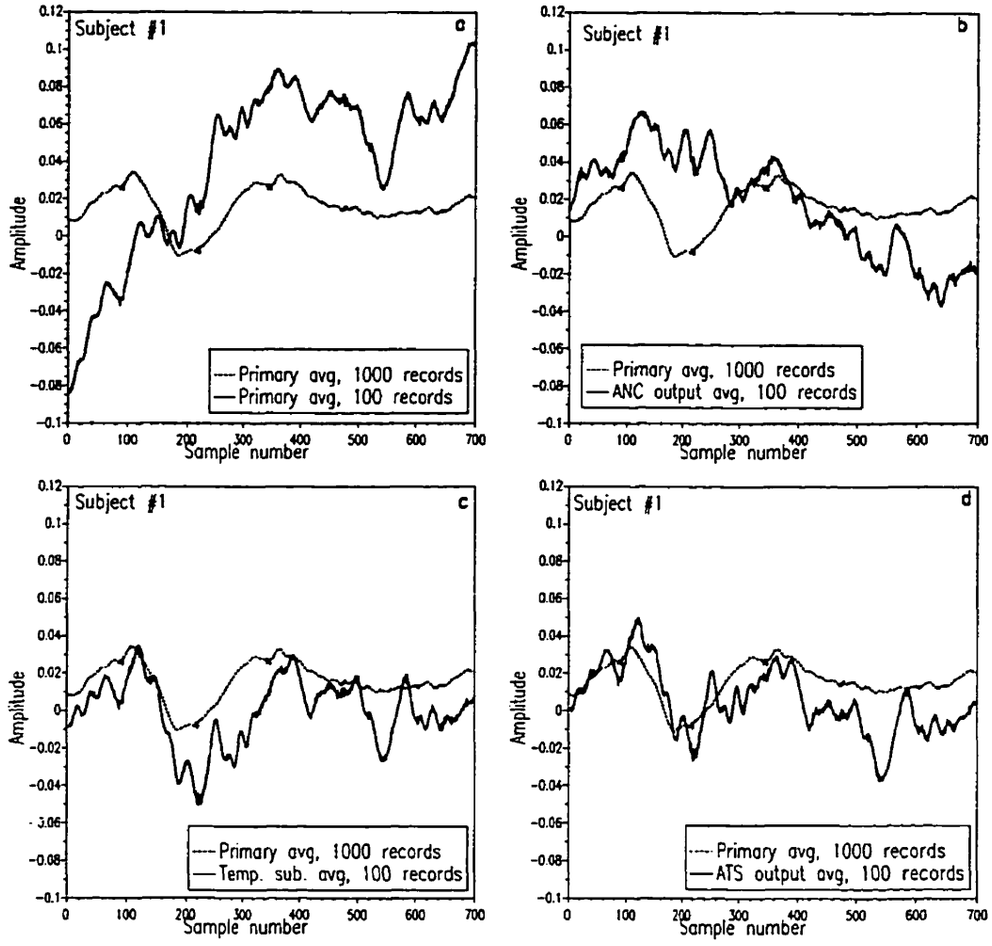

Figure 6.7: ***SSEP estimates by ANC, template subtraction and ATS procedures.***

the abovementioned techniques. Figure 6.8 provides a graphical representation of the ρ_{ECG} measure for two different subjects. From this picture, it is clear that the ATS method procures the best ECG cancellation performance and consequently a better quality SSEP estimate.

6.2.3 A Note on Clipping

So far, the experiments have been confined to collection and processing of unclipped ECG and SSEP data. As mentioned at the beginning of this chapter, it is beneficial

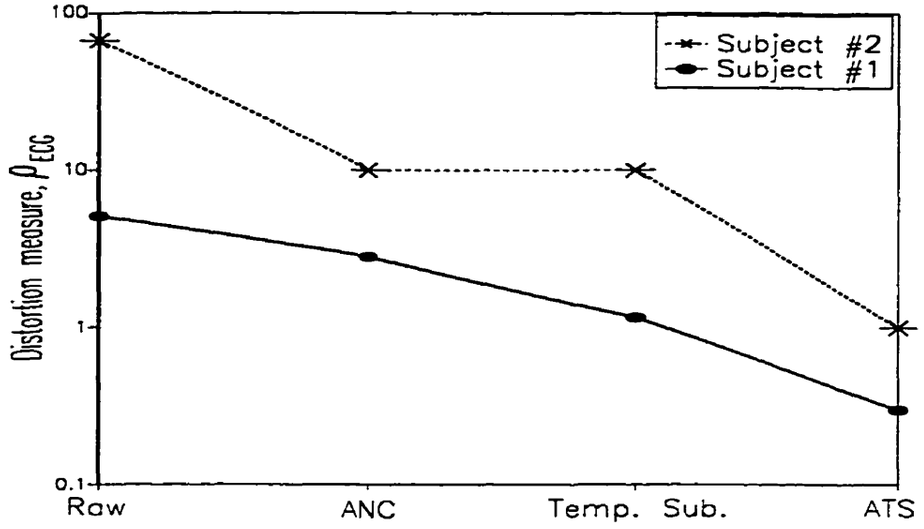

Figure 6.8: ***Distortion measure, ρ_{ECG} for different techniques. Label "Raw" denotes the SSEP estimate obtained without any ECG reduction, "ANC" denotes SSEP estimate at the output of the ANC, "Temp.Sub" refers to the SSEP estimate due to the template subtraction operation and "ATS" refers to the SSEP estimate by the ATS method. All SSEP estimates are ensemble averaged over hundred such records.***

to clip the input data prior to A/D conversion for better SSEP resolution. This is usually achieved by placing back-to-back diodes in the input amplification stage. From the ECG reduction point of view this input clipping operation however manifests itself in the following characteristics:

- Since the clipping operation is nonlinear in nature, the transfer function between the primary and reference ECG waveforms will be nonlinear also. Consequently linear FIR filters, which form the basis for the ANC mode of ECG reduction, will not be effective in reducing the ECG with the clipping circuits in place. Nonlinear Adaptive Filters (NAFs), such as the ones discussed in Chapter 5, may need to be deployed to remove the unwanted ECG interference. The performances of the template subtraction and ATS methods are also similarly affected due to this nonlinearity.

- Since the SSEP and the ECG are additive, the clipping operation results in SSEP distortion when both the SSEP and the ECG occur at the same time. Note that the probability of this event happening is very low (see Appendix VI for probability calculations), and its effect is negligible when an adequate number of SSEP records are ensemble averaged. However, since there is no SSEP information in these ECG contaminated SSEP records, applying ECG reduction techniques to these records will be of very limited use.

The two points discussed above are demonstrated using experimental SSEP data. In Figure 6.9a, a single SSEP record corrupted by the clipped ECG is shown for one of the subjects. The residual ECGs at the outputs of linear and nonlinear ANC schemes for this record are also shown. The linear ANC was realized using a sixty tap FIR filter driven by the LMS algorithm. The nonlinear ANC filter was based on the second order truncated Volterra series as described in Chapter 5. The nonlinear ANC was also driven by the LMS algorithm. From Figure 6.9a, we can see that the clipping mechanism introduces artifacts in the linear ANC output especially when the ECG waveform changes phase. On the other hand, the nonlinear filter appears to handle this well and produce a lower ECG residual. Figures 6.9b-e display the SSEP enhancement results for two different subjects. In each of these plots, the SSEP after an ensemble average of 1000 records, the SSEP after an ensemble average of 100 records, the ensemble average of the same 100 records at the output of the nonlinear ANC and after the "chop-and-discard" method were compared. Let us recall that the "chop-and-discard" method just throws away the ECG contaminated records without any special data processing. From these plots, we see that both the nonlinear ANC and "chop-and-discard" procedure appear to have improved the quality of the SSEP compared to the SSEP which has been averaged using only 100 records. However, the quality of the SSEP estimate obtained through nonlinear ANC is quite similar to that obtained due to "chop-and-discard" method. Thus when working with the clipped SSEP data, the extra computational load carried by the adaptive filtering

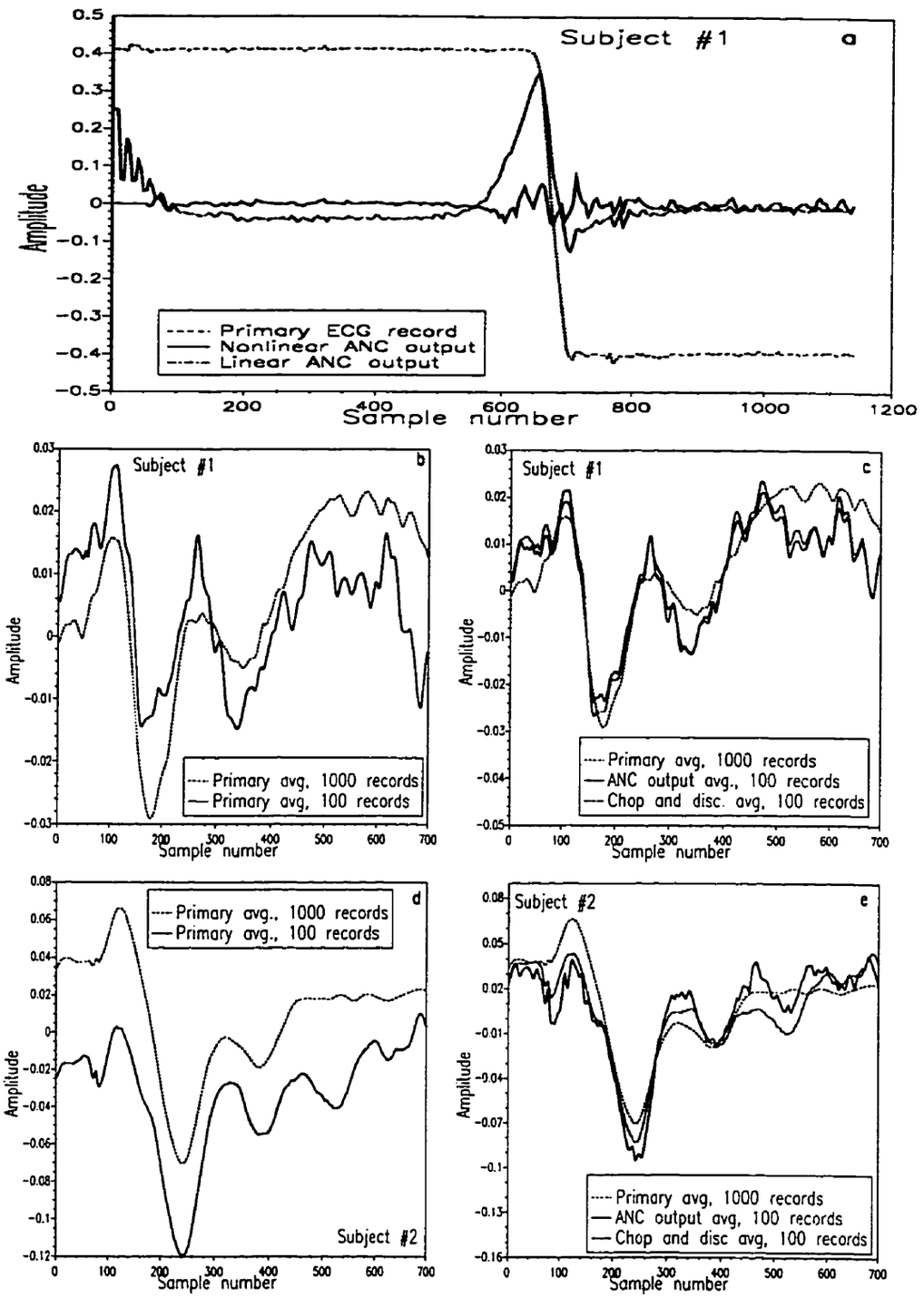

Figure 6.9: ***ECG reduction from SSEP data obtained with clipping diodes in place.***

techniques is not justified.

6.3 Conclusions

In SSEP recording experiments, the larger ECG interference poses a problem. In this chapter several ECG reduction techniques are explored and their performance is compared under different experimental conditions. These techniques are discussed in detail below.

The clipping procedure is the simplest ECG reduction technique. Back-to-Back diodes can be placed in the input path to effectively remove large ECG components. It is also useful in increasing the dynamic range of the SSEP signal and hence is recommended in general situations. However, this technique alone cannot completely solve the ECG problem. The clipping procedure leaves ECG remnants which may still be quite large compared to the SSEP, especially at the higher levels of the spinal cord where the SSEP amplitude is much smaller and the ECG magnitude is larger. Another significant problem with input clipping is the complete loss of the SSEP waveform if it occurs during the clipped time frame of the ECG signal.

The gating procedure offers a relatively effective solution to the ECG problem. In this procedure, all the voltage levels above a certain preset threshold are reset to zero. A subset of the gating procedure, is the "chop and discard" routine where the input data is chopped into SSEP records, and any SSEP record containing a trace of the ECG is discarded. The main problem with this method arises only when more and more SSEP records are corrupted by the ECG and hence are discarded. However in practice, the probability of an ECG occurence in a SSEP record is quite low (around 8-9% for all the subjects participating in this study, see Appendix VI) and hence this method can be very efficient.

With unclipped and continuous ECG data, the ANC produced good results for all the subjects. It is shown that large filter lengths are required for the ANC to provide

good performance indices. Another problem with the ANC is the placement of the reference input. The template subtraction method overcomes this problem of selecting the reference input. By collecting the reference input using the same electrodes as the primary prior to the stimulation procedure, the problem of SSEP, SA and MEI crosstalk is averted. The performance results show that template subtraction alone is on par with the ANC technique with the adaptive template subtraction method outperforming both of them. Thus with continuous unclipped ECG data, adaptive template subtraction is the best method for ECG cancellation. Continuous data collection for SSEP measurements places a strain on the storage requirements. An efficient way of SSEP data storage is to acquire only a time-window after the stimulus pulse. This "chopped" SSEP data collection results in only a part of the ECG being acquired. Thus modifications have to be made to both template subtraction and ATS routines to take this effect into consideration. With these modifications in place, the template subtraction and ATS procedures once again displayed superior ECG cancellation capabilities compared to an ANC.

With the introduction of clipping circuits to increase the range of the SEP, the ANC, template subtraction and ATS methods fail to reduce the ECG. This is because the transfer function between the primary and reference ECGs becomes nonlinear and hence nonlinear ANCs are required to cancel the ECG. Nonlinear ANCs are a magnitude greater than the linear ANCs in terms of computational complexity. Thus, while good SSEP enhancement results may be obtained using the nonlinear ANC procedure, from both the practicality and efficiency point of view, the "chop-and-discard" method appears to be the right technique for ECG reduction. It is also shown that the quality of the SSEP estimates produced by a nonlinear ANC and "chop-and-discard" method are roughly the same.

Thus in essence, it is best to use the adaptive template subtraction method for reducing the ECG interference in unclipped SSEP data and the "chop-and-discard" technique for SSEP data collected with clipping circuits in place.

Chapter 7

Conclusions

7.1 Summary

Somatosensory Evoked Potentials (SEPs) are clinically valuable signals which boast great potential in applications such as spinal cord monitoring during surgery and diagnosis of neuromuscular disorders. The main problem associated with these waveforms when acquired noninvasively is the poor Signal-to-Noise Ratio (SNR). Several noise sources stemming from both biological and nonbiological processes are responsible for this poor SNR. The goal of this thesis was to devise novel signal processing techniques to decrease the influence of these noise sources on the SEP waveform, while still maintaining its essential parameters. To the best of the author's knowledge, this is the first research to investigate the effects and interactions of all the interferences that are encountered in SEP recordings.

The myoelectric interference is the electrical manifestation of the muscular activity. The myoelectric interference is the chief contributor to the poor SNR of the MSEP signal and one of the significant noise sources in the SSEP data collection scenarios. In this thesis, adaptive noise cancellation technique was employed to reduce the myoelectric interference. Two major factors that influence the performance the basic ANC, *viz.* the presence of the uncorrelated noise sources and the signal crosstalk,

were studied both analytically and through simulations. A crosstalk resistant adaptive noise canceller (CRANC), which is a cascade of two ANCs, was then studied in detail. While the CRANC structure is impregnable to crosstalk in the absence of uncorrelated noise sources, it was found that its performance is comparable to an ANC in their presence. Two alternative schemes were developed to mitigate the influence of the uncorrelated noise sources. The first one was the multireference CRANC (MCRANC) structure where a multiple reference ANC was employed in the second stage of the CRANC structure. In addition to "averaging" out the influence of the uncorrelated noise sources, the MCRANC structure also compensates for the jitter in the SEP signal. A significant drawback associated with the MCRANC structure was the requirement of a large number of reference channels in low SEP SNR situations. The second CRANC structure, the ensemble-averaged CRANC (ECRANC), is a more practical solution in this case. The multiple reference ANC structure in the second ANC of the CRANC was replaced by a straight ensemble averager which reduces the computational complexity of the ECRANC significantly. Simulation and experimental results showed that the ECRANC is the CRANC of choice with low SNR SEP data.

The stimulus artifact (SA) is a nonbiological, stimulus dependent interference. Since it occurs in synchrony with the SEP signal, its effect cannot be reduced through plain ensemble averaging. Furthermore, the SA generation mechanism is nonlinear due to the quadratic relationship between the stimulus voltage and the stimulus current. Hence linear signal processing techniques are ineffective in reducing the SA. In this thesis, nonlinear adaptive filter (NAF) structures based on the truncated second order Volterra series were used for the SA reduction. The performance of the NAF was scrutinized under a wide variety of experimental conditions. Several factors which degrade the performance of the NAF such as the suboptimal filter length, the presence of the SEP components, and the background noise were thoroughly investigated. The NAF was shown to perform well with most of the experimental

SEP data. There were some cases where the NAF did not seem to remove most of the SA. This is probably due to "undermodelling" of the SA generation system by the NAF - either due to its suboptimal filter length or due to the presence of higher order nonlinear terms. For these cases, it is worthwhile to investigate the performance of a more generalized nonlinear filter such as the neural network based ANCs.

The ECG forms a significant noise source in SSEP studies. The ECG interference is so large compared to the SSEP signal that clipping circuits may be required in the input to increase the dynamic range of the SSEP waveform. For unclipped ECG data, adaptive noise cancellation technique was once again preferred. By using an ECG template which was obtained prior to the stimulation as the reference input to the ANC, the hazards of the SEP crosstalk and the presence of other correlated interferences was vastly reduced. This method, termed as the adaptive template subtraction (ATS) method, was shown to be the best ECG reduction technique. In addition, the computational complexity of the ATS method is low, making it attractive for real-time ECG reduction scenarios. With clipped ECG data, however, it was found that adaptive noise cancellation technique did not perform any better than just discarding away the ECG contaminated SSEP records. Since the probability of ECG occurance in a SEP record is low, this procedure is preferred with clipping circuits in place.

Several major research contributions are made and these are detailed in the following section.

7.2 Contributions

The major contributions of this research work in reducing different interferences are categorized below:

7.2.1 Myoelectric Interference

- Theoretical development of the Multireference Adaptive Noise Canceller (MRANC).
- Thorough analytical treatment of the Crosstalk Resistant Adaptive Noise Canceller (CRANC) structure backed up by exhaustive simulations.
- Development of two novel variations of the CRANC structure:
    1. Derivation of a constrained CRANC (CCRANC) algorithm which offers computational savings.
    2. A three-sensor Delay and Difference Array Processor (DDAP) and the associated algorithm which exploits the propagation characteristics of the SEP and the MEI.
- Theoretical evaluation of a novel multichannel CRANC (MCRANC) structure, which is robust to the presence of uncorrelated noise, and its validation using simulated and experimental SEP data.
- Development of the Ensemble averaged CRANC (ECRANC) which is effective in low SNR situations.

7.2.2 Stimulus Artifact Reduction

- Application of Nonlinear Adaptive Filters (NAFs) based on second order truncated Volterra series to stimulus artifact cancellation.
- Identification of several issues related to SA cancellation using adaptive filters such as the effect of the SEP in the primary, background noise and filter length and their work-arounds.
- Comparative analysis of LMS and RLS algorithms in SA cancellation under different conditions and recommendations based on this analysis.

7.2.3 ECG reduction

- Comparative analysis of different ECG reduction techniques for different experimental conditions.
- Development of template subtraction and Adaptive Template Subtraction (ATS) methods for ECG reduction with "chopped" unclipped SSEP data.
- Theoretical calculation of the probability of ECG occurence in a SSEP record.
- Investigation of the effects of clipping and recommendations based on this investigation.

7.3 Future Work

This thesis was originally intended to develop a multistage SEP enhancer which will systematically reduce all the interference sources. While this thesis has achieved a substantial mileage in reaching this goal, there are still some issues which need to be further researched. Some of these are

- Development of a SEP enhancement toolbox which amalgamates the best signal processing techniques detailed in this thesis.
- Realtime implementation of some of the signal processing techniques described in this thesis. For example, the comparison of the computational times required by the ECRANC and the B&K signal analyzer to achieve similar SEP quality is an interesting project. Also implementations of the nonlinear LMS algorithm for realtime SA cancellation and of the ATS algorithm for ECG reduction are worth pursuing.
- Alternative signal processing techniques need to be researched for MEI cancellation at high contraction levels. Adaptive filters based on higher order statistics may be quite useful here.

References

[1] O. Agazzi, D.G. Messerschmitt, and D.A Hodges. Nonlinear echo cancellation of data signals. *IEEE trans. on Communications*, 30:2421–2433, 1982.

[2] M.J. Al-Kindi and J. Dunlop. Improved adaptive noise cancellation in the presence of signal leakage on the noise reference channel. *Signal Processing*, 17:241–250, 1989.

[3] M.J. Aminoff. Intraoperative monitoring by evoked potentials for spinal cord surgery: the cons. *Electroencep. clin. Neurophysiol.*, 73:378–380, 1989.

[4] A.T Barker. Determination of the distribution of conduction velocities in human nerve trunks. *Ph.D. Dissertation, Sheffield University, England*, 1974.

[5] S. Benedetto and E. Biglieri. Nonlinear equalization of digital satellite channels. *IEEE J. Selected Areas on Communications*, 1:57–62, 1983.

[6] J. L. Bérubé. Multidimensional signal processing for neuromuscular signals. *Ph.D thesis, University of New Brunswick*, 1995.

[7] J.L. Bérubé, P.A. Parker, and R.N. Scott. Vector velocity filtering for wideband biological signals. *18th CMBEC proceedings, Toronto*, 18:18–19, 1992.

[8] J.L. Bérubé, P.A. Parker, and R.N. Scott. Analysis of a delay and sum beamformer for neuromuscular signals. *19th CMBEC proceedings, Ottawa*, 19:322–323, 1993.

[9] J. Black. A comparison of instrumentation techniques for the suppression of cardiac interference in spinal evoked potential measurements. *B.Sc.E thesis, University of New Brunswick*, 1995.

[10] J. Black, and D.F. Lovely. Reduction of cardiac interference in surface recorded somatosensory evoked potentials using adaptive noise cancellation. *22nd CMBEC proceedings, Charlottetown, PEI*, 22:76-77, 1996.

[11] D. Burke *et al.* Assessment of corticospinal and somatosensory conduction simultaneously during scoliosis surgery. ***Electroencep. clin. Neurophysiol.***, 85:388–396, 1992.

[12] E.G. Dawson *et al* . Spinal cord monitoring: results of the scoliosis research society and the european spnal deformity society survey. ***Spine***, 16:S361–S364, 1991.

[13] J.P.C. de Weerd and W.L.J. Martens. Theory and practice of a a posteriori Wiener filtering of average evoked potentials. ***Biological Cybernetics***, 30:81–94, 1978.

[14] S. Deutsch and E. Micheli-Tzanakou. ***Neuroelectric Systems.*** New York University Press, New York, 1987.

[15] A.M. Dymond. Characteristics of the metal-tissue interface of stimulation electrodes. ***IEEE trans. on BME.***, 23:274–280, 1976.

[16] Babb *et al.* A sample and hold amplifier system for stimulus artifact suppression. ***Electroencep. clin. Neurophysiol.***, 44:315–320, 1971.

[17] K.C. McGill *et al.* On the nature and elimination of stimulus artifact in nerve signals evoked and recorded using surface electrodes. ***IEEE Trans.on BME***, 29:129–137, 1982.

[18] E.R. Ferrara and B. Widrow. Fetal electrocardiogram enhancement by time-sequenced adaptive filtering. ***IEEE trans. on BME.***, 29:458–460, 1982.

[19] J.A. Freeman. An electronic stimulus artifact suppresor. ***Electroencep. clin. Neurophysiol.***, 31:170–172, 1971.

[20] M. Gravenstien, F. Sasse, and K. Hogan. Effects of hypocapnea on canine spinal, subcortical, and cortical somatosensory evoked potentials during isoflourane anaesthesia. ***Journal of Clinical Monitoring***, 8:126–130, 1992.

[21] B.L. Grundy, P.T. Procopio, J.R. Boston, and E. Doyle. Sensory evoked potentials for intraoperative monitoring. ***Proceedings of IEEE conference on engineering in health care***, pages 2.14.1–2.14.3, 1982.

[22] S. Harrison. Adaptive noise cancelling applied to the recording of surface spinal somatosensory evoked potentials. ***M.Sc.E thesis, University of New Brunswick***, 1993.

[23] S. Haykin. ***Adaptive Filter Theory.*** Prentice Hall Publishing Co., Englewood Cliffs, New Jersey, 1991.

[24] A. Javed, B.A. Syrett, and P.A. Goud. Intermodulation distortion analysis of reflection type impatt amplifiers using Volterra series representation. *IEEE trans. on Microwave Theory and Techniques*, 25:729–733, 1977.

[25] C. Jutten and J. Herault. Blind separation of sources. part I: an adaptive algorithm based on neuromimetic architecture. *Signal Processing*, 24:1–10, 1991.

[26] C.J. Kalkman. The role of evoked potentials in neurological monitoring. *Hewlett Packard Advances*, pages 8–9, 1992.

[27] M. Knaflitz and R. Merletti. Suppression of stimulation artifacts from myoelectric evoked potential recordings. *IEEE Trans. on BME*, 35:758–763, 1988.

[28] M.J. Kornfield, J. Cerra, and D.G. Simons. Stimulus artifact reduction in nerve conduction. *Arch. Phys. Med. Rehabil.*, 66:232–235, 1985.

[29] J.L. Lacoume, M. Gaeta, and W. Kofman. Source separation using higher order statistics. *Journal of Atmospheric and Terrestrial Physics*, 54:1217–1226, 1992.

[30] Y.W. Lee and M. Schetzen. Measurement of the Wiener kernels of a nonlinear system by cross-correlation. *International Journal of Control*, 2:237–254, 1975.

[31] G.D. MacEwen, W.P. Bunnell, and K. Sriram. Acute neurological complications in the treatment of scoliosis: A report of the scoliosis research society. *Journal of Bone and Joint Surgery (American)*, 57-A:404–408, 1975.

[32] M. Machida, S.L. Weinstein, T. Yamada, and J. Kimura. Spinal cord monitoring: Electrophysiological measures of sensory and motor function during spinal surgery. *Spine*, 10:407–413, 1985.

[33] A. MacLennan and D. Lovely. Reduction of evoked potential measurement time by a TMS320 based adaptive matched filter. *Medical Engineering and Physics*, 17:248–255, 1995.

[34] G. Madhavan and H. de Bruin. Crosstalk resistant adaptive noise cancellation. *Annals of Biomed. Engineering*, 18:57–67, 1990.

[35] P.Z. Marmarelis and V.Z. Marmarelis. *Analysis of Physiological Systems- A White Noise Approach.* Plenum Press, New York, 1978.

[36] V.J. Mathews. Adaptive polynomial filters. *IEEE Sig. Proc. Magazine*, 5:10–26, 1991.

[37] C.D. McGillem, J.I. Aunon, and D.G. Childers. Signal processing in evoked potential research: Applications of filtering and pattern recognition. *CRC Critical Reviews in Bioengineering*, 9:225–265, October 1981.

[38] C.A McKinley and P.A. Parker. A beamformer for the acquisition of evoked potentials. *IEEE trans. on BME*, 38:379–382, 1991.

[39] L. McLean. An investigation into the waveform characteristics of the spinal somatosensory evoked potential. *M.Sc.E thesis, University of New Brunswick*, 1995.

[40] J.L. Melvin, J.A. Schuchmann, and R.R. Lanese. Diagnostic specificity of motor and sensory nerve conduction variables in the carpal tunnel syndrome. *Arch. Phys. Med. Rehabil.*, 54:69–74, 1973.

[41] J. Minzly, J. Mizrahi, N. Hakim, and A. Liberson. Stimulus artifact suppresor for emg recording during fes by a constant-current stimulator. *Med. & Biol. Eng & Comput.*, 31:72–75, 1992.

[42] G. Mirchandani, R. Zinser, and J. Evans. A new adaptive noise cancellation scheme in the presence of crosstalk. *IEEE trans. on Circuits and Systems- Part II*, 39:681–694, 1992.

[43] E. L. Morin. Investigation of surface-recorded spinal somatosensory evoked potential. *M.Sc.E thesis, University of New Brunswick*, 1984.

[44] T. Nogawa, K. Katayama, Y. Tabata, T. Kawahara, and T. Ohshio. Visual evoked potentials estimated by Wiener filtering. *Electroencep. clin. Neurophysiol.*, 35:375–378, 1973.

[45] P.A. Parker and R.N. Scott. Myoelectric control of prostheses. *CRC critical reviews in Bioengineering*, 13:283–310, 1985.

[46] V. Parsa and P.A. Parker. Multireference adaptive noise cancellation applied to somatosensory evoked potentials. *18th CMBEC proceedings, Toronto*, 18:74–75, 1992.

[47] V. Parsa and P.A. Parker. Performance analysis of the CRANC filter. *19th CMBEC proceedings, Ottawa*, 19:234–235, 1993.

[48] V. Parsa and P.A. Parker. Constrained crosstalk resistant adaptive noise canceler. *Electronics Letters*, 16:1276–1277, 1994.

[49] V. Parsa and P.A. Parker. Multireference adaptive noise cancellation applied to somatosensory evoked potentials. *IEEE trans. on BME*, 41:792–800, 1994.

[50] V. Parsa, P.A. Parker, and R.N Scott. Crosstalk resistant adaptive noise cancellation for somatosensory evoked potential enhancement. *Proceedings of ICASSP 1995, Detroit*, 5:2931–2934, 1995.

[51] V. Parsa, P.A. Parker, and R.N Scott. Performance analysis of a crosstalk resistant adaptive noise canceller. ***accepted for publication in IEEE trans. on Circuits and Systems***, 1995.

[52] V. Parsa. Adaptive myoelectric cancellation techniques applied to somatosensory evoked potential acquisition. ***M.Sc.E thesis, University of New Brunswick***, 1992.

[53] D. Regan. ***Human Brain Electrophysiology.*** Elsevier Science Publishing Co., New York, 1989.

[54] S. Richard. Adaptive myoelectric interference cancellation for the acquisition of somatosensory evoked potentials. ***M.Sc.E thesis, University of New Brunswick***, 1990.

[55] R.N. Scott, L. McLean, and P.A. Parker. Stimulus artefact in somatosensory evoked potential measurement. ***submitted to Med. & Biol. Eng & Comput.***, 1995.

[56] J.C. Slimp, D.E. Rubner, M.L. Snowden, and W.C. Stolov. Dermatomal somatosensory evoked potentials: cervical, thoracic and lumbosacral levels. ***Electroencep. clin. Neurophysiol.***, 84:55–60, 1992.

[57] N.J. Smith ***et al.*** Monitoring cortical evoked potentials in operations on the cervical spine. ***Abstracts from 5th international symposium on spinal cord monitoring, London***, page 31, 1992.

[58] M. Smorto and J. Basmajian. ***Clinical Electroneurography.*** The Williams & Wilkins Company., Baltimore, 1979.

[59] H.J. Spencer. An automatic, optically isolated, biphasic constant current stimulator adapter for artifact suppression. ***Electroencep. Clin. Neurophysiol.***, 51:215–217, 1981.

[60] W.G.S. Stephens. The current-voltage relationship in human skin. ***Med. Electron. Biol. Engg.***, 1:389–399, 1963.

[61] P. Strobach, K. Abraham-Fuchs, and Hårer. Event-synchronous cancellation of the heart interference in biomedical signals. ***IEEE Trans. on BME.***, 41:343–350, 1994.

[62] W. J. Tompkins. ***Biomedical Digital Signal Processing.*** Prentice Hall Publishing Co., Englewood Cliffs, New Jersey, 1993.

[63] S. Van Gerven and D. Van Compernolle. Signal separation by symmetric adaptive decorrelation: Stability, convergence, and uniqueness. ***IEEE trans. on Signal Processing***, 43:1602–1612, 1995.

[64] S.A.B. Harrison and D.F. Lovely. Identification of noise sources in surface recording of spinal somatosensory evoked potentials. *Med. & Biol. Eng & Comput.*, 33:299–305, 1995.

[65] C. Vauzelle, P. Stagnara, and P. Jouvinroux. Functional monitoring of spinal cord activity during spinal surgery. *Clinical Orthopaedics*, 93:173–178, 1973.

[66] D.O. Walter. A posteriori Wiener filtering of average evoked responses. *Electroencep. clin. Neurophysiol.*, 27:61–70, 1969.

[67] E. Weinstein, M. Feder, and A.V. Oppenheim. Multichannel signal separation by decorrelation. *IEEE trans. on Speech and Audio Processing*, 1:405–413, 1993.

[68] D. Westwick. An adaptive matched filter for spinal somatosensory evoked potential monitoring. *M.Sc.E thesis, University of New Brunswick*, 1988.

[69] B. Widrow, *et al* Adaptive noise cancelling: principles & applications. *Proceedings of the IEEE*, 12:1692–1716, 1975.

[70] B. Widrow and S.D. Stearns. *Adaptive Signal Processing.* Prentice Hall Publishing co., Englewood Cliffs, New Jersey, 1985.

[71] N. Wiener. *Nonlinear Problems in Random Theory.* Wiley, New York, 1958.

Appendix I

Constrained CRANC Filter

I.1 Derivation of Constrained CRANC Algorithm

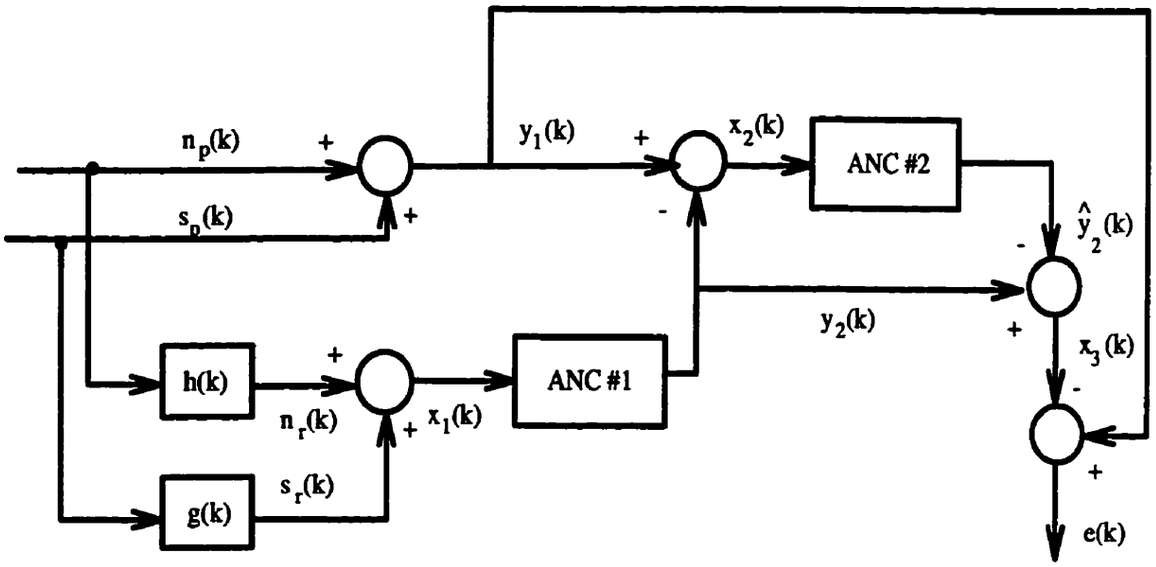

Figure I.1: *Block diagram of the CRANC filter in the absence of uncorrelated noise sources.*

The Z-domain block diagram of the CRANC filter structure in the absence of uncorrelated noise sources is repeated in Figure I.1 (refer to Chapter 4 for a complete description of this block diagram). The Wiener solutions for AF #1 and AF #2 were

derived in Chapter 4, Eqs. 4.1 and 4.5 and are reproduced below,

$$\begin{aligned} W_1(z) &= \frac{1}{H(z)} \\ W_2(z) &= \frac{G(z)W_1(z)}{1 - G(z)W_1(z)} \end{aligned} \tag{I.1}$$

The idea is to use the information possessed by AF #1 in constraining the adaption of AF #2. In other words, the adaption of AF #2 could be constrained to just the G(z) parameters. To simplify notation, let $W(z) = W_1(z)$ and $\widehat{G}(z)$ be the transfer function that needs to be adapted. The objective is to derive a gradient search algorithm that updates $\widehat{G}(z)$ in such a way that $\widehat{G}(z)$ approaches $G(z)$ as the algorithm converges.

Let $\widehat{G}(z) = \hat{g}_0 + \hat{g}_1 z^{-1} + \ldots + \hat{g}_{M-1} z^{-(M-1)}$ and $W(z) = w_0 + w_1 z^{-1} + \ldots + w_{L-1} z^{-(L-1)}$ where M is the length of $\widehat{G}(z)$ and L is the length of $W(z)$. It is assumed that $\widehat{G}(z)$ is of adequate order to model the $G(z)$ transfer function. The derivation of the adaption algorithm starts with the following equation for the error output of AF #2,

$$x_3(k) = y_2(k) - \hat{y}_2(k) \tag{I.2}$$

The gradient vector with respect to the $\widehat{\mathbf{G}}(z)$ transfer function is given by,

$$\widehat{\nabla}\mathbf{J}(k) = \frac{\partial x_3^2}{\partial \widehat{\mathbf{G}}} = -2x_3(k)\frac{\partial \hat{y}_2}{\partial \widehat{\mathbf{G}}} \tag{I.3}$$

where $\widehat{\mathbf{G}}$ is the $\hat{g}$-weight vector defined as $\widehat{\mathbf{G}} = [\hat{g}_0, \hat{g}_1, \ldots, \hat{g}_{M-1}]^T$. Thus the problem now simplifies to finding the partial derivatives of $\hat{y}_2(k)$ with respect to $\widehat{\mathbf{G}}$. To do this, we need to write $\hat{y}_2(k)$ in the time domain in terms of $\hat{g}$s. This can best be done by first starting out in the frequency domain,

$$\begin{aligned} & \hat{Y}_2(z) = \frac{\widehat{G}(z)W(z)}{1 - \widehat{G}(z)W(z)} X_2(z) \\ \Rightarrow \quad & \hat{Y}_2(z)(1 - \widehat{G}(z)W(z)) = \widehat{G}(z)W(z)X_2(z) \end{aligned} \tag{I.4}$$

and

$$\widehat{Y}_2(z)(1-(\widehat{g}_0+\ldots+\widehat{g}_{M-1}z^{-(M-1)})(w_0+\ldots+w_{L-1}z^{-(L-1)}))= \widehat{G}(z)W(z)X_2(z) \quad \text{(I.5)}$$

which can be written as

$$\begin{aligned}\widehat{Y}_2(z)(1-\widehat{g}_0w_0) &= \widehat{G}(z)W(z)X_2(z)+\widehat{Y}_2(z)(\widehat{g}_0(w_1z^{-1}+\ldots+w_{L-1}z^{-(L-1)}) \\ &\quad +w_0(\widehat{g}_1z^{-1}+\ldots+\widehat{g}_{M-1}z^{-(M-1)}) \\ &\quad +(\widehat{g}_1z^{-1}+\ldots+\widehat{g}_{M-1}z^{-(M-1)})(w_1z^{-1}+\ldots+w_{L-1}z^{-(L-1)})) \quad \text{(I.6)}\end{aligned}$$

Transforming the above equation into the time domain, we have

$$\begin{aligned}\widehat{y}_2(k)(1-\widehat{g}_0w_0) &= \widehat{g}_0\sum_{j=1}^{L-1}w_j\widehat{y}_2(k-j)+w_0\sum_{i=1}^{M-1}\widehat{g}_i\widehat{y}_2(k-i)+ \\ &\quad \sum_{i=1}^{M-1}\widehat{g}_i\sum_{j=1}^{L-1}w_j\widehat{y}_2(k-i-j)+\sum_{i=0}^{M-1}\widehat{g}_i\sum_{j=0}^{L-1}w_jx_2(k-i-j). \quad \text{(I.7)}\end{aligned}$$

Due to the explicit dependency of above equation on the weight $\widehat{g}_0$, the partial derivative of $\widehat{y}_2(k)$ with respect to $\widehat{g}_0$ is different from all other $\widehat{g}_i$s. The partial derivative with respect to $\widehat{g}_0$ can be expressed as,

$$\begin{aligned}(1-\widehat{g}_0w_0)\frac{\partial\widehat{y}_2(k)}{\partial\widehat{g}_0}-w_0\widehat{y}_2(k) &= \widehat{g}_0\sum_{j=1}^{L-1}w_j\frac{\partial\widehat{y}_2(k-j)}{\partial\widehat{g}_0}+\sum_{j=1}^{L-1}w_j\widehat{y}_2(k-j)+ \\ w_0\sum_{i=1}^{M-1}\widehat{g}_i\frac{\partial\widehat{y}_2(k-j)}{\partial\widehat{g}_0}+\sum_{i=1}^{M-1}\widehat{g}_i\sum_{j=1}^{L-1}w_j\frac{\partial\widehat{y}_2(k-i-j)}{\partial\widehat{g}_0}+\sum_{j=0}^{L-1}w_jx_2(k-j) \quad . \quad \text{(I.8)}\end{aligned}$$

The partial derivatives with respect to other weights can be similarly derived as

$$\begin{aligned}(1-\widehat{g}_0w_0)\frac{\partial\widehat{y}_2(k)}{\partial\widehat{g}_i} &= \widehat{g}_0\sum_{j=1}^{L-1}w_j\frac{\partial\widehat{y}_2(k-j)}{\partial\widehat{g}_i}+\sum_{j=1}^{L-1}w_j\widehat{y}_2(k-i-j)+\sum_{j=0}^{L-1}w_jx_2(k-j)+ \\ &\quad w_0(\sum_{i=1}^{M-1}\widehat{g}_i\frac{\partial\widehat{y}_2(k-i)}{\partial\widehat{g}_i}+\widehat{y}_2(k-i))+\sum_{i=1}^{M-1}\widehat{g}_i\sum_{j=1}^{L-1}w_j\frac{\partial\widehat{y}_2(k-i-j)}{\partial\widehat{g}_i} \quad \text{(I.9)}\end{aligned}$$

With this information, we can express the gradient vector as

$$\widehat{\nabla}\mathbf{J}(k) = \begin{pmatrix} \frac{\partial \widehat{y}_2(k)}{\partial \widehat{g}_0} \\ \vdots \\ \frac{\partial \widehat{y}_2(k)}{\partial \widehat{g}_{M-1}} \end{pmatrix} \tag{I.10}$$

and the update for $\widehat{g}$ vector is given by

$$\widehat{\mathbf{G}}(k+1) = \widehat{\mathbf{G}}(k) + 2\mu\widehat{\nabla}\mathbf{J}(k)x_3(k) \tag{I.11}$$

where $\mu = [\mu_0, \mu_1, \ldots, \mu_{M-1}]^T$ is the adaption control vector.

I.2 Error Performance Surface

The objective of this Section is derive an expression for the error surface at the output of AF #2 when its adaption is constrained by the above algorithm. This expression not only facilitates theoretical calculation of the minimum mean squared error at the output of AF #2 but also is of immense help in locating possible local minima. Let the transfer function of AF #2 be

$$W_2(z) = \frac{\widehat{G}(z)W(z)}{1 - \widehat{G}(z)W(z)} \tag{I.12}$$

Note that $W(z)$ is known to us from the transfer function of AF #1. The error performance surface for AF #2 is obviously a function of $\widehat{G}(z)$ and, with $z = e^{j\omega}$, can be written as [1]

$$E(x_3^2(k)) = \frac{1}{\pi}\int_0^{\pi} \phi_{x_3x_3}(\omega)d\omega \tag{I.13}$$

Since $x_3(k) = y_2(k) - \widehat{y}_2(k)$, $\phi_{x_3x_3}(\omega)$ on the righthand side in the above expression can be evaluated as

$$\phi_{x_3x_3}(\omega) = \phi_{y_2y_2}(\omega) + \phi_{\widehat{y}_2\widehat{y}_2}(\omega) - 2\Re(\phi_{y_2\widehat{y}_2}(\omega)) \tag{I.14}$$

[1] For simplicity, the sampling frequency, ω_s is set to 2π.

After a few mathematical manipulations and substitutions the above equation simplifies to

$$\phi_{x_3x_3}(\omega) = \phi_{N_pN_p}(\omega) + \phi_{S_pS_p}(\omega)\,|1 - G(\omega)W(\omega)|^2\,[\left|\frac{G(\omega)W(\omega)}{1 - G(\omega)W(\omega)}\right|^2 + \left|\frac{\hat{G}(\omega)W(\omega)}{1 - \hat{G}(\omega)W(\omega)}\right|^2 - 2\Re(\frac{G(\omega)W(\omega)}{1 - G(\omega)W(\omega)}\frac{\overline{\hat{G}(\omega)}\,\overline{W(\omega)}}{1 - \overline{\hat{G}(\omega)}\,\overline{W(\omega)}})]. \quad \text{(I.15)}$$

Thus if we know the spectral densities of the desired signal ($s_p(k)$) and the interference ($n_p(k)$) along with the crosstalk and interference transfer functions, we can theoretically evaluate the error surface for different values of $\hat{G}(\omega)$. This will enable us to determine if the error surface has any local minima.

Appendix II

Delay and Difference Array Processor (DDAP)

II.1 Basic DDAP

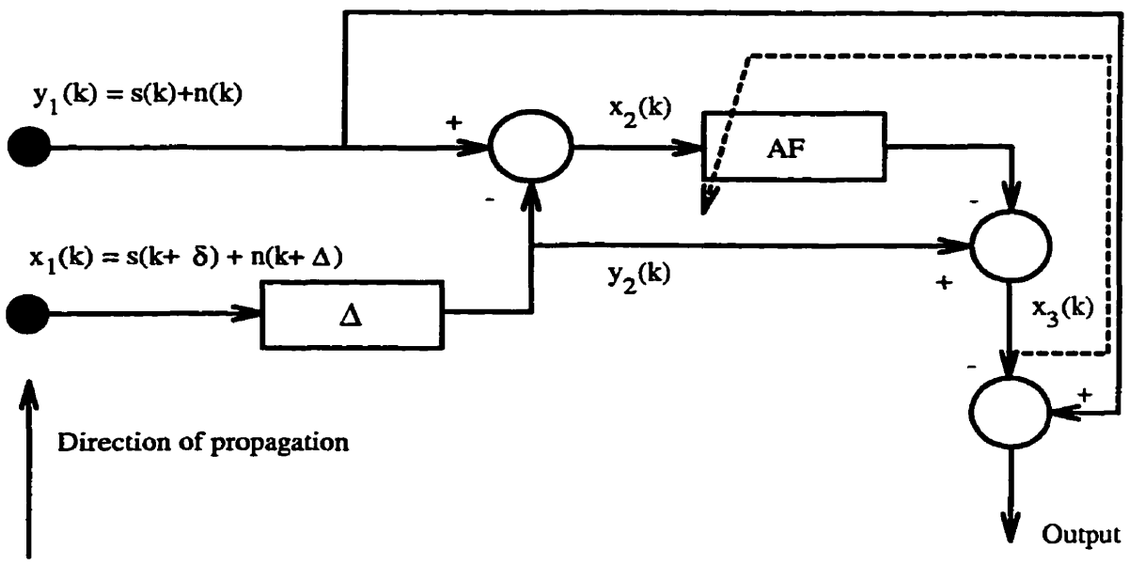

Figure II.1: *Block diagram of the basic Delay and Difference Array Processor (DDAP).*

With the first stage successfully removing the myoelectric interference through

estimating the Δ parameter, we have,

$$y_2(k) = s(k+\delta-\Delta) \tag{II.1}$$

$$x_2(k) = s(k) - s(k+\delta-\Delta). \tag{II.2}$$

The Wiener solution to the adaptive filter is

$$W(z) = \frac{z^{-\varphi}}{1-z^{-\varphi}} \tag{II.3}$$

where $\varphi = \Delta - \delta$ is the difference in MEI and SEP propagating time delays. From Eq.3, we can observe that there is only one unknown parameter, *viz.* the φ parameter. Thus an adaptive algorithm which estimates the φ parameter will considerably reduce the computational burden on the adaptive filter. Let $\widehat{\varphi}$ be the estimate of φ parameter. The idea is to increment or decrement the $\widehat{\varphi}$ value such that the error at the output of the AF (refer to Figure II,1) is minimized. Now the error signal at the output of the AF is given by,

$$x_3(k) = y_2(k) - \widehat{y}_2(k). \tag{II.4}$$

The gradient vector with respect to $\widehat{\varphi}$ is given by,

$$\widehat{\nabla} J(k) = \frac{\partial x_3^2(k)}{\partial \widehat{\varphi}} = -2x_3(k)\frac{\partial \widehat{y}_2(k)}{\partial \widehat{\varphi}}. \tag{II.5}$$

In order to evaluate the $\frac{\partial \widehat{y}_2(k)}{\partial \widehat{\varphi}}$ term, we have to write out $\widehat{y}_2(k)$ as

$$\widehat{y}_2(k) = \widehat{y}_2(k-\widehat{\varphi}) + x_2(k-\widehat{\varphi}) \tag{II.6}$$

which implies

$$\frac{\partial \widehat{y}_2(k)}{\partial \widehat{\varphi}} = \frac{\partial \widehat{y}_2(k-\widehat{\varphi})}{\partial \widehat{\varphi}} + \frac{\partial x_2(k-\widehat{\varphi})}{\partial \widehat{\varphi}} \tag{II.7}$$

Without any ***a priori*** knowledge of the signal characteristics, it is not possible to evaluate the above partial derivatives with respect to $\widehat{\varphi}$. If we use symmetric difference as an approximation to the partial derivatives we have,

$$\frac{\partial \widehat{y}_2(k)}{\partial \widehat{\varphi}} = \frac{\widehat{y}_2(k-\widehat{\varphi}-1) - \widehat{y}_2(k-\widehat{\varphi}+1)}{(\widehat{\varphi}+1)-(\widehat{\varphi}-1)} + \frac{x_2(k-\widehat{\varphi}-1) - x_2(k-\widehat{\varphi}+1)}{(\widehat{\varphi}+1)-(\widehat{\varphi}-1)} \quad \text{(II.8)}$$

With this approximation, the update rule for the $\widehat{\varphi}$ parameter is given by,

$$\widehat{\varphi}(k+1) = \widehat{\varphi}(k) + 2\mu x_3(k)\frac{\partial \widehat{y}_2(k)}{\partial \widehat{\varphi}} \quad \text{(II.9)}$$

$$\begin{aligned}\widehat{\varphi}(k+1) &= \widehat{\varphi}(k) + \mu x_3(k)\{\widehat{y}_2(k-\widehat{\varphi}(k)-1) - \widehat{y}_2(k-\widehat{\varphi}(k)+1) + \\ &\quad x_2(k-\widehat{\varphi}(k)-1) - x_2(k-\widehat{\varphi}(k)+1)\}\end{aligned} \quad \text{(II.10)}$$

where μ is the convergence control parameter. The above algorithm poses a significant problem: Due to the feedback nature, any error in the initial gradient estimates recycles through the algorithm making it unstable (even for smaller values of μ. Thus correct initialization is required which implies that for this algorithm to be viable, we need to have ***a priori*** knowledge of the signal.

We can enhance this algorithm by modifying the structure of the DDAP. The modified DDAP is shown in Figure II.2 where an extra sensor is utilized. Once again assuming that the first stage has successfully estimated the Δ parameter, we have at nodes #1 and #2,

$$y(k) = s(k) - s(k+2\delta-2\Delta) = s(k) - s(k-2\varphi), \quad \text{(II.11)}$$

$$x(k) = s(k) - s(k+\delta-\Delta) = s(k) - s(k-\varphi). \quad \text{(II.12)}$$

If we construct an adaptive structure, as shown in Figure II.3, with $x(k)$ as the reference input and $y(k)$ as the primary input, the optimal solution to the AF block is,

$$W(z) = 1 + z^{-\varphi}. \quad \text{(II.13)}$$

Instead of implementing the AF block as a standard FIR filter, which may require quite a few number of taps if the φ parameter is large, let the AF block have a transfer function, $1 + z^{-\widehat{\varphi}}$, where $\widehat{\varphi}$ is an estimate of φ. Once again, the objective is to derive

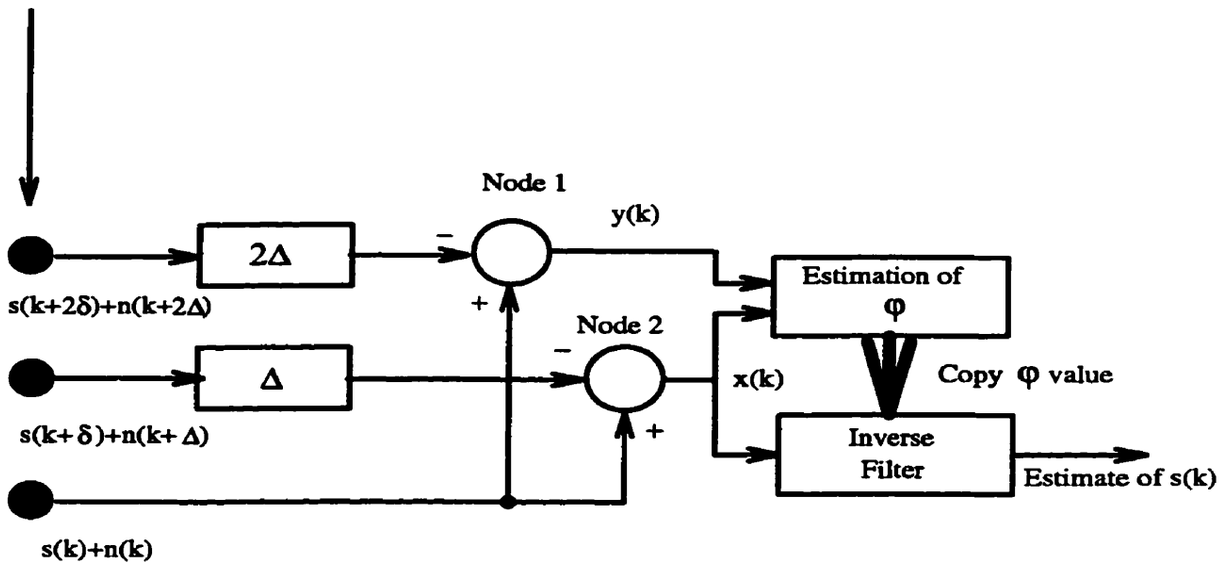

Figure II.2: ***Modified DDAP.***

an adaptive algorithm for iterative updating of the $\widehat{\varphi}$ value in the form of

$$\widehat{\varphi}(k+1) = \widehat{\varphi}(k) - \mu \frac{\partial e^2(k)}{\partial \widehat{\varphi}} \tag{II.14}$$

which simplifies to

$$\widehat{\varphi}(k+1) = \widehat{\varphi}(k) + 2\mu e(k) \frac{\partial \widehat{y}(k)}{\partial \widehat{\varphi}}. \tag{II.15}$$

From Figure II.3, we have

$$\widehat{y}(k) = x(k) + x(k - \widehat{\varphi}) \tag{II.16}$$

and

$$\frac{\partial \widehat{y}(k)}{\partial \widehat{\varphi}} = \frac{\partial x(k - \widehat{\varphi})}{\partial \widehat{\varphi}}. \tag{II.17}$$

Once again, if we have ***a priori*** knowledge of the signal, the above partial derivative can be derived exactly. In the absence of any such information, the partial derivative is substituted by the symmetric difference approximation resulting in,

$$\frac{\partial \widehat{y}(k)}{\partial \widehat{\varphi}} = \frac{x(k - \widehat{\varphi} - 1) - x(k - \widehat{\varphi} + 1)}{(\widehat{\varphi} + 1) - (\widehat{\varphi} - 1)}. \tag{II.18}$$

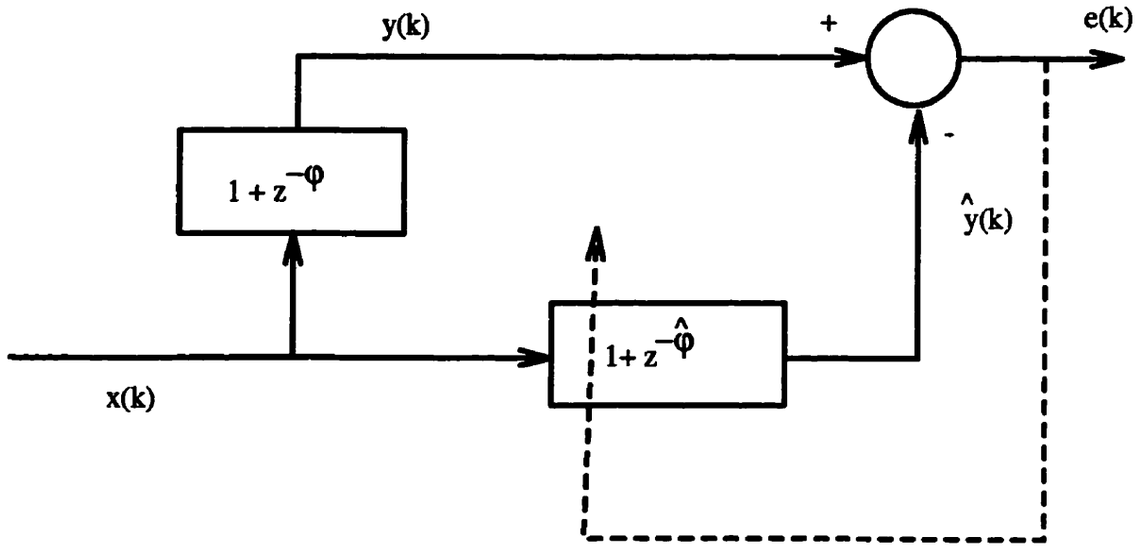

Figure II.3: *Second stage of the modified DDAP.*

Thus the updating algorithm for the φ estimate is

$$\hat{\varphi}(k+1) = \hat{\varphi}(k) + \mu e(k)\{x(k-\hat{\varphi}-1) - x(k-\hat{\varphi}+1)\}. \tag{II.19}$$

Once again we can derive an expression for the error surface at the output of the second stage as a function of $\hat{\varphi}$. We start with,

$$E(e^2(k)) = \frac{1}{\pi}\int_0^{\pi} \phi_{EE}(\omega)d\omega \tag{II.20}$$

From Figure II.3,

$$e(k) = y(k) - \hat{y}(k) \tag{II.21}$$

which implies

$$\phi_{EE}(\omega) = \phi_{YY}(w) + \phi_{\hat{Y}\hat{Y}}(\omega) - 2\Re\{\phi_{Y\hat{Y}}(\omega)\} \tag{II.22}$$

which simplifies to

$$\phi_{EE}(\omega) = \phi_{XX}(\omega)\left|1 + z^{-\varphi}\right|^2 + \phi_{XX}(\omega)\left|1 + z^{-\hat{\varphi}}\right|^2 - 2\Re\{\phi_{XX}(\omega)(1 + z^{-\varphi})(1 + z^{\hat{\varphi}})\}. \tag{II.23}$$

Appendix III

Theoretical Analysis of the MCRANC

III.1 Optimal Weight Vector Derivation

The block diagram of the MCRANC is shown in Figure III.1 where $s_p(k)$ is the desired SEP signal, $n_p(k)$ and $n_r(k)$ are the primary and reference MEI sources, $u_p(k)$ and $u_r(k)$ are the primary and reference uncorrelated noise sources, $h(k)$ is the MEI transfer function, $g(k)$ is the crosstalk transfer function, $W_1(z), W_{21}(z) \ldots W_{2M}(z)$ are the adaptive filters and M is the number of reference channels. The parameter D in the second stage of the MCRANC structure represents a delay of one stimulus period. Essential for the successful operation of this structure is to allow the first ANC to converge before the advent of the SEP. The Wiener solution of AF #1 is then given by,

$$\begin{aligned} W_1(z) &= \frac{\phi_{N_pN_p}(z)H(z^{-1})}{\phi_{N_pN_p}(z)\,|H(z)|^2 + \phi_{U_rU_r}(z)} \\ &= \frac{1}{H(z)\{1+\Gamma_r(z)\}} \end{aligned} \tag{III.1}$$

where $\Gamma_r(z)$ is the ratio of uncorrelated and MEI power spectral densities in the

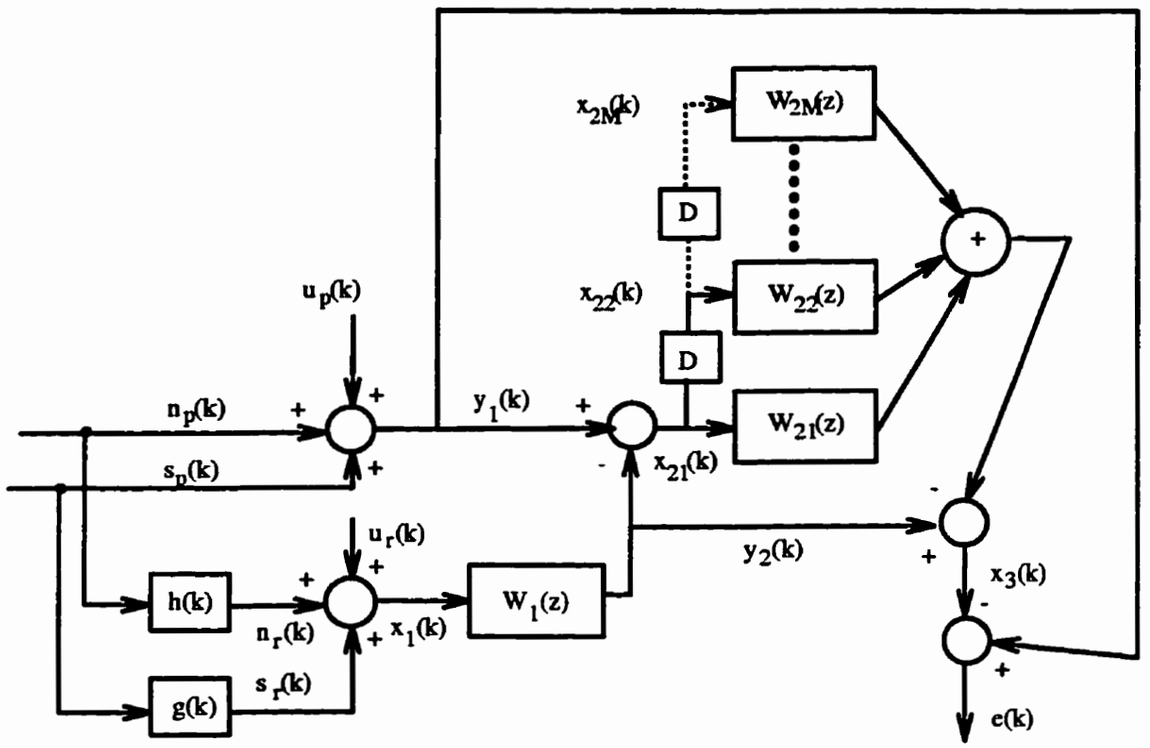

Figure III.1: *Block diagram of the MCRANC.*

reference input to AF #1. The unconstrained Wiener solution to the second stage of the MCRANC is a set of optimal transfer functions represented by,

$$\mathbf{W}(z) = \begin{pmatrix} W_{21}(z) \\ W_{22}(z) \\ \vdots \\ W_{2M}(z) \end{pmatrix} \tag{III.2}$$

and is given by the discrete Wiener-Hopf equation,

$$\mathbf{W}(z) = \boldsymbol{\phi}_{\mathbf{XX}}{}^{-1}(z)\boldsymbol{\phi}_{\mathbf{YX}}(z) \tag{III.3}$$

where $\boldsymbol{\phi}_{\mathbf{XX}}(z)$ is the reference input spectral density matrix given by

$$\boldsymbol{\phi}_{\mathbf{XX}}(z) = \begin{pmatrix} \phi_{X_{21}X_{21}}(z) & \phi_{X_{21}X_{22}}(z) & \cdots & \phi_{X_{21}X_{2M}}(z) \\ \phi_{X_{22}X_{21}}(z) & \phi_{X_{22}X_{22}}(z) & \cdots & \phi_{X_{22}X_{2M}}(z) \\ \cdot & \cdot & \cdot & \cdot \\ \phi_{X_{2M}X_{21}}(z) & \phi_{X_{2M}X_{22}}(z) & \cdots & \phi_{X_{2M}X_{2M}}(z) \end{pmatrix} \tag{III.4}$$

where $\phi_{X_{2i}X_{2j}}(z)$ is the cross-spectral density between the ith and jth reference channels of the second stage of MCRANC. The cross-spectral density between the primary and reference inputs is $\boldsymbol{\phi}_{\mathbf{YX}}(z)$ which can be expressed as

$$\boldsymbol{\phi}_{\mathbf{YX}}(z) = \begin{pmatrix} \phi_{Y_2X_{21}}(z) \\ \phi_{Y_2X_{21}}(z) \\ \vdots \\ \phi_{Y_2X_{21}}(z) \end{pmatrix} \tag{III.5}$$

Let

$$\begin{aligned} \phi_A(z) &= \phi_{S_pS_p}(z)G(z)W_1(z)\{1 - G(z^{-1})W_1(z^{-1})\}, \\ \phi_B(z) &= \phi_{S_pS_p}(z)\,|1 - G(z)W_1(z)|^2, \text{ and} \\ \phi_C(z) &= \phi_{N_pN_p}(z)\,|1 - H(z)W_1(z)|^2 + \phi_{U_pU_p}(z) + \phi_{U_rU_r}(z)\,|W_1(z)|^2. \end{aligned} \tag{III.6}$$

If we make the following reasonable assumptions:

- The MEI and the uncorrelated noise sources are wide sense ergodic processes,
- The SEP repeats itself faithfully every D seconds, and
- Both the MEI and uncorrelated noise sources are uncorrelated with themselves after D seconds.

then,

$$\phi_{\mathbf{XX}}(z) = \begin{pmatrix} \phi_B(z) + \phi_C(z) & \phi_B(z) & \cdots & \phi_B(z) \\ \phi_B(z) & \phi_B(z) + \phi_C(z) & \cdots & \phi_B(z) \\ \cdot & \cdot & \cdot & \cdot \\ \phi_B(z) & \phi_B(z) & \cdots & \phi_B(z) + \phi_C(z) \end{pmatrix} \tag{III.7}$$

and

$$\phi_{\mathbf{YX}}(z) = \begin{pmatrix} \phi_A(z) \\ \phi_A(z) \\ \vdots \\ \phi_A(z) \end{pmatrix} \tag{III.8}$$

giving us the Wiener solution for the second stage of the MCRANC as

$$\mathbf{W}(z) = \begin{pmatrix} \frac{\phi_A(z)}{M\phi_B(z)+\phi_C(z)} \\ \frac{\phi_A(z)}{M\phi_B(z)+\phi_C(z)} \\ \vdots \\ \frac{\phi_A(z)}{M\phi_B(z)+\phi_C(z)} \end{pmatrix}. \tag{III.9}$$

Note that under the stationarity assumption, all of the adaptive filters have the same optimal transfer function. The output signal estimate can be easily calculated as,

$$\widehat{S}_p(z) = S_p(z)\{1 - G(z)W_1(z)\}\{1 + MW_{21}(z)\} \tag{III.10}$$

Now,

$$\begin{aligned} 1 + MW_{21}(z) &= 1 + \frac{M\phi_A(z)}{M\phi_B(z) + \phi_C(z)} \\ &= 1 + \frac{\phi_A(z)}{\phi_B(z) + \frac{\phi_C(z)}{M}} \end{aligned} \tag{III.11}$$

and,

$$\begin{aligned} \lim_{M\to\infty} 1 + MW_{21}(z) &= 1 + \frac{\phi_A(z)}{\phi_B(z)} \\ &= 1 + \frac{\phi_{S_pS_p}(z)G(z)W_1(z)\{1 - G(z^{-1})W_1(z^{-1})\}}{\phi_{S_pS_p}(z)\,|1 - G(z)W_1(z)|^2} \\ &= \frac{1}{1 - G(z)W_1(z)} \end{aligned} \tag{III.12}$$

From Eqs. III.10 and III.12, we can see that as the number of reference channels in the second stage MCRANC tends to infinity, the SEP estimate at the output of the MCRANC approaches the undistorted input SEP.

The MEI and uncorrelated noise components at the output of the MCRANC filter can be expressed as

$$\phi_{N_oN_o} = \phi_{N_pN_p}(z)\left|(1 - H(z)W_1(z))(1 + (1 + z^{-D} + \ldots + z^{-(M-1)D})(1 + W_{21}(z))\right|^2 \tag{III.13}$$

and

$$\begin{aligned} \phi_{U_oU_o} = \phi_{U_pU_p}(z)\left|1 + (1 + z^{-D} + \ldots + z^{-(M-1)D})W_{21}(z)\right|^2 + \\ \phi_{U_rU_r}(z)\left|W_1(z) + (1 + z^{-D} + \ldots + z^{-(M-1)D})W_1(z)W_{21}(z)\right|^2 \end{aligned} \tag{III.14}$$

As the number of channels tends to infinity, these can be expressed as,

$$\phi_{NM}(z) = \lim_{M\to\infty} \phi_{N_oN_o}(z) = \phi_{N_pN_p}(z)\,|1 - H(z)W_1(z)|^2 \tag{III.15}$$

$$\phi_{UM}(z) = \lim_{M\to\infty} \phi_{U_oU_o}(z) = \phi_{U_pU_p}(z) + \phi_{U_rU_r}(z)\,|W_1(z)|^2 \tag{III.16}$$

Thus the SNRGAIN, γ, achieved by the MCRANC filter has an upper bound given by

$$\gamma_{max} = \frac{\oint \phi_{N_pN_p}(z)dz + \oint \phi_{U_pU_p}(z)dz}{\oint \phi_{NM}(z)dz + \oint \phi_{UM}(z)dz} \tag{III.17}$$

with the integrals evaluated on the unit circle in the Z domain. Thus, as the number of reference channels in the second stage of MCRANC is increased, the SNRGAIN increases until it reaches the maximum value while the signal distortion decreases regardless of the amount of signal crosstalk and even in the presence of uncorrelated noise sources.

Appendix IV

SA Cancellation in the Presence of an SEP

IV.1 Introduction

As discovered in Chapter 5, the presence of an SEP, even if it is in the primary input to the adaptive filter, drastically affects the convergence of the adaptive filter resulting in undesirable SEP distortion. A detailed study of the perils of adaptive filtering operation on the SEP is therefore undertaken in this appendix. For pedagogical reasons, two cases are considered separately: a) primary and reference SAs related through a linear transfer function, and b) primary and reference SAs related through a second order Volterra model.

IV.2 Linear SA transfer function

The reference SA, $SA_r(k)$, in all the ensuing simulations is an experimentally acquired SA waveform which has been ensemble averaged to diminish the background noise. The primary SA, $SA_p(k)$, for this section is generated through filtering the reference SA using a linear filter whose impulse response is given by

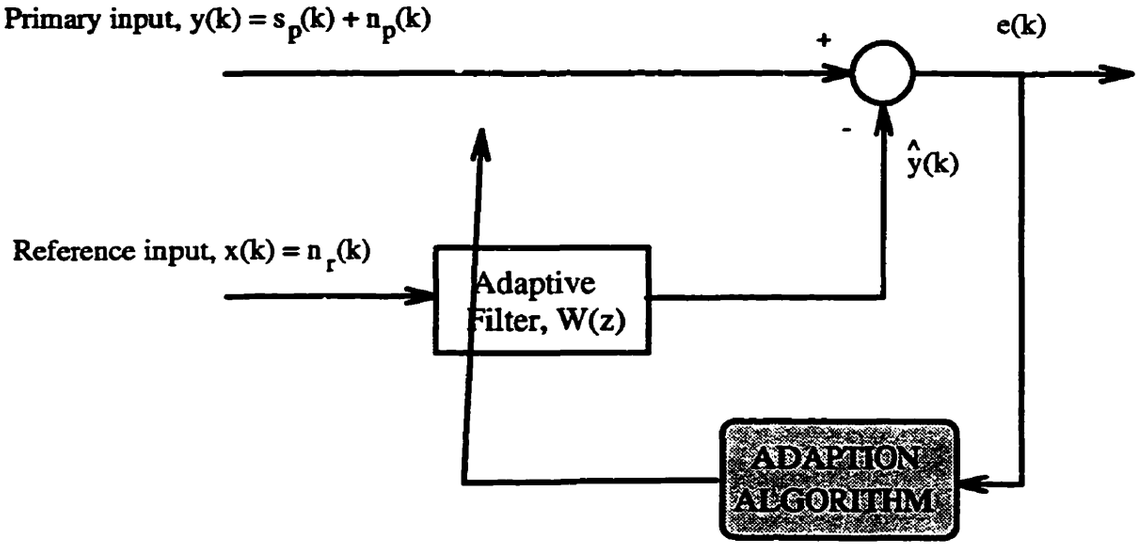

Figure IV.1: *SA cancellation block diagram.*

$$H_{lin}(k) = e^{-k/10} \qquad k = 0, \ldots, 19 \tag{IV.1}$$

Figure IV.2 shows the primary and reference SAs used for this study. The desired SEP was generated using the analytical model given in Chapter 5. This SEP waveform is delayed and added to the SA_p waveform to generated the primary input to the adaptive filter, $y(k)$ (refer to Figure IV.1). The SEP+SA composites for four different SEP positions are shown in Figures IV.2 c-f. Let us call these four different primary inputs as $y_{150}(k)$, $y_{100}(k)$, $y_{50}(k)$ and $y_{20}(k)$ respectively with the number designating the start of the SEP waveform in the SEP+SA composites. Now the Wiener solution for the adaptive filter in the time domain is given by,

$$\mathbf{w}_{opt} = \mathbf{R}_{xx}^{-1}\mathbf{P}_{yx} \tag{IV.2}$$

where $\mathbf{R}_{xx}$ is the auto-correlation matrix given by

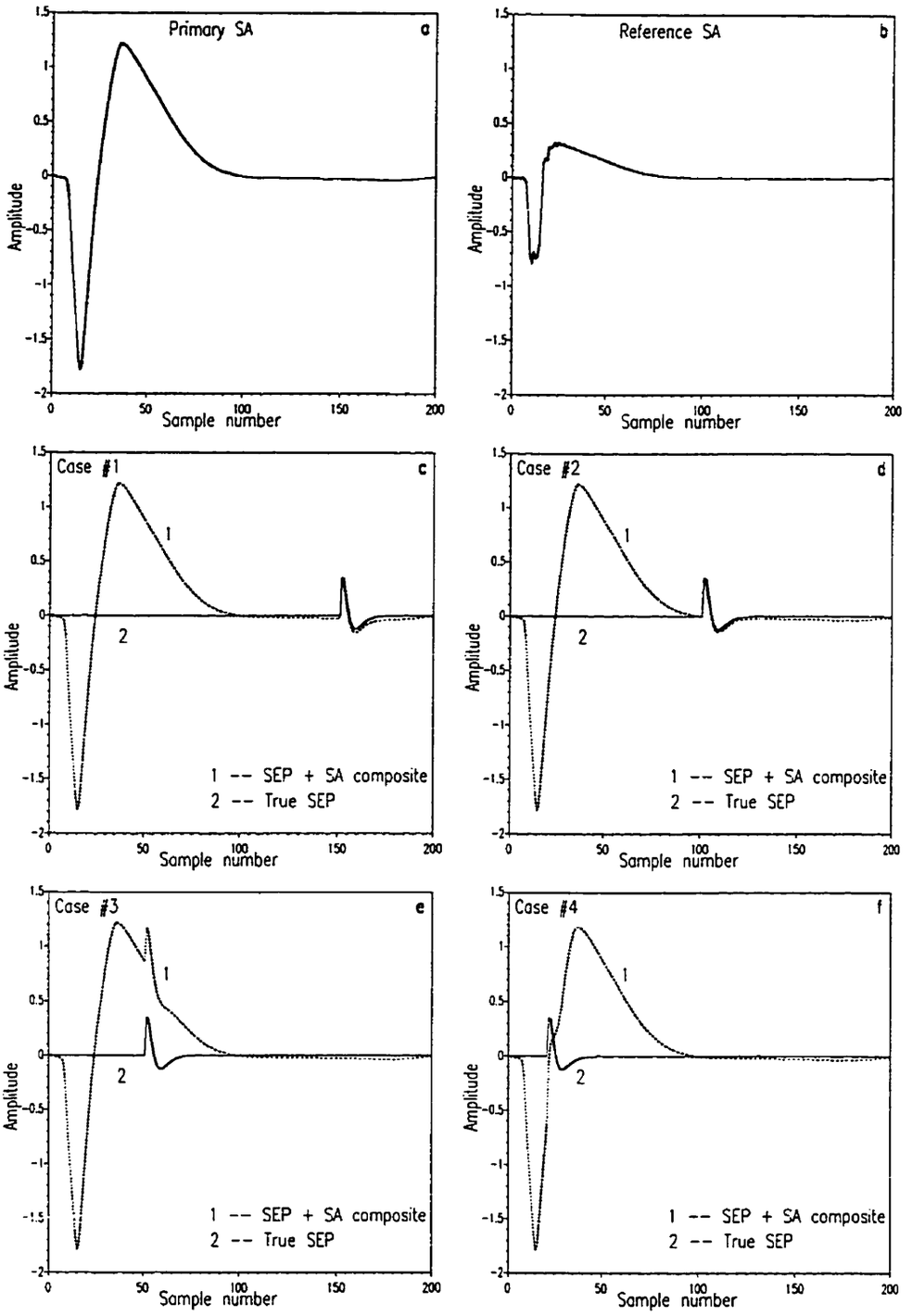

Figure IV.2: ***Simulated SEP and SA data to demonstrate the effects of adaptive filtering on the SEP.***

$$\mathbf{R}_{xx} = \begin{pmatrix} r_{xx}(0) & r_{xx}(1) & \cdots & r_{xx}(N-1) \\ r_{xx}(1) & r_{xx}(0) & \cdots & r_{xx}(N-2) \\ . & . & . & . \\ r_{xx}(N-1) & r_{xx}(N-2) & \cdots & r_{xx}(0) \end{pmatrix} \tag{IV.3}$$

where N is the filter length and

$$r_{xx}(a) = E'(x(k)x(k-a)) \tag{IV.4}$$

and $\mathbf{P}_{yx}$ is the cross-correlation vector given by

$$\mathbf{P}_{yx} = \begin{pmatrix} p_{yx}(0) \\ p_{yx}(1) \\ \vdots \\ p_{yx}(N-1) \end{pmatrix} \tag{IV.5}$$

where

$$p_{yx}(a) = E'(y(k)x(k-a)). \tag{IV.6}$$

As the SEP and SA are additive in the primary input to the ANC, the cross-correlation vector can be split into

$$\mathbf{P}_{yx} = \mathbf{P}_{SA} + \mathbf{P}_{SEP-SA} \tag{IV.7}$$

where $\mathbf{P}_{SA}$ corresponds to the cross-correlation between the SA components in the primary and the reference, and $\mathbf{P}_{SEP-SA}$ represents the cross-correlation between the SEP in the primary input and the reference SA. It is this $\mathbf{P}_{SEP-SA}$ function that is the root cause of SSEP distortion. If the SEP and SA and were uncorrelated waveforms, this term would have been zero and the Wiener solution would have depended solely on the SA characteristics. Unfortunately due to the deterministic nature of the SEP and SA waveforms, $\mathbf{P}_{SEP-SA}$ is usually non-zero. The $\mathbf{P}_{SEP-SA}$ functions for the four different SEP positions are depicted in Figure IV.3. The non-zero cross-correlation function between the SEP waveform and the reference artifact is evident in this figure.

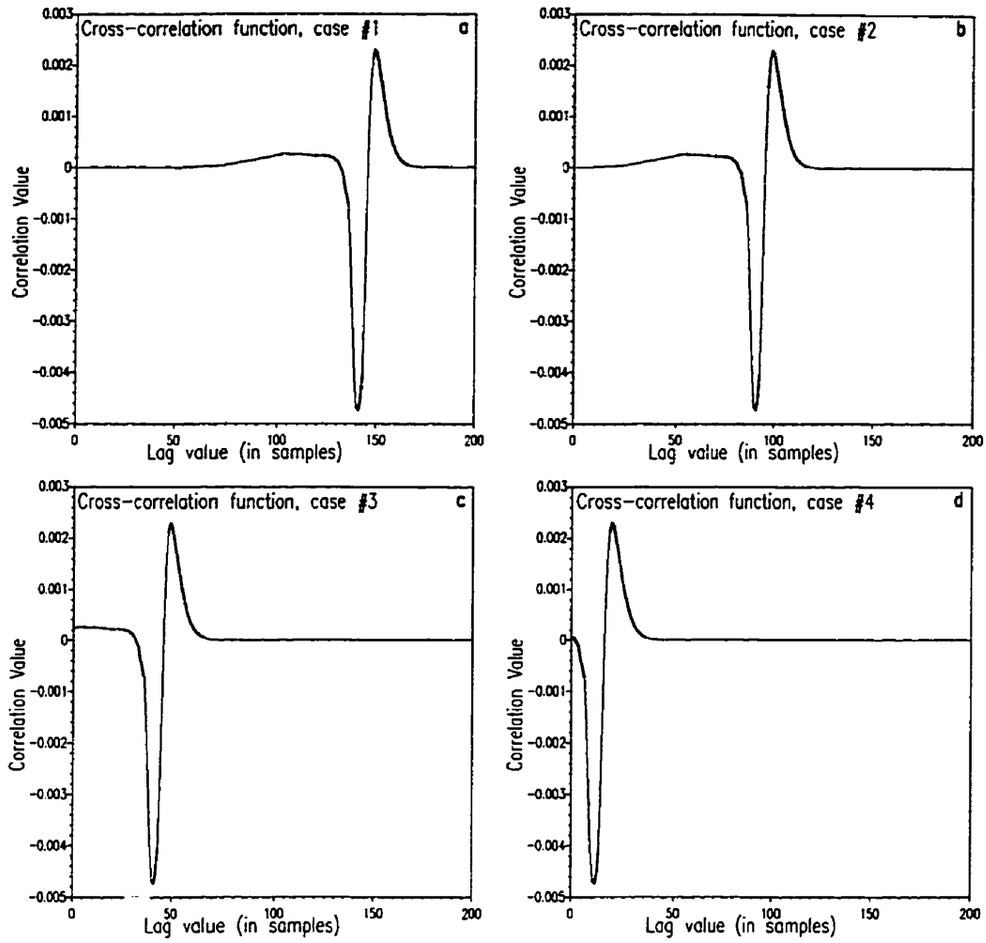

Figure IV.3: ***SEP-SA cross-correlation. The cross-correlation function between the primary SEP and the reference SA for four different SEP positions are depicted in this figure.***

However, notice that the cross-correlation function is tied to the position of the SEP and hence there is a range of "close-to-zero" cross-correlation values. **These values are key to the successful operation of an adaptive filter.** If the length of the adaptive filter is constrained to be within this "close-to-zero" cross-correlation value range, the SEP distortion will not be noticeable. To explain this fact further, let us look at Figure IV.3a. The cross-correlation values are not significant until around a lag value of 130 samples. Thus, as long as the length of the adaptive filter is less than 130, the distortion incurred by the SEP will not be noticeable. In the same way, filter

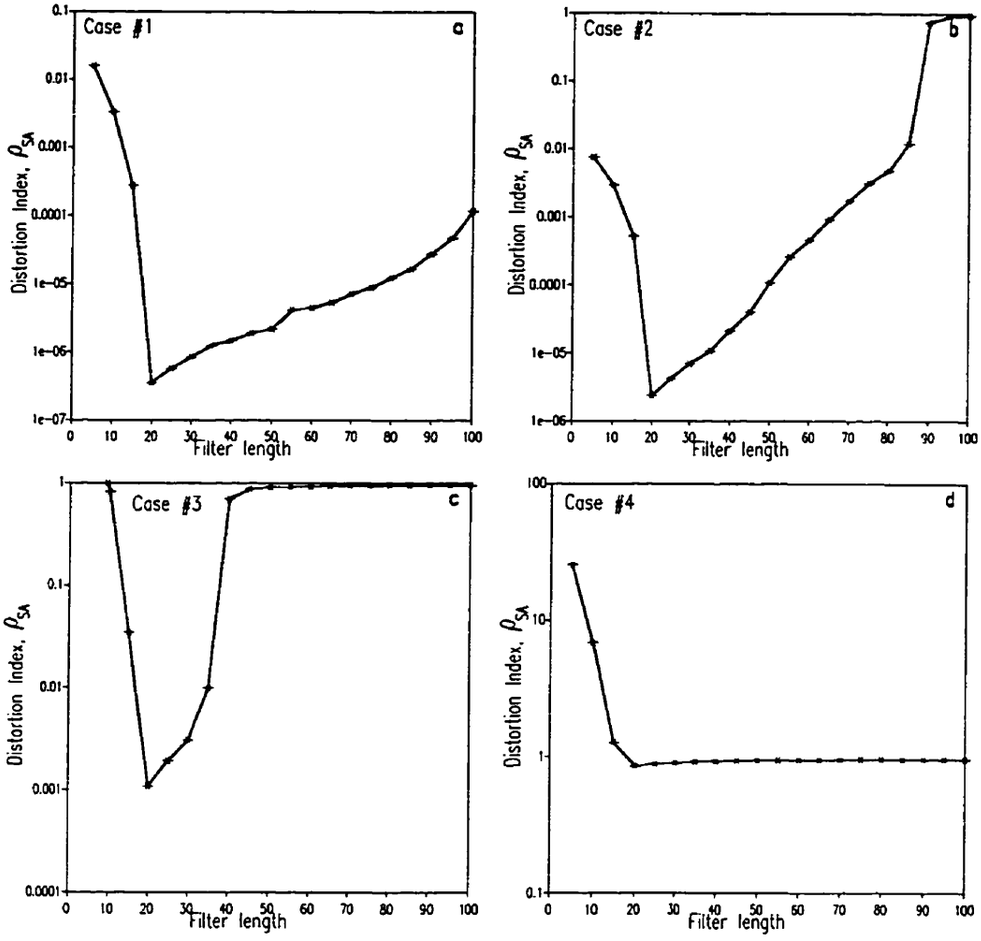

Figure IV.4: ***Effect of filter length on SEP distortion. Distortion indices for different adaptive filter lengths for each of the four cases are shown here.***

lengths of greater than 80 taps will cause distortion for the case in Figure IV.3b and a 30 tap filter will introduce distortion for the case in Figure IV.3c. Figure IV.3d is the worst case as any non-zero filter length will result in significant SEP distortion.

The effect of filter length on SEP distortion is demonstrated for each of the four cases. Adaptive filters of varying filter lengths were employed to cancel the SA, with each of the four composites shown in Figure IV.2c-f as the primary inputs and the SA waveform shown in Figure IV.2b as the reference input. Once the adaptive filter has converged, the SEP estimate at the output of the adaptive filter is retrieved and

the amount of SEP distortion is quantified once again using the following distortion index,

$$\rho_{SA} = \frac{\sum_{n=0}^{L-1}(s(k) - \hat{s}(k))^2}{\sum_{n=0}^{L-1} s^2(k)} \tag{IV.8}$$

where $\hat{s}(k)$ is the SEP estimate at the output of the adaptive filter. Figures IV.4a-d depict the distortion indices obtained for the four cases corresponding to different SEP positions. The following comments can be made based on these results:

- For all the cases, the distortion index ρ_{SA} is the lowest at a filter length of 20. This is to be expected as the optimal filter length for total SA cancellation is 20.

- For filter lengths less than 20, the adaptive filter is "under-modeled" for SA reduction. The adaptive filter, consequently leaves substantial artifact residue and this causes the SEP to appear distorted. Note that for these filter lengths the true SEP waveform is unaffected but it is the residual artifact that is responsible for the distortion index.

- For filter lengths greater than 20, the distortion index can be seen to steadily increase for cases #1 to #3. This is due to the effect of the finite cross-correlation between the SEP and SA. For these filter lengths, the adaptive filter is "over-modeled" to cancel the SA and the extra filter weights are affected by the presence of the SEP, thereby creating some distortion.

- The distortion index jumps sharply as the filter length approaches the "non-zero" cross-correlation region. In case #1, the SEP and SA are comfortably separated and hence even a filter length of 100 did not result in significant distortion (less than 0.1%). For case #2, there is a sharp increase in the distortion index around 85. This, from Figure IV.3b, can be seen as the start of the non-zero SEP-SA cross-correlation. Similarly,for case #3, there is a sharp increase in the distortion index around a filter length of 35 which once again corresponds

to the beginning of the non-zero phase of the cross-correlation function. Note that the distortion index saturates to unity as the filter length increases. This means that the **SEP is being canceled by the adaptive filter as well!**. The increased filter lengths enable the adaptive filter to model the SEP+SA composite in the primary based on the reference SA! (A pictorial example of this phenomenon is given in Figure IV.5). Case #4 is the worst case as the distortion index is close to 1 for filter orders greater than 15. This means that, for this case, no matter what filter length is used, severe SEP distortion will occur. Case #4 makes one point clear: if the SEP is positioned close to the SA peak, there is no least squares filtering technique that will retrieve an undistorted SEP from SEP+SA composite. Fortunately, the SEP and SA are usually separated in time and thus there is hope for applying least squares filtering techniques in SA cancellation.

As a last example for this section, the "creation" of the SEP component by the adaptive filter at higher filter lengths is displayed in Figure IV.5. The primary, $y(k)$ (refer to Figure IV.1), and reference, $x(k)$, inputs used for this simulation example are shown in Figures IV.5a and b. The adaptive filter outputs, $\widehat{y}(k)$ for two different filter lengths are displayed in Figures IV.5c and d. It can be observed that for a filter length of 20 taps, the adaptive filter produced an output which matched only the SA component in the primary input. Thus the error output, $e(k) = y(k) - \widehat{y}(k)$ will be the SEP estimate with very little distortion. On the other hand, the adaptive filter with a length of 50 taps, "created" the SEP component as well in its output. This when subtracted from the primary input results in a highly canceled SEP. This example therefore effectively demonstrates the **perils** associated with using high filter lengths for SA cancellation. The only solution to this problem is to segment the adaptation such that the presence of the SEP does not affect the convergence of the adaptive filter. Note that even a segmented adaptation approach will be difficult to implement for the case #4.

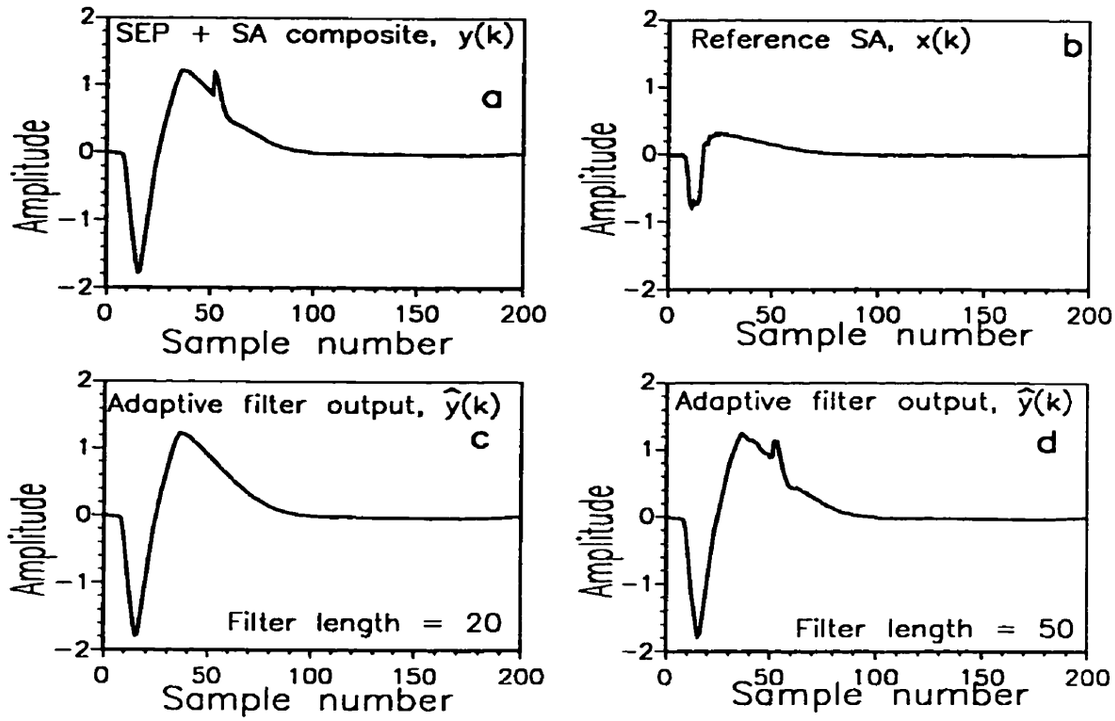

Figure IV.5: *Pictorial demonstration of the SEP cancellation phenomenon. The primary and reference inputs to the adaptive filter are given in a) and b). The adaptive filter outputs for two different filter lengths are shown in Figures c) and d). Note that for a filter length of 20, the adaptive filter estimates the interfering artifact but a filter length of 50 estimates the SEP component as well.*

IV.3 Nonlinear SA transfer function

If the SA transfer function were linear, the above discussion (based on SEP-SA cross-correlation) neatly describes the SEP cancellation phenomenon. With a nonlinear function modelling the relationship between the primary and reference SAs, this method of demonstration, however, is not possible. However, we can still investigate the effect of the filter length on the SEP distortion through simulations in much the same way as in the previous section.

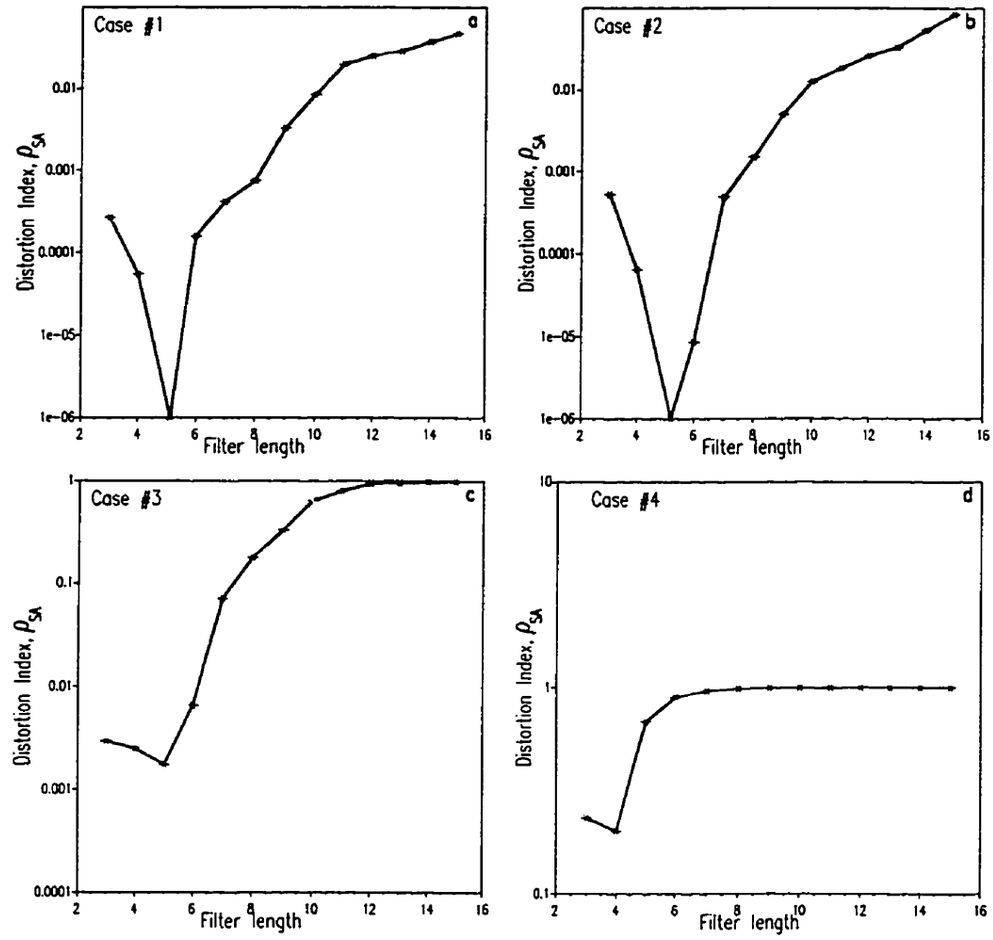

Figure IV.6: ***Effect of nonlinear filter length on SEP distortion. Distortion indices for different nonlinear adaptive filter lengths for each of the four cases are shown here.***

The nonlinear model between the reference and primary SA was a second order Volterra filter of filter length 5 given by (reproduced from Chapter 5)

$$H_{nonlin}(k) = \begin{cases} 0, & \text{for k=0} \\ e^{\frac{-(k-1)}{10}}, & \text{for k = 1,2,...,20} \end{cases} \tag{IV.9}$$

The primary SA was generated by passing the reference SA through the above filter. To the primary SA, once again, the SEP was delayed and added just as in the previous section. For the four cases of SEP position, nonlinear adaptive filters

(NAFs) based on second order Volterra series and of varying filter lengths were employed to cancel the primary SA. Once convergence was established, the output SEP estimate was once again retrieved and the distortion index, ρ_{SA}, given by Eq. IV.1 was computed. This distortion index for the four different cases is depicted in Figures IV.6a-d. Once again, we can make the following observations:

- Once again, except for case #4, the distortion index, ρ_{SA}, is lowest when the filter length of NAF is 5, which is the optimal filter length.

- Interestingly, the distortion indices for cases #1 and #2 are almost identical. This is probably due to the fact that the position of the SEP far exceeds the filter memory in both the cases.

- For all the cases, the distortion indices resulting from using the NAFs are higher compared to the distortion indices obtained using the linear adaptive filters of same filter lengths. This shows that, in general, the NAFs will be more severe on the SEP distortion than their linear counterparts. This is due to the additional second order terms that are present in the nonlinear adaptive filter. Note that, the effective number of parameters for an NAF of filter length N, is $N + \frac{N(N+1)}{2}$. Thus for a filter length of 15, the effective number of coefficients is 135! Thus even though the filter length is 15, the parameter space has a dimension of 135 and thus an NAF can be dangerous even if the SEP and SA are separated comfortably. This can be seen in Figure IV.6a and b where the distortion index is close to 10 % for a filter length of 15, while the linear filters exhibited a distortion index of 0.1% for a filter of 100 for the same data.

In essence, the finite cross-correlation between the SEP and SA has a direct influence on the convergence behavior of an SA cancelling adaptive filter. The amount of this influence is directly tied to the relative position of the SEP to the SA waveform. If the filter length of the linear filter within a certain range, called the "close-to-zero"

range of the SEP-SA cross-correlation, then the SEP undergoes negligible distortion. If the filter length exceeds this range, the adaptive filter attempts to model the SEP+SA composite, and tremendous signal cancellation occurs.

Due to the presence of second order terms, the NAF has more degrees of freedom and hence is more affected by the presence of the SEP in the primary input. This affect manifests itself in significant SEP distortion which may still be present even if the SEP and SA are comfortably separated. Thus extreme caution has to be exercised in employing either linear or nonlinear filter to the task of SA cancellation.

Appendix V

RLS and LMS algorithms in Nonlinear SA Cancellation

V.1 Nonlinear Adaptive Filtering

Any discrete, causal nonlinear system can be represented by the infinite Volterra series expansion [35, 36] given by

$$y(n) = h_0 + \sum_{a_1=0}^{\infty} h_1(a_1)x(n-a_1) + \cdots + \sum_{a_1=0}^{\infty}\sum_{a_2=0}^{\infty}\cdots\sum_{a_p=0}^{\infty} h_p(a_1,a_2,\ldots,a_p)x(n-a_1)x(n-a_2)\ldots x(n-a_p) + \cdots \quad \text{(V.1)}$$

where $x(n)$ is the input to the nonlinear system, $y(n)$ is the output and $h_p(a_1, a_2, \ldots, a_p)$ is the p-th order Volterra kernel of the nonlinear system. While the infinite Volterra series can precisely characterize a nonlinear system, due to obvious constraints on the data and computational capacities of a signal processing system one has to work with truncated Volterra series [36]. The second order truncated Volterra series response can be expressed as:

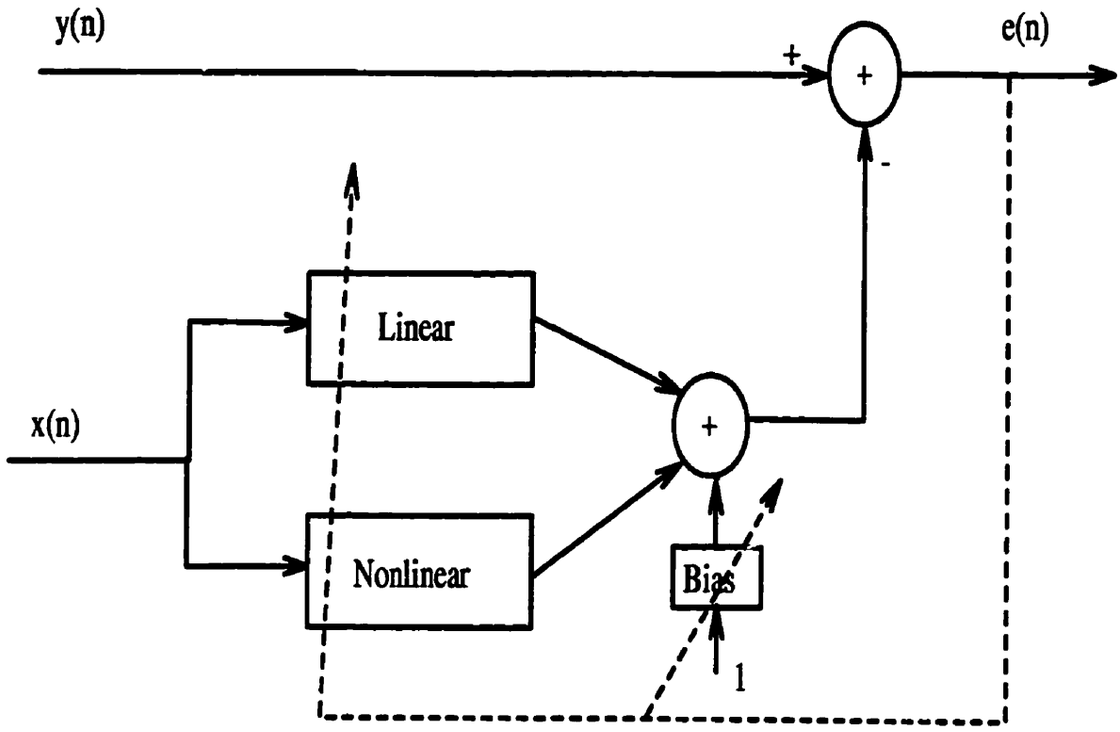

Figure V.1: *Block diagram of the NAF structure as applied to SA cancellation.*

$$y(n) = h_0 + \sum_{i=0}^{N-1} h_1(i)x(n-i) + \sum_{i=0}^{N-1}\sum_{j=i}^{N-1} h_2(i,j)x(n-i)x(n-j) \qquad \text{(V.2)}$$

where N is the system memory, and h_0, h_1 and h_2 are the zero, first (the linear part), and second order (the nonlinear part) Volterra kernels respectively. The Volterra kernels in Eq. V.2 can be adaptively estimated by using an NAF whose block diagram is depicted in Figure V.1. The linear, nonlinear and bias weights are iteratively updated according to some form of adaptation algorithm. Mathematically,

$$\hat{y}(n) = H^T(n)X(n) \qquad \text{(V.3)}$$

and

$$e(n) = y(n) - \hat{y}(n) \qquad \text{(V.4)}$$

where $H(n) = [h_0(n), h_1(0;n), \ldots, h_1(N-1;n), h_2(0,0;n), h_2(0,1;n), \ldots, h_2(N-1,N-1;n)]$ is the kernel vector and $X(n) = [1, x(n), \ldots, x(n-N+1), x^2(n), x(n)x(n-1), \ldots, x(n)x(n-N+1), \ldots, x^2(n-N+1)]$ is the input data vector. The function of an adaption algorithm is to vary the kernel vector H in such a way that some cost function based on $e(n)$ is minimized. Two adaption algorithms are widely used: the Least Mean Square (LMS) algorithm and the Recursive Least Squares (RLS) algorithm. The development of these algorithms is an extension of the LMS and RLS algorithms used for linear FIR filtering, with appropriate changes to the data and weight vectors [36]. A brief theoretical background of these algorithms is given in the following section.

V.2 ADAPTION ALGORITHMS FOR THE NAF

Adaption algorithms of the first type attempt to minimize the mean squared error function. The method of steepest descent and the LMS algorithm fall into this category. The cost function, J(n), [23], can be expressed as

$$J(n) = E'(e^2(n))$$

$$
\begin{aligned}
&= E'((y(n) - H^T(n)X(n))^2) \\
&= E'(y^2(n)) - E'(H^T(n)y(n)X(n)) - E'(y(n)X^T(n)H(n)) + \\
&\quad E'(H^T(n)X(n)X^T(n)H(n)) \\
&= \sigma_y^2 - H^T(n)P - P^T H(n) - H^T(n)RH(n) \qquad \text{(V.5)}
\end{aligned}
$$

where E' is the time-average operator[1], σ_y^2 is the variance of the primary input $y(n)$, P is the time-averaged crosscorrelation vector and R is the time-averaged autocorrelation matrix. The gradient of the mean square function with respect to the kernel vector can be expressed as

$$\nabla J(n) = -2P + 2RH(n). \qquad \text{(V.6)}$$

In the method of steepest descent, the kernel vector $H(n)$ is updated in the direction opposite to the gradient. In other words,

$$
\begin{aligned}
H(n+1) &= H(n) + \frac{1}{2}\mu(-\nabla J(n)) \\
&= H(n) + \mu(P - RH(n)) \qquad \text{(V.7)}
\end{aligned}
$$

where μ is a constant which controls the convergence of the algorithm. The following are the salient features of the steepest descent algorithm [23]:

- The steepest descent algorithm computes the gradient vector **exactly** by using the true autocorrelation matrix and crosscorrelation vectors. Thus it does not suffer from gradient estimation noise and converges to the minimum mean square error.

- The adaptation parameter, μ, is bounded by the largest eigenvalue of the autocorrelation matrix, R. In other words,

$$0 < \mu < \frac{2}{\lambda_{max}} \qquad \text{(V.8)}$$

  where λ_{max} is the largest eigenvalue of the autocorrelation matrix.

[1]In this paper, since we are dealing with single time series records rather than an ensemble of them, time averaged statistics will be used rather than the ensemble average statistics. This approach is more pertinent to the SA data as the artifact is a deterministic waveform.

- The convergence rate of the kernel vector H, is determined by the eigenvalues of the autocorrelation matrix. The eigenvalue spread, $\chi(R)$, of the autocorrelation matrix is defined as

$$\chi(R) = \frac{\lambda_{max}}{\lambda_{min}} \tag{V.9}$$

where λ_{min} is the smallest eigenvalue.

- The total number of eigenvalues in our case is $M = \frac{(N+2)(N+1)}{2}$. The kth natural mode of the algorithm decays exponentially with a time constant given by

$$\tau_k = \frac{-1}{\ln(1-\mu\lambda_k)} \simeq \frac{1}{\mu\lambda_k} \qquad for \quad \mu \ll 1 \tag{V.10}$$

The overall convergence rate of the kernel vector is determined by the weighted sum of M such exponentials each associated with an eigenvalue of the R matrix. Thus small values of μ and λ_{min} result in a slow rate of convergence.

The abovementioned algorithm will not be useful in realtime SA cancellation problems as it requires the true autocorrelation and crosscorrelation information. Thus in realtime situations stochastic gradient search algorithms such as the Least Mean Square (LMS) algorithms are required. In the LMS algorithm the exact gradient vector, $\nabla J(n)$, is replaced by the instantaneous estimate,$\hat{\nabla} J(n)$, given by [23]

$$\hat{\nabla} J(n) = -2y(n)X(n) + 2X(n)X^T(n)\hat{H}(n) \tag{V.11}$$

and the kernel vector update equation is given by

$$\begin{aligned} \hat{H}(n+1) &= \hat{H}(n) + \mu X(n)\{y(n) - X^T(n)\hat{H}(n)\} && \text{(V.12)} \\ &= \hat{H}(n) + \mu X(n)e(n) && \text{(V.13)} \end{aligned}$$

where μ is convergence control parameter. For guaranteed kernel vector convergence, the value of μ is constrained by following bound,

$$0 < \mu < \frac{2}{trace(R)} \tag{V.14}$$

where trace(R) is the sum of all eigenvalues of the R matrix. From Eq. V.13, we see that the LMS algorithm is a very simple algorithm from the implementation point of view. The computational complexity of the algorithm is O(M). However, the instantaneous estimate of the gradient vector manifests itself as noisy kernel vector convergence and contributes to the excess mean squared error [23]. The misadjustment, Θ, which is defined as the ratio of the excess mean squared error to the minimum mean squared error, can be approximated by the following equation,

$$\Theta \approx \frac{\mu(N+2)(N+1)\lambda_{av}}{2} \tag{V.15}$$

where λ_{av} is the average eigenvalue of the autocorrelation matrix. Thus there is a tradeoff in choosing the value of μ, as higher values of μ not only speed up the convergence rate but also result in larger misadjustment. Now taking the expectation on both sides of Eq. V.12, we have,

$$\begin{aligned} E'(\hat{H}(n+1)) &= E'(\hat{H}(n)) + \mu E'(X(n)\{y(n) - X^T(n)\hat{H}(n)\}) \\ &= E'(\hat{H}(n)) + \mu\{P - RE'(\hat{H}(n))\}. \end{aligned} \tag{V.16}$$

Comparing Eq. V.16 with Eq. V.7 we see that the expected value of the kernel vector update in the LMS algorithm follows the steepest descent mechanism. Thus in simulations where the true autocorrelation and crosscorrelation information is readily available, the convergence exhibited by the steepest descent algorithm can be used as the theoretical mean trajectory of the kernel convergence achieved by the LMS algorithm.

Algorithms of the second type attempt to minimize the exact squared error. Instead of estimating the gradient and then applying a correction factor in the direction opposite to it, these algorithms directly work on the autocorrelation and crosscorrelation information. The exponential Recursive Least Squares (RLS) algorithm is one such algorithm wherein the cost function that needs to be minimized is

$$J(n) = \sum_{i=1}^{n} \lambda^{n-i} e^2(i). \tag{V.17}$$

The optimum kernel vector is given by $\hat{H}(n) = R^{-1}(n)P(n)$. The autocorrelation matrix and the crosscorrelation vector can be computed recursively as [23],

$$R(n) = \lambda R(n-1) + X(n)X^T(n) \tag{V.18}$$

$$P(n) = \lambda P(n-1) + y(n)X(n). \tag{V.19}$$

Note that the optimum solution for the kernel vector requires the inverse of the autocorrelation matrix R. Utilizing the matrix inverse lemma, the RLS algorithm for the kernel update is given by, [23],

$$\begin{aligned} G(n) &= 1 + \lambda^{-1} X^T(n) R^{-1}(n-1) X(n) \\ K(n) &= \frac{\lambda^{-1} R^{-1}(n-1) X(n)}{1 + G(n)} \\ \hat{H}(n) &= \hat{H}(n-1) + K(n)\{y(n) - \hat{H}^T(n-1)X(n)\} \\ R^{-1}(n) &= \lambda^{-1} R^{-1}(n-1) - \lambda^{-1} K(n) X^T(n) R^{-1}(n-1). \end{aligned} \tag{V.20}$$

The RLS algorithm therefore, by calculating the autocorrelation matrix and crosscorrelation vector, extracts more information from the input data and hence converges at a faster rate relatively insensitive to the eigenvalue spread of the autocorrelation matrix. This improvement in convergence, however, comes at a penalty of increased computational complexity, of the order $O(M^2)$ where $M = \frac{(N+1)(N+2)}{2}$, N being the filter length of the NAF. Since M increases quadratically with N, small changes in filter lengths of the NAF immensely increase the computational complexity of the RLS based NAFs. Thus RLS based NAFs find themselves close to impractical for realtime SA cancellation except for small filter lengths.

V.3 SIMULATION

V.3.1 Introduction

The main objective of this simulation study is to examine the convergence behavior and computational time of the RLS and LMS algorithms in nonlinear SA cancellation under a wide variety of conditions. Typically, data from a nonlinear system exhibit large eigenvalue spreads. Also, almost always, the true filter length of the underlying nonlinear system is unknown and one has to work with a suboptimal filter length and also in a noisy environment. Thus the main issues that are addressed in the simulations are

- Convergence behavior of the LMS and RLS based NAFs for varying values of eigenvalue spreads.
- Combined effect of suboptimal filter length and large eigenvalue spread on the NAF convergence.
- Effect of background noise on the NAF convergence.
- Computational times for RLS and LMS based NAFs to reach the same plateau of performance for the above three conditions.

V.3.2 Simulation # 1

In this section, the convergence properties of the LMS and RLS based NAFs are investigated for three different values of eigenvalue spread of the data autocorrelation matrix. A five filter length second order Volterra system was simulated using the following kernel vector

$$H_1(k) = \begin{cases} 0, & \text{for k=0, } i.e \text{ no bias weight} \\ e^{\frac{-(k-1)}{10}}, & \text{for k = 1,2,...,20.} \end{cases} \qquad \text{(V.21)}$$

In the first case the input, $x(n)$, to this nonlinear system was a zero mean Gaussian white noise of unit variance and its output is $y(n)$. In the second experiment, $x(n)$, was a colored noise input which was generated by passing zero mean Gaussian white noise through a shaping filter whose impulse response is given by

$$p(n) = K(2 - cnT)e^{-ncT}, \qquad \text{c = 500, T=0.1 msec and K = 400.} \qquad \text{(V.22)}$$

Finally, in the third simulation, an *in vivo* SA waveform which was sufficiently ensemble averaged to reduce the background noise was employed as $x(n)$. The corresponding eigenvalue spreads were calculated as 8.2, 7.9e+3 and 9.9e+7 respectively. In each of these cases, a five filter length NAF driven separately by RLS and LMS algorithms with $y(n)$ as the primary input and $x(n)$ as the reference, was utilized. Thus in each of these simulations, once convergence is established, the kernel vector estimated by the NAF should be equal to the kernel vector given by Eq. V.21. Figure V.1 displays the convergence of two different weights in the NAF-estimated kernel vector for each of the abovementioned simulation cases. Each of these plots compares the convergence rate of the RLS, LMS algorithm and steepest descent algorithms. For the steepest descent algorithm, given by Eq. V.7, the time averaged autocorrelation matrix and crosscorrelation vector were estimated. Two different values of μ were chosen for each of the simulation experiments involving LMS and steepest descent algorithms, with the first value close to the upper bound posed by Eq. V.14 and the second value about an order lower than the first. Note that the theoretical misadjustment for the LMS algorithm in all the above three cases is zero, as theoretical minimum mean squared error is zero. Thus the choice of μ is not that critical as long as it satisfies the constraint imposed by Eq. V.14.

Comparing the convergence trajectories, we can see that the RLS algorithm is insensitive to the eigenvalue spread. Even for the SA input, where the eigenvalue spread is close to 1e+8, the RLS algorithm converged to the optimal solution in less than 50 iterations. The convergence rates of the LMS and steepest descent algorithms

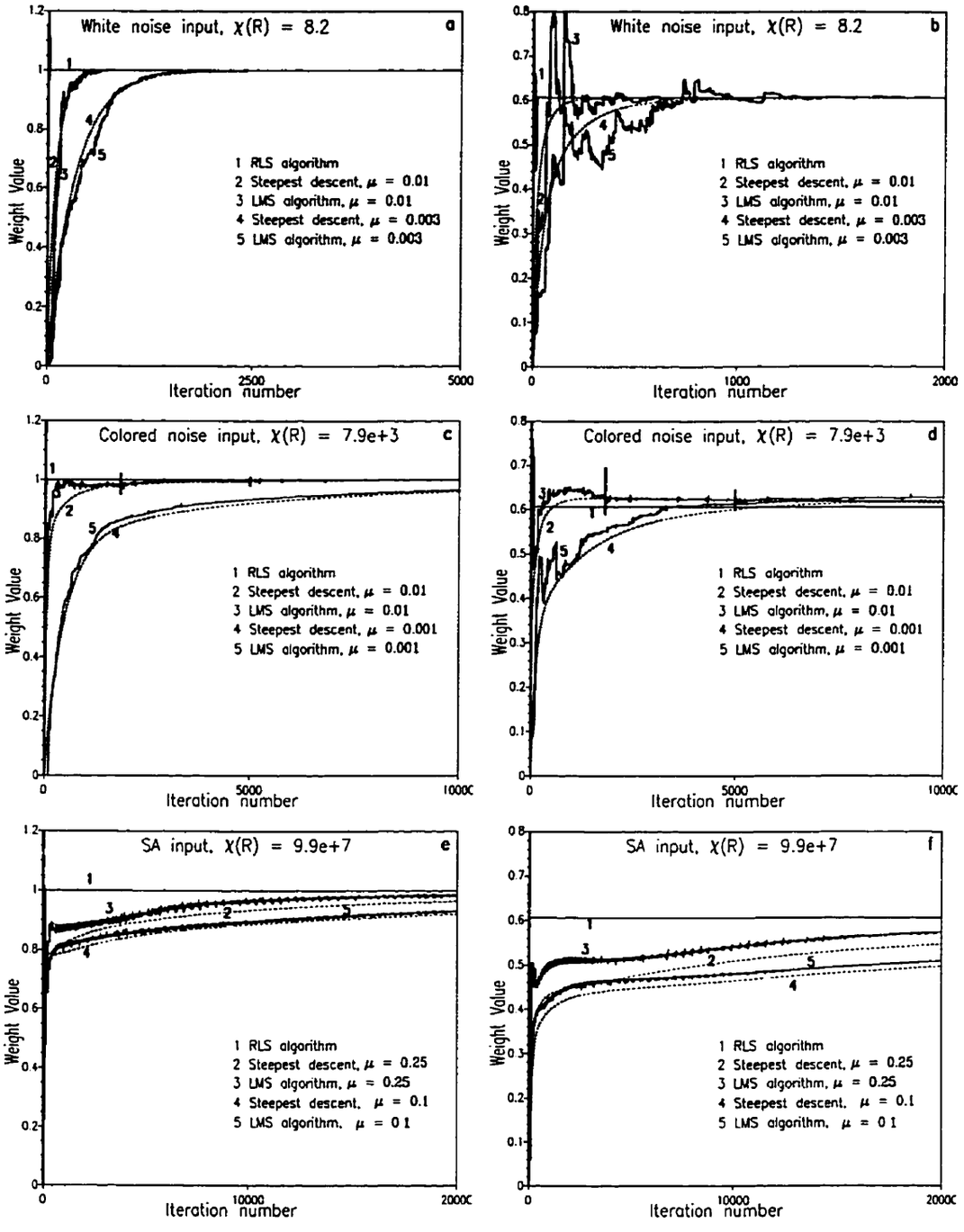

Figure V.2: ***Convergence of the RLS, LMS and steepest descent algorithms for varying eigenvalue spreads.***

on the other hand, are acutely affected by the eigenvalue spread. For the specific case of the SA input, the LMS and steepest descent algorithms can be still seen to be converging even after 20000 iterations. Thus with the SA data which usually possesses large eigenvalue spread, the RLS algorithm achieves significantly faster convergence rates thereby giving better performance in a shorter time.

V.3.3 Simulation # 2

In this section simulations were performed to scrutinize the convergence behavior of the RLS and LMS algorithms with suboptimal filter lengths. With experimental SA data, the underlying filter length is normally unknown. Thus one usually has to work with suboptimal filter lengths in SA cancellation problems. The main thrust behind these simulations is to study the combined effect of large eigenvalue spread and suboptimal filter length on the convergence of these adaption algorithms. The simulation data used for this study are described in the previous section. However, in place of an NAF with a filter length of five (which is the optimal value), an NAF of filter length three was employed. For each of these simulation cases, the theoretical least squares kernel vector was calculated by $H^* = R^{-1}P$ where R is the time-averaged autocorrelation matrix of the reference input and P is the time-averaged crosscorrelation vector. The convergence trajectories of all the three algorithms in reaching this least squares vector are shown in Figure V.3 for two different weight values in the kernel vector. Once again two μ values were assigned for the LMS and steepest descent algorithms. Note that in this simulation case, the theoretical minimum mean squared error is nonzero, and hence larger values of μ for the LMS algorithm result in noisier convergence and excess mean squared error.

The graphs displayed in Figure V.3 illustrate this point where the convergence curves of the LMS algorithm are shown to be noisy for large values of μ. For smaller values of μ, the convergence can be seen to be smoother. Note that the convergence of the steepest descent does not suffer from gradient estimation noise even for large

values of μ, as it uses the exact gradient estimate in calculating its kernel update. From Figures V.3 g-h, we can observe that the LMS algorithm is far away from the optimal solution even after 50,000 iterations. Thus the combination of suboptimal filter length and large eigenvalue spread will have a compounded effect in slowing down the convergence rate of the LMS algorithm, rendering it inefficient for SA cancellation. Another interesting point in Figures V.3 a-h is that the convergence of the RLS algorithm is also affected, except in the case of the SA data. In the case of the white noise and colored noise input data, the RLS algorithm has consumed substantially more data samples for its convergence. This characteristic, however, is not seen with the SA data. A probable reason for this is the estimation errors in computing autocorrelation and crosscorrelation information that is necessary for the RLS algorithm. With suboptimal filter lengths and random input data, the RLS algorithm requires more data samples to compute the auto- and crosscorrelation information. With a deterministic data stream such as the SA data, this estimation does not require a large number of data samples and hence the RLS algorithm converges in approximately the same number of iterations as in the SA cancellation simulation given in the previous section.

V.3.4 Simulation #3

All the simulations performed before were concerned with high ANR (Artifact-to-Noise Ratio) SA data. However, in online SA cancellation experiments the NAF has to combat the omnipresent background noise to cancel the SA. Thus the motivation for this simulation study is to examine the behavior of the LMS and RLS algorithms in the presence of background noise. The SA data used in these simulations are generated as described in the previous two sections. Zero mean white Gaussian noise is then added to both the primary and the reference SA data. The reference ANR was defined as

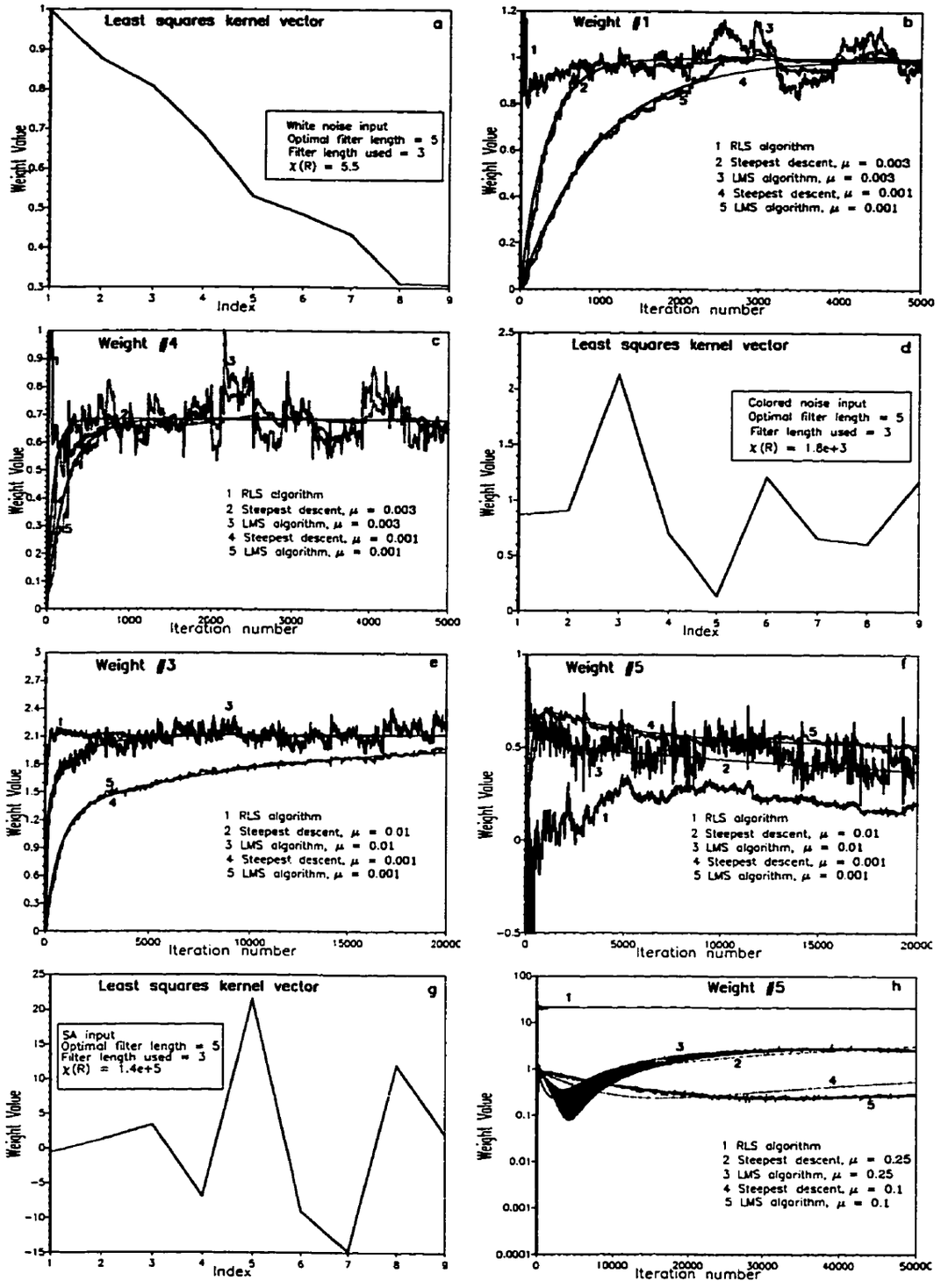

Figure V.3: ***Convergence comparison with suboptimal NAF filter length and large eigenvalue spread.***

$$ANR = 20 \log_{10} \frac{SA_{pref}}{\sigma_N} \tag{V.23}$$

where SA_{pref} is the peak amplitude of the reference SA and σ_N is the standard deviation of the background noise. The ANR for this experiment was found to be 18 dB. Two sets of simulations were performed, one employing an NAF of filter length five and the other utilizing an NAF of filter length three. The results from the simulations are depicted in Figure V.4. Figure V.4a displays the least squares kernel vector for the first set of simulations which was once again computed from the time-averaged autocorrelation and crosscorrelation information. Figures V.4b-c show the convergence of two weights in the kernel vector for the RLS, LMS and steepest descent algorithms. Perhaps the most notable feature among these plots is the fact that the convergence rate of the LMS algorithm is on par with the RLS algorithm. The same feature can be observed in figures V.4e-f where the convergence behaviors of RLS and LMS algorithms for a three filter length is compared. Thus in the presence of noise, the LMS algorithm exhibits convergence speed similar to that of the RLS algorithm.

There are two main reasons for this phenomenon: 1) The eigenvalue spread reduces with the addition of background noise. Note that for the noise free SA data considered in Sections V.3.2 and V.3.3, the eigenvalue spread is close to 1e+8. With the addition of white background noise, the eigenvalue spread dropped to 1e+3 which led to a faster convergence rate, and 2) The convergence speed of the RLS algorithm is slowed down due to the fact that the autocorrelation and crosscorrelation information that is needed for the RLS algorithm suffers from estimation errors in the initial stages due to random background noise and small number of data samples. Thus in an online SA cancellation situation, LMS based NAFs are most suitable as they exhibit similar convergence rates as the RLS based NAFs and are computationally less expensive.

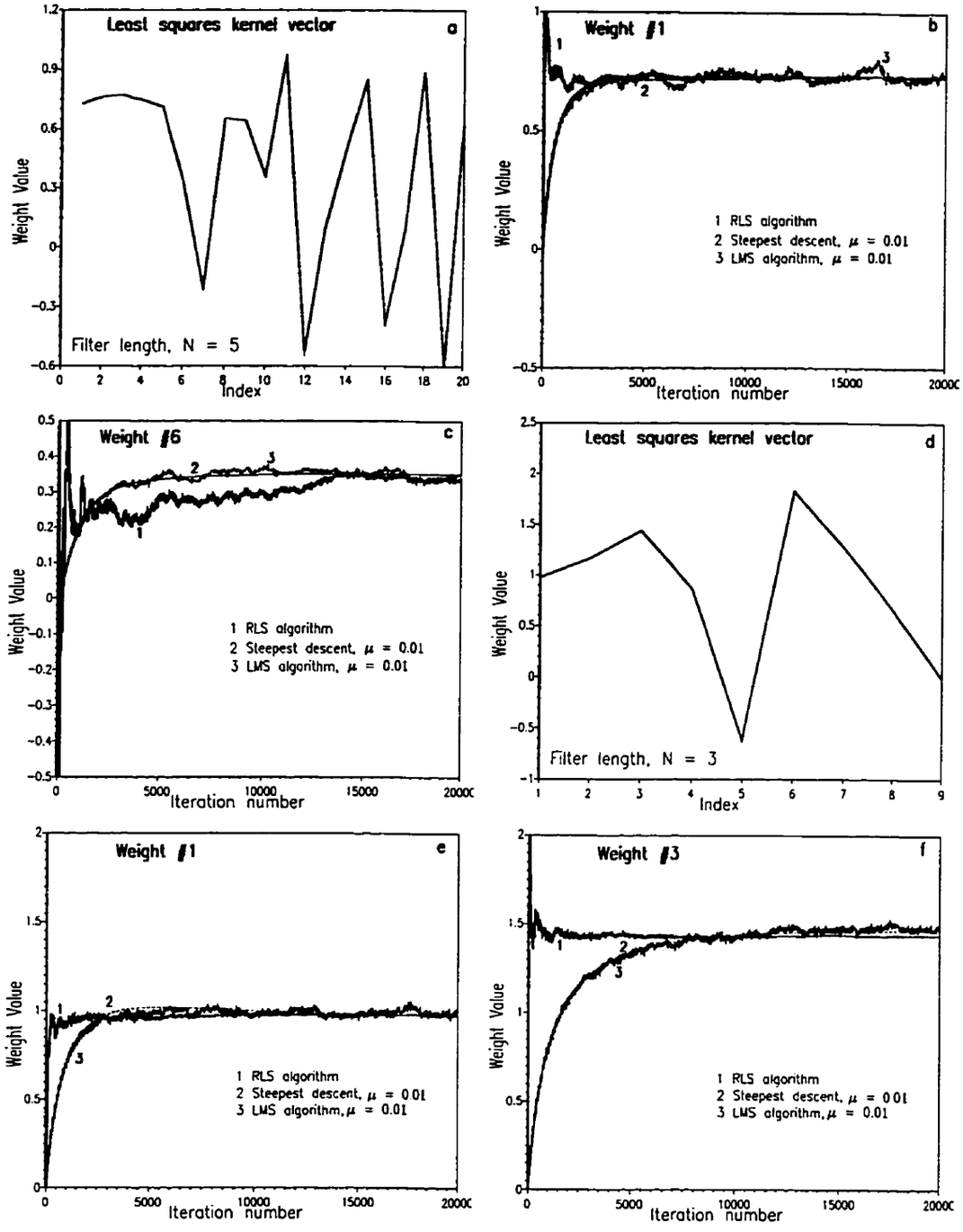

Figure V.4: *Convergence characteristics with noisy SA data.*

V.3.5 Absolute Convergence Times

It was mentioned before that the RLS algorithm is computationally more complex than the LMS but it takes fewer samples to converge to the optimal solution, mainly in high ANR SA environment. However, the absolute time taken by each of the algorithms to converge to the optimal solution is not calculated. The main question is: is the LMS algorithm which is computationally simpler but requires more iterations to converge faster/slower than the RLS algorithm in terms of absolute processing time? This section attempts to answer this question via a table (Table V.1) which tabulates the convergence times (both in number of data samples and seconds) for each of the simulation scenarios described in the previous sections. The following normalized mean squared error criterion was used to assess convergence at the nth iteration (data sample) :

$$\frac{\sum_{i=0}^{M-1}(H^*(i) - H(i,n))^2}{\sum_{i=0}^{M-1}(H^*(i))^2} < 1e^{-3} \tag{V.24}$$

where H^* is the least squares kernel vector, M is the total number of elements in the kernel vector and n is the iteration number. This criterion was evaluated at each iteration and the iteration number and the time taken (in seconds) to satisfy the above criterion were noted down. These values are displayed in Table V.1. Several points can be construed from this table:

- The RLS algorithm takes comparatively fewer data samples and less time to reach a convergence plateau when the optimal filter length is used in the NAF.
- In general, the steepest descent algorithm consumes less computational time than the LMS algorithm. This is because for the steepest descent mechanism given Eq. V.7, the R matrix and the P vector are given *a priori* while the LMS algorithm has to work on the raw data samples and thus carries extra computational baggage.

Simulation case	RLS		LMS		Steepest descent	
	No. of Samples	Time (in secs)	No. of Samples	Time (in secs)	No. of Samples	Time (in secs)
1) White noise input. $\chi(R) = 8.2401$ Optimal filter length=5 Filter length used=5	20	0.3095	485 ($\mu = 0.01$)	4.1354 ($\mu = 0.01$)	371 ($\mu = 0.01$)	1.0052 ($\mu = 0.01$)
			1227 ($\mu = 0.003$)	11.9795 ($\mu = 0.003$)	1241 ($\mu = 0.003$)	3.0257 ($\mu = 0.003$)
2) Colored noise input. $\chi(R) = 7.94e+3$ Optimal filter length=5 Filter length used=5	18	0.2905	2956 ($\mu = 0.01$)	32.0857 ($\mu = 0.01$)	2471 ($\mu = 0.01$)	6.0001 ($\mu = 0.01$)
			19014 ($\mu = 0.001$)	200.1375 ($\mu = 0.001$)	24708 ($\mu = 0.001$)	58.0788 ($\mu = 0.001$)
3) Stimulus Artifact input. $\chi(R) = 9.92e+7$ Optimal filter length=5 Filter length used=5	30	0.3482	28,700 ($\mu = 0.25$)	239.4006 ($\mu = 0.25$)	54,896 ($\mu = 0.25$)	132.4723 ($\mu = 0.25$)
			109,500 ($\mu = 0.1$)	902.1112 ($\mu = 0.1$)	137,241 ($\mu = 0.1$)	337.8875 ($\mu = 0.1$)
4) White noise input. $\chi(R) = 5.5012$ Optimal filter length=5 Filter length used=3	2584	25.9229	4660 ($\mu = 0.001$)	38.2960 ($\mu = 0.001$)	3573 ($\mu = 0.001$)	8.3897 ($\mu = 0.001$)
			3531 ($\mu = 0.003$)	26.3623 ($\mu = 0.003$)	1190 ($\mu = 0.003$)	2.6559 ($\mu = 0.003$)
5) Colored noise input. $\chi(R) = 1.8e+3$ Optimal filter length=5 Filter length used=3	7420	96.2729	NA* ($\mu = 0.01$)	NA* ($\mu = 0.01$)	96,221 ($\mu = 0.01$)	225.0997 ($\mu = 0.01$)
			> 2,620,000 ($\mu = 3e{-}4$)	> 43,699 ($\mu = 3e{-}4$)	2,699,310 ($\mu = 3e{-}4$)	5.1433e+3 ($\mu = 3e{-}4$)
6) Stimulus Artifact input. $\chi(R) = 1.4077e+5$ Optimal filter length=5 Filter length used=3	34	0.3816	NA* ($\mu = 0.25$)	NA* ($\mu = 0.25$)	> 2,590,645 ($\mu = 0.25$)	> 5.6784e+3 ($\mu = 0.25$)
			> 10e+7 ($\mu = 3e{-}4$)	> 10e+4 ($\mu = 3e{-}4$)	> 1e+7 ($\mu = 3e{-}4$)	> 50e+3 ($\mu = 3e{-}4$)
7) SA + noise input. $\chi(R) = 2.621e+3$ Filter length used = 5	19201	516.1992	NA* ($\mu = 0.1$)	NA* ($\mu = 0.1$)	163,372 ($\mu = 0.1$)	417.2019 ($\mu = 0.1$)
			> 10e+7 ($\mu = 1e{-}4$)	> 10e+4 ($\mu = 1e{-}4$)	> 1e+7 ($\mu = 1e{-}4$)	> 50e+3 ($\mu = 1e{-}4$)

Table V.1: *Quantification of convergence rates for RLS, LMS and steepest descent algorithms. Entries under the LMS algorithm marked by asterisks denote μ values for which the convergence criterion was not achieved. This is due to the misadjustment incurred due to large μ values. For these μ values, the convergence times of the steepest descent algorithm can be used as comparative estimates.*

- In most of the cases, the LMS and the steepest descent algorithms take approximately the same number of data samples. In a few cases, the LMS appears to require fewer data samples than the steepest descent. This is probably due to the fact that the LMS update contains gradient estimation noise which can result in the convergence criterion being satisfied even though convergence in the mean has not yet been achieved.

- With suboptimal filter lengths and in the presence of background noise, the RLS algorithm appears to take more computational time, except for the SA case (case #6 in Table V.1). This is, as stated before, due to the large estimation errors in the initial stages of the RLS algorithm with random data. With deterministic data such as the SA data, there is no such problem and the RLS converges much faster.

- With suboptimal filter lengths and in the presence of background noise, the LMS algorithm never satisfies the convergence criterion for large values of μ. This is due to the misadjustment created by the large μ values.

- In the previous section, we stated that in the presence of background noise the convergence rate of the LMS algorithm is on a par with the RLS algorithm. However, that statement is not clear from this table (case #7). This is due to the way the convergence criterion was defined in Eq. V.24, which as mentioned before is never satisfied for large values of μ. If we were to slightly relax the convergence criterion and state that convergence to 1% misadjustment is acceptable — which is common practice in LMS based adaptive filtering applications — then the LMS convergence times will be comparable with those of the RLS.

V.4 EXPERIMENTAL RESULTS

The purpose of this section is to compare the performance of the LMS and RLS algorithms using experimental SA data. Comparative SA reduction by these algorithms with and without SEP is undertaken.

V.4.1 High ANR SA Cancellation

The first set of experiments was concerned with assessing the cancellation capabilities of RLS and LMS based NAFs with noise- and SEP-free SA data. Thus both the primary and reference SA data were obtained through subthreshold stimulation of the peripheral nerve under study. The raw data were then ensemble averaged to diminish the background noise level. One thousand records were used for the SA data acquired from the spinal cord region and two hundred SA records were averaged for the data collected from the wrist region. The ensemble averaged primary and reference artifacts were then fed to an NAF of filter length ten driven by RLS and LMS algorithms separately. The primary and reference SA records were recycled through the respective algorithms until convergence was achieved. Figure V.5 shows the results of this SA cancelling experiment with SA data collected from different subjects using different recording procedures. In each of these plots the ensemble averaged primary SA, the residual SA at the output of the RLS-NAF after the RLS algorithm has passed through 3 SA records and the residual SA by the LMS based NAF after processing 200 SA records are shown. In each of these experiments, the μ value for the LMS algorithm was chosen close to the upper limit given by Eq. V.14.

In Figure V.5a, the primary SA was recorded from the lumbar region while the reference SA was acquired using the second recording channel. The primary SA shown in Figure V.5b was also recorded at the lumbar region but from a different subject. The reference SA utilized for the cancellation of this primary SA was obtained using the same recording channel but at a lower stimulus voltage level. Figures V.5 c

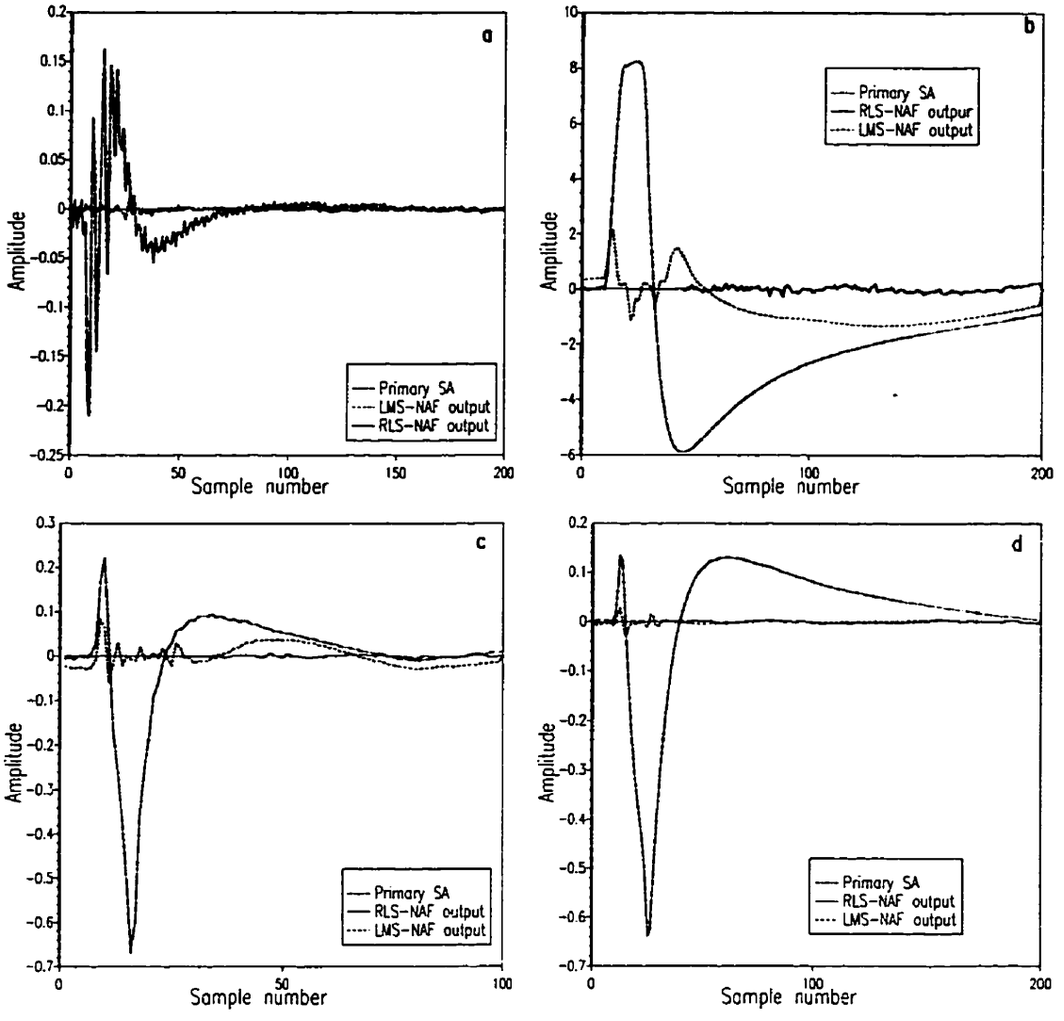

Figure V.5: ***Performance of the RLS and LMS driven NAFs in cancelling*** in vivo ***ensemble averaged SA data collected from different subjects.***

and d display the SAs recorded from the wrist region from two different subjects. The primary SA shown in Figure V.5c was acquired using the Ag-AgCl electrodes while that shown in Figure V.5d was obtained using the stainless steel electrode array. In both the cases the reference SA waveform was obtained using a separate reference channel. From the SA cancellation results, we can observe that the RLS based NAFs significantly reduce the artifact with just 3 SA records irrespective of the data collection protocol. The LMS based NAFs, on the other hand, still produce substantial residual SAs at their output even after 200 records. Thus with high ANR SA data, the RLS based NAFs are the NAFs of choice for SA cancellation.

This point can be put in a different perspective by comparing the performances of the RLS-NAFs and LMS-NAFs for the above experimental data. To quantify the performance of these NAFs, let us define two performance indices, ρ_1 and ρ_2 as

$$\rho_1 = \frac{|SA_p(n)|_{max}}{|SA_o(n)|_{max}} \tag{V.25}$$

$$\rho_2 = \frac{\sigma_{SA_p(n)}}{\sigma_{SA_o(n)}} \tag{V.26}$$

where $SA_o(n)$ is the SA residual at the output of the NAF, $|SA_p(n)|_{max}$ and $|SA_o(n)|_{max}$ are the peak absolute voltage values of the input and residual artifacts respectively, and σ denotes the standard deviation. The performance indices of the RLS and LMS based NAFs for the experimental SA data described above are shown in Figure V.6. Each row in this figure graphs the two performance indices corresponding to each of the experimental cases shown in Figure V.5. These plots can be used as alternatives to the convergence plots described in the simulations section. They also convey more information than the standard weight convergence plots as they offer an inkling about the actual SA cancellation. From each of these graphs, we can observe that the performance of the RLS based NAFs has reached close to its maximum value in approximately 5-10 SA records. The LMS based NAFs are still in the process of convergence even after 200 SA records. Thus in cancelling ensemble averaged SA data, RLS based NAFs are more efficient than their LMS based counterparts.

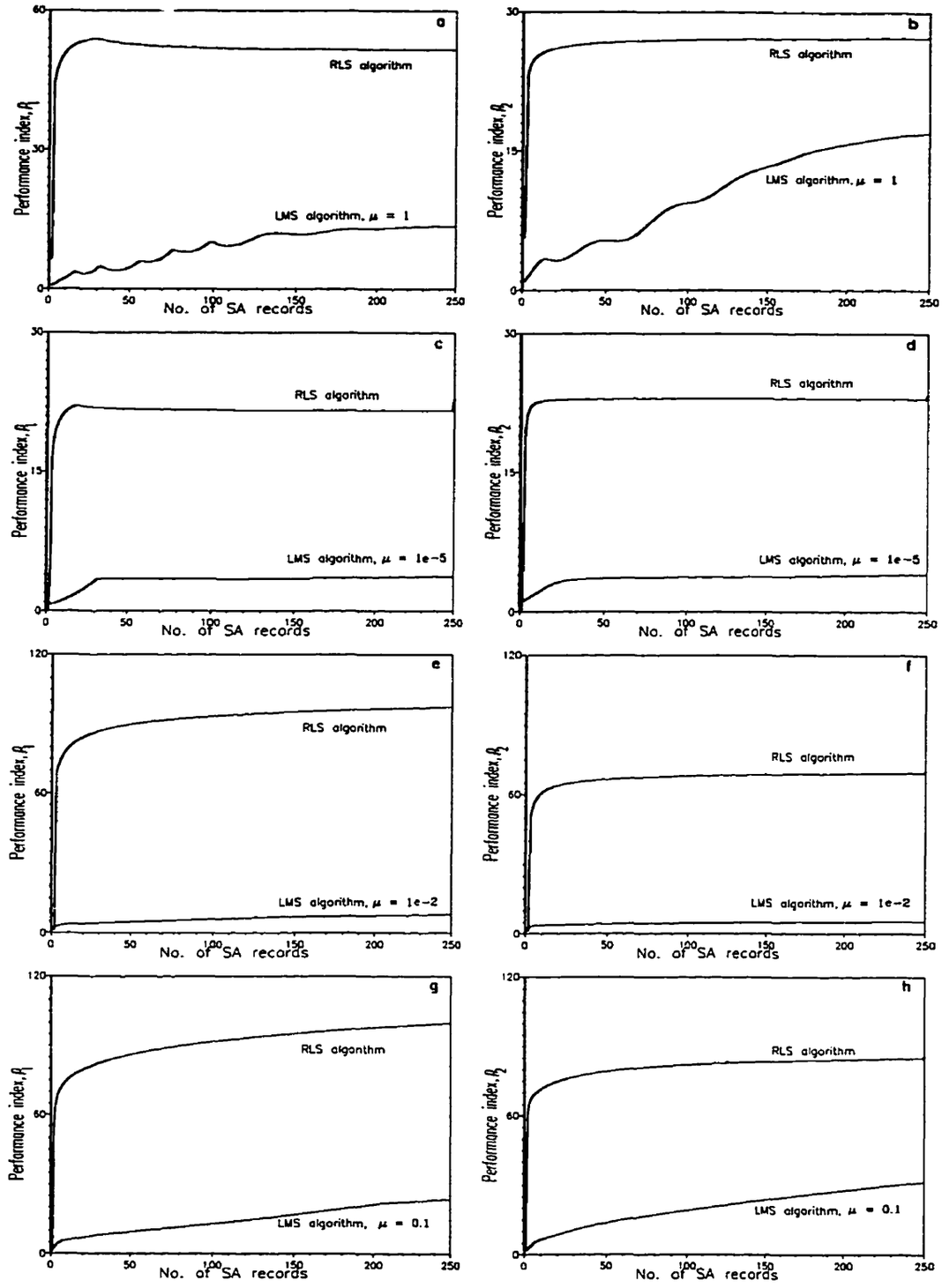

Figure V.6: ***Performance comparison of RLS driven and LMS driven NAFs in cancelling ensemble averaged SA data.***

V.4.2 SA Cancellation in the presence of background noise

It is clear from the previous section that good SA cancellation results can be obtained with noise-free primary and reference SA data. However, in realtime SA cancellation applications, the NAF algorithm has to deal with the background noise. In simulations, it has been noted that in the presence of background noise, LMS-NAFs exhibit comparable convergence rates to the RLS-NAFs. In this section, an experimental example is given to illustrate the effect of background noise on the performance of the NAFs.

The primary and reference inputs were collected from the wrist region using the stainless steel electrode array. Once again the stimulus voltage level was set below the threshold of the median nerve ensuring that no SEP was recorded. The reference ANR was calculated to be 15 dB in this case. The raw primary and reference data were then fed to an NAF of filter length ten driven separately by the RLS and LMS algorithms. Both the algorithms converged to the steady state kernel vectors within 20 SA records. The primary input after the 20th SA record is shown in Figure V.7a. Figure V.7b and V.7c show the residuals at the output of the RLS and LMS based NAFs respectively for the same data. It can be seen that both the algorithms were successful in reducing the SA down to the background noise level. Figure V.7d compares the ensemble averaged primary SA with the residual averaged SA at the output of the two NAFs. The ensemble averages for both the NAFs were computed after the first 20 SA records. From this picture, we can note that the SA cancellation ability of an NAF is affected by the presence of noise and that the LMS based NAF produced an output similar to that of the RLS driven NAF. Thus in the presence of background noise, LMS based NAFs display levels of performance similar to the RLS based NAFs. This is due to the fact that the huge eigenvalue spread associated with the averaged data reduces considerably with the addition of background noise.

V.4.3 SEP + SA data

All the experimental results described so far have been SEP-free. To scrutinize the effectiveness of the NAF in enhancing the SEP from the interfering SA, both *in vivo* MSEP and SSEP data corrupted by the SA were processed. The MSEP data were acquired by placing Ag-AgCl electrodes approximately over the nerve axis. The tail of the artifact can be seen to interfere with the initial stages of the MSEP in Figure V.8. The reference SA waveform in this case was obtained through subthreshold stimulation. The SSEP data were recorded from the lower lumbar region of the spinal cord using Ag-AgCl electrodes. The SA waveform in this case not only seems to interfere with the initial phase of the SEP but also seems to induce a bias in the SEP. The reference SA was obtained from the second recording channel. Two hundred records were averaged for the MSEP data and one thousand records were averaged for the SSEP data.

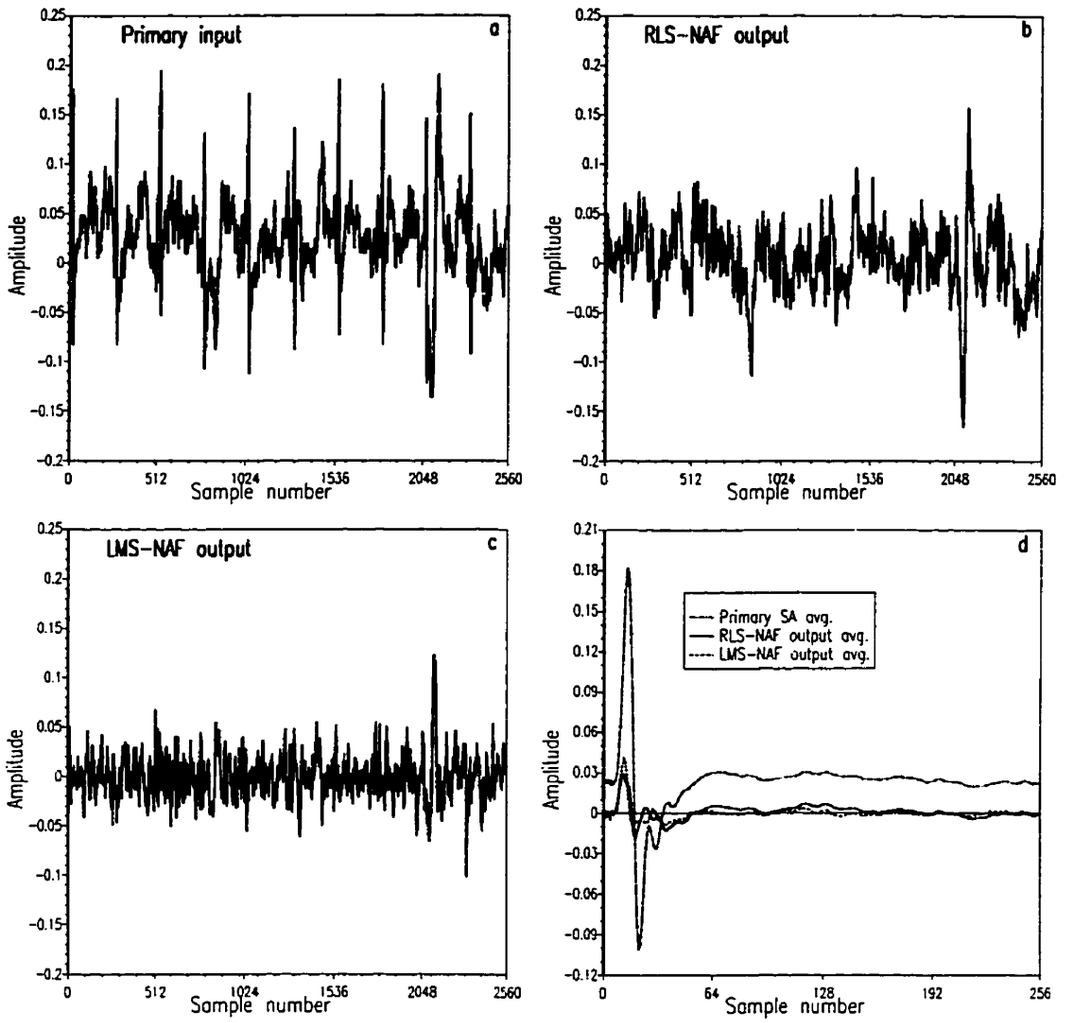

Figure V.7: ***Performance of the RLS and LMS driven NAFs in cancelling*** in vivo ***SA in the presence of background noise.***

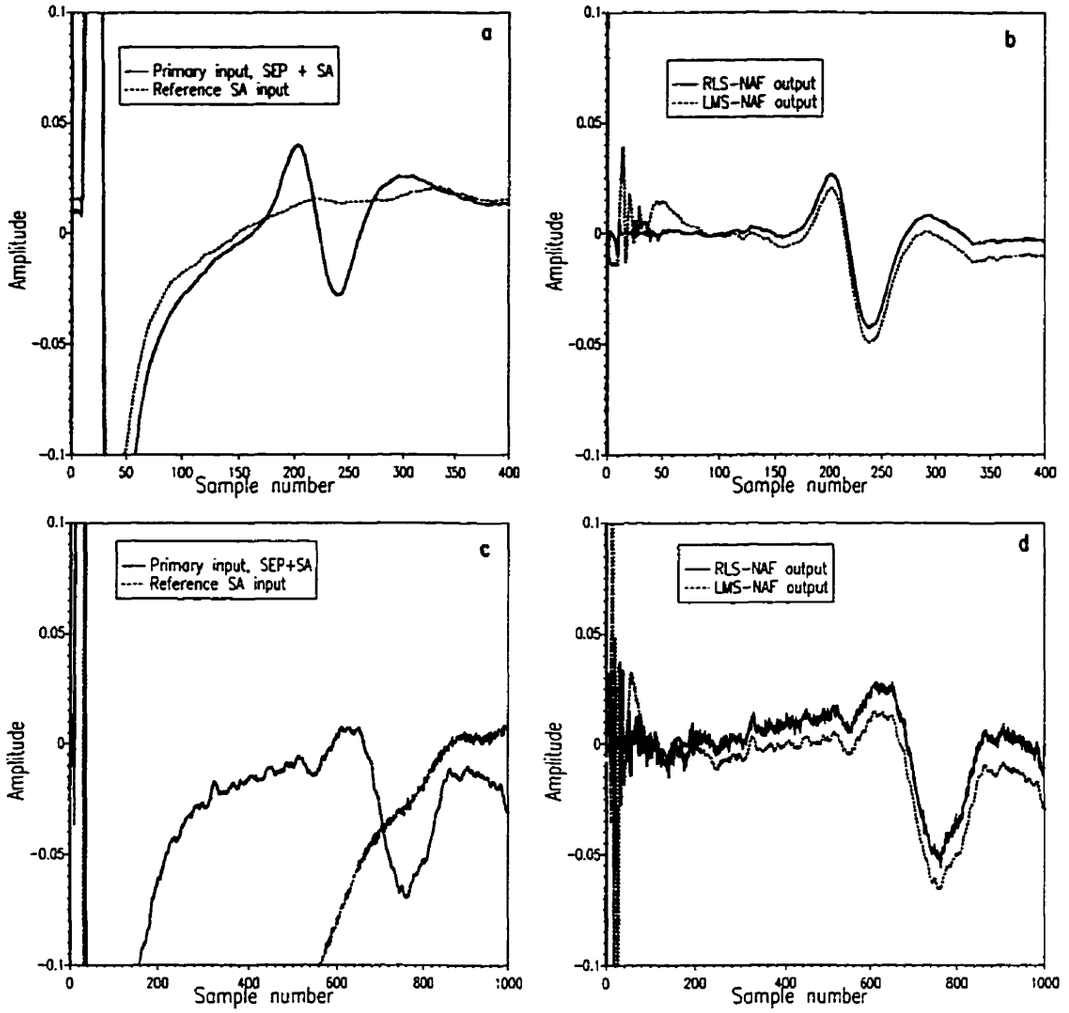

Figure V.8: ***SEP enhancement by RLS and LMS based NAFs.***

A slight modification was made to the RLS and LMS adaption algorithms to cancel the SA. The algorithms were allowed to update the kernel vectors only during the supposed SA phase *i.e* during the first 100 samples for the MSEP data and first 500 samples for the SSEP data. The reason for this segmented adaption procedure was the negative effect of the SEP in the primary channel on the kernel convergence, as explored in Appendix IV. The kernel vector at the end of the SA region is then fixed and these kernel weights are used to filter the remaining data. From the results shown

in Figures V.8b and V.8d we can observe qualitatively that RLS based segmented NAFs provide a good quality SEP estimate which is devoid of much of the artifact and any bias. The LMS based NAF on the other hand still contains substantial artifact even after 200 SA records. Thus RLS based NAFs offer good SEP enhancement results when utilized with ensemble averaged SEP data.

V.5 Discussion

Nonlinear adaptive filters based on second order truncated Volterra series are shown to be effective in reducing the SA interference. One of the important factors dictating the performance of an NAF is its adaption algorithm. Different adaption algorithms are available in the literature and the choice is still a hotly pursued research area. There are a variety of trade-offs involved with each of these adaption algorithms and an understanding of these trade-offs is essential before putting these algorithms to the task of SA cancellation. In this appendix, we concentrated on the two basic algorithms *viz.* the LMS algorithm and the RLS algorithm. From both the simulation and experimental results, we can see that the RLS based NAFs significantly outperform LMS based NAFs with high ANR data. The main reason for this is the huge eigenvalue spread associated with the high ANR SA data. With the addition of background noise, however, the eigenvalue spread decreases and the LMS based NAFs exhibit comparable convergence rates and performance indices to RLS based NAFs. Thus the answer is clear: use RLS-NAFs for SA cancellation in ensemble averaged SEP data and LMS-NAFs for realtime SA cancellation. This is intuitively quite appealing as the LMS-NAFs are computationally less complex and are best suitable for realtime SA cancellation. The drawback, however, is that there is a significant amount of residual artifact at the output of the NAF in the presence of background noise. The only way to diminish this artifact is to ensemble average at the reference input of the NAF. This brings us to the next question: when to average and when

not to average? This point is discussed under four scenarios, the first three are offline processing experiments and the last one is a realtime SA cancellation scenario:

1. **Time invariant SA and time invariant SEP**. This is the most benign situation in which ensemble averaging can be performed on both the primary and reference SA data, and an RLS based segmented NAF can be employed to significantly reduce the SA.

2. **Time varying SA and time invariant SEP**. Here once again, ensemble averaging can be performed on both the primary and reference channels and the resultant averages can be used for SA cancellation by the RLS-NAF. The time varying nature of the SA is not a factor, as the NAF will converge to the *averaged* Volterra model between the primary and reference SAs.

3. **Time varying SEP**. In most of the surface recorded SEP experiments, the initial Signal-to-Noise Ratio (SNR) is small and ensemble averaging needs to be performed in order to unveil the SEP. In rare cases, it might be required to track the single sweep SEPs from record to record. Even in this case, ensemble averaging can still be performed on the **reference input** and an RLS based segmented NAF can be employed. Since the NAF is primarily affected by the statistics of the reference SA data, the averaged reference SA waveform will result in good SA cancellation while still protecting the time varying properties of the SEP.

4. **Realtime SA cancellation**. In realtime SA cancellation situations, the LMS based NAFs are the filters of choice mainly because of their computational simplicity and their equally good performances as the RLS-NAFs. However, as discussed in Chapter 5 and Appendix IV, the adaptation process should be segmented to avoid the perils associated with the presence of the SEP in the primary input to the NAF.

Appendix VI

Probability of an ECG Occurance in an SSEP Record

A rough calculation of the probability of an ECG occurence in an SSEP record is undertaken in this Appendix. The problem can be formulated based on Figure VI.1. Before we actually formulate the problem, the following assumptions are in order about the ECG and SSEP characteristics:

- The heart beat is 60/min *i.e* there is only one ECG waveform every second.
- The stimulus rate for the SSEP generation is greater than or equal to one per second, thus making sure that there is at least one SSEP every second.
- The ECG does not simultaneously occur in two SSEP records which is true in SSEP experiments as the stimulus rate is low.

Figure VI.1 depicts an ECG waveform and an SSEP record. Here N_{ECG} denotes the length of the ECG window (in samples) during which the ECG is deemed to have significant effect on the SSEP record, and N_{SEP} is the length of the SSEP record (again in samples). An ECG is said to have occured in a SSEP record if there is at least a

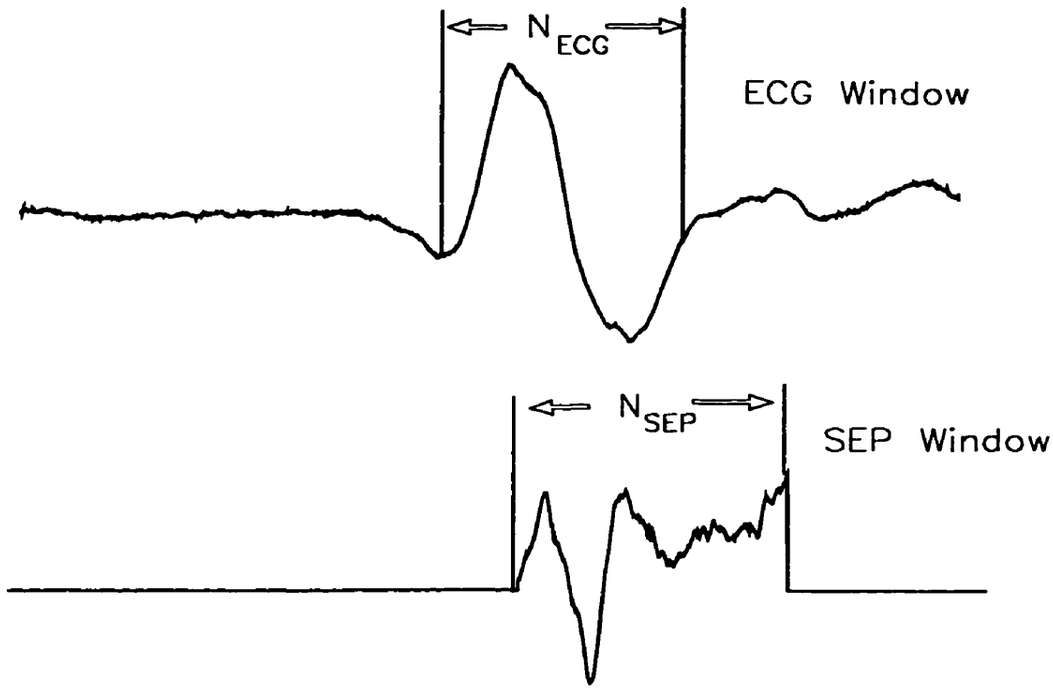

Figure VI.1: *ECG and SSEP waveforms for probability calculation. Note that the two waveforms are not drawn to scale.* N_{ECG} *is the length of the "effective" ECG window and* N_{SEP} *is the length of the SSEP data record. The problem is to find the probability of intersection of these two windows.*

sample overlap between these two windows. Assuming there is only one SSEP per second (*i.e* the stimulus rate is 1 Hz), this probability can be calculated as,

$$P(ECG_{occurence}) = \frac{N_{ECG} + N_{SEP} - 2}{N_{samp}} \tag{VI.1}$$

where N_{samp} is the total number of samples per second. As an example, if 1024 samples are collected with each stimulus at a sampling rate of 20,000 Hz and the effective ECG window length is 1500 samples, then the probability is,

$$\begin{aligned} P(ECG_{occurence}) &= \frac{1500 + 1024 - 2}{20000} \\ &= 0.1262 \text{ or } 12.61\% \end{aligned} \tag{VI.2}$$

If the stimulus rate is greater than 1 Hz, the probability value given by Eq. VI.1 is divided by the stimulus rate. Table VI.1 summarizes the probability values calculated from experimental SSEP data from various subjects along with the predicted theoretical values. From this table we can see that the experimental probability values are higher than the theoretical values for all the subjects. This is probably due to the fact the theoretical calculations assume the ECG rate is only 60/min. In practice, however, the rate is closer to 72/min which results in higher probability of ECG contamination. In addition, the actual stimulus rate used in the experiments was approximately 2.6/sec which also contributes to the difference between the theoretical and predicted values.

Subject	SSEPs with ECG	P (ECG) (Exp.)	N_{ECG}	N_{SEP}	N_{samp}	P(ECG) (Theory)
subject #1	93 out of 1000	9.3 %	1500	1024	20000	6.3%
subject #1	89 out of 1000	8.9%	750	512	10000	6.3%
subject #2	72 out of 1000	7.2%	750	256	10000	5.1%
subject #2	89 out of 1000	8.9%	750	512	10000	6.3%
subject #3	106 out of 1000	10.6%	1500	1024	20000	6.3%
subject #4	23 out of 250	9.2 %	750	256	10000	5.1%
subject #5	81 out of 1000	8.1%	750	256	10000	5.1%

Table VI.1: *Probability of ECG occurence in a SSEP record for different subjects. A stimulus rate of 2 Hz and an ECG rate of 60/min is used for calculating the theoretical probability values.*